Novel Atmospheric Monitoring for the H.E.S.S. site and its Industrial Applications

HADJICHRISTIDIS, CHRISTOS

Novel Atmospheric Monitoring for the H.E.S.S. site and its Industrial Applications

Christos N. Hadjichristidis, M.Sci.

A Thesis presented for the degree of
Doctor of Philosophy

Very High Energy Gamma Ray Group
Department of Physics
Durham University
England

Dedication

Στον Νίκο που το θέλησε πιότερο κι από μένα

Novel Atmospheric Monitoring for the H.E.S.S. site and its Industrial Applications

Christos N. Hadjichristidis

Submitted for the degree of Doctor of Philosophy

Abstract

This thesis concerns the atmospheric monitoring instrumentation for the H.E.S.S. (High Energy Stereoscopic System) γ-ray telescope site and the adaptation of such instruments for commercial use. The effect of the atmosphere on the H.E.S.S. telescopes' response has been demonstrated and the technicalities associated with the atmospheric monitoring instruments have been studied in depth. The responses of a LIDAR (Light Detection And Ranging) and a transmissometer have been checked by customised MODTRAN (MODerate resolution atmospheric TRANsmission) routines. This process revealed a malfunction of the LIDAR, whose raw data was independently treated to yield meaningful results. More importantly, the 'Durham-designed' transmissometer, manufactured to operate during the night in parallel with the H.E.S.S. telescopes, was successfully adapted for day-light operation. As a result Durham prototype gained strong interest from Aeronautical & General Instruments Limited (AGI) in Dorset, who are particularly interested in the airport applications, and see the Durham instrument as a potential replacement for the transmissometer which they manufacture currently and is coming to the end of its useful design life. Durham University and AGI drew up a license agreement to pursue further development of the instrument. The resulting Durham aviation transmissometer meets the accuracy requirements for the Runway Visual Range (RVR) assessment imposed by both the World Meteorological Organisation (WMO) and the International Civil Aviation Organisation (ICAO). Moreover, the Durham instrument is easy to align, uses very little power, and is lightweight and portable, enabling its use not only in civil airports, at altitudes exceeding all prior-art aviation transmissometers, but also in tactical military applications, such as remote landing strips.

Declaration

The material contained within this thesis has not previously been submitted for a degree at the University of Durham or any other University. The research reported within this thesis has been conducted by the author unless indicated otherwise.

Acknowledgements

There are too many people to acknowledge for their assistance and support throughout the long and winding road that led to the completion of this thesis. I am especially indebted to my supervisors, Dr. J.L. Osborne and Dr. P.M. Chadwick, for their assistance, friendliness and good advice. John, thanks for your support including the lucullian dinners offered by your kind wife. Paula, thanks for undertaking the inelegant task of proofreading the many versions of this thesis and for your gentle push towards the finishing line. It is also a pleasure to acknowledge the expert help received by two good colleagues and friends, Mr. David Allan and Dr. Roland Le Gallou, without whom the construction of the Durham aviation transmissometer would have been impossible. I would also like to thank Dr. Andrew Kirby and Mr. Chris Moore for their invaluable technical expertise.

This thesis has been made possible through the provision of facilities in the Department of Physics at Durham University. I wish to especially thank Prof. Mike Pennington and The Ogden Trust for partially funding my work through the Teaching Fellowship Scheme. I also wish to express my gratitude to Mr. Ian Clark, Mr. Chris Gardiner and Mr. Paul Robson of Aeronautical & General Instruments Limited (AGI) for their confidence in Durham's aviation transmissometer leading to two successive grants under the PPARC (now STFC) Industrial Programme Support Scheme (PIPSS).

I would like to thank all the past and present colleagues at the VHE γ-ray group for their good company and advice. Denise, Joy, Anthony and Alistair for their ability to put up with sharing an office with me. Sam, Michael, Ian, Hugh and Cameron for their help when it was most needed. My good friends Aris and Ulisses for making me feel at home. Steve who never failed to send me his infamous donkey

Christmas cards and the list goes on and on ...

Last but by no means least, I wish to express my gratitude to my parents and my own Lia, Aaron and Vangelis for their continuous love and support.

Contents

List of Figures

List of Tables

Chapter 1

Thesis Overview and Personal Contribution of the Author

1.1 Introduction

This thesis is concerned with the atmospheric monitoring of the *H*igh *E*nergy *S*tereoscopic *S*ystem (H.E.S.S.) experiment in Namibia and explores the adaptation of the 'purpose built' transmissometer for industrial uses. A short overview of each chapter followed by an analytical description of the author's personal contribution will be drawn in the following Section.

1.2 Author's Personal Contribution

- The second chapter consists of a general introduction to the field of the ground based γ-ray astronomy. The different production mechanisms of energetic γ-rays are briefly sketched. The principles of the imaging atmospheric Cherenkov technique are discussed followed by the presentation of the H.E.S.S. experiment. The chapter concludes with simulations of a stand-alone H.E.S.S. telescope under different atmospheric assumptions. The author's original contribution is drawn below:

  1. generating γ-ray induced showers using a modified version of MOCCA (*Mo*nte *C*arlo *Ca*scade) program,

2. adapting the CameraHess simulation package in order to accept more efficiently the simulated γ-rays, and
3. writing a Root program to automatically calculate the stand-alone H.E.S.S. telescope effective area from the results obtained after feeding the MOCCA generated γ-ray showers into the camera simulation program.

- The third chapter provides the motivation for atmospheric monitoring of the H.E.S.S. site, which constitutes the main responsibility of the Durham University VHE Gamma Ray Group. A detailed description is given for each instrument commissioned. Special emphasis is placed on the *D*urham *N*ight-time *T*ransmissometer (DNT), considering its later adaptation for industrial use. Finally, the results obtained from the transmissometer are utilised by the MODTRAN (i.e. **MOD**erate spectral resolution atmospheric **TRAN**smittance algorithm and computer program) for the generation of nightly site-specific atmospheric models allowing the quantification of the atmospheric effect on the telescopes efficiency (i.e. trigger rate, effective area). The author's personal contribution was to:

  1. analyse the transmissometer data,
  2. adapt the MODTRAN code in order to generate atmospheric transmission tables based on the transmissometer readings, and
  3. explore the limitations in incorporating the transmissometer within the H.E.S.S. active atmospheric calibration scheme.

- The fourth chapter is dedicated to the two commercial LIDARs (*Li*ght *D*etection *A*nd *R*anging) operating in the Namibian site. The work has focused on the new ALS 450 XT LIDAR with the hope of extracting optical depths that can be directly fed into the H.E.S.S. simulations. The author's contribution in this chapter was to:

  1. identify that the LIDAR was operating below specifications in terms of its power output,

2. prove that the LIDAR manufacturer used an erroneous assumption for the LIDAR ratio yielding meaningless atmospheric extinction profiles,
3. derive a realistic LIDAR-ratio based on site-specific analytical back trajectories and satellite measurements of the aerosol index,
4. compare the corrected LIDAR signal against both MODTRAN simulations and the telescopes' cosmic-ray trigger-rate with positive results, and
5. derive an alternative use of MODTRAN code that utilises the transmission directly as an atmospheric model selector as opposed to the wind speed.

- The fifth chapter marks a turn from H.E.S.S. oriented research to the adaptation of the DNT for industrial use. Initial investigations suggested that the innovative design of this instrument could have applications in the airport industry if we could make an instrument that would operate during daylight hours whilst simultaneously reducing the manufacturing costs. This task was undertaken by the author that was appointed to work half-time on the PPARC project. Co-investigator Dr. Roland Le Gallou provided his knowledge from the construction of the transmissometer in Namibia until he left Durham for a post in his native France in April 2006. Mr. David Allan and Mr. Chris Moore provided expertise in camera control and printed circuit board design respectively. Mechanical parts (mount, protective hoods etc.) were manufactured by the workshop in the Department of Physics at Durham. The author's personal contribution to the project was to:

  1. select reliable components for the quick development of the daylight-operating prototype,
  2. incorporate the DNT's operational algorithm within the selected camera's driving program,
  3. optimise the system's hardware and software for daylight use (i.e. eliminating background noise, averaging-time and spot-size optimisation),
  4. calibrate the instrument and check its performance,

5. estimate the transmissometer's uncertainty budget, thereby identifying ways of error minimisation, and
6. liaise with possible licensees for promoting Durham's transmissometer into a commercial instrument.

- Finally the sixth and seventh chapters provide the status of the current work that aims to transfer Durham's daylight-prototype into an reliable aviation transmissometer. The author was appointed to work full time on the project with the following responsibilities:

  1. identify the specifications needed for a commercial instrument by working with the licensee and distributor;
  2. select instrument components and optimise the optical design taking the above specifications into account;
  3. write and optimise the measurement algorithms (i.e. implementation of centroid algorithm, use of innovative modulation on both CCD exposure time and LED driving current to optimise the instrument's dynamic range, derivation of the large aperture background threshold-based measuring algorithm, etc);
  4. calibrate the instrument check its linearity and ensure that the device is performing to specification;
  5. derive an innovative design and method allowing for the online monitoring of the instrument's window contamination without being in conflict with already patented designs, and finally
  6. explore the possibilities for an automatic calibration of the instrument without the need of user intervention.

  David Allan is responsible for the translation of the control software into Visual Basic, the design of the 'front end' for users, the design of the temperature-controlled LED and the mechanical construction of the instrument.

Chapter 2

Very High Energy Gamma Ray Astronomy

2.1 Brief History of γ-ray Astronomy

The initiation of γ-ray astronomy is usually identified with Morrison's paper, which was the first to focus on the feasibility and merits for γ-ray detection of astrophysical origins (Morrison, 1958). The cosmic γ-ray flux, however, had been measured prior to that by both balloon and rocket experiments (Bergstrahl and Schroeder, 1952; Johnson et al., 1954). These first measurements, coupled with more extensive research triggered by Morrison's paper, led to the detection of hard solar events and provided crude upper limits to the cosmic γ-ray fluxes of the order of 1 photon $\mathrm{cm}^{-2}\,\mathrm{s}^{-1}$ (Peterson and Winckler, 1958; Peterson, 1997). It soon became apparent that the predicted fluxes were optimistic. In addition, background effects caused by the charged cosmic ray particles triggered extensive design development that led to production of the active anti-coincidence shield originally suggested by Frost and Rothe (Frost and Rothe, 1962). A device based on this design aboard the spacecraft OSO-III was used for the first firm detection of γ-rays with energies of $\sim$ 100 MeV from the centre of the galaxy (Kraushaar et al., 1972). In the following years, the launch of NASA's SAS-2 (Fichtel et al., 1975), followed by the European COS-B satellite, resulted the first mapping of the galactic plane and the discovery of discrete sources such as the Vela pulsar. The field of high energy (50

MeV− 100 GeV) γ-ray astronomy was brought to maturity with the launch of the *C*ompton *G*amma *R*ay *O*bservatory (CGRO) in 1991. The EGRET instrument on-board CGRO was successful in detecting 271 γ-ray sources at energies above 100 GeV (3^{rd} ERGET catalog shown in Fig. 2.1, (Hartman et al., 1999)). At the time of concluding this thesis (May 2009) there exist two satellite based high energy γ-ray experiments namely AGILE (Tavani et al., 2008) and the recently launched GLAST, renamed Fermi (Lichti and von Kienlin, 2008).

Above energies of $\sim$ 100 GeV the γ-ray fluxes become too small to be measured by satellites due to effective area limitations imposed by their physical restrictions. Thus, in the energy regime $>$ 100 GeV γ-ray astronomy is conducted from the ground. This thesis will revolve around the most promising technique of ground based γ-ray astronomy, namely the *I*maging *A*tmospheric *C*herenkov *T*echnique (IACT). The IACT will be discussed in detail in Section 2.5.5 after the brief presentation of the production of *V*ery *H*igh *E*nergy (VHE) $\gamma-$rays that follows .

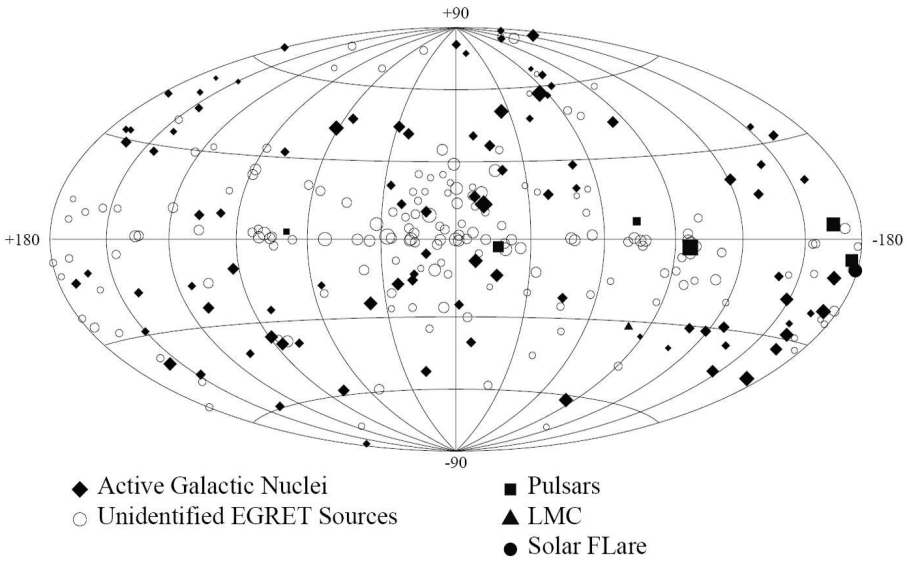

Figure 2.1: The 3^{rd} EGRET catalogue shown in galactic coordinates. The size of each symbol represents the relative intensity of the source as registered by EGRET. Extracted from Hartman et al. (1999).

2.2 Production of TeV γ-rays

The detected population of credible TeV γ-ray sources of various classes implies that the main sources of γ-ray and cosmic-ray (CR) emission are the same. The production of the CR's could be categorised in a very general manner as follows:

- **Bottom up**: charged low energy particles are accelerated to high energies. The most popular model for charged particle acceleration is the second order Fermi mechanism,

- **Top-down**: highly energetic particles are produced from the decay or annihilation of a massive particle M_x (10^{14}-10^{16} GeV). These particles may be produced continuously as decay products of some topological defects (such as magnetic monopoles and super-contacting strings) or may have been directly produced in the early universe and, due to some unknown asymmetry, have a lifetime that exceeds the age of the universe (Sigl, 2001).

Even though top-down scenarios could provide a "by definition" explanation for the particles observed with HiRes (Abbasi et al., 2008) (not although those observed with AGASA (Teshima, 2001), with energies apparently exceeding the Greisen-Zatsepin-Kuzmin cutoff (Greisen, 1966; Zatsepin and Kuzmin, 1966)), they appear to be ruled out by the high GeV γ-ray intensity produced from cascades initiated by X-particle decay (Protheroe and Stanev, 1996). Moreover, topological defects predict that the highest energy CR's are predominantly photons, a fact which seems to disagree with the experimental evidence (Unger, 2007; Arisaka et al., 2007). At the time of concluding this thesis (May 2009), HiRes and Auger observations strongly support the existence of the GZK cutoff (Sokolsky, 2008).

No matter what the scenario of the production of highly energetic CR's, the generic mechanism of the high-energy γ-ray process is the interaction of a relativistic electron or nucleon with matter or in a magnetic field. The physical processes responsible for γ-ray production of energies relevant to ground based astronomy (100 GeV - 100 TeV) are briefly outlined below.

2.2.1 Hadronic γ-ray Production

γ-rays can be produced from the decay of π°, which in turn could be the product of nucleon-antinucleon annihilation or the inelastic collision of CR's (predominantly protons) with the interstellar matter. This process is illustated in Fig. 2.2.

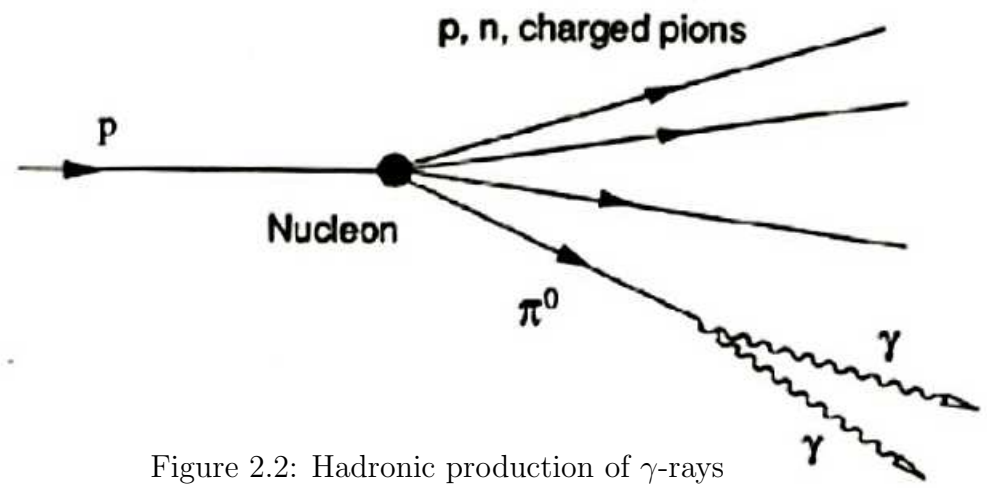

Figure 2.2: Hadronic production of γ-rays

The produced gamma ray spectrum is a convolution of the incident proton spectrum with the inter-stellar matter density. Each resulting γ has an energy which equals half the π^o rest mass (i.e. m =135 MeV/c^2) in the π° rest frame.

There is a strong debate whether sources that emit the highest energy γ-rays like *A*ctive *G*alactic *N*uclei (AGN) are accelerating protons, heavier elements (i.e. iron) or electrons or perhaps a mixed composition. One of the most recent works on the composition of UHECR comes from the analysis of the Pierre Auger Observatory spectrum (Arisaka et al., 2007). The observed spectrum can be fitted by models assuming different injected spectra including pure protons and Fe nuclei beams. The most probable scenario is that the sources responsible for the highest energy particle production accelerate a mixed composition of protons and heavier elements (i.e iron, oxygen) (Arisaka et al., 2007). It is not yet clear, however, whether proton or iron dominates the spectrum and composition at the highest energies.

2.2.2 γ-ray Production by Dark Matter Annihilation

Although there is compelling evidence that the Universe is a strong component of non-baryonic *D*ark *M*atter (DM), as indicated by the rotational curves of spiral galaxies, DM remains elusive. The candidates are numerous but the most studied ones are the *W*eakly *I*nteracting *M*assive *P*articles (WIMPs). The annihilation of WIMPS might yield detectable γ-ray fluxes above the H.E.S.S. threshold by the hadronisation of gauge bosons and heavy quarks. Direct production of γ-rays through loop processes is also possible but less probable, yielding to the emission of γ-ray lines that is a 'smoking gun' for the existence of the dark matter (Bertone et al., 2005).

For ground-based γ-ray detectors like the *H*igh *E*nergy *S*tereoscopic *S*ystem (H.E.S.S.) the possibility of detection would be optimum from regions of high DM densities. Indeed, the flux expected from a DM annihilation depends on the annihilation rate, which is proportional to the square of the dark matter density (Bertone et al., 2005). Thus, our Galactic centre is the prime candidate. H.E.S.S. observations have recently revealed a source of VHE γ-ray with a significance of 37.9 σ, namely HESS J1745-290 that lies within 0.1° from the Galactic Centre (Aharonian et al., 2004*b*). However, the power law energy spectrum with a spectral index of $2.5 \pm 0.04(\text{stat}) \pm 0.10(\text{syst})$ does not agree with the DM annihilation hypothesis (Aharonian et al., 2006*b*). The spectrum from a DM annihilation is expected to rise for $E << M_{DM}$, be stabilised for values in between $0.01 < E/M_{DM} < 0.1$, and quickly drop approaching M_{DM}. Thus, the very high energy cut-off in excess of 10 TeV suggests an unrealistic mass for the DM particle (Bertone et al., 2005).

The search for dark matter is stronger than ever and the recently launched Fermi could hold the key for its detection.

2.2.3 γ-ray Production by Accelerated Charged Particles

In this category there are three different physical processes via which γ's can be produced, namely Bremsstrahlung, synchrotron and curvature radiation. A very brief introduction for each mechanism is given below.

Bremsstrahlung Radiation

The 'breaking radiation' is emitted in the form of energetic γ-rays when an accelerated electron is deflected in the presence of the electromagnetic field of an atomic nucleus or electron. The energy of the emitted γ-rays depends upon the size of the deflection and can be comparable to that of the electron under extreme circumstances. Light particles suffer severe energy loss via Bremsstrahlung, since the rate of energy loss is inversely proportional to the square of the mass of the particle. This mechanism is crucial for high matter densities, which is often the case in the vicinity of the production site. A diagram for this process is shown in Fig.2.3

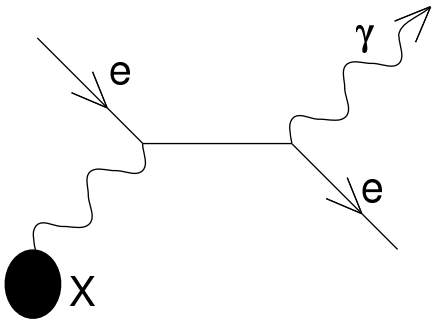

Figure 2.3: Schematic illustration for 'breaking radiation' or Bremsstrahlung.

Synchrotron Radiation

Synchrotron radiation is emitted when a relativistic charged particle is travelling in a magnetic field, due to transverse acceleration (Fig.2.4). Relativistic electrons trace a helical path within the magnetic field lines, resulting in an oscillating electromagnetic field which is emitted as photons. If one observes the emitted photons along the field lines the radiation is circularly polarised and strongly beamed towards the direction of the net particle motion.

The typical energy, in GeV, of the γ-rays produced via synchrotron emission is given by:

$$E_\gamma \cong 20BE_e^2 \tag{2.1}$$

where the electron energy E_e is measured in EeV and the magnetic field B in μG. Thus, the energy of the emitted γ-rays is several orders of magnitude lower than that

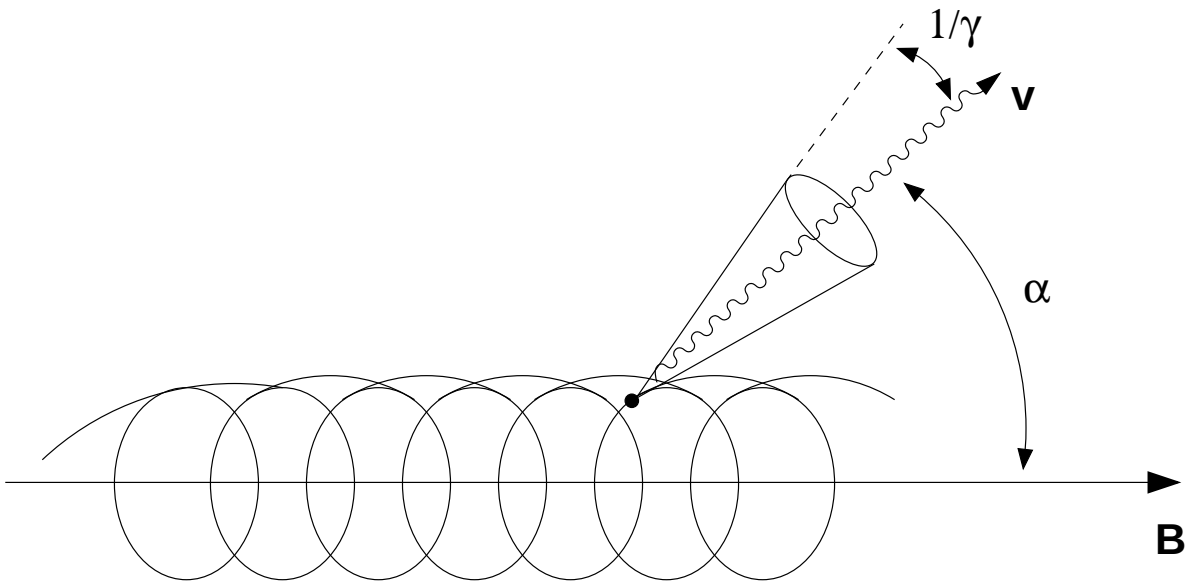

Figure 2.4: The synchrotron emission mechanism.

of the electron and, therefore, synchrotron γ-rays are unlikely to trigger atmospheric Cherenkov telescopes. However, their detection by other means provides a clear signature of relativistic electrons which could produce very energetic gamma rays via other mechanisms.

Curvature radiation

Coherent curvature radiation was proposed as an explanation of the very high brightness temperature of pulsars' radio emission which implies the presence of a coherent emission mechanism (Sturrock, 1971). Curvature radiation can be described in terms of emission by a relativistic electron constrained to follow the strong curved magnetic field lines (B$\sim 10^{12}$G) in the vicinity of a pulsar. Even the most energetic electrons will be forced to follow the magnetic lines very closely since any deviation will result in damping by synchrotron emission. In order for γ's to be produced via curvature radiation, magnetic fields greater than 10^{12}G are needed.

Inverse Compton Scattering

The inverse Compton scattering effect (see Figures 2.5 and 2.6) is a process by which a relativistic electron scatters low energy ambient photons to higher energies.

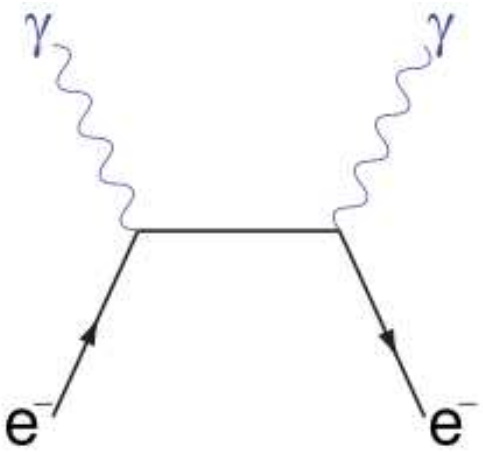

Figure 2.5: s-channel Feynman diagram for $\gamma e^- \rightarrow \gamma e^-$.

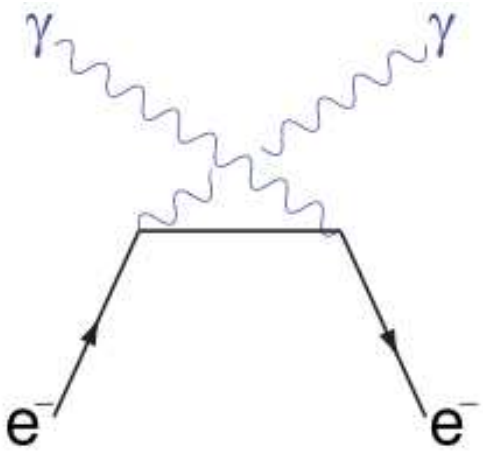

Figure 2.6: u-channel Feynman diagram for $\gamma e^- \rightarrow \gamma e^-$.

Indeed, in the frame of the relativistic electron ($E_e = \gamma m_e c^2$) the photon energy transforms as $E' = \gamma(E + cp_l)$, where p_l is the longitudinal component of the photon's momentum. Thus, in the case of a head on collision and assuming that all the electron's momentum is transferred in the interaction, the photon will be promoted to an energy $E'' = 2\gamma^2 E$. Targets of low energy photons can be the ambient *I*nfra-*R*ed (IR) starlight or the *C*osmic *M*icrowave *B*ackground (CMB).

2.3 Attenuation of VHE γ-rays

2.3.1 Absorption by photons

Energetic photons could be absorbed on background light by pair production of electrons above an energy threshold:

$$\gamma + \gamma_{bg} \longrightarrow e^- + e^+ \quad above \quad E\epsilon = \frac{2(mc^2)^2}{1 - \cos\theta} \tag{2.2}$$

where E and ϵ are the energy of the high-energy and background photon respectively (in the centre of mass frame) and θ is the angle between the two photons. The above equation implies that TeV photons will be absorbed by the IR-light, PeV photons on the CMB and EeV photons on radio waves over astrophysical distances (see Fig. 2.7). Therefore, a crucial parameter for VHE γ-ray astronomy is the in-

teraction length of the γ-γ pair production process. An accurate calculation was not possible until recently due to our poor knowledge of the spectral distributions of the IR and γ-ray photons. The recent observations of extragalactic blazars (e.g. H 2356-309 at z= 0.165 and 1ES 1101-232 at z=0.186) have been used to constrain the *E*xtragalactic *B*ackground *L*ight (EBL) flux (Aharonian et al., 2006*a*).

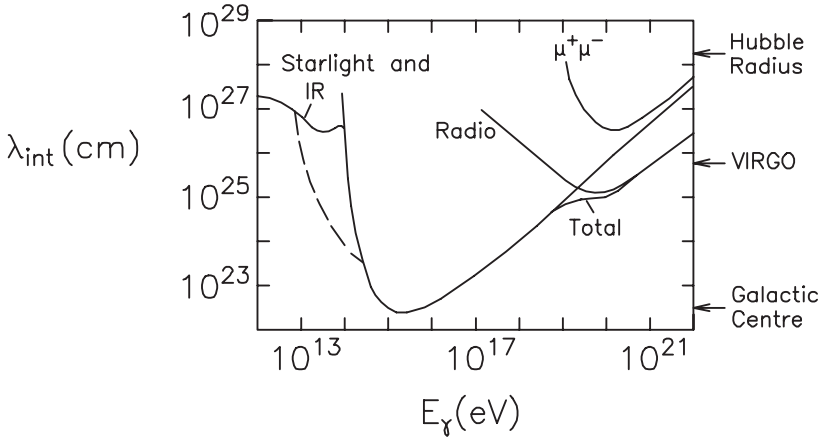

Figure 2.7: Energy dependence of γ-ray attenuation length. The dotted line indicates possible effects due to the IR background. Extracted from Halzen and Hooper (2002).

2.3.2 Attenuation by strong magnetic fields

γ-rays could also be attenuated within their astrophysical sources of production via the single photon pair mechanism. According to this process a single photon could split into two lower energy photons by the scattering of a virtual photon. This process can only occur in the presence of magnetic fields close to the quantum critical field ($B_c = 4.13 \times 10^{13} G$). Magnetic fields of this magnitude can only occur on the vicinity of neutron stars, thus putting a constraint on the γ-ray flux produced from these sites.

2.4 Observation Techniques and the γ-ray Spectrum

The starting point of the γ-ray region in the electromagnetic spectrum is usually defined by the lowest energy γ-rays that can be produced by matter-antimatter annihilation (511 keV). Since the end of the known γ-ray spectrum is limited only by detector sensitivity, the γ-ray spectrum covers currently nine decades in energy and different techniques have been developed to map it. The distinction of the γ-rays according to their detection technique is illustrated in Table 2.1.

In the low to high energy region (0.5 MeV - 30 GeV) γ-rays are measured with pair production detectors. The e^- and e^+ produced by the interaction of γ-rays with matter carry information about the direction, energy and polarisation of the primary γ-ray. At these energies, the earth's atmosphere is opaque to γ's leaving no choice other than the use of space vessels (balloons, satellites). A typical space instrument is shown in Fig. 2.8 (left-hand side). It is comprised of (Weekes, 2001):

- a spark chamber (or, in more recent instruments, a silicon strip detector) within which the γ-ray interacts and the resulting e^- and e^+ tracks are registered,
- a sodium iodide crystal which is used as a calorimeter that registers the total energy of the absorbed electrons,
- an anti-coincidence shield that covers the spark chamber and rejects the dominant CR flux.

These space detectors have large fields of view (1 sr) but their sensitivity is inevitably constrained by their sizes (effective area $\leq$1 m^2). Indeed, the flux of the incident photons decreases with energy and in the region of 1 TeV the background flux of particles is about 10^{-3} cm^{-2} sr^{-1}. Thus, in this energy region larger telescopes are needed for sensitive measurements within typical satellite lifetimes.

At the highest energies (>50 TeV), the products of *E*xtensive *A*ir *S*howers (EAS), produced by the interaction of a γ-ray with the earth's atmosphere, can

reach the ground level and, therefore, be detected by an array of scintillators or a large water tank. A few such detectors are currently operational (e.g. TIBET (Amenomori et al., 2008), MILAGRO (Walker, 2007)) making the detection of the highest energy photons possible.

The *I*maging *A*tmospheric *C*herenkov *T*echnique (IACT) comes in to fill this gap in the energy spectrum. Within this region, the flux is not adequate for satellite observation and nor can the EAS particles reach ground level. The detection technique is based on mapping the faint Cherenkov radiation produced by the EAS. The means of detection is therefore a big mirror with an array of photomultiplier tubes at its focus (see Fig. 2.8 [right hand-side]). In this way the atmosphere becomes a vital part of the detector. The key to success for the IACT is the suppression of the dominant background of shower from nuclear CR's by analysis of the shower images. The small but significant differences in the cascades resulting from the impact of a proton or a photon in the upper atmosphere lead to a separation efficiency of 99.7% (Aharonian and Akerlof, 1997).

Compared to the satellite detectors, Cherenkov telescopes have a small field of view ($\sim$ few degrees) and a low duty cycle ($\sim$10%) due to the 'clear and moonless night sky' restriction. The beauty of the Cherenkov technique, however, is that the effective area of the telescope is much greater than its instrumental area thus reaching $\sim$ few 10^4 m^2. Moreover, the energy resolution achieved is $\sim$15% and the angular resolution is 0.1° per event, which is better than that of satellite telescopes by an order of magnitude (Volk, 2005). A discussion about ground based γ-ray astronomy entailing a detailed description of the IACT follows.

2.5 Ground-Based γ-ray Astronomy

2.5.1 Brief History

The production of Cherenkov radiation by cosmic-ray induced EAS was first predicted by the Nobel Laureate P.M.S. Blackett who suggested that it might account for 10^{-4} of the mean light of the night-sky (Blackett, 1948). The experimental physicists Galbraith and Jelley (1953) realised that the Cherenkov light induced by the

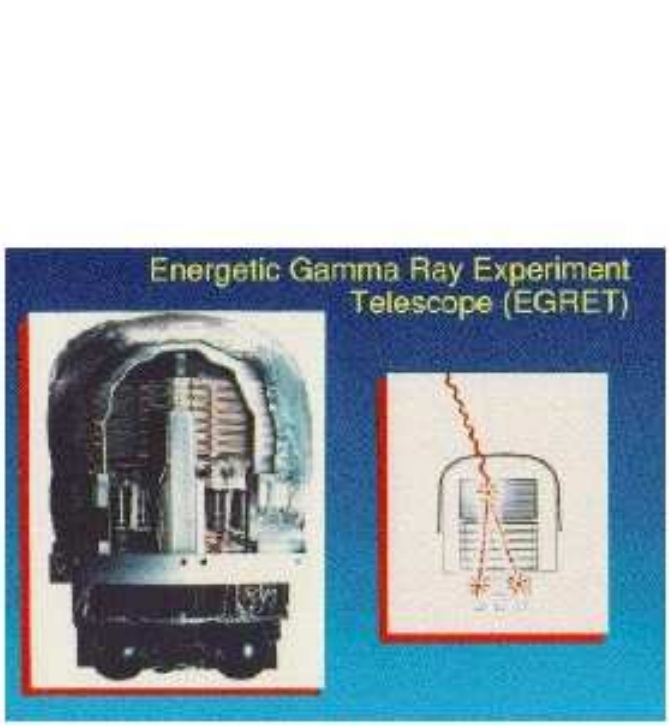

Figure 2.8: (Left) The EGRET instrument of the Compton Gamma Ray Observatory (CGRO). (Right) The 10m Whipple telescope of VERITAS collaboration. Extracted from (Volk, 2005).

Table 2.1: The separation of the γ-rays in terms of their detection technique. From (Weekes, 1996).

Energy Range	**Classification**	**Technique**
0.5-5 MeV	Low Energy (LE)	Scintillation Detector (Satellite)
5-30 MeV	Medium Energy (ME)	Compton Telescope (Satellite)
0.03-30 GeV	High Energy (HE)	Spark Chamber / Silicon Strip (Satellite)
0.03-50 TeV	Very High Energy (VHE)	Atmospheric Cherenkov Detector (Ground Based)
0.05-10^5 PeV	Ultra High Energy (UHE)	Scintillation Detector Array (Ground Based)

cosmic shower would have a characteristically small duration (i.e. $\sim$ 10 ns) allowing for its detection above the night-sky background. Their device consisted of a single photomultiplier (PMT) at the focus of a 25 cm parabolic mirror. It was was placed at the centre of a square of 180 m, each side of which included 5 equidistant 200 cm^2 *G*eiger-*M*uller (G-M) tubes. By demanding coincidence between the photomultiplier and at least one of the G-M tubes they observed $\sim$ 1 large pulse per minute under clear skies. The experiment was performed under heavy clouds in which case the frequency of the signal was reduced by a factor of two, demonstrating for the first time the limitations of the newly-born technique (Marshall, 1954). A few years later, and soon after the publication of Morrison's paper (see Section 2.1), Cocconi predicted the detectability of TeV emission from the Crab Nebula by registering the γ-ray induced showers with particle array experiments (Cocconi, 1959). Even though the flux was overestimated by a factor of 1000, this paper provided the stimulus for much experimental work and marked the start of the era of VHE γ-ray astronomy. Experiments utilising particle detectors were deployed with negative results. It was soon realised that to win in this game one has to lower the

energy threshold by optically detecting the γ-ray induced showers. Astronomy was performed, in the TeV energy regime, by searching for anisotropies in the arrival directions of the air showers over the isotropic cosmic-ray background without discriminating between γ-ray and hadronic-induced showers (Weekes, 1996). An array of twelve light detectors was operated in Crimea by the Lebedev Institute based on Cocconi's predictions (see Fig. 2.9). Four years of operation (i.e. 1960-64) yielded upper limits capable of restricting the overoptimistic theoretical predictions (Chudakov et al., 1967). Twenty years later Hillas (1985) provided the necessary tool for the discrimination between γ-ray and proton-induced showers based on the analysis of the second moments of the Cherenkov images they produce on the telescope's camera. Soon after, a new window in high-energy astronomy was opened by the firm detection of TeV γ-ray emission from the Crab nebula, registered by Whipple telescope (Kwok et al., 1989). Since then, over seventy TeV γ-ray sources have been identified (i.e. May 2009 see Fig. 2.10). Prospects of future discoveries are imminent as the catalogue of the detected sources increases on a weekly basis.

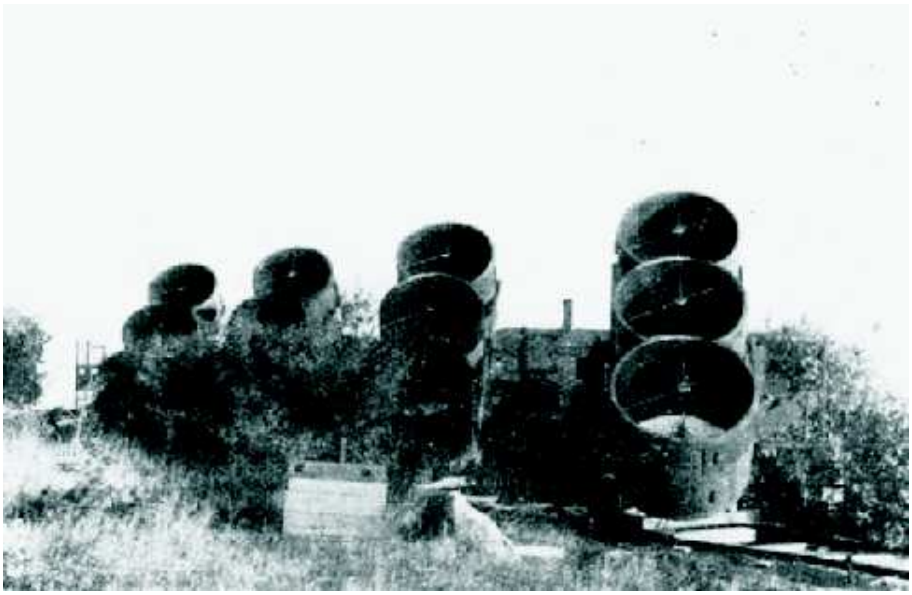

Figure 2.9: Past: The first VHE γ-ray telescope operated in Catsiveli, Crimea between 1960-64. Although no source detection was made, it paved the way for future more sensitive instruments. Extracted from Lidvansky (2006).

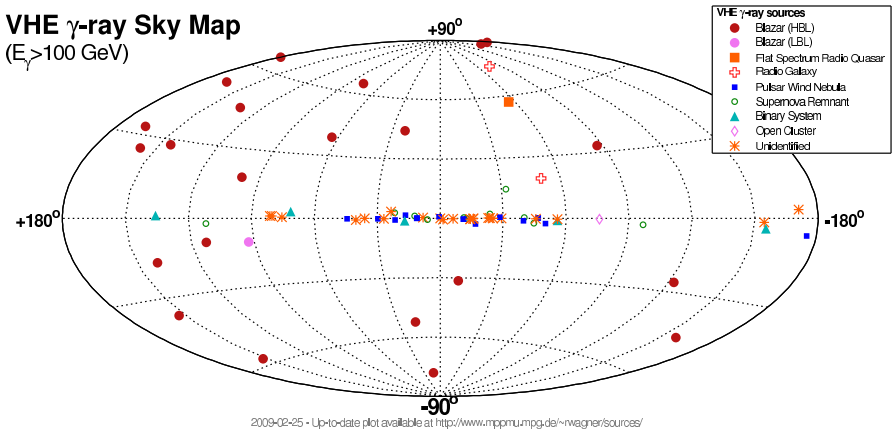

Figure 2.10: Present: Sky map of γ-ray sources with energies in excess of 100 GeV. H.E.S.S. is the culprit for detecting more than 70 sources in the last few years. Courtesy of Robert Marcus Wagner.

2.5.2 Cherenkov Radiation

The first manifestation of Cherenkov radiation observed occurred in the early radioactivity researches as the faint blue glow emitted by strong radioactive sources; an effect that became more apparent when the sources were diluted in a transparent medium (Jelley, 1955). Mallet was the first to investigate this radiation with results published in three papers; however, a theoretical account for the phenomenon was not provided (Mallet, 1926, 1928, 1929). Cherenkov, in the mid-30s, performed thorough experiments and discovered the unique polarisation and directional properties of the radiation which was named after him. A proper theoretical treatment of Cherenkov radiation, based solely on classical electromagnetic theory, was provided by Frank and Tamm (1937). A brief description of Cherenkov theory is provided below.

Cherenkov radiation is emitted when a charged particle traverses a dielectric medium at a speed that exceeds the phase velocity of the light in that medium. The angle of emission depends on the refractive index of the dielectric medium. Fig. 2.11 shows the effect of an electron's passage at a speed v through a solid medium with refractive index n. The electromagnetic field produced by the moving electron causes the displacement of the bound electrons along its track, forming dipoles. The

dipoles return immediately to the former neutral state as soon as the particle passes. If the electron's velocity within the medium is relatively slow (i.e. $v < c/n$, Fig. 2.11) then the polarisation is symmetric along and around the electron's trajectory and, therefore, the net electric field cancels out (i.e. destructive interference).

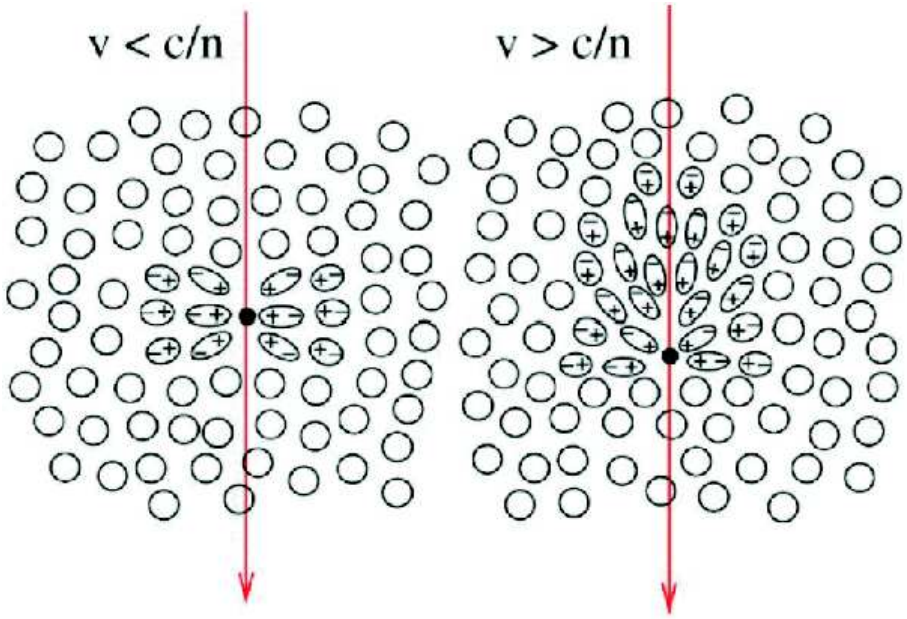

Figure 2.11: The polarisation produced in a medium when an electron passes through it at different velocities as indicated in the diagram.

On the other hand, if the electron possesses higher velocity than the phase velocity of light in this medium (i.e. $v > c/n$), the polarisation symmetry is not preserved along the electron's axis of motion, yielding a net electric field. Indeed, dipoles can only be created behind the relativistic particle. Thus each finite element of the track emits Cherenkov radiation that will interfere constructively in the forward direction. This process is demonstrated by the Huygens construction and results in Cherenkov emission at an angle θ defined as (see Fig. 2.12) :

$$\cos\theta = \frac{AC}{AB} = \frac{1}{\beta n} \tag{2.3}$$

where the relativistic velocity of the particle is $v = \beta c$, n the refractive index and c the speed of light in vacuo. The limiting case ($\beta = 1/n$ and $\theta = 0$) can be associ-

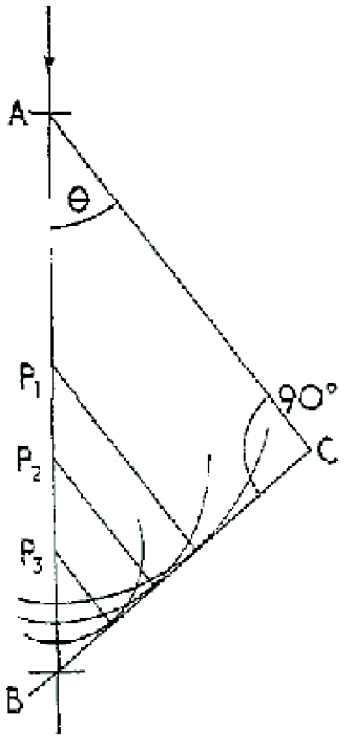

Figure 2.12: Cherenkov light generation: The charged particle traverses along AB with relativistic velocity ($v > c/n$) through a medium of refractive index n emits Cherenkov photons at points P. The elemental wavefronts at each point yield a net emission of Cherenkov light over the surface of a cone with semi-vertical angle θ (Jelley, 1955; Shaw, 1999).

ated with an energy threshold of the relativistic particle below which no Cherenkov radiation occurs:

$$\beta_{min} = \frac{1}{n(\lambda)} \Longleftrightarrow E_{min} = \frac{m_0 c^2}{\sqrt{1-\beta_{min}^2}} \tag{2.4}$$

where m_0 is the rest mass of the particle and the dependence of the refractive index on the wavelength has been restored. Cherenkov radiation can only be emitted at wavelengths for which $n(\lambda) > 1$. The refractive index of a typical medium is positive for wavelengths between the U.V. and microwave regions of the electromagnetic spectrum and negative at higher frequencies (i.e. X-ray and γ-ray). Thus, Cherenkov radiation may only be emitted for wavelengths between about 100 nm and 2 cm.

The angle of emission θ can also be restricted by the maximum relativistic velocity of the moving particle $\beta \rightarrow 1$:

$$\theta_{max} = \arccos(1/n) \tag{2.5}$$

The number of Cherenkov photons (N) emitted by a relativistic particle per unit path length between the wavelengths λ_1 and λ_2 can be calculated as follows (Bernlöhr, 2000):

$$\frac{dN}{dx} = 2\pi\alpha z^2 \int_{\lambda_1}^{\lambda_2} \left(1 - \frac{1}{(\beta n(\lambda)^2}\right) \frac{1}{\lambda^2} \tag{2.6}$$

where α is the fine structure constant, z is the charge number and $\beta = v/c$. From equation 2.6 it is evident that the energy emitted per wavelength interval scales as λ^{-3}, which explains the bluish-white colour of Cherenkov radiation.

Equations 2.3, 2.5 and 2.6 allow the computations of the minimum energy, maximum angle and photon yield for the relativistic particles generated via energetic γ-ray and cosmic-ray interactions with the atmosphere (see Section 2.5.4).

2.5.3 Extensive Air Showers

γ-ray initiated showers

A γ-ray cascade is initiated when a VHE γ-ray interacts with the atmospheric nuclei to produce a shower which is purely electromagnetic in origin. The longitudinal development of this shower can be viewed as the repetition of the following processes:

1. pair production process while the incident γ-ray is within the Coulomb field of an atmospheric atom. The photon must possess energy in excess of $2m_ec^2$ (i.e. ~ 1 MeV) and the presence of an atom is necessary for energy and momentum conservation (Longair, 1999) (i.e. $\gamma + X \longrightarrow X + e^- + e^+$),

2. electrons with energies above 84 MeV will undergo Bremsstrahlung when deflected by the field of a nucleus (i.e. $e + X \longrightarrow X + e + \gamma$).

This process will continue until particle energies are too low for further interactions to occur. The presence of muons within the shower is possible but very rare since the cross-section of photo-nuclear interactions is three orders of magnitude less than the the one for pair production. The shower will reach its maximum number of particles when the electron energy drops below the threshold of a photon to be pair produced (i.e. $E_c = 84.2$ MeV in air). After that, the shower energy is quickly dissipated by ionisation of the atmosphere. Moreover, the cross-section for pair production reduces until Compton scattering and photo-electric absorption become dominant, resulting in limiting the cascade's growth.

The energy loss per unit length of relativistic electrons undergoing Bremsstrahlung is proportional to its energy. Thus, radiation length can be defined as the length $L_\circ$ over which the electron loses a fraction of $(1 - 1/e)$ of its initial energy. The radiation length could be expressed in terms of the total air mass per unit cross-section travelled by the electron (Longair, 1999):

$$-\frac{\mathrm{d}E}{\mathrm{d}x} = -\frac{\mathrm{d}E}{\mathrm{d}t}\frac{1}{\rho L_\circ} = \frac{E}{X_\circ} \tag{2.7}$$

where ρ is the air density and $X_\circ = \rho L_\circ$. For a relativistic electron (i.e. ~ 300 GeV) radiating Bremsstrahlung photons in air, the radiation length is $X_0 = 37$ gcm^{-2}.

If we consider particles with energies well above the critical energy (E_c), Compton scattering and collision losses can be neglected when calculating the development of the shower. In addition, for high energy electrons we can assume a "complete screening" limit for both Bremsstrahlung and pair production processes. Indeed, since both processes require the presence of the field of an atomic nucleus, they will be screened by the atomic electrons for impact parameters exceeding the radius of the atom (Gaisser, 1990). Thus, in the high energy limit, atomic screening sets an upper cutoff to the impact parameter for all relevant wavelengths in these processes, the so-called complete screening limit. Finally, by making the assumption of complete screening and neglecting Compton scattering and collision losses, one can derive simple models for the longitudinal development of the shower, in which the radiation length of Bremsstrahlung equals the interaction length for pair production (Allan, 1971) (see Fig. 2.13).

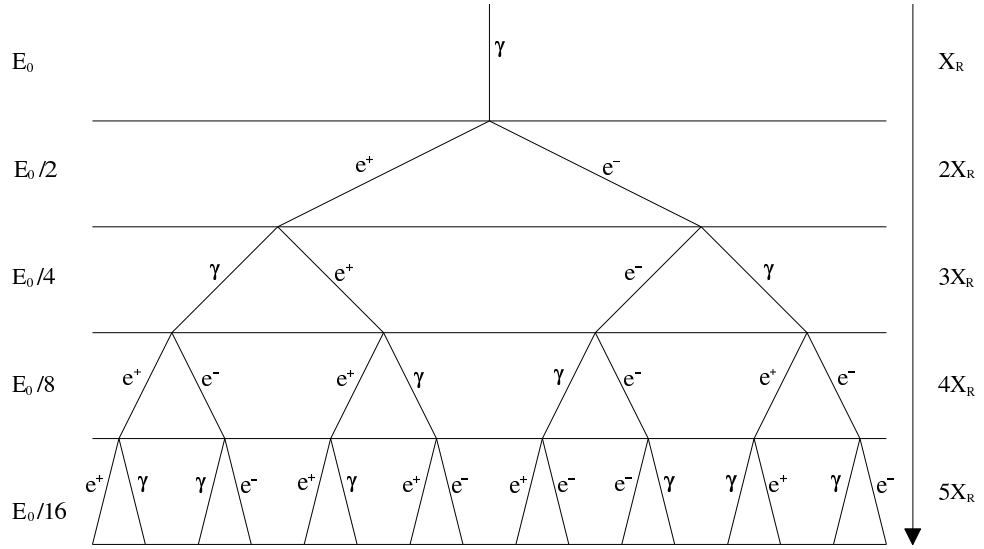

Figure 2.13: A toy model for a γ-ray EAS. Extracted from Allan (1971).

In this simple but efficient model the probability of an electron undergoing either process at a depth X is:

$$e^{-X/X_\circ} \longrightarrow X = X_\circ \ln 2 \tag{2.8}$$

Under the assumption that the total energy of the shower is conserved one can see that the remaining mean particle energy will be half that of the parent after each radiation (interaction) length and will be divided equally between the secondaries (e^-, e^+ and γ's). If the energy of the parent γ-ray is $E_\circ$ after n cascade lengths, the collective number of particles would be 2^n and their average energy $< E_\circ > /2^n$ if the continuous losses of the shower are neglected. The shower maximum will be reached when the average energy of the cascade particles becomes E_c:

$$E_\circ \, 2^n_{max} \simeq E_c \Longrightarrow X_{max} \simeq X_\circ \ln\left(\frac{E_\circ}{E_c}\right) \tag{2.9}$$

Scaling to the relevant units (i.e. VHE γ-rays of a few hundred GeV have $X_\circ = 300$ gcm^{-2}) and by considering an exponential atmosphere model with a height scale= 7 km (see also Section 2.5.4) an altitude of ~ 8 km can be calculated. This is lower than the actual altitude since the electrons within the shower suffer energy loss by ionisation.

The lateral spread of particles within a γ-ray shower is determined by the mechanism that produces the largest opening angle between the secondary particles; that is the multiple Coulomb scattering of the electrons and positrons in the atmosphere. The average angle at which an electron will be scattered is given by:

$$\langle \delta\theta^2 \rangle \cong \left(\frac{21MeV}{E} \right)^2 \delta\chi \tag{2.10}$$

where $\delta\chi$ is the radiation length tranversed by the electron in gcm^{-2}. Since the distribution of the scattered angles is Gaussian one can calculate the angular spread of the shower, for a given energy and shower length, as $\sqrt{< \delta\theta >^2}$.

Cosmic-ray initiated showers

The isotropic flux of cosmic ray nuclei is a much richer source of EAS in comparison with the γ-ray induced ones ($\gamma-$ray : cosmic-ray EAS = 1:1000). It consists mainly of protons ($\sim$ 90%) and some heavier elements, the most abundant component of which is helium nuclei. The development of a shower resulting from the interaction of an energetic proton ($E \sim 100$ GeV) with an atmospheric nucleus is shown in Fig. 2.14. The path length of this hadronic interaction is on average 86 gcm^{-2} after which the proton (or heavier nucleus) will interact to produce a triplet of pions together with the fragments of the parent particles. In this first interaction the primary particle will retain almost half of its original energy, leaving approximately 50 GeV for pion production. Wolfendale suggested that the number of pions generated by this mechanism can be approximated by: $N_p = 2.7\, E_p^{0.25}$ where E_p is the available energy (i.e. $\approx$ 50 GeV in our case). (Wdowczyk and Wolfendale, 1972). Thus, about 7 pions will be produced in the initial stage of the cascade with no preferential direction in π^+, π^- or π° creation. The neutral pions, due to their short life time of 1.78×10^{-16} s in their rest frame of reference, decay immediately to two γ-rays, which in turn initiate an electromagnetic shower as described in Section 2.5.3. The charged pions, however, possess a greater life time (i.e. 2.551×10^{-8} s) allowing them to interact before decaying. Thus pions will be multiplied by their hadronic interaction with the atmospheric nuclei, a process that can be theoretically continued until the energy per particle becomes lower than about 1 GeV which is required for multiple

pion production (Longair, 1999). In practice, the probability of the charged pion to decay becomes greater after each interaction. Thus, many of the charged pions would decay as follows:

$$\pi^+ \rightarrow \mu^+ + \nu_\mu \tag{2.11}$$

$$\pi^- \rightarrow \mu^- + \bar{\nu}_\mu \tag{2.12}$$

The produced muons are more stable than pions and lose energy chiefly by ionisation. Some of the muons will be produced in the first stages of the cascade (i.e. at high altitudes) and, therefore, could possess a kinetic energy of a few MeV. Such muons could have Lorentz factors in excess of 20 which boosts their mean lifetime of 2.2×10^{-6} s, in their rest frame of reference, allowing them to reach the ground. At the other extreme, low energy muons could decay, producing electromagnetic showers:

$$\mu^+ \rightarrow e^+ + \nu_e + \bar{\nu}_\mu \tag{2.13}$$

$$\mu^- \rightarrow e^- + \bar{\nu}_e + \nu_\mu \tag{2.14}$$

Finally, the protons comprising the nucleonic part of the cascade will suffer ionisation losses, and the less energetic ones (i.e. $E < 1$ GeV) are eventually brought to rest. Thus, a hadronic shower consists of a muonic component fed by the charged pion decays, multiple electromagnetic sub-showers generated via the decays of pions and muons, and a nucleonic core (see Fig. 2.14). The description of the hadron initiated showers has been simplified in that it neglects secondaries such as kaons that might also been produced via the hadronic interaction. However, it provides the main characteristics of the shower upon which a discrimination from the γ-ray initiated shower can be made. The main differences between γ-ray and cosmic-ray initiated air showers will be the subject of the next Section.

γ/Hadronic Shower Differences

The differences between hadronic and γ-ray initiated EAS arise mainly from the nature of the strong and electromagnetic interactions responsible for their production.

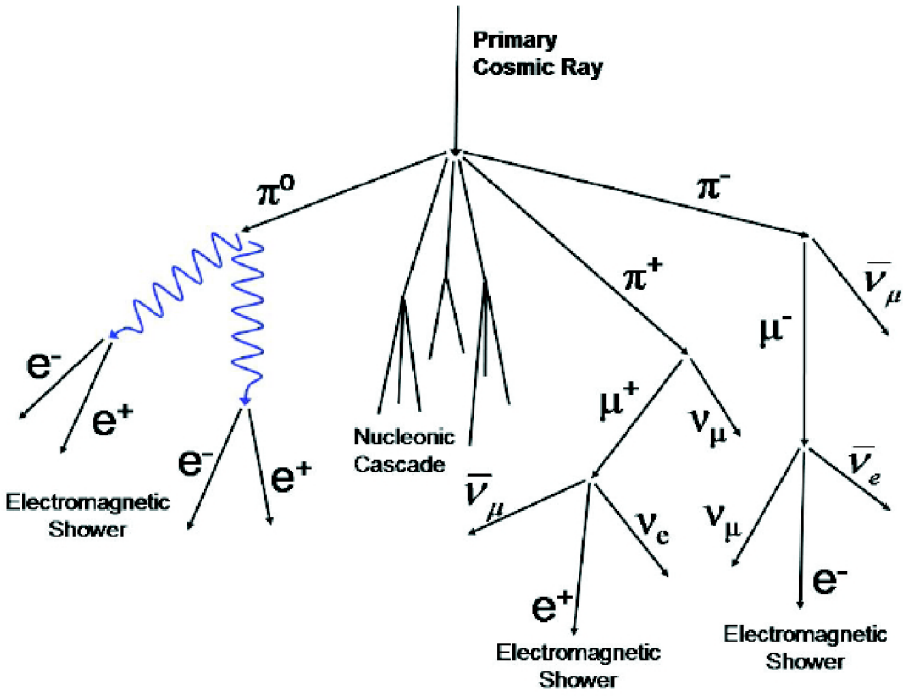

Figure 2.14: The typical development of a cosmic-ray initiated extensive air shower within the Earth's atmosphere. From Longair (1999).

The most profound differences are listed below:

- the pions, that are chiefly produced via inelastic p-p collisions, convey larger transverse momenta in comparison with particles produced via electromagnetic processes. Thus, this component of the hadronic cascade could be well separated from the axis of the parent particle, and the same holds for the π°-induced electromagnetic showers. In conclusion, the lateral extent of a cosmic-ray initiated shower is much greater than that of a γ-ray induced shower;

- as the interaction length of protons travelling in the atmosphere superpasses by far the γ-ray one (i.e. 80 gcm^{-2} as opposed to 38 gcm^{-2}), proton showers will develop further in the atmosphere in comparison with γ-ray of the same energy;

- the electromagnetic part of the hadronic cascade is a combination of the individual electromagnetic showers, produced by the decay of π° and $\mu^{\pm}$, in contrast to the simpler structure of the γ-ray cascade. Thus, the creation of

secondary particles varies greatly within an hadronic cascade (and, indeed, between different hadronic showers) in comparison with the γ-ray EAS. That is reflected in the lateral distribution of a cosmic-ray EAS at the ground, which consists of different peaks relating to decay products of different sub-showers.

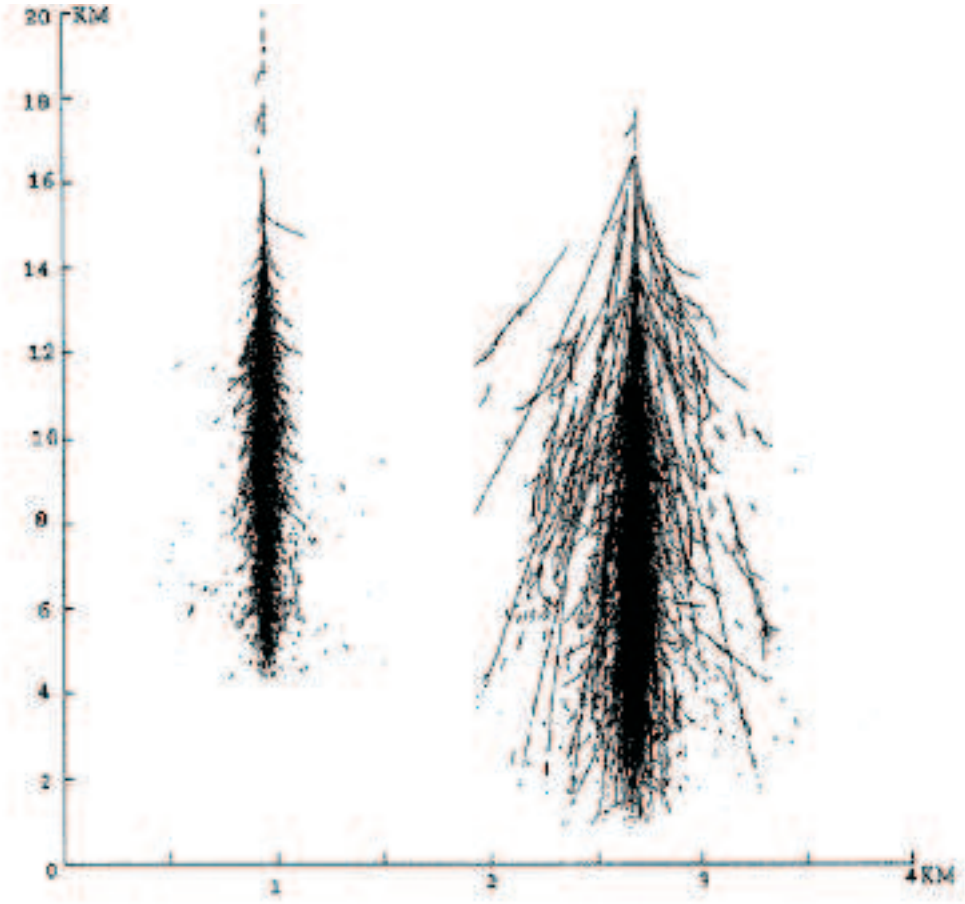

Figure 2.15: Monte Carlo simulation of the development of a 300 GeV γ-ray shower (left) and a 900 Gev hadron shower (right) in the atmosphere. Taken from Fegan (1997).

All in all, γ-ray showers tend to be much more compact and more stable in terms of both particle production and heights of maxima than the hadron showers.

The signal of an IACT consists of Cherenkov photons emitted by the relativistic products of γ-ray and cosmic-ray initiated showers. Thus, a successful discrimination between the two should translate the differences described above in terms of variations in the Cherenkov light emitted via the γ-ray or cosmic-ray cascade route.

In the next section the production and development of Cherenkov radiation in the atmosphere will be presented.

2.5.4 Production of the Atmospheric Cherenkov Radiation

In the case of VHE γ-ray astronomy, one is interested in the Cherenkov light produced in the atmosphere from the products of γ-ray and hadron- induced air showers. It has already been seen (see Section 2.5.2) that the refractive index of the medium determines the threshold for Cherenkov emission, the angle of emission and the Cherenkov photon yield. The refractive index of standard air is (e.g. Edlen, 1966):

$$(n-1)_s \times 10^8 = 8342.13 + 2406030(130-\sigma^2)^{-1} + 15997(38.9-\sigma^2)^{-1} \qquad (2.15)$$

where σ is the vacuum wave number in $\mu\mathrm{m}^{-1}$. In γ-ray astronomy the relevant window of wavelengths is $300-600$ nm, within which $(n(\lambda)-1)_s$ changes only by 5% (Bernlöhr, 2000). Thus, the index of refraction can be fixed at a value of 1.000293 at sea level. The refractive index of air depends on atmospheric pressure, temperature and water vapour and can be calculated via empirical equations very accurately (Edlen, 1966). If one makes a further assumption of an isothermal atmospheric model, the refractive index would be proportional to the air's mass density, which scales exponentially with altitude (Jelley, 1955):

$$\eta(h) = \eta_\circ \exp\left(\frac{-h}{H_\circ}\right) \qquad (2.16)$$

where $\eta = n-1$, $\eta_\circ$ is the value at sea level and $H_\circ$ is the scale height of the atmosphere ($H_\circ = \frac{\kappa T}{mg} \simeq 7.1$ km) (McCartney, 1976).

Equations 2.4 and 2.5, in conjunction with the knowledge of the refractive index altitude profile, allow the computations of the minimum energy and maximum angle for the relativistic particles:

$$E_{min} = \frac{mc^2}{\sqrt{1-\beta_{min}^2}} = \frac{mc^2}{\sqrt{1-(1+\eta(h))^{-2}}} \simeq \frac{mc^2}{\sqrt{2\,\eta(h)}} \qquad (2.17)$$

Thus, the threshold energy for the charged particles of γ-ray and cosmic ray showers at sea level ($\eta_\circ = 2.93\times10^{-4}$) are 38 GeV, 21 MeV, 5.6 Gev, 3.4 GeV and 151.5 GeV

for protons, electrons, pions, muons and α's respectively. Thus, positrons and electrons are responsible for most of the Cherenkov light generation as they are more numerous and possess lower energy thresholds for photon emission than the rest of the secondary particles.

The maximum angle of Cherenkov emission at the limit $\beta \to 1$ is:

$$\cos\theta_{max} = \frac{1}{n} = \frac{1}{1+\eta(h)} \simeq 1 - \eta(h) \Longrightarrow \tag{2.18}$$

$$\theta_{max} \simeq \sqrt{2\eta(h)} \tag{2.19}$$

This gives a value of $\sim 1.3^\circ$ at sea level. This is a very important characteristic that makes astronomy with Cherenkov photons possible, as the original direction of the primary photon is retained. The spread of the Cherenkov photons' light pool on the ground can be determined easily given the altitude and the maximum angle of emission. For instance, for a vertical shower possessing a maximum at 9 km above sea level and a maximum emission angle of $\sim 1^\circ$, the light pool would have a maximum radius of ~ 160 m. In practice, the light of Cherenkov photons collected within a radius of ~ 125 m is proportional to the energy of the parent γ-ray. That provides a collection area of $> 5 \times 10^8$ cm^2 that can be harvested even by small optical detectors (Weekes, 1996).

The photon yield (i.e. number of photons created per unit path length) can be calculated under the justified assumption of a wavelength independent η in the PMT's sensitive wavelength window. In this case, Equation 2.6 becomes:

$$\begin{aligned} \frac{\mathrm{d}N}{\mathrm{d}x} &= 2\pi\alpha\left(\frac{1}{\lambda_1} - \frac{1}{\lambda_2}\right)\left(\frac{1}{1-(\beta n)^{-2}}\right) \\ \beta \to 1 &\Leftrightarrow \sin^2\theta_{\max} \simeq \theta^2 \simeq 2\eta(h) \Longrightarrow \\ \frac{\mathrm{d}N}{\mathrm{d}x} &\simeq 0.45\exp(-h/H_\circ)\ \text{photons}\,\text{cm}^{-1} \end{aligned} \tag{2.20}$$

Thus, the altitude profile of the refractive index affects the photon yield that is considered proportional to the number of particles in the cascade, which in turn is used to infer the energy of the primary γ-ray. In addition, the emitted Cherenkov photons will be attenuated by the atmospheric molecules and aerosols before reaching the detector. The impact of different atmospheric profiles, which affect directly

both Cherenkov production and transmission, on the light density registered by a ground telescope, will be quantified in Section 4.4.2.

2.5.5 The Basics of Imaging Atmospheric Cherenkov Technique

Today's imaging atmospheric Cherenkov telescopes have opened a new window on the 100 GeV-100 TeV γ-ray sky with more than 70 detected sources, the number of which expands on a weekly basis. Their basic design is just a magnification of the first detectors, which consisted of a single PMT in a focal plane of a 25 cm diameter parabolic mirror (see Section 2.5.1). For example, each H.E.S.S. telescope consists of a camera made of 960 PMTs placed at the focal point of a 12 m diameter mirror (see Fig. 2.19). In both cases, there is a minimum amount of recorded PMT counts above which an event can be treated as a signal and not a random fluctuation of the Night Sky Background (NSB). The flux of the NSB exceeds the Cherenkov flux by a factor of 10^4. However, Cherenkov photons from a single cascade arrive at the detector within a time gate of a few nanoseconds. In addition, the Cherenkov emission peaks at short wavelengths (see Section 2.5.2) compared to the NSB. Thus, by selecting a PMT sensitive to the Cherenkov light emission and setting its integration window to a slightly longer interval than the Cherenkov pulse width (i.e. $t \sim 10$ ns) the chances of detection improve drastically.

The noise registered by a PMT, within the integration window t, due to the NSB is (Weekes, 2005):

$$S_b \simeq \Phi_{nsb} A t \Omega \eta \rightarrow N = \sqrt{S_b} = \sqrt{\Phi_{nsb} A t \Omega \eta} \tag{2.21}$$

where Φ_{nsb} is the flux of NSB photons (photons/m^{2}s sr^2), η is the collection efficiency of the PMT, which is the convolution of its quantum efficiency, mirror reflectivity and any other known parameters (i.e. transmission of the light-collection funnels in front of the PMTs for H.E.S.S. cameras (see Fig. 2.24)) determining the fraction of the light collected by the PMT, A is the area of the mirror (m^2) and Ω is the solid angle subtended on the sky by the PMT (sr). The fluctuation of the background

signal follows a Poisson distribution and thus the noise can be expressed as $\sqrt{S_b}$.

The PMT signal S due to the Cherenkov photons during the same interval t is:

$$S \simeq \psi A t \eta \tag{2.22}$$

where $\psi = \rho\, E^{-1}$ is the Cherenkov photon yield, ρ is the density of Cherenkov light (photons m^{-2}) with E being the energy of the primary γ-ray.

The signal-to-noise ratio can be easily calculated from 2.22 and 2.21:

$$\frac{S}{N} \simeq E\psi\sqrt{\frac{\eta A}{\Phi_{nsb}\Omega t}} \tag{2.23}$$

Since the minimum detectable signal is inversely proportional to the signal-to-noise ratio, the minimum energy of a primary γ-ray capable of producing such a signal is (Weekes, 2005):

$$E_T \propto \sqrt{\frac{\Phi_{nsb}\Omega t}{\eta A}}\ \psi^{-1} \tag{2.24}$$

Thus, the mirror area would dictate the threshold energy of a Cherenkov Telescope. The area of each H.E.S.S. telescope mirror (i.e. 107 m^2) was optimised for a threshold around 100 GeV under the assumption of a typical photon yield $\psi = 100$ m^{-2} TeV^{-1} at an altitude of 2 km a.s.l. and taking into account mirror reflectivities of $80 - 90$ %, a similar transmission for the light-collecting funnels in front of the PMTs and a quantum efficiency of 15% for the PMTs.

In practice, the energy threshold can be defined as the energy that maximises the convolution of the telescope's *E*ffective *S*ensitive *A*rea (ESA) with the intrinsic differential energy spectrum of the observed γ-ray source. (i.e. $E^{\alpha} \times ESA(E)$). The effective sensitive area of a Cherenkov detector relates to the detector efficiency (η) and its sensitive area, determined from the Cherenkov deposition on the ground and usually greater than $\sim 5 \times 10^4$ m^2. The ESA also depends on the zenith angle of observation as Cherenkov photons registered at different zenith angles correspond to different optical depths. The derivation of the ESA and, therefore, energy threshold (E_T) is achieved by detailed simulations, an example of which will be presented in Section 2.9.1.

2.5.6 Imaging Principle

In the previous Section it was shown how the battle between Cherenkov light and NSB can be easily won. The discrimination between Cherenkov light produced by γ-ray and cosmic-ray showers proved to be more tedious and led to the development of the imaging atmospheric technique. A Cherenkov telescope uses a big reflector to focus the light from an EAS onto an array of PMTs that can be considered as a vast digital camera with an extremely short exposure time ($\sim$ ns). The camera registers a picture of an EAS if a given number of pixels (i.e. PMTs) exceed the background noise. The Cherenkov telescope's camera might contain 'dead', 'hot' and 'grey' pixels, so a flat fielding is implemented to account for each pixel's response (see Section 2.7.1). Finally, the dark-counts from the PMTs are subtracted by measuring their value in the absence of Cherenkov light, similar to the use of dark frames.

After image cleaning (see Section 2.7.2), the shape and orientation of the surviving image may be used to discriminate between γ-ray and cosmic-ray induced showers. The effectiveness of the IACT approaches 100% in eliminating the cosmic-ray induced background while retaining 50-80% of γ-ray induced events (Fegan, 1997), and this success is based chiefly on (Weekes, 1996):

- Physics:

  The most prominent difference between the development γ-ray and cosmic-ray showers is the smaller transverse momentum associated with the electromagnetic compared with the hadronic interactions. Thus a γ-ray shower is more closely packed along the projected path of the primary than a hadronic shower (see Fig. 2.15). The angle of Cherenkov emission is chiefly dictated by the particle's energy and within the window of VHE γ-ray astronomy (100 GeV $-$ 100 TeV) would be about 1° and thus differences in the lateral distribution between γ-ray and hadronic showers will be reflected in the mapping of the Cherenkov light. A γ-ray image should be much more compact than a cosmic-ray one. Moreover, due their larger interaction length (see Section 2.5.3) the hadronic cascades will bring the Cherenkov producing particles much closer to the detector. In addition, many of the charged muons, products

of the charged pions' decay, will reach the detector, producing intense local peaks at the points of impact (Fegan, 1997). A muon image will appear as a ring on a single Cherenkov telescope (i.e. when operating in stereo-mode muons will be eliminated). A γ-ray, cosmic-ray and muon event are shown in Fig. 2.16.

- Geometry:

  In γ-ray astronomy, observations are achieved by aligning the telescope's optical axis with the coordinates of a known or expected source. Thus, showers arriving from the direction of the source will form an elliptical image that points to centre of the camera. On the other hand, cosmic-ray events are isotropically distributed and so their images should not possess any preferred orientation. A very nice illustration of the technique is presented in Fig. 2.17 (Noutsos, 2006). For practical reasons, the development of the γ-ray shower can be divided into three parts regarding the Cherenkov emission (see Fig. 2.17 (1)). The high part is located between the point of the first interaction and is ~ 2 km above the shower maximum (i.e. upper end of box). The light from the upper part consists of 25% of the total light. The emission angle will increase with decreasing altitude which in turn means that light from different altitudes will arrive at the camera at approximately the same time. However, the light from region (a) will arrive closer to the centre of the camera than the lower part (b). The second region (b) contains the shower maximum and almost 50% of the total light is emitted from this region. The light coming from region (b) is the most representative and reflects the energy of the primary γ-ray (Weekes, 2005). Finally, the last 25% comes from the lower part (c) and is furthest away, mapped from the centre of the camera. It is prone to large fluctuations due to the exponential shower decay below the shower maximum. This part also suffers atmospheric attenuation due to aerosols that when present occupy the first $2-3$ km above the telescope's site.

  Figure 2.17 (2) reveals both the lateral and longitudinal spread of the shower. The long axis of the ellipse (i.e. a-c) points backwards to the source of the primary γ-ray and relates to the longitudinal development of the shower. The

width (i.e. b-b) relates to the lateral spread of the shower. Finally, the registered image will be parametrised by the use of Hillas parameters that are the subject of the next section.

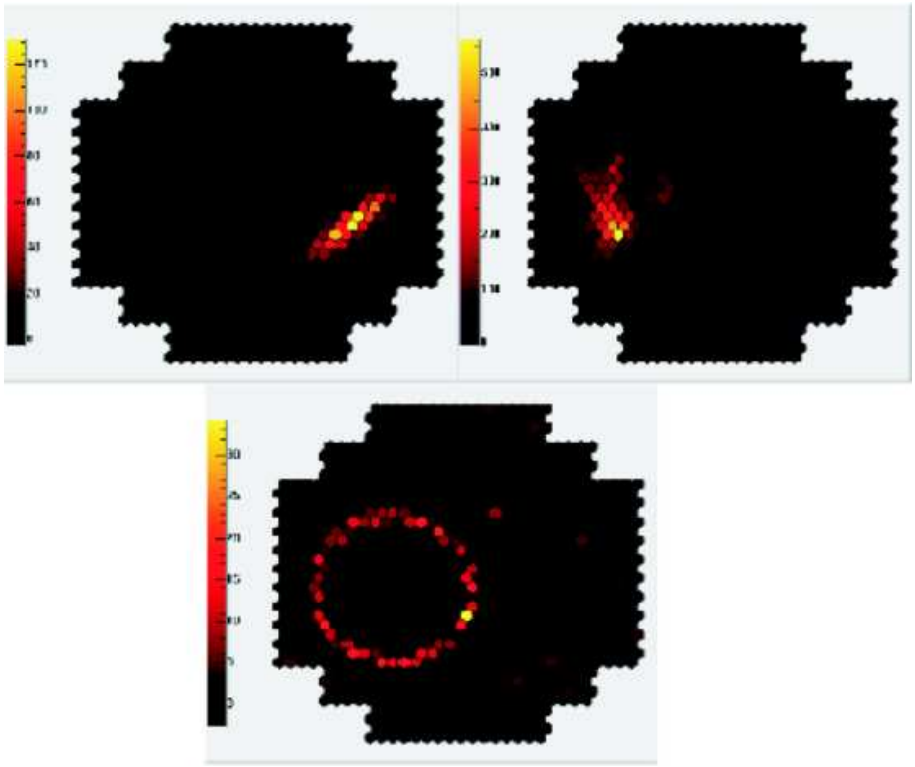

Figure 2.16: Cherenkov images from the H.E.S.S. telescopes corresponding to: (a) a γ-ray event, (b) a cosmic-ray event and (c) a muon. The colour scale corresponds to the light intensity. Courtesy of the H.E.S.S. collaboration.

2.5.7 Hillas Parameters

The differences between the lateral and longitudinal development of γ-ray and hadron initiated showers affect the shape of the Cherenkov image formed by the triggered PMT's on the focus of the telescope mirrors. In order to quantify these differences Hillas (1985) introduced a parameterisation of the elliptical images produced by induced protons or γ-rays; the so-called Hillas parameters. In Fig. 2.18 a graphical representation of the Hillas parameters is given, followed by a brief explanation, which is provided in Table 2.2.

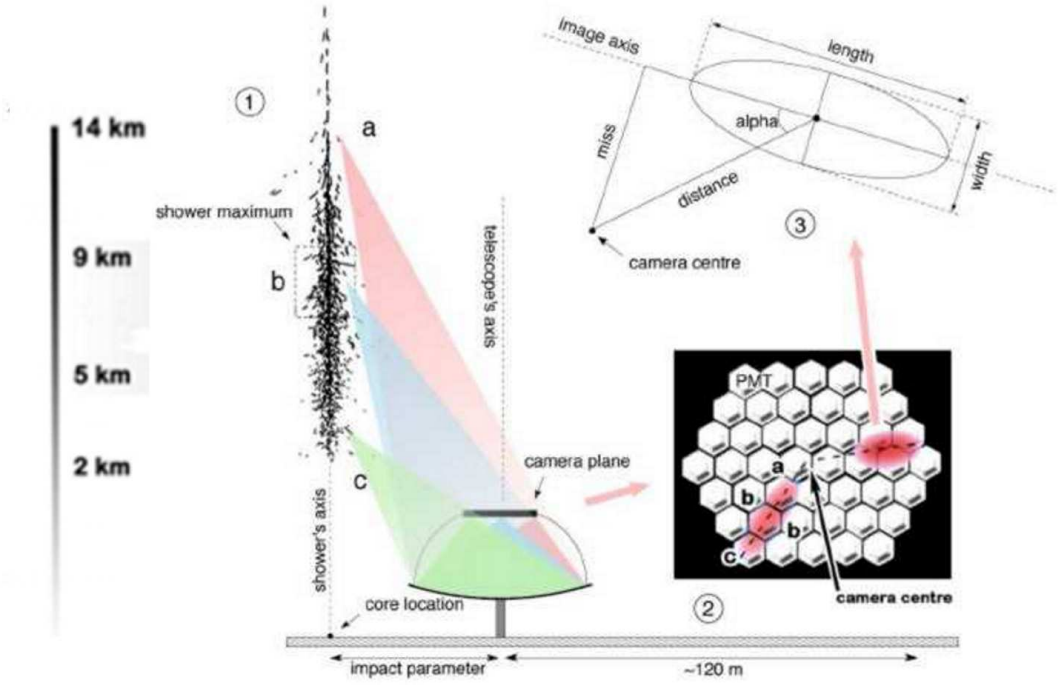

Figure 2.17: Schematic diagram illustrating the IACT at work: (1) Development of the γ-ray shower and Cherenkov radiation produced in three different altitudes, (2) The shower's image containing both the lateral and longitudinal profile of the shower and (3) Hillas parameters. See text for more details. Note that the vertical axis shows the important altitudes for the Cherenkov light emitting regions and that the horizontal scale has been magnified for a better demonstration of the technique. From Noutsos (2006).

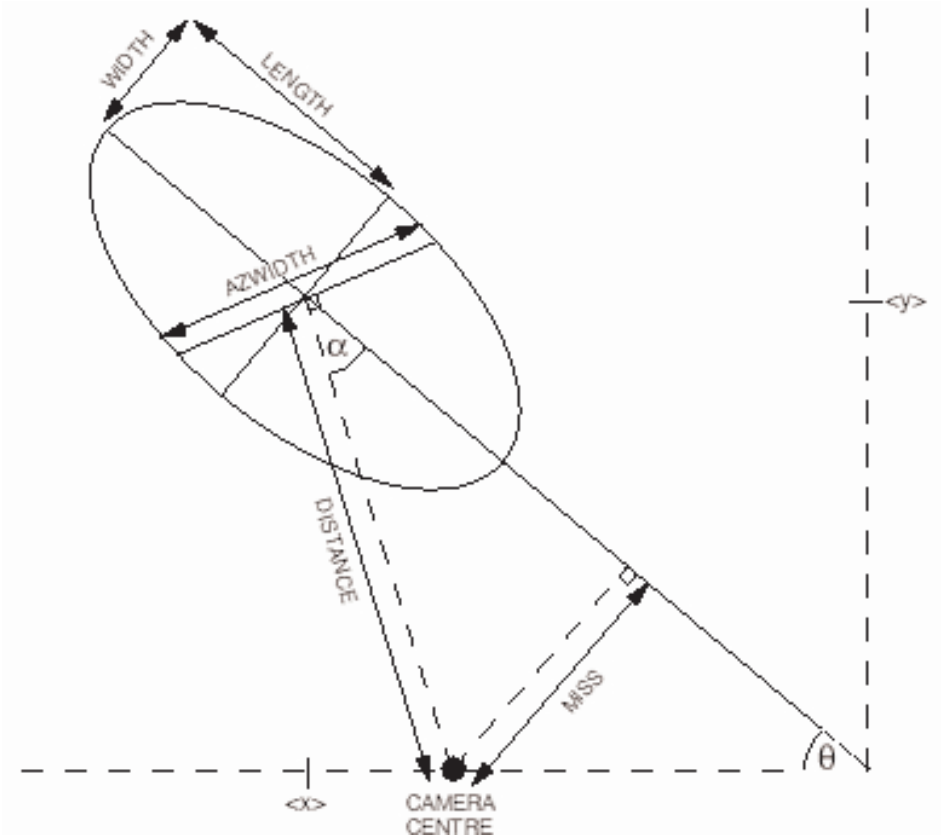

Figure 2.18: Schematic illustration of Hillas parameters.

Hillas Parameter	Definition
Size	The collective number of ADC counts summed over all the triggered tubes
Width	The RMS spread of of light along the minor axis of the image A measure of the lateral development of the cascade
Length	The RMS spread of of light the major axis of the image A measure of the vertical development of the cascade
Azwidth	The RMS spread of light perpendicular to the line connecting the image centroid with the centre of the field of view A measure of both width and pointing
Distance	Distance from the centroid of the image to the centre of the field of view
Miss	Perpendicular distance between the major axis of the image and the centre of the field of view A measure of the shower orientation
Alpha	Angle between the major axis of the ellipse and a line joining the centroid of the ellipse to the centre of the field of view
Asymmetry	Measure of how asymmetric the image is. γ-ray images should have tails which preferentially point away of the source position.

Table 2.2: Hillas parameters explained (Fegan, 1997).

2.6 The High Energy Stereoscopic System (H.E.S.S.)

2.6.1 Introduction

H.E.S.S. is currently the the workhorse of VHE γ-ray astronomy, providing the most detections of any ground-based telescope. It is located in the Khomas Highlands of Namibia at an altitude of 1.8 km a.s.l. H.E.S.S. currently consists of four identical telescopes located at the corners of a square with 120 m side (see Fig. 2.20). The telescopes' distances match the lateral spread of a typical Cherenkov light pool (see Section 2.5.4) and allow for maximum sensitivity at a low energy threshold of $\sim$ 100 GeV. In what follows a brief description of different aspects of the system will be presented.

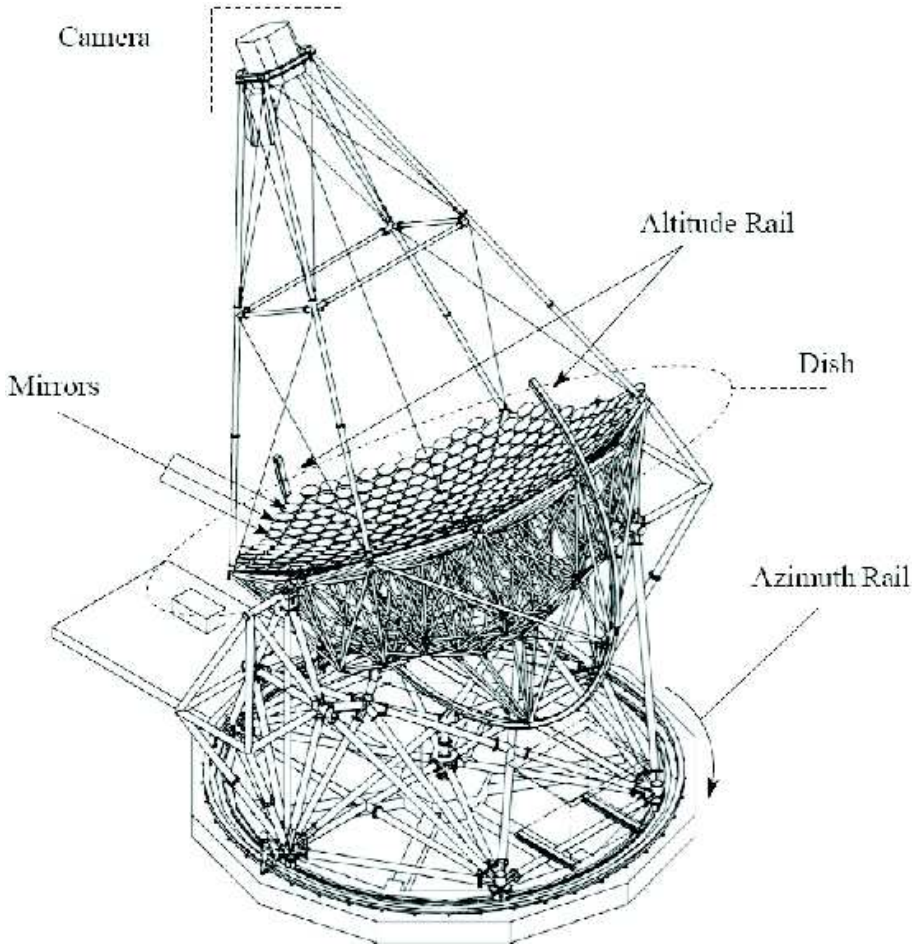

Figure 2.19: A drawing of a H.E.S.S. telescope. Courtesy of the H.E.S.S. Collaboration.

Figure 2.20: A panoramic view of the H.E.S.S. array. Courtesy of the H.E.S.S. Collaboration.

2.6.2 Mirrors

We have already discussed that the reflector of a Cherenkov telescope is an important tool for lowering the energy threshold and its specification determines, together with the PMTs performance, the efficiency of the the whole instrument (see Section 2.5.5). The reflector of each telescope consists of 380 mirror facets with a radius of 30 cm, corresponding to an area of 107 m^2 (see Figures 2.21, and 2.22). The choice of a Davies-Cotton design over a parabolic dish was a trade off between good off-axis imaging and small time dispersion. The Davies-Cotton design was selected as the better off-axis performance optimises the mapping of extensive sources (Bernlöhr, 2003).

The alignment of the 380 mirror facets is paramount in order to exploit the mirrors' optical qualities and optimise the telescopes' detection resolution. Each mirror is attached to a steerable base that is controlled by two stepping motors. The fully automated alignment uses the lid of the telescope camera as a screen for the projected image of a chosen star. A CCD camera installed at the centre of the telescope's mount takes a picture of the lid with all facets being mid-way of their allowed movement. Then each facet moves in both directions, the result is registered on the CCD camera and a ideal position is selected. This process is repeated for each facet and the net result of the alignment is shown in Fig. 2.23. The blind Cherenkov telescope is guided with the help of a second CCD camera that is mounted off-axis for a clear sky view. The details of the fully automated alignment are provided in depth in Cornils et al. (2003).

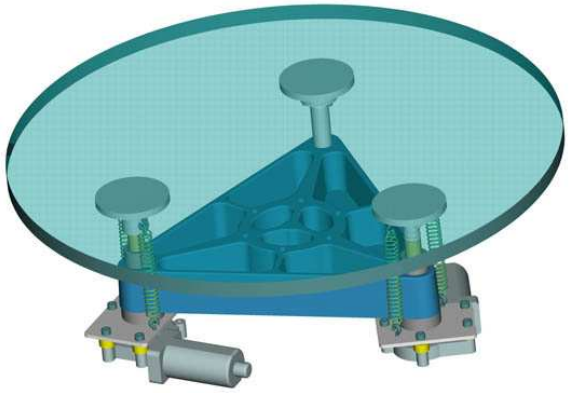

Figure 2.21: A diagram of H.E.S.S, mirrors revealing the motors responsible for its alignment. Courtesy of the H.E.S.S. Collaboration.

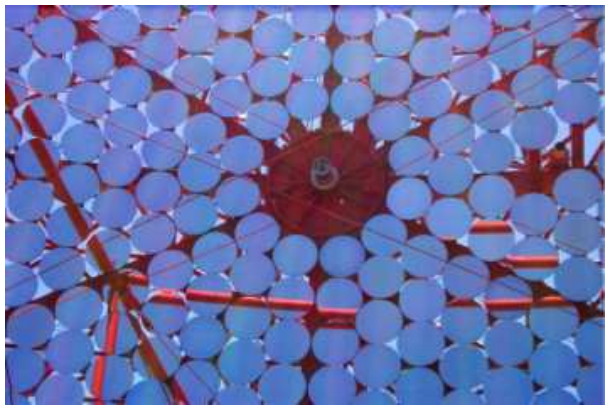

Figure 2.22: A close view of a H.E.S.S. telescope's reflector. The CCD camera at the centre of the dish that is used for the auto alignment in also visible. Courtesy of the H.E.S.S. Collaboration.

2.6.3 The Cameras

The cameras of the H.E.S.S. telescopes were designed with two considerations in mind:

- a field of view large enough to cover the full apparent size of the possible sources, and
- a pixel size small enough for the detailed mapping of γ-ray sources.

Both criteria were met by constructing a gigantic camera with 5° field of view by the combination of 960 PMTs, each having an minimum aperture of 0.16° (see Fig. 2.24). The Photonis XP2960 PMTs are grouped in 60 modules (i.e. drawers) each one consisting of 16 PMTs (see Fig. 2.25). The PMTs are the natural detectors of choice as their rise time is quicker than the Cherenkov light pulse width (i.e $\sim$ ns) and their spectral response can be chosen to match the Cherenkov light emission. The Achilles heel of the PMTs is the low quantum efficiency that usually ranges between $15-20\%$. Some improvement was made by the provision of Winston cones for each PMT to optimise the amount of Cherenkov light collected by reflecting the light that falls in-between the PMTs, while preventing a fraction of the background light from reaching their window by constraining their field of view to the angular

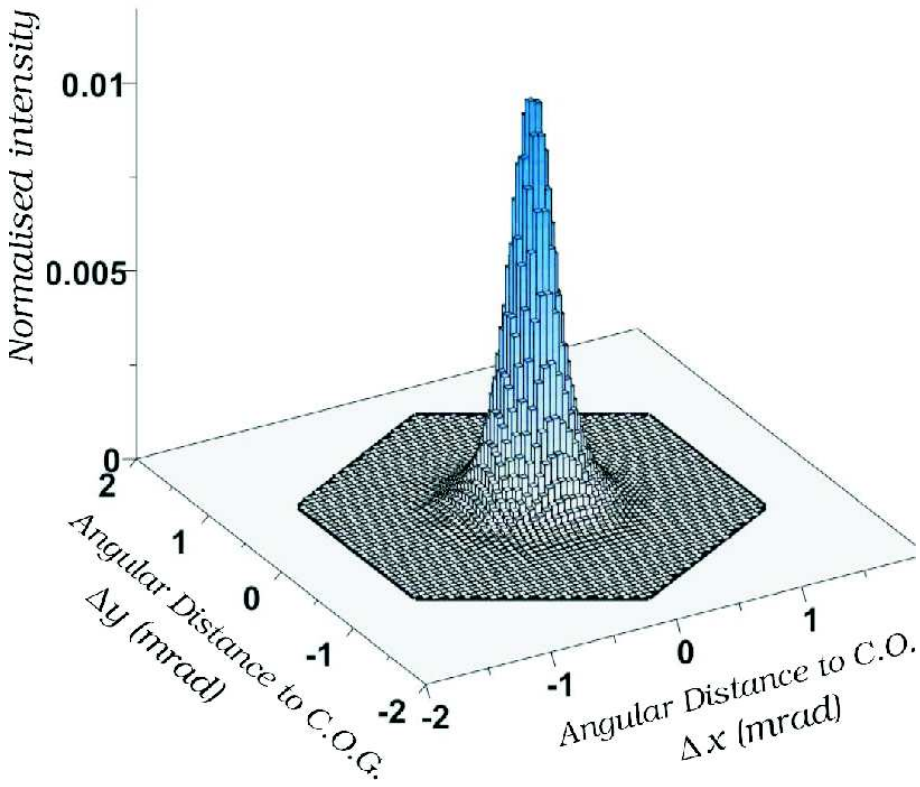

Figure 2.23: The intensity distribution of a a star projected to the lid after alignment. The hexagonal base is relates to the size of a single PMT. The Point Spread Function can be contained by a single PMT. The C.O.G is an abbreviation for the centre of gravity. From Cornils et al. (2003).

size of the mirror (Vincent et al., 2003). The drawers can be easily replaced from the front of the camera body. In addition to the 16 PMTs, each drawer contains two read-out cards and the control/trigger card. The digitised PMT signal is sent to the acquisition and control systems, which are located in the rear of the camera. The signal from each PMT is divided between a high gain (HG) and a low gain (LG) channel with different amplification factors, while an extra channel is used for the trigger. The HG channel is used for signals containing 100 *p*hoto-*e*lectrons (p.e.) while the LG offers a dynamic range of $16 - 1500$ p.e.

The PMT signals are sampled at a rate of 1 GHz by the *A*nalogue *R*ing *S*ampler (ARS) developed by the ANTARES collaboration (Feinstein, 2003). The analogue signal from the PMT is stored in ARS's 128 cells while awaiting for the trigger signal.

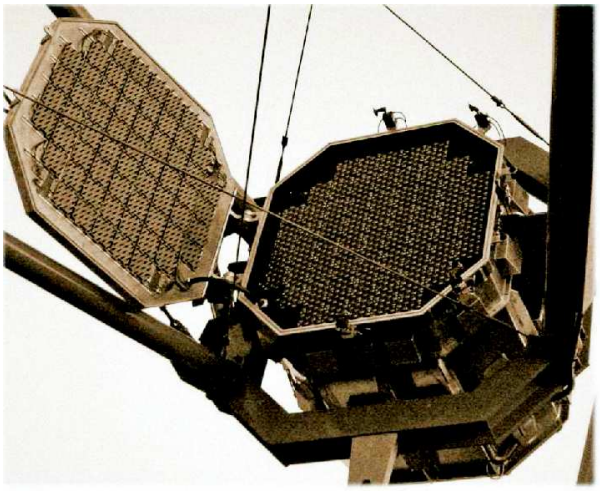

Figure 2.24: The H.E.S.S. camera. The shown part of the lid supports the LEDs and associated diffusers that are used for the determination of individual PMT gain when the telescope is not observing (see Section 2.7.1).

Figure 2.25: A drawer containing 16 PMTs and the associated electronics. Courtesy of the H.E.S.S. Collaboration.

Upon receipt of a trigger, the sampling stops, the ARS memory is read within a programmable window (i.e. usually set at 16ns around the triggered signal) and the signal is digitised and stored.

For deriving a trigger for a single H.E.S.S. telescope, each camera is divided in 38 overlapping sectors each consisting of 64 PMTs. In the present configuration of the camera, a trigger occurs if three PMTs within the same sector exceed the equivalent of four photo-electrons within a window of 1.5 ns (i.e. sector threshold 3, pixel threshold 4). The trigger rate of a single telescope is dominated by cosmic-ray events, while for energies close to the telescope's threshold of $\sim$ 100 GeV the flux of penetrating single muons increases (Funk et al., 2004). By requiring coincidence between two telescopes one can reduce the cosmic-ray background, with the lateral distribution of γ-ray showers being more homogeneous than that of the cosmic-rays, and diminish single muon events. The coincidence window is currently defined at 80 ms.

The camera response, based on the signal of the triggered pixels, will reveal (after appropriate analysis) a γ-ray source. Its calibration, therefore, is of crucial importance and consists the first step of the H.E.S.S standard analysis that will be the subject of the next section.

2.7 H.E.S.S. Standard Analysis

2.7.1 Calibration

The raw signal of each PMT consists of *A*nalog/*D*igital *C*onverter (ADC) counts. Since each PMT might possess a slightly different efficiency, its response must be normalised to the mean efficiency over the whole camera. The term calibration refers to the factors necessary to convert the raw ADC signal into corrected photoelectrons (Aharonian et al., 2004*a*).

We have already seen (Section 2.6.3) that the measured signal (ADC counts or ADU) is obtained from both high and low gain channels (ADU^{HG}, ADU^{LG}). The derivation of the corrected amplitude in photoelectrons is provided below:

$$A^{HG} = \frac{ADU^{HG} - P^{HG}}{\gamma_e^{ADU}} \times FF \tag{2.25}$$

$$A^{LG} = \frac{ADU^{LG} - P^{LG}}{\gamma_e^{ADU}} \times (HG/LG)FF \tag{2.26}$$

where P^{HG} and P^{LG} are the ADU pedestal position, γ_e^{ADU} is the gain of the HG channel in (p.e./ADU), HG/LG is the amplification ratio between the two channels and FF is the flat-fielding coefficient.

In practice, one of the following values is selected for image analysis:

$$\mathrm{ADU} < 150\mathrm{p.e.} \quad : \quad A^{HG} \tag{2.27}$$

$$\mathrm{ADU} > 200\mathrm{p.e.} \quad : \quad A^{LG} \tag{2.28}$$

$$150 < \mathrm{ADU} < 200\mathrm{p.e.} \quad : \quad A = (1-\epsilon) \times ADU^{HG} + \epsilon \times ADC^{LG} \tag{2.29}$$

where $\epsilon \approx (ADU^{HG} - 150)/(200 - 150)$

For the calculation of the FF coefficients a Durham-made flat-fielding unit is used. By providing a uniform illumination across the camera, the different responses of the PMTs due to variations on their optical properties or efficiencies can be measured and corrected (Aye et al., 2003). The flat-fielding coefficients are independent of electronics, therefore, one FF value is assigned to each pixel.

The the PMT gains are usually measured every two days. Dedicated *L*ight *E*mitting *D*iodes (LEDs), coupled with diffusers, are used to create an signal of 1 p.e./pixel, with the aid of which each pixel's gain is calculated (see Fig. 2.24)

The pedestal position is defined as the mean ADU value registered in the absence of Cherenkov light. It consists, therefore, of the electronic noise and the noise due to the NSB light. The electronic noise (dark pedestal) is produced chiefly by the PMT dark counts that originate from thermal emission of photoelectrons. The dark pedestal can be measured with the camera lid closed and, as expected, depends on temperature. A typical H.E.S.S. run takes 28 minutes within which a variation of 1°C in temperature might occur (Aharonian et al., 2004*a*). That translates to a shift that can reach a value of -50 ADU/degree and thus pedestal positions are usually calculated every minute. In practise, the pedestal is calculated from the triggered events as a usual shower image is constrained usually in 20 pixels. Part of the noise is due to NSB light, but it has been proven that that its pedestal position remains constant over the 16 ns integration time (Aharonian et al., 2004*a*).

2.7.2 Image Analysis

The corrected amplitudes of the triggered PMTs have to pass through a filter before being selected for image analysis. This is known as 'image cleaning', and for H.E.S.S. analysis requires each PMT to have an amplitude greater than 10 (5) p.e. and a neighbouring pixel to have an amplitude greater than 5 (10) p.e. respectively.

After the image cleaning, the surviving signal is used for the the moment calculations that are parametrised in a Hillas-analysis fashion (Hillas, 1985). A short description of the Hillas parameters has been given in Section 2.5.7 and their analytical expression in terms of statistical moments is provided in the Appendix. These parameters fall in two main categories, namely those that correspond to the shape

of the image (size, width and length) and those that correspond to the position and orientation of the image (alpha, distance, miss). Standard H.E.S.S. analysis requires that all signals must be above a minimum total signal (size cut). In addition, the image centre of gravity is required to be less than 0.2° from the centre of the camera (Benbow, 2005). This distance cut guarantees that the whole image is mapped onto the camera while the size cut secures a good reconstruction of the image.

Images that pass both criteria should trigger at least two telescopes simultaneously in order to be used for event reconstruction.

2.7.3 Geometrical Reconstruction

The determination of the shower direction, which points back to the γ-ray source, and the position of the shower core is achieved through algorithms capable of geometrically reconstructing each event. The technique utilises the major axis of each elliptical image. The images are grouped in pairs and the direction of the shower is calculated as the weighted average of the intersections of all pairs of major axes projected in telescope's the field of view (Benbow, 2005).

In a similar manner, the intersections of the shower axis relative to each telescope's position are projected in a plane orthogonal to the telescope's pointing, and can be used to define a mean location for the shower core.

For the background rejection one expects that width and length will be powerful discriminants as they are related to the physical extent of the shower. It was realised that a set cut on width or length is energy dependent. Indeed, for primaries of higher energies, the shower maximum is expected to be closer to the detector, and thus, both parameters would have greater values. Standard H.E.S.S. analysis uses two purpose-built parameters, namely Mean Reduced Scale Width (MRSW, and MRSL for length) that can be defined as (Benbow, 2005):

$$MRSW = \frac{1}{N_{tel}} \sum_{i=0}^{N_{tel}} \frac{width_i - < width_i >}{\sigma_i} \tag{2.30}$$

where, N_{tel} is the number of triggered telescopes, $width_i$ is the width measured by the relevant telescope, $< width_i >$ and σ_i are the width and its standard deviation for

the expected γ-rays estimated via Monte Carlo simulations based on image intensity, reconstructed impact parameter and zenith angle. The MRSL is defined similarly.

Finally, a cut that relates to the image's pointing, θ^2, is used for point γ-ray sources. This is defined as the square angular difference between the reconstructed shower position and the source position. The H.E.S.S. standard analysis uses three sets of cuts (standard, hard, loose) optimised for a maximum detection probability. They depend on the source spectral index that most of the time constitutes one of the unknowns. A more detailed description on the subject can be found in (Benbow, 2005) from which this short account was drawn.

2.8 EAS Simulations

The discussion of the standard H.E.S.S. analysis shows the importance of simulations in ground based astronomy. It would have been more convenient to calibrate our telescopes by pointing them to a standard γ-ray source, but in its absence one should rely on detailed simulations of γ-ray sources. In the following Sections, work performed in the early stages of H.E.S.S.'s operation, aiming to simulate the effect of different atmospheric assumptions on the effective sensitive area of a stand-alone telescope, will be presented.

Simulations of γ-ray Showers

In practice one has to use elaborate Monte Carlo codes in order to model the production of the particles within the showers. Simulations of the electromagnetic cascades consider both pair production and Compton scattering for photons, while for electrons, Bremsstrahlung, Coulomb scattering and ionisation losses are taken into account. As briefly discussed (see Section 2.5.3) multiple Coulomb scattering dictates the shower's "opening angle"; it also dictates the smallest interaction length among the shower's processes. At the energies considered here the amount of computing time required to follow all interactions completely would be prohibitive. In our case the simulation program MOCCA (**Mo**nte **C**arlo **Ca**scade) (Hillas, 1997) is used, in which the electrons are assumed to follow straight paths of length $\sim 0.1 - 3$ gcm^{-2}

(Nolan, 2002). Then the correction for the total deflection is applied in the middle of each segment. The individual segments are assigned with a characteristic angle ψ so that only a fraction ($\sim 40\%$) of events are expected to be scattered at an angle greater than ψ. For the events with scattered angles up to ψ, the RMS of ψ is calculated and a sample is extracted from a normal distribution with the same width. Events with deflections greater than ψ are simulated individually (Nolan, 2002).

A main feature of the MOCCA code is the adaption of a "thin sampling" method. According to this technique, only a reduced proportion of the low-energy particles is followed. In order to compensate for that, a weight greater than 1 is assigned to the particles followed below the critical energy. The critical energy up to which all particles are followed (E_{thin}) is usually 20MeV, but this may be altered by the user. Below E_{thin} a proportion of $\sim \frac{E}{E_{thin}}$ of particles with energy E are followed. Even though "thinning" is not necessary today, it allowed for the first time the creation of a significant number of EAS whose analysis with the relevant program (simulating the Whipple camera response), led to the confirmation of the Hillas Parameters.

2.9 Simulations of a stand-alone H.E.S.S. telescope response

57409 γ-ray induced showers were generated using a modified version of MOCCA for an inclination of 50° within the energy range 0.1-30 TeV. For each shower the light deposited in a H.E.S.S. telescope is allowed to move 4 times randomly within a radius between 700-1000m depending on the shower's energy (i.e. 700m for $0.1 < E/\mathrm{TeV} < 1$, 800 m for $1 < E/\mathrm{TeV} < 10$ and 1 km for $10 < E/\mathrm{TeV} < 30$).

In order for the photons arriving at the telescope mirrors to be translated into photoelectrons assigned to the camera's PMTs, the simulation package CameraHESS is applied (Konopelko, 2001). Thus, the simulation program must take into account all the efficiencies of the Cherenkov light's journey through the atmosphere and from the reflector to the single camera pixel, namely:

- The PMT's quantum efficiency. The typical quantum efficiency for the PMT

is $< 20\%$ over the wavelength range $300 - 500$ nm and has a peak of 26% at $\sim$400 nm. The variation of the collection efficiency as a function of the wavelength is also taken into account.

- The mirror's reflectivity, which is better than 80% over the wavelength range from 300-800 nm with the maximum value 85% occurring at $\sim$400 nm.
- Winston cone transmission and collection efficiency of 73% for all wavelengths.
- Attenuation of the showers (produced by MOCCA) due to the atmosphere is calculated within the telescope response program. According to this procedure, a wavelength is randomly assigned to each photon read from the MOCCA file in accordance with the Cherenkov power law spectrum ($\propto \lambda^{-2}$). Then the attenuation is calculated, from a table characteristic of the specific atmosphere chosen, taking into account the altitude of emission of the photon (see Fig. 2.26).

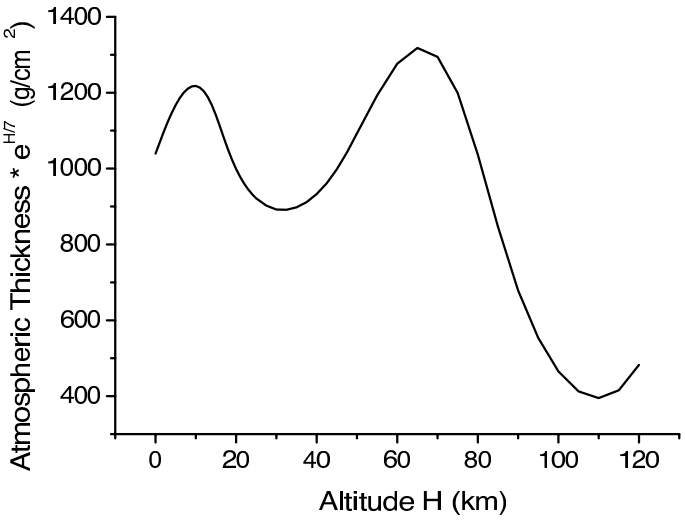

Figure 2.26: Variation of the normalised atmospheric thickness for the tropical atmosphere. Extracted from CameraHESS program (Konopelko, 2001).

A collective attenuating factor is then calculated from the convolution of all aforementioned factors with :

- a correction accounting for the Davies-Cotton design of the H.E.S.S. mirrors,

- a reduction of $10 - 12\%$ of the incident or reflected light which is obscured by the camera support structure.

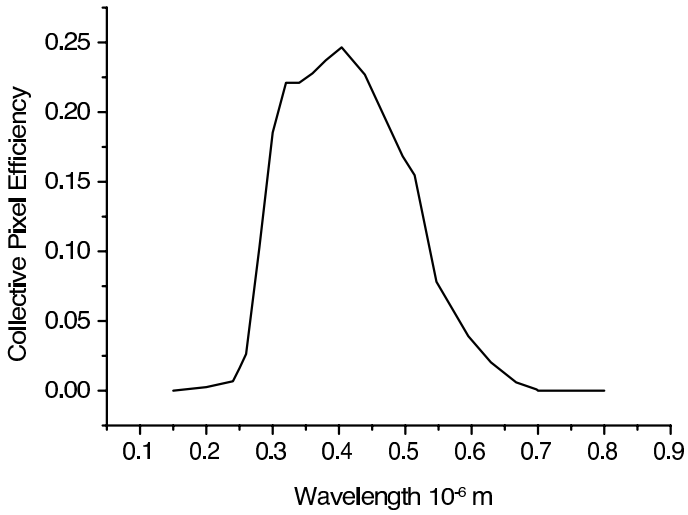

Figure 2.27: Collective pixel efficiency taking into account the PMT's efficiency,the mirror's reflectivity and the Corning blue filter value.

Rather than tracing each photon through the mirror system, a time delay is randomly added to the arrival time of each photon to account for the distribution of delays introduced by the design of the mirrors. Then the photons are translated into photoelectrons in a Monte Carlo fashion. Thus, the net attenuating factor for each photon written in the MOCCA file is compared with a random number ranging 0-1. According to the result, either the photon is killed or it is promoted to a photo-electron. Finally, the assignment of a PMT number to the photo-electron is accomplished using geometrical arguments.

In order to determine the response of the camera, each photo-electron collected from the PMT's cathode within a shower is written to a file. The response of each PMT will then be compared with the single photo-electron pulse shape. Thus, the accurate determination of the photo-electron pulse profile is of crucial importance for determining the performance of IACT's. The trigger pulse shape used for these simulations has a rise time of 1.5ns and a width of 2.1 ns and was provided by Guy (2001). The pixel threshold for one photo-electron is 25.7 mV. Finally, the camera response is decided upon the triggering criteria that currently demand a coincidence

of 4 pixels (each having 5 photoelectrons or more) in one of 38 overlapping groups of 64 pixels each.

The problem with the old version of CameraHESS was that the program was executed once for each shower, producing a vast number of separate output files and requiring MOCCA to be run in the same mode. The author made the necessary alterations for the the automatic incorporation of MOCCA within the CameraHess program. Moreover, a Root program for calculating the effective area of the results (obtained after the feeding of the MOCCA files into the camera simulation program) was devised by the author. This program enables the production of a histogram that gives the number of the triggers and total number of showers within 24 energy and 10 distance intervals.

2.9.1 Effective Area and Energy Threshold calculations for various Atmospheric Models

As mentioned before, the beauty of the imaging atmospheric Cherenkov technique is that the Effective Sensitive Area (ESA) of a telescope exceeds by far its mirror area. The exact value of the ESA for a specific telescope will depend upon all the attenuation Cherenkov light processes which are modelled by CameraHESS. A very important feature of the ESA is its dependence on the zenith angle chosen for observation (θ). In our case $\theta = 50°$, which is relatively high compared to other simulations among H.E.S.S. collaboration, a fact that implies that a slightly higher effective area must be expected. This can be explained by the fact that as the distance between the shower maximum and the telescope increases, the light is spread over larger distances. This has some disadvantage though, since in this way the threshold energy (E_T) of the telescope is also increased (see Fig. 2.29)

In practice, after the data of the CameraHESS files have been extracted, one is able to plot:

$$\left(\frac{trig \pm \sqrt{trig}}{\text{total } \gamma\text{s}} \right) \times \pi \times r_{max}^2 \tag{2.31}$$

against energy, where r_{max} is the maximum selected distance of collection (i.e. 700

– 1000 m depending on shower's energy), and *trig* refers to the number of showers that passed the triggering criteria from the total number of simulated γ-rays. The triggering criterion for the case of a stand-alone H.E.S.S. telescope required 4 PMTs in one sector to have a signal greater than 4 photoelectrons. The error is just the 1σ Poissonian noise of the number of triggered events within each bin.

A practical way to define E_T is to plot the convolution of ESA with the intrinsic differential energy spectrum of the source observed (the Crab nebula with an integral index of -1.59 in our case) as a function of energy. The energy at which this function peaks will reveal E_T. The ESA and E_T for a stand-alone H.E.S.S. telescope for the simulated γ-rays has been produced for two atmospheric models that best represent H.E.S.S. site (Fig. 2.28, 2.29 respectively).

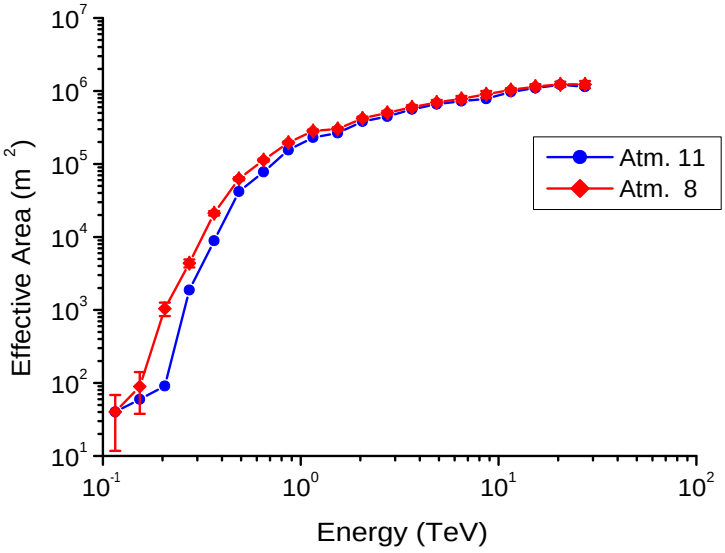

Figure 2.28: The effective area of a single H.E.S.S. ACT for triggering by γ-rays incident at 50^o angle for two characteristic aerosol profiles. Presented in Aye et al. (2003).

The atmospheric structure close the H.E.S.S. site has been studied by radiosonde measurements. Comparison with the available MODTRAN (see also Section 4.4) models showed that the atmosphere above the H.E.S.S. is best represented by the 'tropical' atmospheric profile (see Section 4.4.2). The most crucial mechanism for the

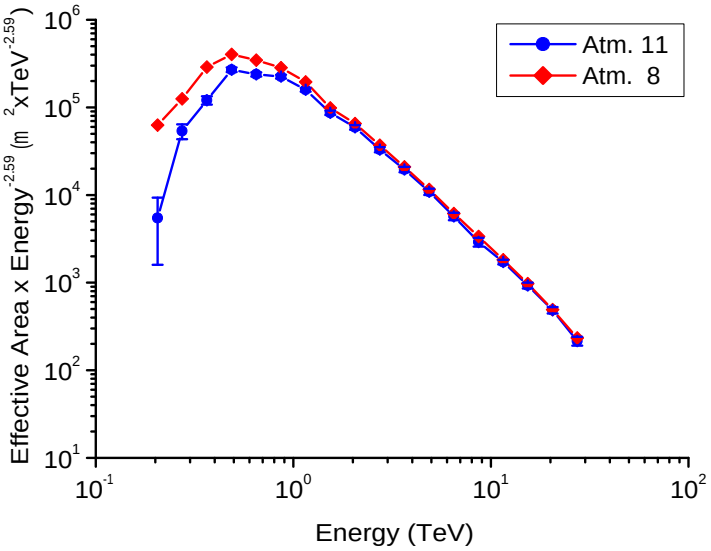

Figure 2.29: The effective area convolved with an energy spectrum of -1.59 integral index for triggering γ's at 50^o angle for two characteristic aerosol profiles. Atm.8 has the ground level at sea level and Atm.11 has the ground level 1.8 km above the sea level.

atmospheric attenuation of Cherenkov light is Mie scattering. This process depends upon the structure and composition of aerosol molecules that varies noticeably with time within the 'boundary layer' (i.e. first $\sim$ 2 km above the site). In this work the aerosol attenuation model that has been adapted consists of:

- a maritime haze model for boundary layer ($0-2$ km). This model is a combination of ocean and continental aerosol types and tends to give lower attenuation than the rural haze model,
- a spring-summer model for the troposphere (2-10 km). This model compensates for the slightly increased aerosol concentration during spring-summer period,
- a stratospheric aerosol model (10-30 km). At this region the aerosol concentration is uniform so a layer of background stratospheric dust is added.

The two models used, referred as Atm.8 and Atm.11 in Figures 2.28 and 2.29 have exactly the same structure, the only difference being the selection of the ground level. The H.E.S.S. site is at an altitude of 1800 m, so setting the ground level at sea level (Atm.8) leaves only 200 m of atmosphere for the Cherenkov light to be attenuated by the maritime haze. At the other extreme, the ground level has been set at the telescope altitude (Atm.11). In Fig. 2.28 the reduction of the ESA of the simulated γ-rays when placing the ground at the telescope altitude is evident. The effect is greater at lower energies since the photon yield depends on the shower's energy. Thus the attenuation effect will be more prominent for less energetic showers. A comparison of the energy threshold is difficult to make, however, due to the plateau around the peak (see Fig. 2.29). Clearly, the generation of more showers and better fitting of the ESA is necessary for any differences to be revealed. From Fig. 2.29 one can see that the threshold energy is $\sim$0.5 TeV for both atmospheric models used. This is higher than the estimated threshold energy of a single stand alone H.E.S.S. telescope (i.e. 40-100 GeV); it is also expected because we use simulated γ-rays at a zenith angle of 50° while the lowest energy threshold for the telescope is achieved for low observation zenith angles.

2.10 Alternative Astronomies using protons and/or neutrinos

2.10.1 Protons

As charged particles, protons will be deflected in the magnetised interstellar medium, which washes out their directional information. At the highest energies, however, proton astronomy may be possible. For energies E of $\sim$50 PeV and above, protons point back to their sources with an accuracy determined by their gyro-radius E_{gyro} in the intergalactic magnetic field (B) (Halzen and Hooper, 2002):

$$\theta \cong \frac{d}{R_{gyro}} = \frac{d \times B}{E} \tag{2.32}$$

where d is the distance to the source. Thus, for a 100 Mpc distant source

producing UHE particles (e.g. 3×10^{20}eV), the resolution may lie anywhere from sub-degree to nonexistent, depending on the chosen value for the strength of the inter-galactic magnetic field ($10^{-7} < \frac{B}{Gauss} < 10^{-12}$) in the local cluster (Halzen and Hooper, 2002).

At these energies, protons will interact with the background light, mainly by photo-production of a Δ resonance, as follows:

$$p + \gamma_{CMB} \longrightarrow \Delta \longrightarrow \pi + p \quad for \quad 2E_p\epsilon > (m_\Delta^2 - m_p^2) \tag{2.33}$$

where E_p, ϵ are the energies of the proton and the background photon respectively. The length scale of this process is:

$$\lambda_\pi \cong \frac{1}{\sigma_\pi n_{CMB}} \quad thus\ for\ :\xrightarrow[\sigma_\pi \cong 10^{-25} cm^2]{n_{CMB} \cong 422 cm^{-3}} \cong 20 \text{ Mpc} \tag{2.34}$$

where n_{CMB} is the number density of CMB photons and σ_π the π production cross section ; both numbers are known with reasonable accuracy (Sigl, 2001). This is the so-called *Greisen-Zatsepin-Kuzmin* (GZK) cutoff (Greisen, 1966; Zatsepin and Kuzmin, 1966)) that establishes a universal upper limit on the energy of CR's, assuming their astrophysical production. However, events above the GZK cutoff have been observed, leaving open the window of exotic physics (e.g. top-down scenarios discussed in the section 2.2).

In conclusion, proton astronomy may be possible at the highest energies depending on the strength of the inter-galactic magnetic field but with a CR flux of 1 particle per km^2 per century one has to instrument very large areas and be very patient. Recent results from the Auger experiment suggest there may be a correlation between arrival direction of the highest energy cosmic rays and active galactic nuclei (Abraham et al., 2007).

2.10.2 Neutrinos

The neutrino seems to be the ideal candidate to probe the most cataclysmic phenomena of our Universe. Indeed, the low cross-section of the weak interaction allows neutrinos to both escape their production sites and travel cosmological distances

without attenuation. For exactly the same reason, however, ν's are very difficult to catch. The preferred technique for observing ν's at energies usually above 100 TeV is to detect the faint Cherenkov radiation emitted by relativistic μ's which in turn are the products of the charged-current ν interaction with nuclei in the vicinity of the detector. The cheap way to do this is to use natural means (sea water/ice) both as your target and active Cherenkov medium. Then one has to go deep ($\sim$ 4km) in order to reduce the huge CR background (signal to noise $\sim 10^{-11}$ on the sea level) and instrument large areas of water/ice with large photomultiplier tubes (Resvanis, 1999). The effective area needed to compensate for the low ν cross-section is about 1 km^2. These instrumental challenges have prevented high-energy neutrino astronomy from flourishing yet. For example, the Antarctic Muon And Neutrino Array (AMANDA), after operating for seven years, has set limits on the diffuse neutrino flux but a source detection is still elusive (Xu, 2008). The birth of the field is expected in the near future by the completion of the first 1km^3 neutrino detector (e.g. Walter, 2007; Migneco, 2008). The achievable angular resolution in reconstructing muons tracks of such a detector will be dictated by the kinematics of neutrino production and the multiple scattering. The angular resolution will be optimum for a sea water telescope in comparison with one emerged on ice due to the reduced light scattering in clear sea water. The expected angular resolution for the Mediterranean KM3NeT (km^3 Neutrino Telescope) will approach 0.1° at $\sim$ 30 TeV, which is the limit imposed by the kinematics of the neutrino interaction (Distefano, 2009). Moreover, the detection point sources will be possible for known bursts, but unlikely if there is no prior knowledge of the location and time of the burst. However, neutrino detection from a point source would be strong evidence for hadronic acceleration in the vicinity of the source.

2.11 Summary

This chapter meant to serve as a brief introduction to the field of the ground based γ-ray ray astronomy. A short historical review was provided for γ-ray astronomy via satellites, but mainly concentrated on ground-based detectors, the maturity of

which came later. The processes responsible for the production and attenuation of γ-rays were briefly sketched. More emphasis was given in describing the details of the Imaging Atmospheric Cherenkov Technique. The physics behind the γ-ray and cosmic-ray cascades responsible for producing the Cherenkov signature of signal and background respectively onto the telescope's camera was underlined and methods of separation identified. The components of the most successful operating instrument, H.E.S.S., were discussed and the need for detailed simulation became clear. Finally, the author's original work in his first steps in the field, concerning simulation of a stand-alone H.E.S.S. telescope response under different assumption for the prevailing atmospheric conditions, has been presented.

Chapter 3

Atmospheric Monitoring for the H.E.S.S. Site

In this chapter the atmospheric monitoring instruments currently operating at the H.E.S.S. site in Namibia, with the exception of the LIDAR (see Chapter 4), will be discussed in detail. The overall status of the weather is monitored by a fully automated weather station while the Heitronics KT19 infrared radiometers provide vital information on the clouds crossing the H.E.S.S. telescopes' field of view. In addition, two LIDARs and a transmissometer, the latter of which has been conceived and constructed in Durham University, are being used to estimate the local atmospheric transmittance changes, chiefly due to aerosol variations.

3.1 Motivation

In ground-based gamma ray astronomy the atmosphere becomes an integral part of the detector. It is the target medium with which γ and cosmic rays interact, the active detector medium responsible for the emission of Cherenkov photons and the transport medium for those photons. Thus, even though Cherenkov telescopes are being constantly monitored and routinely calibrated to provide accurate information on their performance, one must remember that they consist of only a minor part of the whole detector. The telescopes' calibration is relevant from the time that the Cherenkov photons reach the telescopes' mirrors until they have been registered by

the PMTs. One has to take into account, therefore, the mechanisms of both production and extinction of Cherenkov light before it even reaches the IACT mirrors, caused by the most important part of the detector: the atmosphere itself.

The vertical atmospheric density profile determines both the particle shower development and the Cherenkov emission. Moreover, the amount of Cherenkov light that cosmic and γ-rays produce per unit path length, and its angle of emission, depend solely on the atmosphere's local refractive index. The probability of these Cherenkov photons reaching the IACT is determined by the atmospheric transparency which is a function of both altitude and wavelength. MODTRAN (Berk et al., 1999) was used to calculate the direct vertical transmission of light from 100 km above sea level down to the H.E.S.S. altitude of 1.8 km (see Figure 3.1). This plot shows that for the sensitive wavelength region of H.E.S.S.'s mirrors and PMTs (i.e. 250 - 700nm) the total light extinction depends on ozone molecular absorption and more significantly on Rayleigh scattering off all atmospheric molecules and Mie scattering (and to a much lesser extent absorption) by aerosols. In the case of clear atmospheric conditions, Rayleigh scattering is dominant at lower wavelengths caused by its λ^{-4} dependence whereas aerosol (Mie) scattering becomes dominant above 400nm (Bernlöhr, 2000). Both aerosol and ozone densities are highly time-variable so their monitoring is essential for the interpretation of the Cherenkov signal.

The presence of clouds passing across the field of view of the telescope causes a noticeable drop in its count rate as seen in Figure 3.4. The Durham group has a long tradition of using infrared radiometers, aligned par-axially with an IACT, in order to measure variations of the sky brightness temperature due to the presence of clouds and water vapour. A very clear inverse correlation between the radiometers' readings and telescope counting rate will be illustrated in the relevant section.

The detailed knowledge of the atmospheric conditions above H.E.S.S. site is essential when studying variable sources such as AGNs. One has to be certain that any short variation in the telescopes' count rate is due to the source itself and not to a sharp change of the atmospheric conditions. In addition, atmospheric corrections are necessary when calculating the flux of an object. Indeed, the most crucial factor

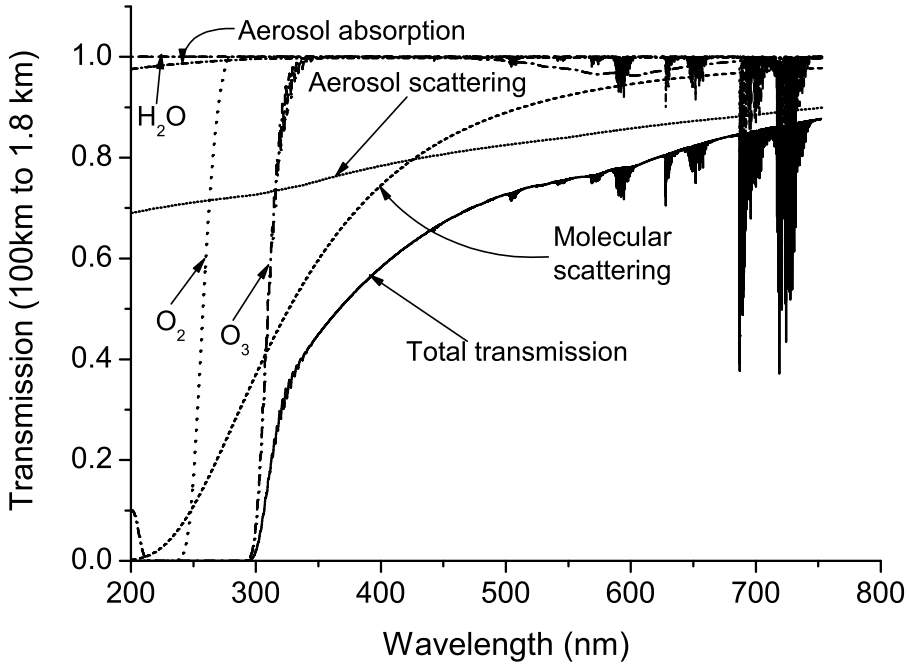

Figure 3.1: MODTRAN's estimation of the direct vertical transmission of light from 100 km above sea level to H.E.S.S. altitude of 1.8 km.

in determining telescopes' effective sensitive area is the atmospheric model used to represent the site's atmospheric conditions. The uncertainty introduced by the use of an inappropriate atmospheric model may lead to a systematic error of 20% in the absolute flux calibration of the standard candle for γ-ray astronomy (i.e. the Crab nebula) (Bernlöhr, 2000).

There is a plethora of ways for monitoring sky clarity. The response of the IACT to the Cherenkov light produced by the *C*osmic *R*ay *B*ackground (CRB) is often used to quantify changes in atmospheric transparency (LeBohec and Holder, 2002). This method is based on the assumption that the cosmic ray spectrum is almost constant for the Cherenkov telescope's operational range of energies (Gaisser, 1990). Thus, any fluctuation in the signal registered between different cosmic ray induced showers (observed by the same telescope and at the same zenith angle) reflects the difference in the atmospheric conditions between observations. The Achilles heel of this method, however, is that it depends on the performance of the Cherenkov

telescope itself, which might be difficult to quantify. Even though detailed Monte Carlo simulation should be used for the better understanding of the fluctuations of a Cherenkov telescope's sensitivity, the use of a cosmic ray background for relative calibration is a useful tool that allows quick corrections especially when observing variable γ-ray sources. An independent method, borrowed from optical telescopes, is the monitoring of the brightness of a star within the field of view of the Cherenkov telescope (Armstrong et al., 1999). This technique has numerous disadvantages: one cannot use relatively bright stars (i.e.: $m_v \sim 3$ or more) as they induce background noise in the telescope's PMT's, leaving a smaller window for the signal. On the other hand, the monitoring of a faint star with cheap CCD sensors tends to be noisy, giving a poor estimate of the atmospheric clarity (Daniel, 2002).

In order to address these problems, the H.E.S.S. experiment opted for atmospheric monitoring with the combined use of a weather-station, infrared radiometer and a "Durham made" transmissometer. A detailed description of each instrument will be given in the following sections. The LIDAR will be discussed separately in Chapter 4 due to its special contribution to atmospheric modelling.

3.2 Weather Station

A fully automatic weather station that meets the UK Meteorological Office specifications has been installed at the H.E.S.S. site since 2003. It comprises a barometric pressure sensor, temperature and relative humidity probe, a rain gauge and a combined anemometer and wind-vane for the measurement of wind speed and direction respectively. The standard outputs of these instruments accompanied by the relevant accuracies are presented in Table 3.1. The weather station is shown in Fig. 3.2.

The weather station is fully integrated within the H.E.S.S. central *d*ata *acq*uisition system (DAQ) and is monitored continuously. The weather data can be used as an extra safety net: a relative humidity threshold is used to cut off the high voltage on the camera electronics in order to prevent humidity-induced shorts.

Weather station data, however, are used chiefly for the generation of model atmo-

Measured Quantity	Range	Accuracy
Ambient Temperature (°C)	−10°C to +60°C	±0.35°C at −10°C ±0.6°C at +60°C
Relative Humidity (%)	10% to 100%	±2% at 10%, ±3% at 90% ±6% at 90 − 100%
Atmospheric Pressure (mbar)	600mbar to 1100mbar −40°C to +60∘C	±0.5mbar, −10°C to +50°C ±1.5mbar, −20°C to +60°C ±2.0mbar, −40°C to +60°C
Wind Speed ($\mathrm{m\,s^{-1}}$)	$0.2\,\mathrm{m\,s^{-1}}$ to $> 75\,\mathrm{m\,s^{-1}}$	$\pm 0.1\,\mathrm{m\,s^{-1}}, 0.3 - 10\,\mathrm{m\,s^{-1}}$ $\pm 1\%\,\mathrm{m\,s^{-1}}, 10 - 55\,\mathrm{m\,s^{-1}}$ $\pm 2\%\,\mathrm{m\,s^{-1}}, > 55\,\mathrm{m\,s^{-1}}$
Wind Direction (°)	360° mechanical angle continuous rotation allowed	±2° obtainable in winds $> 5\,\mathrm{m\,s^{-1}}$
Rainfall ($\mathrm{mm\,h^{-1}}$)	$0\,\mathrm{mm\,h^{-1}}$ to $> 133\,\mathrm{mm\,h^{-1}}$	4% at $25\,\mathrm{mm\,h^{-1}}$ 8% at $133\,\mathrm{mm\,h^{-1}}$

Table 3.1: Atmospheric information available from H.E.S.S. automatic weather-station and its limitations.

spheres via MODTRAN. We have seen (Fig. 3.1) that Mie scattering by aerosols is expected to be the most time-variable component of atmospheric attenuation. The wind speed can be directly inserted in MODTRAN's desert aerosol model. Under calm conditions, the desert aerosol is composed of particles with radii between 0.02 and 0.5 μm that represent the global aerosol background rather than the underlying soil. Under windy conditions, however, aerosols can be injected and transported over long distances. If wind speed exceeds a threshold (the value of which varies as a function of soil) new aerosols can be generated via sand-blasting processes (Kneizys et al., 1996). In that case, the size distribution of the additional aerosols would be similar to that of the underlying soil (Gillete et al., 1972). The wind speed, therefore, affects both the density and the size distribution of the local aerosols. The knowledge of the current wind speed is necessary for a realistic calculation of the light attenuation due to aerosols. A more quantitative description of the wind speed

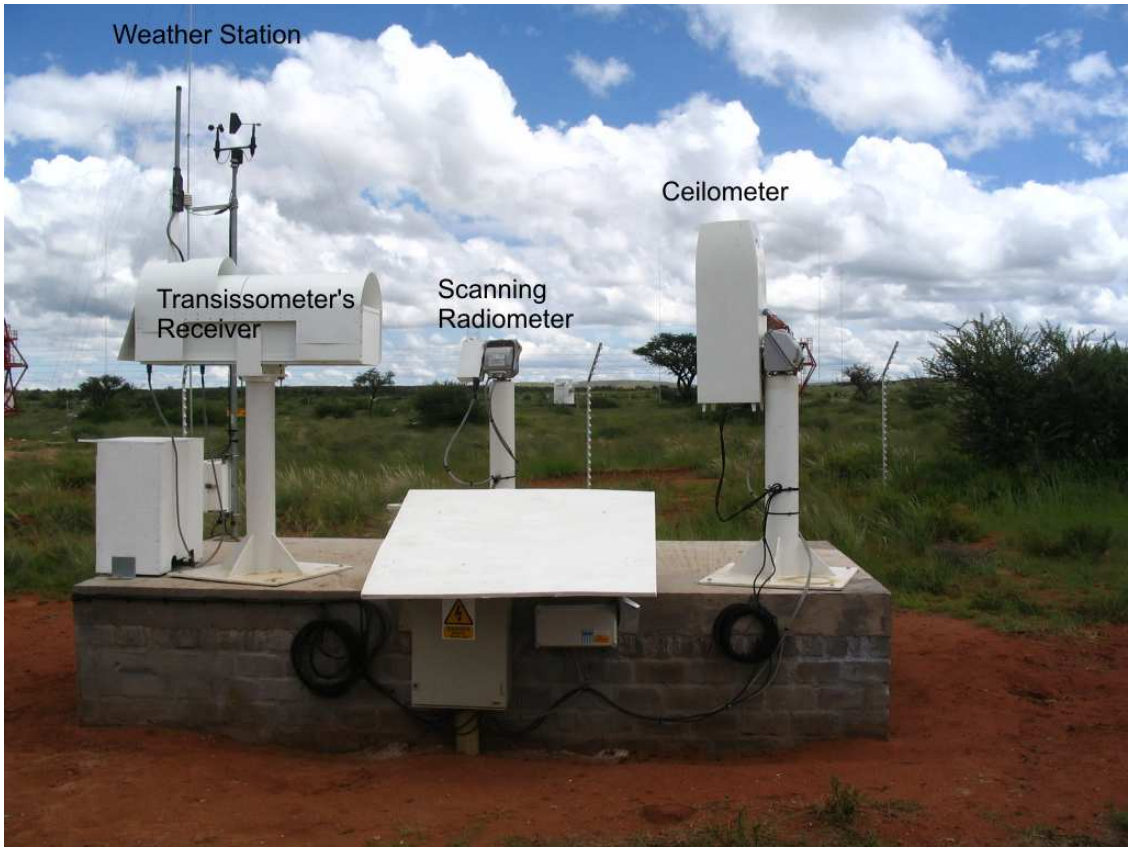

Figure 3.2: Photograph of the H.E.S.S. weather station, transmissometer's receiver, scanning radiometer and Vaisala ceilometer.

effect will be provided in Section 4.4.2.

Aerosol properties can also be affected by relative humidity. As relative humidity increases, water vapour condenses onto the aerosol particles leading to their hygroscopic growth. In addition to this size increase, the aerosols' chemical composition and refractive index will be altered too. However, it has been shown that Saharan desert dust consists mainly of non-hygroscopic mineral components and a water soluble component (see Section 4.3.3). Thus, the physical and chemical properties of desert aerosols posses a very small dependence upon relative humidity, solely due to the water soluble component, that can be safely ignored (Ackermann, 1998). The relative humidity is related to the molecular extinction and can be used directly in MODTRAN atmospheric package, in conjunction with transmissometer and LIDAR measurements, for the production of site-specific atmospheres.

3.3 Radiometer

3.3.1 Background Theory

The detection of clouds and water vapour is crucial in determining the cause of a variation in the telescopes' count rate. Infrared thermometry is a well established method for detecting clouds and monitoring their progress in the relevant field of view. Sloan, Show and Williams (Sloan et al., 1955) showed that measuring the infrared radiation of the sky, in the wavelength region between $8 - 14\mu m$, provides a good cloud detection tool.

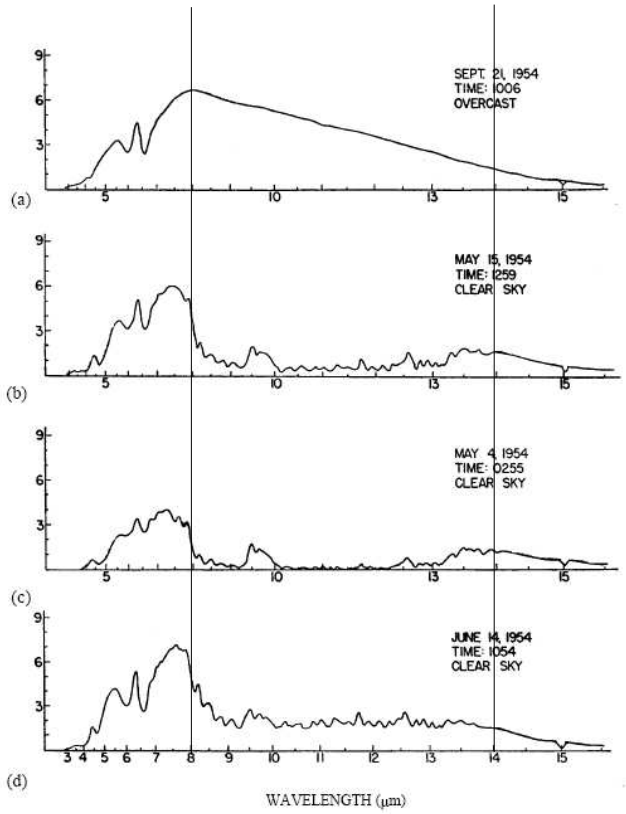

Figure 3.3: Zenith sky spectra obtained under different atmospheric conditions. The values of water-vapour concentration (gm^{-3}), measured 6 feet above the ground, are: (a) 15.2, (b) 9.3, (c) 5.9 and (d) 20.3. Taken from Bird et al. (1997) (after Sloan et al. (1955)).

Figure 3.3 shows that the spectrum of an overcast sky (Figure 3.3(a)) resembles emission of a blackbody having about ground-level temperature and is clearly

distinguishable from clear sky emission. Although an increase in the value of relative humidity leads to higher water-vapour infrared emission (Figure 3.3(d)), cloud emission stands well above this background as Figure 3.3(a) testifies. Indeed, even for increased values of relative humidity (Figure 3.3(d)) the presence of a cloud is easily detectable (Bird et al., 1997).

Within the selected wavelength range of $8-14\mu$m the atmosphere is almost transparent as it only contains O_3 emission lines at 9.6μm. This region is surrounded by the emission lines of H_2O at lower wavelengths (i.e. 7μm) and by the emission lines of CO_2 at 15μm. Carbon dioxide contributes no more than 0.035% of the total atmospheric gas content and is uniformly mixed up to 80 km. CO_2 varies slightly with season (Chandrasekhar, 1960) but can be considered invariant for infra red emission. Ozone concentration is minimal for altitudes ranging from the surface level up to the stratosphere. At ground level, O_3 concentration may be high due to industrial activities (factories, airports), but can be safely considered minimal in the case of γ-ray telescope sites. On the other hand, water vapour concentration varies both seasonally and daily and is also a function of altitude and latitude (Farmer, 2001*a*). It possesses continuum emission due to the association of water vapour molecules in pairs which are more pronounced when the partial pressure is high (Houghton, 2002). Thus, the most important atmospheric absorber for the wavelength region between 8 and 14μm is water vapour which also comprises the major source of Cherenkov light attenuation due to cloud formation. It, therefore, makes sense to monitor the atmosphere in the infra-red window by the use of radiometers.

Infra-red detectors are usually based on the pyroelectric effect. Pyroelectric materials possess a permanent electric dipole moment along a uniquely defined direction (Ludlow et al., 1967). Infra-red radiation can cause small changes in the material's temperature that correspond to a slight displacement of the material's lattice spacing. That in turn leads to a change in the internal dipole moment which can be measured by the application of an external field capable of reversing the direction of the moment. The reversal of the moment is needed as the electrical charge along the direction of ferromagnetic materials becomes neutralised by stray charges (trapped in the material's surface) that cannot relocate themselves quickly in the presence of

a large external field. Thus, the change in the dipole moment can in this way be measured (Ludlow et al., 1967).

3.3.2 KT19.82 II Radiometers

Durham was the first γ-ray group to mount *m*id *i*nfra-*r*ed (MIR) radiometers onto a γ-ray telescope (namely Durham's Mark 6 telescope located in Narrabri Australia) (Chadwick et al., 1999) for monitoring the sky clarity. The usefulness of this technique was quickly proven, as the anti-correlation between telescope's count rate and radiometer's measured temperature, shown in Figure 3.4, testifies.

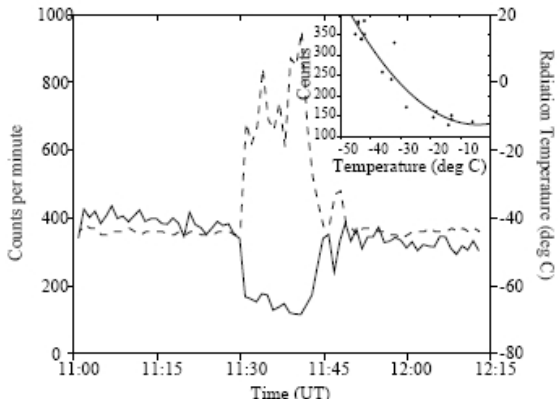

Figure 3.4: The clear anti-correlation between the Mark 6 γ-ray telescope's background counting rate (solid line) and radiative temperature of the sky (broken line). The inner diagram reveals the fluctuation of the count rate as a function of sky radiative temperature. Taken from Buckley et al. (1999).

The Heimann model KT19.82 II mid infra-red radiometer was selected for the H.E.S.S. site which is an upgrade of the KT17 model used at the Mark 6 telescope. The KT19 operates in the $8-14\mu$m wavelength range which is sensitive to the water vapour concentration due to H_2O's continuum emission. The transmission window for a horizontal path of 500 m at H.E.S.S.'s altitude of 1.8km and a desert aerosol distribution has been estimated using the MODTRAN4 program (Berk et al., 1999) and is presented in Figure 3.5.

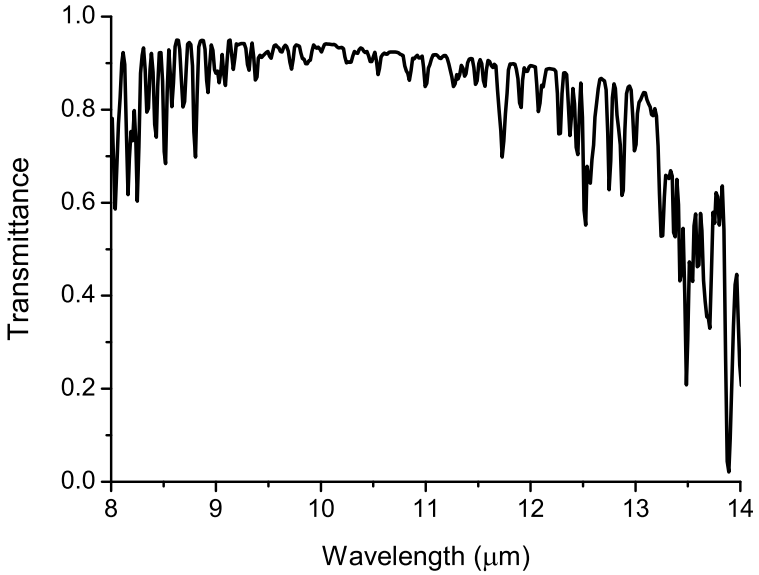

Figure 3.5: Transmittance window for a horizontal 500m path at the H.E.S.S site as calculated by MODTRAN4 program (altitude of 1.8 km and desert aerosol distribution for a wind speed of 10 m/s).

There are currently five KT19 radiometers operating at the H.E.S.S site. Each of the four H.E.S.S. telescopes is equipped with a radiometer paraxially aligned to it (see Figure 3.6) and one is mounted on an autonomous steerable base (see Figure 3.2), allowing for a full sky scan. The telescopes' radiometers are constantly monitoring the temperature of the part of sky that is being observed by the telescope allowing for correlation studies between sky brightness temperature and telescope's count rate. In addition, the scanning radiometer provides a full sky overview including cloud coverage and approaching weather fronts.

The radiometers are fully embedded within the H.E.S.S. data acquisition (DAQ) software. Figure 3.7 shows a graphical representation of the scanning radiometer's output as displayed to the shift crew. Each triangular sector of the polar diagrams corresponds to a zenith angle bin. The colour coding ranges from red to blue corresponding to a span of high to low sky temperatures. The left display shows the raw radiometer data mostly in the blue which corresponds to cold (hence clear) skies. The temperature registered by the radiometer increases with the zenith angle

Figure 3.6: KT 19 radiometer paraxially mounted in one of the four H.E.S.S. telescopes.

due to the thicker part of the atmosphere being observed (Buckley et al., 1999). Therefore, a correction in order to take out the zenith angle dependence needs to be implemented. Such a correction has been applied to the raw data and is shown in the right display of Figure 3.7. In this case, the correction consists of taking the difference between the current scan from the averaged previous one as it is shown in the right part of Figure 3.7. The four green rings appearing on the upper part of both displays are caused by the radiometer's steerable base dead zone. The red pixels in the periphery of the polar plots correspond to objects entering the field of view of the scanning radiometer at low elevations (Aye, 2004).

In conclusion, H.E.S.S. paraxial radiometers provide a tool for the immediate detections of clouds in the field of view of the telescope's camera while the scan-

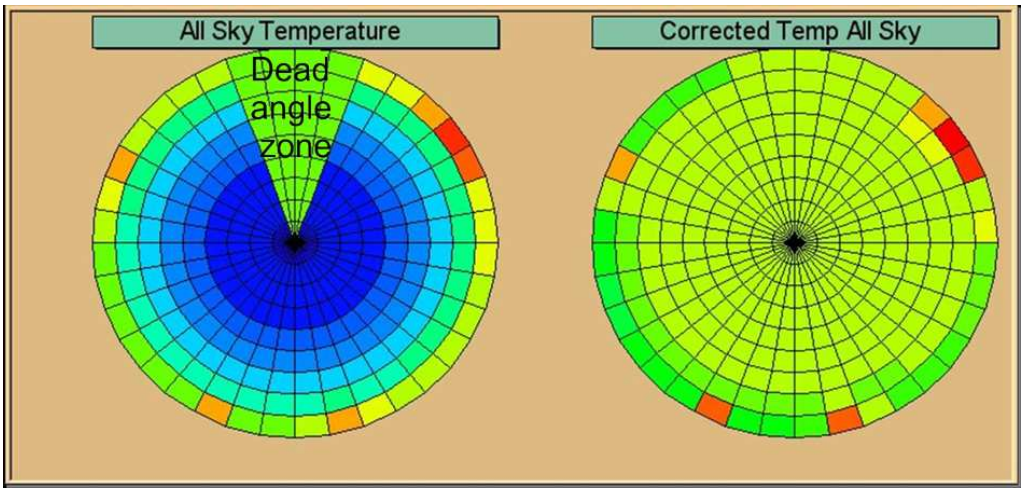

Figure 3.7: Display of the scanning radiometer available for H.E.S.S. shift crew.

ning radiometer alerts the observers for approaching weather fronts. The paraxial radiometers' data are mainly used for selecting cloud free runs for analysis. Radiometer measurements can in theory provide an estimate of the atmosphere's water vapour content which in turn can be used for atmospheric modelling.

3.4 Durham Night-time Transmissometer (DNT)

In order to have a direct measure of transmittance, the Durham group manufactured an novel transmissometer that operates in parallel with the γ-ray telescope array in Namibia. The DNT is composed of two separate units (i.e. receiver and transmitter) with a horizontal separation of 29.8 km and a vertical separation of 550 m. Specifically, the light source is located at the top of the Gamsberg, being the highest hill in the vicinity and offering an unblocked view to the H.E.S.S. site, whereas the receiver is located near the other atmospheric instrumentation on the H.E.S.S. site (see Fig. 3.2). While the difference in height between transmitter and receiver, as dictated by the Gamsberg's altitude, limits the transmittance measurement to the first 550 m above the H.E.S.S. site, the horizontal distance of 29.8 km is suitable for maximising the instrument's sensitivity (see Section 3.5). The transmitter-receiver communication is achieved via a radio link and the generic scheme of the DNT system can be found in Figure 3.8.

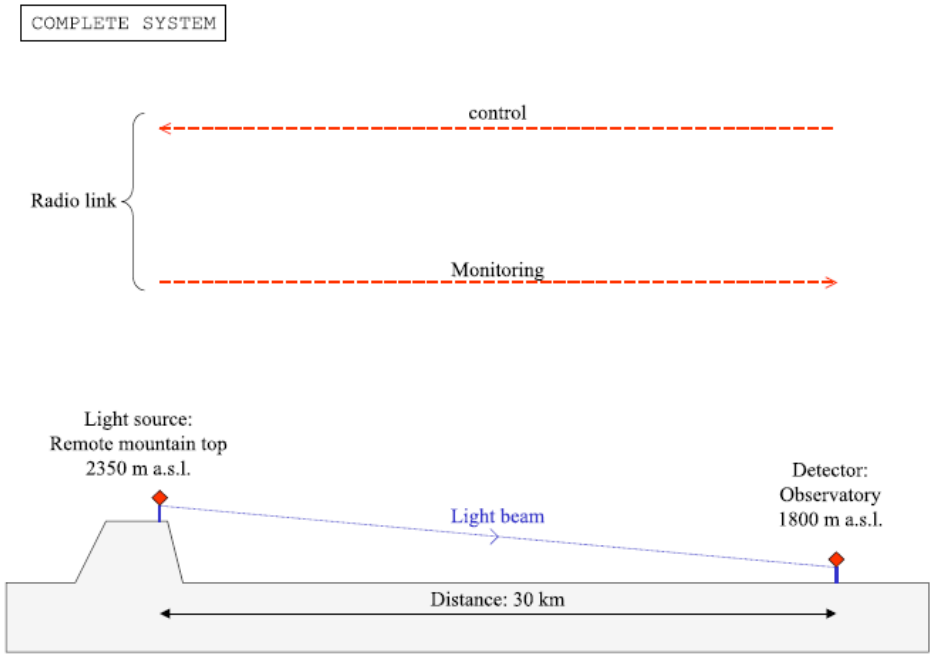

Figure 3.8: Schematic set-up of Durham's Night-time Transmissometer. Taken from (Le Gallou, 2005).

The novelty of the DNT is two-fold:

- the transmitter consists of four super-bright LEDs, operating at wavelengths of: 390 nm, 455 nm, 505 nm and 910 nm respectively,
- the receiver employs a Charge Coupled Device (CCD) camera that sits behind a 200 mm Newtonian telescope.

Prior art transmissometers generally consist of gas discharge bulb light sources and photodiode receivers. In comparison with the super bright LEDs, the gas discharge bulbs are expensive, high in power consumption and have shorter mean time between failures (MTBF). As a result the usage of bulbs, as opposed to LEDs, increases the cost of both manufacture and operation of the transmissometer. Moreover, the use of the photodiode drastically limits the field of view of the light receiver, making the correct alignment of its components very difficult. In order to overcome alignment issues, one has to build concrete bases to mount both transmitter and receiver units, which increase the manufacture cost of the transmissometer and limits its uses.

The combination of the above factors makes the instrument easy to align and enable it to operate for long periods with minimal maintenance. In addition, the system is able to operate autonomously via a solar-powered supply. However, the DNT operates only during the night since it was built to assist γ-ray observations.

In the following sections a full description of the instrument's hardware, control and results obtained during the 2 years of operation will be given. The DNT software will be briefly presented due to its similarity with the software for a later model presented in more detail in Chapter 5.

3.4.1 Hardware

The Transmitter Unit

The transmitter unit is mounted on a communication mast located on the top of Gamsberg hill 30 km away from the H.E.S.S. site (see Figure 3.9). The robust design of the light source is clearly presented in this picture. In addition, the water tank can be used for automatic cleaning of the transmitter's transparent lid, thereby maximising the time between maintenance. Figure 3.10 gives the internal construction of the receiver. It consists of four LEDs two of which (i.e. 320 nm and 910 nm) are sitting behind two identical camera lenses with focal length of 50 mm whereas the 455 nm and 505 nm LEDs are mounted behind polycarbonate lenses. The specification of the LEDs can be found in Table 3.2.

The four LEDs are driven by a PCB (see Appendix B.2), produced in Durham, capable of providing a stable current independent of temperature fluctuations. Two photodiodes are employed to constantly monitor the LEDs' output, allowing for post-data calibration. In addition, the PCB allows the monitoring of the LEDs' driving current and temperature, used for quality assurance of the data.

The communication between the transmitter and receiver units is achieved by a licence-free radio connection with the aid of a 500 mA radio modem and a dipole antenna. As the light source needs to be operated in a remote location, it is powered by solar panel and a car battery.

Figure 3.9: The transmitter mounted at Gamsberg's telecommunication mast. One can see the antenna, light emitter and the water tank (left to right). From Le Gallou (2005).

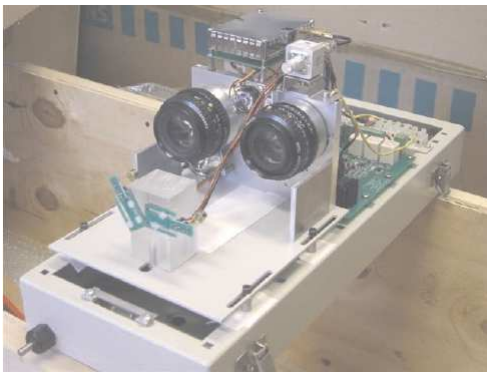

Figure 3.10: Inside the transmitter. The two identical lenses are sitting in front of 390 nm and 910 nm LEDs while the two polycarbonate lenses are responsible for focusing the 455 nm and 505 nm LEDs. The two photodiodes responsible for monitoring the LEDs output are also visible (i.e. looking towards each camera lens). Extracted from Le Gallou (2005).

The Receiver Unit

A schematic representation of the light receiver is shown in Figure 3.12. It is built around the ST4-CCD camera that is mounted behind a 200 mm Newtonian telescope. The camera offers a wide field of view, making the alignment between receiver and transmitter easy. The dynamic range of its sensor, coupled with an 8-bit digitiser, provides reasonable resolution for transmittance monitoring above the H.E.S.S. site. As shown in Figure 3.12, the receiver consists of two separate units:

- An all weather enclosure protecting the receiver's optics (CCD camera and telescope). The enclosure's window is equipped with a heater-demister. The

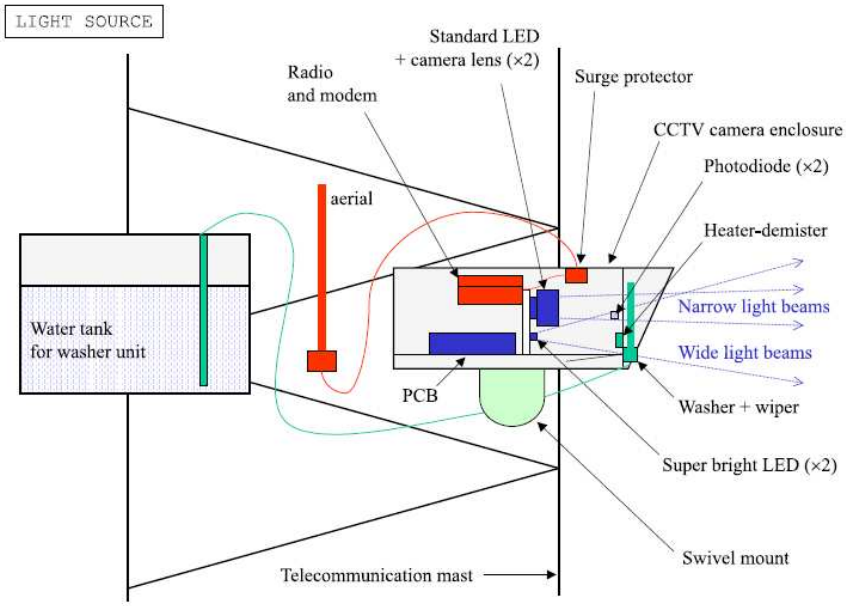

Figure 3.11: Schematic diagram of the light emitter of DNT. Taken from (Le Gallou, 2005).

detector unit is mounted on a steerable base with provision of mechanical alignment. A lid protects the CCD camera from direct sun exposure and is always closed during the day. The detector unit can be seen in Figure 3.13.

- An electronics cabinet containing: server, CCD controller, power supply and reception switch. The components of the electronics cabinet can be clearly identified in Figure 3.14.

This construction allows for reasonable temperature stability within the detector unit, taking into account that the transmissometer needs to operate only during the night. The relatively low temperatures of Namibian nights, combined with the CCD camera's low resolution (i.e. 256 levels of grey), lead to a hardly measurable temperature induced noise.

The CCD controller operates the camera via a modem and RS232 cabling. The distant light source is also driven by RS232 with the aid of a radio modem located in the detector's enclosure (see Figure 3.12).

Table 3.2: LED specifications

LEDs Specifications	1	2	3	4
Make	SMD	Luxeon© Star		ELD
Reference	Toyoda Gosei (2004)	Lumileds (2006)		EPIGAP (2004)
Centre Wavelength (nm)	390	455	505	910
Driving Current (mA)	20	350	350	100
Luminous Flux (lm)			45	
Radiometric Power (mW)	4.1	220		30
FWHM of beam (^{o})	2.3	10	4	15

3.4.2 Software

Algorithm

The program that drives the transmissometer is responsible for the operation of both LEDs and the CCD camera. The measuring algorithm is very similar to the day-light prototype one (presented in more detail in Section 5.4.1) and consists of the following tasks (Le Gallou, 2005):

- Day/Night discrimination. The photodiode voltage is read with the LED switched off every 15 min until night has been detected. This initiates the beginning of a full measurement cycle:
- the 455 nm LED is turned on,
- the CCD camera takes an exposure, using a default exposure time that produces a signal optimised for the camera's dynamic range under a typical night,
- the frame taken is scanned and the brightest 3×3 cluster of pixels is located. The LED produces a circular spot of $\sim$ 10 pixels Full Width Half Maximum (FWHM),

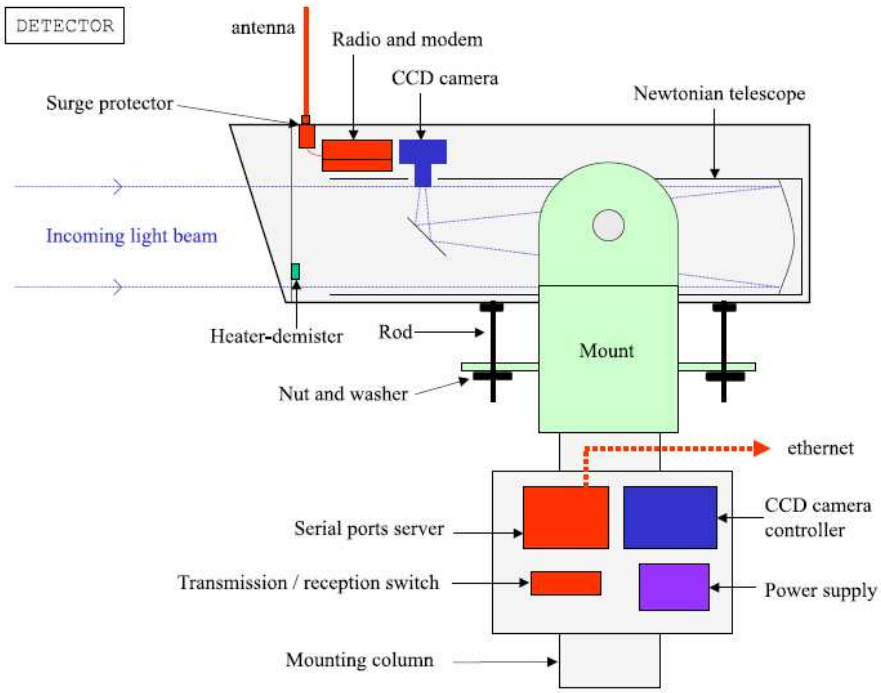

Figure 3.12: Schematic diagram of the light receiver of DNT. Taken from Le Gallou (2005).

- a loop over exposure time is initiated requiring the brightest 3×3 cluster intensity to be between 170 and 255 ADUs,
- when the optimised exposure time has been reached, the intensity $(R_{on} + R_{off})$ of a 25×25 cluster centred around the brightest spot is calculated. The background intensity is then calculated by computing the average value of the intensity R_{off1} of the cluster located between 13 and 19 pixels from the centre of the light spot. The LED's received intensity (R_1) is finally calculated by subtracting the overall intensity from the normalised average background intensity,
- the LED is switched OFF,
- a dark frame is taken with the the same exposure time as before,

Figure 3.13: Light receiver with the lid open. Taken from Le Gallou (2005).

Figure 3.14: Inside the electronic cabinet. Starting from the upper right side and proceeding clockwise one can clearly identify: server, CCD controller, power supply unit and connection box. Extracted from Le Gallou (2005).

- a second value of the LED's received intensity (R_2) is computed by subtracting the summative values of pixels consisting of a 39×39 square of the dark frame from the summative value of the same area taken from the ON frame,
- the calculated values (R_1, R_2) are divided by the exposure time used in order to express the intensities as count rate (i.e. ADUs/s), and
- the same process is repeated for the 505 nm, 910 nm and 390 nm LEDs until daylight has been detected.

3.4.3 Practical Estimation of Transmissivity

Transmissometers generally consist of a light source and one or more receivers. The transmitter sends a narrow beam of light of known intensity towards the receiver that records the intensity of the surviving beam hitting its sensor. Transmissometers, therefore, measure the transmittance directly from the attenuation of the emitted light due to scattering and/or refraction, using:

$$t_b = exp(-\sigma b) \tag{3.1}$$

where:
b denotes the length of the optical path, and
σ is the extinction coefficient.

Thus, transmissometers give us the intensity of the initial beam after it has travelled a path length x through the atmosphere (I). If the initial intensity is known (i.e. the intensity at $x = 0$, calibration factor) one can directly calculate the transmittance, which is related to the extinction coefficient via equation 3.1. The transmittance is calculated from the following formula:

$$T = \frac{I}{I_0} = e^{-\sigma x} \tag{3.2}$$

The overall extinction coefficient is the sum of absorption and scattering of both aerosols and gases. Since within the optical band the only light-absorbing molecule is ozone, σ can be expressed as:

$$\sigma(h, \lambda) = \sigma_R(h, \lambda) + \sigma_{O_3}(h, \lambda) + \sigma_{AER}(h, \lambda). \tag{3.3}$$

where:
$\sigma_R(h, \lambda)$ is the extinction due to molecular scattering
$\sigma_{O_3}(h, \lambda)$ is the extinction due to ozone
$\sigma_{AER}(h, \lambda)$ is the extinction due to aerosol scattering and absorption
and h denotes the the elevation above sea level.

It should be noted that the above equation can be solved for $\sigma_{AER}(h, \lambda)$ because $\sigma_{O_3}(h, \lambda) = 0$ (for the wavelength region of interest and for altitudes lower than

10km) and σ_R can be independently derived from measurements of atmospheric pressure and temperature. That is important when transmissometer results are to be compared with ceilometer's backscatter readings as in Figure 5.1. It should be stressed that even though $\sigma_{O_3}(h, \lambda) = 0$ is a safe assumption for the H.E.S.S. site in Namibia, it is not valid at airports where our daylight-prototype (see Chapters 5 and 6) is most likely to operate. In this case the absorption due to the ozone produced by aviation fuel must be accounted for.

3.4.4 Transmissivity for Receiver and Transmitter at different altitudes

Equation 3.2 applies for the calculation of horizontal transmittance. As one of the major advantages of Durham's transmissometers is that the transmitter can be mounted much higher that normal transmissometers (see Fig. 3.9), one needs to calculate the vertical transmittance:

$$T(d) = e^{-\frac{d}{x}} \tag{3.4}$$

where:
d is the vertical distance between receiver and transmitter.

For a known baseline (D) between transmitter and receiver the optical length x can be expressed in terms of the transmissometer's measurement and calibration coefficient as follows:

$$x = \frac{D}{ln(\frac{I_0}{I})} \tag{3.5}$$

The combination of Equations 3.4 and 3.5 gives:

$$T(d) = \left(\frac{I_0}{I}\right)^{\frac{d}{D}} \tag{3.6}$$

For the case of the DNT $d = 550$ m and $D = 29.8$ km and the above equation can be written:

$$T(d) \sim \left(\frac{I_0}{I}\right)^{-0.0185} \tag{3.7}$$

In practice, for the calculation of transmittance over both horizontal and slant paths, I is measured as the received minus the background intensity. The latter is calculated by two independent methods (i.e. R_1, R_2 see Section 3.4.2). Using the calibration coefficient (i.e. the intensity expected to reach the camera if the atmosphere was 100% transparent) the transmittance can be calculated using Equation 3.7. Both measured and estimated intensities are normalised over their exposure time (ADUs/ms).

3.4.5 Results and Simulations

The DNT has been operational since March 2005. During this three years of operation it has proven reliable. Indeed, the DNT's log book testifies that it was not operational for only two long term periods namely, $9/7/05 - 21/08/05$ and $6/11/06 - 18/12/07$. On both occasions, a power cut due to the dying battery caused the problem. However, after the replacement of the receiver unit (February 07), short term technical problems have increased.

As the H.E.S.S. site was selected partly based upon its excellent optical properties, the typical transmissometer reading fluctuates slightly around an average value of 0.98 transmittance. However, the DNT has proven its usefulness under dusty episodes that can decrease telescope's trigger rate by as much as 50%. In cases of relatively low atmospheric transmissivity, the transmissometer's readings can be divided in two broad categories:

- stable nightly measurements that imply that the measured transmittance over 550 m and along ~ 30 km separating transmitter-receiver units, is relevant to the local H.E.S.S. atmospheric conditions and

- relatively unstable measurements. In this case, the transmittance value must be checked against LIDAR and trigger rate readings in order for the relevance of the local atmospheric conditions to γ-ray measurements to be established.

In Figure 3.15 the transmittance measured during the night of 16^{th} of September 2006 using the 505 nm LED is shown. The variation around the average value of 0.96 is small (i.e. $\sim 0.4\%$) and becomes apparent in the histogram presented in

Figure 3.16. In addition, the good agreement between the two different methods for calculating the signal's intensity is evident in Figure 3.17. An example of a relatively unstable transmittance values taken on the night of 18^{th} of June are presented in Figures 3.18, 3.19 and 3.20 respectively. In this case, the RMS fluctuation has increased by a factor of 2 in comparison with the more stable transmissivity measurements on the 16/09/2006. Moreover, the agreement between the I_1 and I_2 background calculation is broken indicating that the measurements are affected by spatial and temporal variations respectively.

The overall plot showing transmissivity values measured at three different wavelengths, from April 2005 to December 2006, as a function of run number can be found in Figure 3.21. The measurements at 455 and 505 nm follow each other closely, while the 910 nm transmittance is significantly lower. That is easily explained by the gaseous absorption spectral bands in the atmosphere above the H.E.S.S. site. In the usually aerosol-free Namibian skies the absorption of light depends chiefly on the spectral absorption of water vapour and oxygen and to a much lesser extent the ozone absorption bands. Figure 3.25 shows the percentage transmission over a 550 m vertical path, for a desert extinction model with a 4.5 m/s wind speed, for a wavelength range covering the operating range of the LEDs used. In the visual range window, the transmittance is very high as ozone is the only absorbing gas with just detectable absorption spectra. The decrease in transmittance occurring in the near-infrared band is caused by molecular water vapour absorption. In addition, the uncertainty involved with transmittance estimation within the 910 nm LED range (i.e. 910 ± 40 nm) is large, explaining the exclusion of this LED's data from the comparative Figure 3.26. This is due to the lower power of the infra-red LED as opposed to the visible ones at 455 nm and 505 nm.

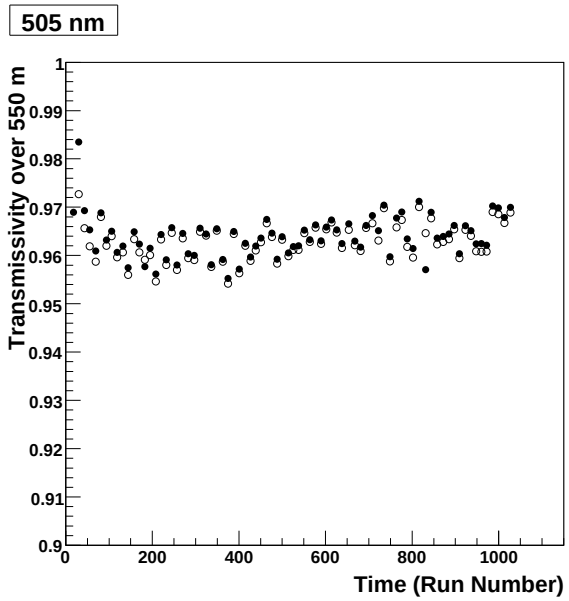

Figure 3.15: Transmissivity of the first 550 m above the H.E.S.S. site as a function of time for the stable night of 16^{th} of September 2006. Black and white dots correspond to R_1 and R_2 intensity measurements respectively (see 3.4.2).

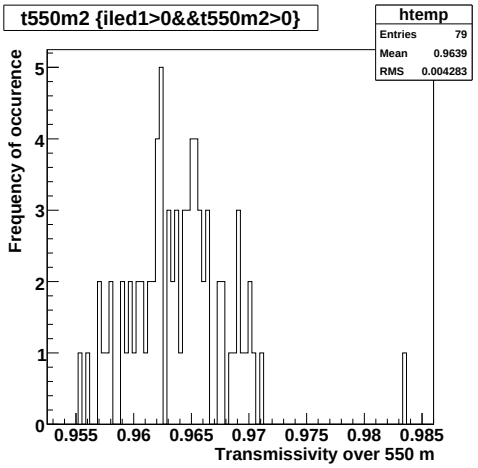

Figure 3.16: Distribution of transmittance measurements during 16/09/06.

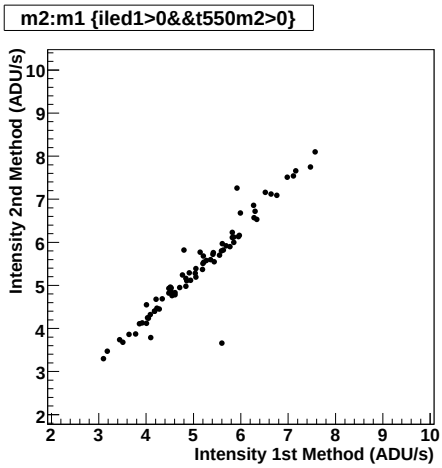

Figure 3.17: Correlation between the raw intensity values calculated via the two different methods (as described in Section 3.4.2) registered on 16/09/06.

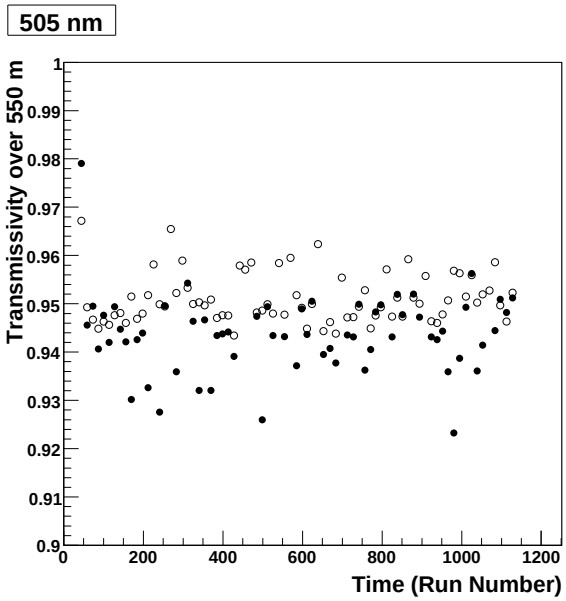

Figure 3.18: Transmissivity of the first 550 m above the H.E.S.S. site as a function of time for the stable night of 18$^{\text{th}}$ of June 2006. Black and white dots correspond to R_1 and R_2 intensity measurements respectively (see Section 3.4.2).

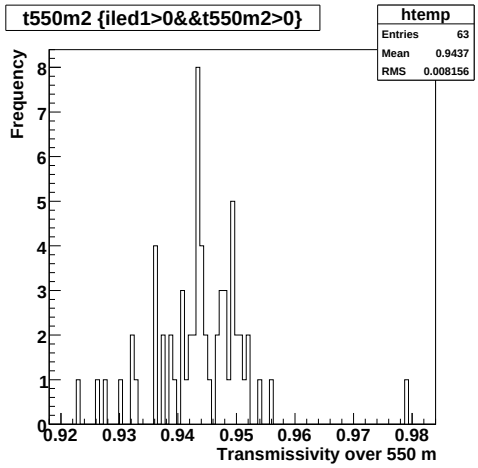

Figure 3.19: Distribution of transmittance measurements during 18/06/06.

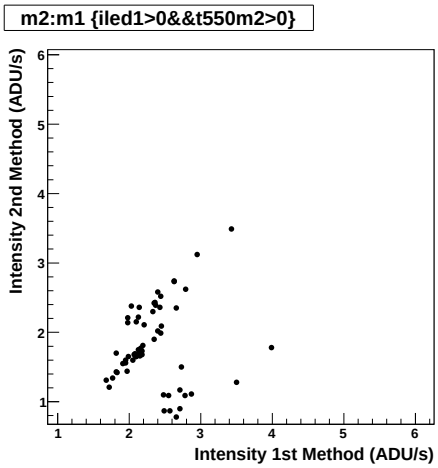

Figure 3.20: Correlation between the raw intensity values calculated via the two different methods (as described in Section 3.4.2) registered on 18/06/06.

In February 07 the telescope located at the DNT's receiving end was changed. Even though an 'in-situ' re-calibration was not performed, due to time restrictions, an off-line calibration factor is applied to data taken after 4$^{\text{th}}$ February 2007. Figure 3.22 presents data taken via the 455 nm LED within the period 3$^{\text{rd}}$ March 2005 - 31$^{\text{st}}$ April 2007, excluding some erratic nights due to technical problems or unstable atmospheric conditions. Due to technical problems there was no data-taking during February, while there was only one night's worth of data in January and six in March 2007. Thus, one cannot make conclusive remarks about the yearly periodicity of atmospheric transmissivity based on the DNT data available. The periodicity of this atmospheric effect is better demonstrated by TOMS (Total Ozone Mapping Spectrometer) satellite instruments measurements of aerosol index (A_I) taken between 1996 and 2005 over the H.E.S.S. overpass site (i.e. 23.2 S, 16.7 E) see Fig. 3.23. TOMS A_I is a measure of the total backscatter radiation as registered by the instrument at 360 nm in comparison to the backscatter produced in a ideal molecular atmosphere (i.e. $A_I = 100 \log \frac{I^{obs}_{360}}{I^{theor}_{360}}$) and relates to the optical depth (TOMS, 2008). The seasonal variation of the optical depth has also been independently measured by ground based measurements of AERONET (*Ae*rosol *Ro*botic *Net*work on the Etosha Pan site (19.30 S, 15.51 E) as seen in Fig. 3.24) (Privette et al., 2005).

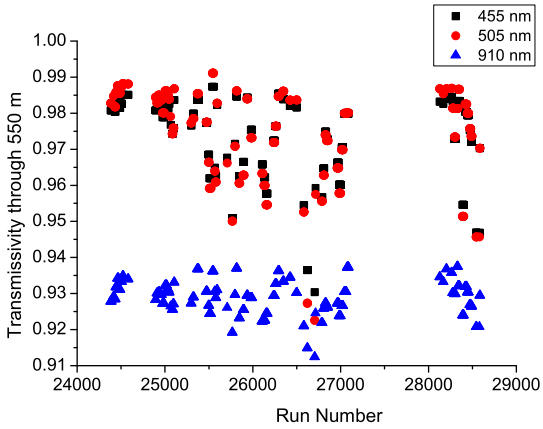

Figure 3.21: Distribution of transmittance measurements at 455, 505 and 910 nm from April to December 2005.

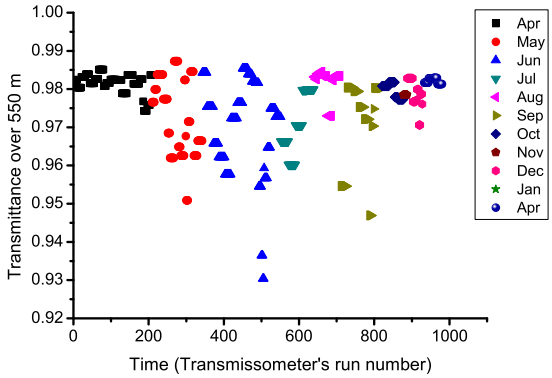

Figure 3.22: Collective transmissometer readings at 455 nm from 3/3/05 to 31/4/06.

Thus, low level dust-storms are expected on the H.E.S.S. site during the period

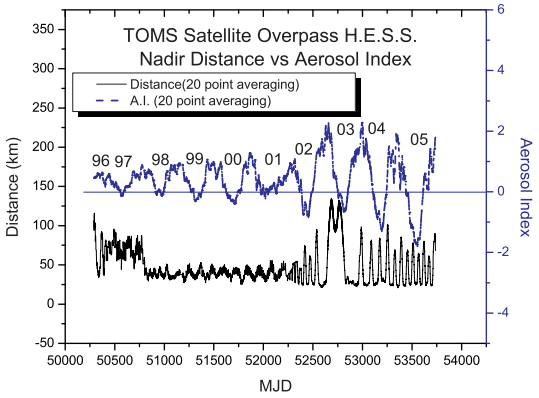

Figure 3.23: Distribution of TOMS aerosol index for the years 1996 to 2005 at the overpass H.E.S.S. site. The distance from the overpass site (nadir centre of the TOMS field of view) has also been plotted to account for the large fluctuations between the years 2002-2006. The data have been downloaded from TOMS (2008).

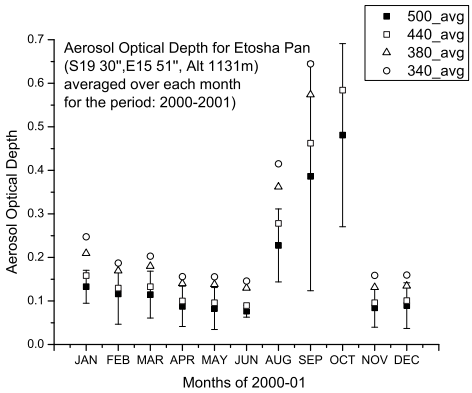

Figure 3.24: Monthly average values for the optical depth obtained during the year 2001 at AERONET's ground based station in Etosha Pan. The data for this plot were obtained from (Privette et al., 2005).

between June and September (see Fig. 3.23) , a fact that is verified by the transmissometer's minima occuring during June and September (see Fig. 3.22). At the Etosha Pan site the relevant period of increased dust storms is between August - October, while there is no available data for July. One should note the wide spread of optical depths during dusty months (i.e. September, as demonstrated by the relevant error bars in Fig. 3.24) that is also seen by the transmissometer during the Namibian winter, with dusty event episodes occurring between very clear atmospheres (see Fig. 3.22). This can provide a handy calibration tool when seeking correlations between the telescopes' count-rate and the DNT's readings.

3.5 Conclusions

In this chapter the instruments used for the atmospheric monitoring of the H.E.S.S. site in Namibia have been presented. Special emphasis was given on the role of

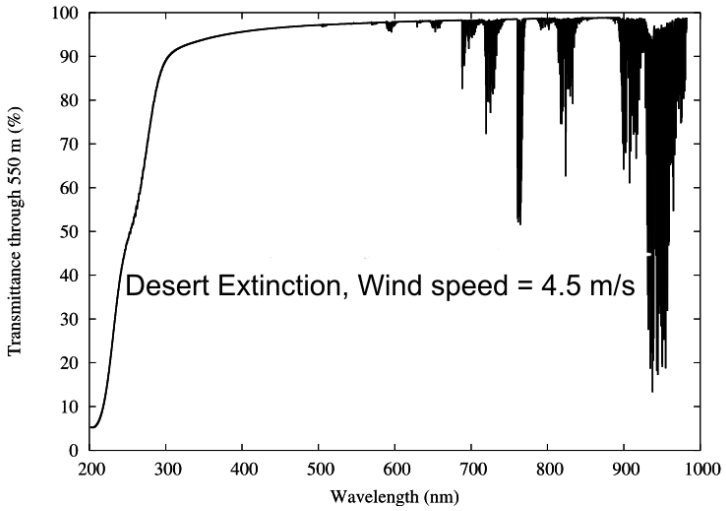

Figure 3.25: MODTRAN calculated transmissivity for desert aerosol extinction at a wind speed of 4.5 m/s.

each instrument on the production of site-specific atmospheric models. Specifically, the weather station measurements (i.e. surface temperature and wind speed) can be imported into the MODTRAN software package for a realistic calculation of the atmospheric transmissivity in conjunction with the transmissometer and LIDAR measurements. The radiometers cannot be used to extract the atmosphere's water vapour content but they are utilised for cloud and approaching weather fronts detection. Specifically, a cut on the radiometer *r*oot *m*ean *s*quare (RMS) readings is utilised for the selection of telescope data under clear atmospheric conditions. The use of LIDAR in atmospheric modelling will be discussed in Chapter 4. In what follows the use of DNT as atmospheric model selector and its limitations will be discussed in detail.

The major motivation for the DNT was the prediction of nightly site-specific atmospheric transmission tables giving the optical depth as a function of both wavelength and altitude. One can use these transmission tables to filter simulated Cherenkov showers in order to access the atmospheric effect on the telescopes' trigger rate and effective area (see Section 2.9.1). The MODTRAN4 (Berk et al., 1999) program is used to generate transmission tables. A comparison of MODTRAN transmissivities calculated with the desert extinction model and transmissometer

data taken during typical clear and dusty nights is shown in Figure 3.26. The transmissometer's data can be matched by adapting the desert extinction model (which represents best the H.E.S.S. site aerosol characteristics) and altering the wind speed to evoke the aerosol concentration which, in turn, controls the atmospheric transmissivity. It should be stressed that the wind speed fine tuning is merely a technical trick and does not correspond to the actual wind speed at ground level on the time of the measurement. Indeed, by examining the monthly distribution of wind speeds (see Figures 3.27, 3.28) one can extract the maximum values 1.5 and 1 m/s for the nights of 18/06/06 and 14/05/06 respectively, a difference too small to account for the transmittance variation. A method of setting the atmospheric visibility directly from the transmissometer's reading while using the actual wind speed as registered from the meteorological station was later discovered by the author and will be presented in Section 4.4.2.

The transmissometer has not proven extremely useful in the active atmospheric calibration due to its inherent altitude constraint at 550 m. Thus, it can be only used for selecting the aerosol model for the boundary layer (i.e. 0-2 km) under the assumption of homogeneous atmosphere over the boundary layer. In the case of unstable atmospheric transmissivity measurements (e.g. see Fig. 3.20) the relevance between the DNT extracted local atmospheric transmissivity to the γ-ray measurements should be checked against the CT25K data. Since the CT25K LIDAR's backscatter signal cannot be inverted to provide meaningful extinction profiles (see Section 4.1.2), one could only search for correlation between backscatter and transmissivity values during the examined period. In addition, the DNT's atmospheric transmissivity measurement in the infrared has proven to be unreliable due to the low power output of the relevant LED. Thus, the best one can do is to seek for correlation between the CT25K and DNT responses operating at different wavelengths. These reasons prevented the transmissometer from being a part of H.E.S.S. active calibration scheme (see Section 4.4.2).

However, it was quickly realised that the DNT's innovative design could have industrial applications (i.e. environmental monitoring, airport visibility monitoring) if the instrument was adapted for daylight operation. In addition to the changes

needed for the daylight operation, the DNT accuracy should be drastically improved in order to be competitive in the transmissometer market. Indeed, the DNT inventor Dr. Roland le Gallou had estimated a combined uncertainty of ±20% for the transmittance measurements (based on R_1 and R_2 intensity readings, see Section 3.4.2) at 455 nm and 505 nm (Le Gallou, 2005). The relevant uncertainty on the atmospheric transmissivity over the first 550 m above the H.E.S.S. site can be calculated via Equation 3.7 (i.e. $\sigma_{T(d)} = {\sigma_T}^{d/D} = {\sigma_T}^{0.01846}$). Thus, an ±20% error in transmittance corresponds to an uncertainty of just ±0.4% in the transmissivity over 550 m. In contrast, aviation transmissometers measure the horizontal transmittance over short baselines, thus requiring a much improved accuracy.

The author, working closely with the DNT inventor Dr. Roland Le Gallou, was aware of the following limitations that compromised the instrument's accuracy:

- the transmissometer data were not corrected for the LED output and temperature fluctuations,
- an active calibration was not implemented reducing the frequency of instruments calibration to the major maintenance intervals,
- the light sources (LEDs) are current but not temperature stabilised, and
- the light output of the 320 nm and 910 nm LEDs was low compromising their signal-to-noise ratio.

The concept of the DNT, despite the limitations inherent to the original design, has proven to be a gold mine for Durham's University γ-ray group leading to two successive grants dedicated to the production of a daylight and an industrial aviation transmissometer prototype respectively. The author was chiefly responsible for both projects, the results of which will be the subject of Chapters 5 and 6, 7 respectively.

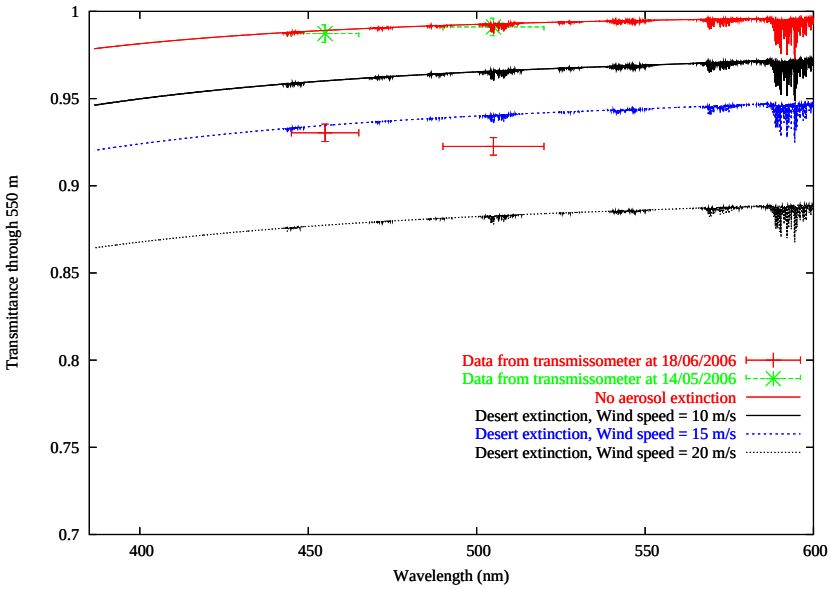

Figure 3.26: MODTRAN calculated transmissivities for desert aerosol extinction at varying wind speeds and two extreme values from DNT as a function of wavelength. A MODTRAN calculation of atmospheric transmission without aerosol extinction is also presented and matches perfectly the highest transmittance values seen by the transmissometer.

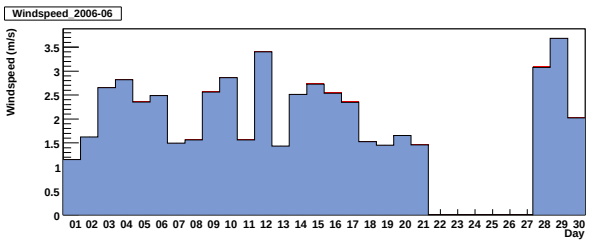

Figure 3.27: Distribution of wind speed measurements during June 2006.

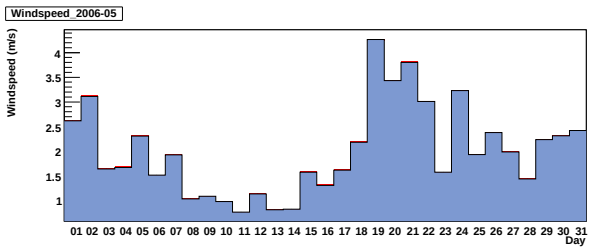

Figure 3.28: Distribution of wind speed measurements during May 2006.

Chapter 4

Towards the construction of a realistic 'in-situ' atmosphere for the H.E.S.S site

In this chapter the construction of realistic transmittance tables, providing the atmospheric transmittance above the H.E.S.S. site as a function of altitude and wavelength, will be discussed. The Durham group is responsible for the operation of two LIDARs (namely, a Vaisala CT25K and a Leosphere ALS450XT). The main focus of this chapter will be to retrieve the prevailing atmospheric transmittance from the LIDARs' response generated by elastic scattering at an angle = 180° (elastic backscattering). Both LIDAR systems will be described and the LIDAR theory will be discussed extensively. The initial unsuccessful attempts to retrieve physically meaningful information from the CT25K backscatter signal, leading to the acquisition of the ALS450XT, will be considered. In addition, the backscatter signal of the ALS450XT LIDAR, during the observation of LS 5039 under dusty conditions, will be inverted with a LIDAR-independent algorithm in order to retrieve realistic profiles for both scattering and extinction coefficients. The implied atmospheric transmissivity will be applied to simulated cosmic ray events to allow comparison with the telescope's observed trigger rate. Finally, the MODTRAN code used extensively in this thesis for the modelling both the atmosphere and the atmospheric monitoring instruments' response will be discussed in detail. In addition, a method

of producing variable aerosol models, chiefly responsible for the atmospheric transmissivity, using the prevailing visibility as opposed to the surface wind speed will be presented.

4.1 Ceilometer

4.1.1 Theory of Operation

The general operational principle of a LIDAR (Light Detection And Ranging) consists of shooting a short laser pulse into the atmosphere and measuring the intensity of the backscattered photons reflected by the atmospheric particles (i.e. aerosols and gas molecules) intercepting the beam path. A fraction of these scattered photons will be collected by the LIDAR's receiver, usually consisting of a PMT, and the signal strength will be registered. The time delay between the transmitted light pulse and received backscattered photons corresponds to the height of the responsible scatterer. The accuracy of this estimated height is restricted by the pulse width (i.e. 100 ns $\Rightarrow$ 30 m). The amplitude of the signal of the backscattered light can be used for retrieving the properties of the scattering site. The laser beam is likely to be scattered either by atmospheric gas molecules (O_3, H_2O) or by aerosols. Atmospheric molecules are smaller than the beam's wavelength so they will Rayleigh scatter the beam's photons. Aerosols, on the other hand, scatter photons according to Mie theory, being larger than the wavelength of the scattered light beam. Both scattering processes are elastic, so the measured backscattered photons will have the same wavelength as the emitted photons. It should be noted, however, that atmospheric gas molecules could also Raman scatter the laser. In this case the wavelength of the scattered photon changes, depending on the responsible scatterer. Thus, one can take advantage of this property by using a multi-frequency laser transmitter LIDAR with wavelength targeted for extracting the distribution of specific molecular scatterers (e.g. Whiteman et al., 1992). Finally, by measuring the Doppler shift of the backscattered light one can estimate the wind speed from the bulk motion of the scattering medium (e.g. Chanin et al., 1989).

4.1.2 Vaisala CT25K Ceilometer

The first LIDAR bought by the Durham Group was the commercial Vaisala CT25K ceilometer, a picture of which is shown in Figure 4.1.

Figure 4.1: CT25K Vaisala LIDAR installed at the H.E.S.S. site in Namibia.

The CT25K LIDAR uses a rapidly pulsed diode laser with an output wavelength centred at 905 ± 5 nm. The LIDAR's energy output lies in the μJ range that, combined with the transmitter's optics, meets the requirements of the EN60825-1 standard for safety. Eye-safety is ensured by constant regulation and monitoring of both the laser's driving voltage and temperature (Vaisala, 1999). This compliance with the eye-safety regulations translates into an instantaneous backscatter signal smaller than the ambient background. The high repetition rate of 5.57 kHz, however, allows the accumulation of many low energy signals leading to a reasonable signal to noise ratio.

The novelty of the CT25K LIDAR system arises from the usage of single lens optics for both transmitter and receiver units (see Fig. 4.2). In this way, the received signal is strong throughout the measuring range allowing the usage of signals

corresponding to very low altitudes.

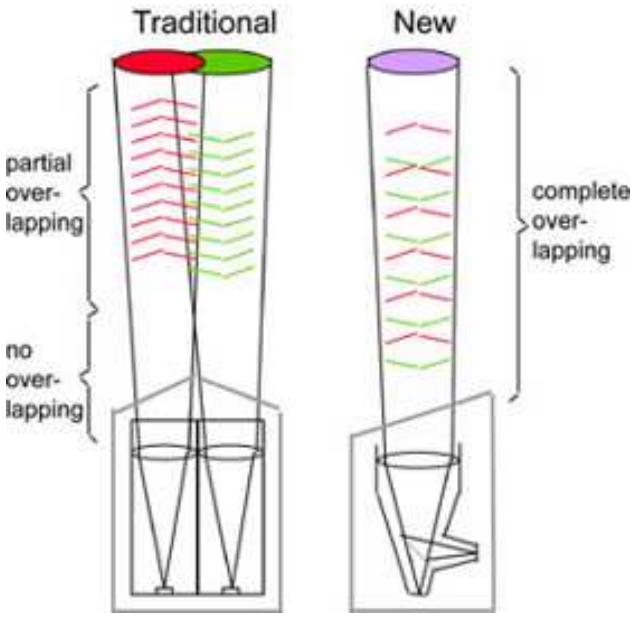

Figure 4.2: The single lens optics geometry of CT25K ceilometer. From Vaisala (1999).

Problems with the CT25K LIDAR

The raw data of the backscatter signal collected by the CT25K LIDAR are processed by an inaccessible algorithm that ultimately provides information about cloud heights and vertical visibilities. The user does not have access to the raw backscatter signal, a fact that prevents testing the noise cancellation processes on the full backscatter profile provided.

The confusion produced by the copyright protected algorithm was evident under both very clear and dusty atmospheric conditions. An example of a backscatter profile generated under a very clear atmosphere can be seen in Fig. 4.4. The clarity of the atmosphere was independently demonstrated by the transmission data simultaneously registered by Durham's transmissometer. In Figure 4.4 the backscatter signal fluctuates around zero between $600 - 1000$ m heights, a region at which one expects good noise to signal ratio. The fact that the LIDAR cannot detect any backscatter signal from this region indicates that its power output is too low to

detect the minimal aerosol concentration usually related with the clear skies above the H.E.S.S. site. Above 1 km this fluctuation flattens out corresponding to the small electronic noise variation.

In the case that a strong backscatter signal is detected (see Figure 4.6), the software seems to perform a height correction up to the level of the detected backscatter signal (i.e. about 2.4km) but not up to the full range of the measurement as the flattening of the backscatter signal collected at heights exceeding 2.4 km indicates (see Fig. 4.7). Thus, it is impossible to extract the atmospheric transmissivity from the backscatter signal retrieved from heights greater than the aerosol event. During this measurement the only available data from the transmissometer were produced by the 910 nm LED that approximately matches the wavelength of the ceilometer (see Fig. 4.8). A first indication of the response of Durham's transmissometer can be obtained by comparing the 910 nm transmission over the first 550 m above the H.E.S.S. site as shown in Figures 4.5 and 4.8.

In conclusion, the unavailability of CT25K raw data combined with the unclear function of the 'black-box' algorithm and laser's output of 905 ± 5 nm (being outside the region between 250 to 700nm where H.E.S.S.'s photomultipliers and mirrors are sensitive) resulted in the failure to extract meaningful optical depth values for the H.E.S.S site (as shown in (Aye, 2004)). However, CT25K's backscatter data up to 1.5-2.0 km above the H.E.S.S. site can still provide a handy tool for assessing the sky clarity and to validate the 'Durham-made' transmissometer - which measures directly the transmittance of the first 550 m above the H.E.S.S. site - as shown in Section 3.4 and Fig. 5.1.

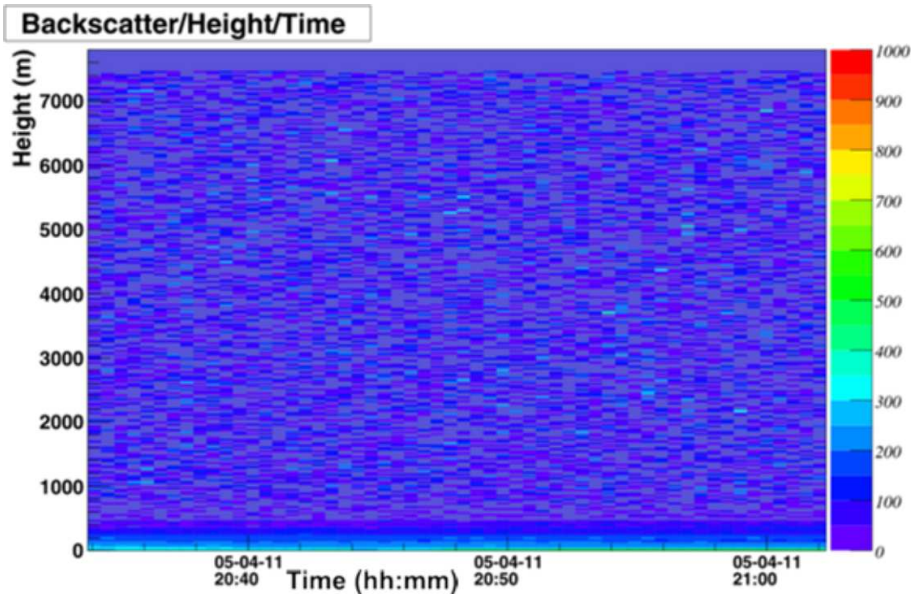

Figure 4.3: Two-dimensional profile of attenuated backscatter on 11th of April 2005 showing a very clear night.

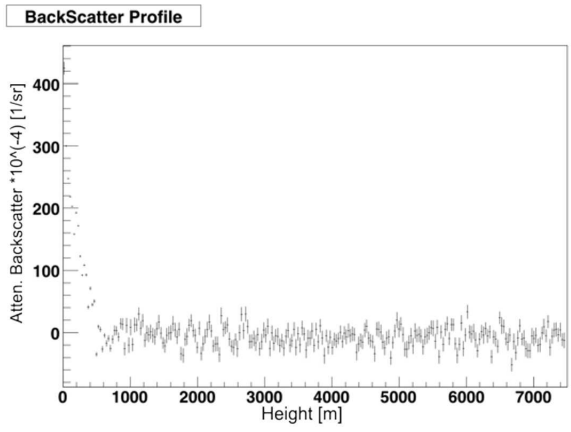

Figure 4.4: Attenuated backscatter profile on 11th of April 2005. Note the signal fluctuation around zero for heights between $600 - 1000$ m; a region expected to posses good signal-to-noise ratio.

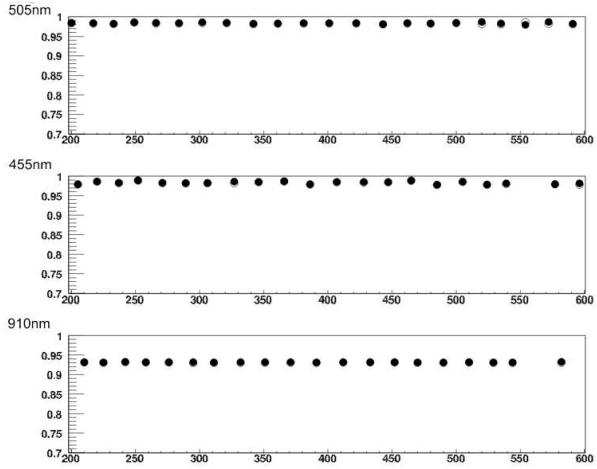

Figure 4.5: Transmittance over the first 550 m above the H.E.S.S. site. Measurements are collected at 505, 455 and 910 nm indicating an aerosol-free atmosphere on 11 April 2005.

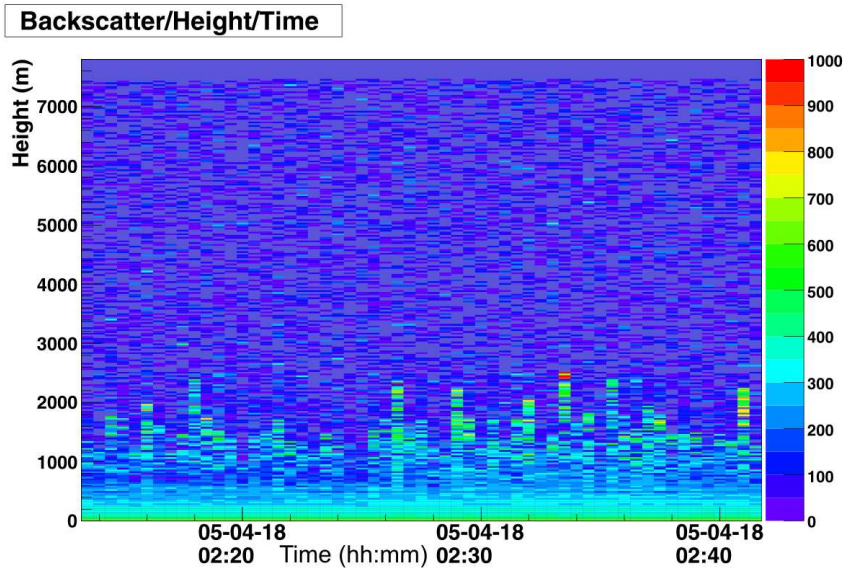

Figure 4.6: Two-dimensional profile of attenuated backscatter on 18th of April 2005 showing a population of aerosols for the first 2 km above the H.E.S.S. site.

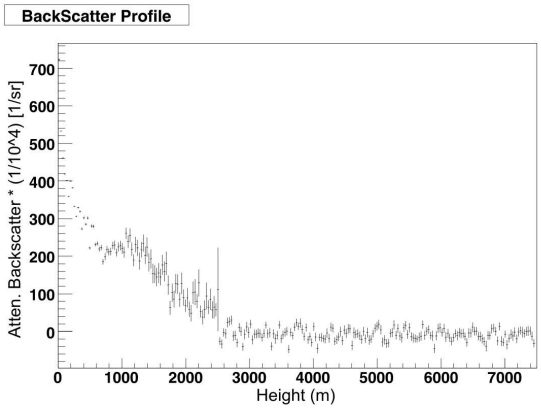

Figure 4.7: Attenuated backscatter profile on 18th of April 2005. The flattening of the signal at heights greater than approximately 2 km makes the retrieval of any physical information impossible.

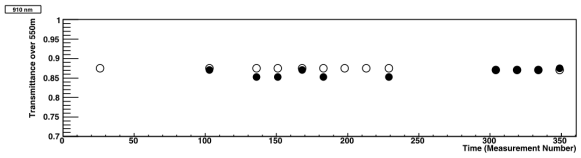

Figure 4.8: Transmittance over the first 550 m above the H.E.S.S. site measured at $\lambda = 910$ nm on 18/04/05. The black and white dots correspond to the different methods of calculating the background noise (i.e. black: background calculated from the On frame [R_1]; white: background calculated via On-Off frames [R_2], see also Section 3.4.2).

4.1.3 Leosphere's ALS 450 XT LIDAR

Following the impossibility of extracting optical depth profiles with the CT25K LIDAR, the Durham group set out to the LIDAR market with the following additional requirements in mind:

- availability of raw extinction ratio data,
- laser wavelength within 320 to 550 nm,
- measurements up to 15 km, and
- minimum spatial resolution of 15 m.

Leosphere's ALS 450 XT Easy LIDAR operating at 355 nm was selected and has been installed at the H.E.S.S site as of March 2007 (see Fig. 4.9). A comparison of some technical details and the performance of the two LIDARs can be found in Table 4.1.

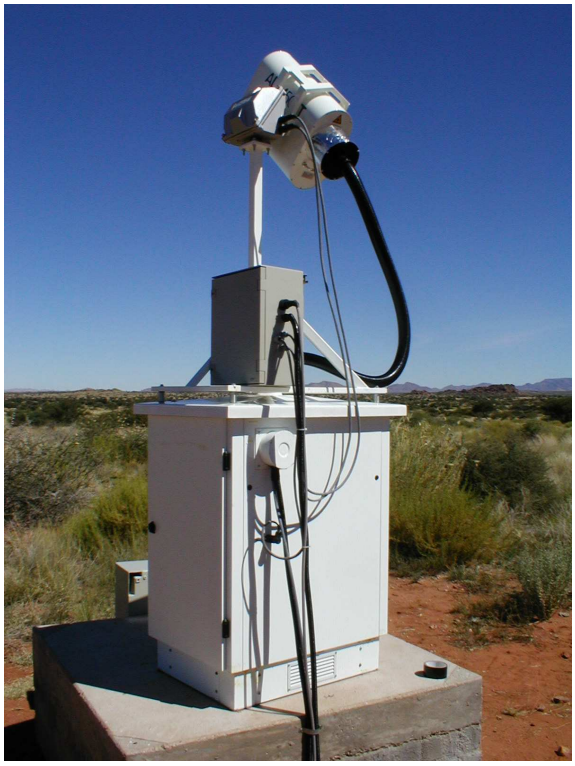

Figure 4.9: ALS 450 XT Leosphere Ceilometer installed at H.E.S.S. site in Namibia

Table 4.1: Comparison between ALS450XT and CT25K performance

Performance	Leosphere ALS450XT	Vaisala CT25K
Laser Source	Nd:Yag diode laser	InGaAs diode laser
Center Wavelength	355 nm	905 ± 5 nm at 25^oC
Repetition Rate	20 Hz	5.57 kHz
Pulse Energy	16 mJ	1.6 μJ
Range	75 m up to 15 km	0 up to 7.5 km
Spatial Resolution	1.5 m	30 m

The new LIDAR consists of two separate units connected together (Leosphere, 2005):

- the optical head that contains the emitter (Nd:Yag pulsed laser) and receiver (photomultiplier tube),
- the control housing containing all the necessary electronics.

The architecture of the optical head is monostatic biaxial. Thus, as opposed to the CT25K configuration where the laser beam and receiver's field of view coincide (monostatic coaxial), the transmitter and receiver of the ALS 450 XT LIDAR are closely packed together. The overlap between the laser beam and receiver's FOV begins at 75 m above the LIDAR's level so backscatter signals below this altitude can not be registered.

The algorithm analyses the backscatter raw data to produce vertical profiles of total and particulate extinction. In the following sections the LIDAR theory will be presented. Then, the assumptions behind the 'black-box' algorithm will be revealed by extracting the extinction to backscatter ratio (S) and compare it with statistical and analytical studies found in the literature. In addition the LIDAR reconstructed optical depth will be compared with that produced by well-established algorithms.

4.2 LIDAR Theory

As previously noted, the Durham group is responsible for two single-wavelength pulsed LIDARs operating at 905 nm and 355 nm respectively. The received power of each LIDAR can be expressed, under the simplifying single-scattering assumption, by the LIDAR equation (Klett, 1981):

$$P(\lambda, R) = \frac{c\,\tau}{2} P_0 \kappa(\lambda) O(R) \frac{A}{R^2} \beta(\lambda, R) \exp^{-2\int_0^R \sigma(\lambda, r) d(r)} . \tag{4.1}$$

where:

P_0, $P(R)$ are the instantaneous transmitted and received power respectively;

R is the distance between the scatterer and the receiver expressed in km. For the special case of an upward looking LIDAR, R corresponds to the altitude of the scattering medium;

τ is the pulse duration and c the velocity of light, expressed in s and km/s respectively;

$O(R)$ is the overlap function, defining the part of the backscattered laser beam that falls within the receiver's field of view;

$\kappa(\lambda)$ is the wavelength-dependent overall efficiency of the LIDAR (i.e. extinction from the optical components of transmitter and receiver together with the receiver's detection efficiency);

A is the area of the receiver's optics (i.e. telescope or lens);

$\beta(r)$ is the backscatter coefficient, usually expressed in m sr^{-1};

and $\sigma(r)$ is the extinction coefficient of the atmosphere expressed in m^{-1}.

For the sake of clarity, one can isolate the terms depending solely on the LIDAR's characteristics and geometry (Wandinger, 2005).

$$C = \frac{c\,\tau}{2} P_0 \kappa(\lambda) A \tag{4.2}$$

$$G(R) = \frac{O(R)}{R^2} \tag{4.3}$$

Let's assume that a laser pulse of power P_0 leaves the receiver at $t_0 = 0$. The energy of the outgoing beam is $E_0 = P_0\tau$. After time t a backscatter signal is

recorded due to a scatterer at a distance $R = ct/2$. The original pulse length was τ, so the receiving gate must remain open for the same time, corresponding to a measured backscatter laser-beam produced within a spatial resolution of $\Delta R = c\tau/2$. These quantities, along with the effective aperture of the receiver (A) and the efficiency of the overall system ($\kappa(\lambda)$) either remain constant (i.e. c, A) or their values are constantly monitored (i.e. κ, P_0) during the LIDAR's operation so that each variation is compensated. Therefore C can be determined by the experimental set-up of the LIDAR.

The term $G(R)$ represents the dependence of the measured backscatter signal due to the system's geometry. Indeed, different LIDAR configurations correspond to a difference in the overlap function between receiver and laser beam, as Fig. 4.2 clearly demonstrates. The inverse quadratic relation of the measured signal with range is explained if one thinks of an imaginary sphere ($r = R$) connecting the receiver with the centre of the isotropically scattering medium.

It is worth noticing that the term $\exp^{-2\int_0^R \sigma(r)d(r)}$ is the *O*ptical *D*epth (OD) or transmission of the LIDAR light up to the distance of interest (i.e R). As light from the LIDAR's light source covers the distance R, twice the OD of the Cherenkov light, over this distance R would be half the OD of the LIDAR light (which explains the factor of 2 in front of the integral).

The instantaneous response of a vertical monostatic single wavelength LIDAR depends, therefore, on (Masonis et al., 2002):

1. the power of the ejected laser beam,

2. the instrument's calibration constants,

3. the concentration of scattering material (i.e. aerosols and molecules) at the altitude corresponding to the travelling time of the receiving signal,

4. the tendency of the scattering material at this altitude to scatter light in a direction of 180° in comparison with the other directions, and

5. the number of photons lost during the beam travelling over the in and outgoing paths.

Instrumental calibration coefficients and their corresponding uncertainties (i.e. 1,2) are provided in each instrument's manual (Vaisala, 1999; Leosphere, 2005) and are altitude independent. While scatterer concentration (3) is the quality of interest one cannot know separately the answers to (4) and (5) by solely relying in the monostatic LIDAR response. Thus, the LIDAR equation 4.1 contains two unknowns: the backscatter and extinction coefficient, both altitude dependent.

This difficulty necessitates the assumption of a relationship between backscatter and extinction profiles typically prescribed in the backscatter to extinction ratio (i.e. S). They are mainly two algorithms that facilitate the analysis of LIDAR response, namely Klett's (Klett, 1981) and Fernald's (Fernald, 1984). The advantage of Fernald's method is that it discriminates between aerosol and molecular scatterers, calculating via Rayleigh theory an altitude-independent value for the molecular backscatter to extinction ratio. Klett also modified his solution to account for the effects of Rayleigh scattering (Klett, 1985). In this case, the aerosol ratio S depends on the wavelength of the received light, aerosol size distribution, aerosol refractive index (i.e. composition) and shape. These optical characteristics depend on the location of the LIDAR's site and change with time (Barnaba et al., 2004). Air masses' back trajectories and satellite measurements will be used to extract the size distributions and the refractive index of the aerosol population above the H.E.S.S. site. In the next sections the Klett and Fernald methods will be discussed in an effort to validate the H.E.S.S. LIDARs and to invert their signal, extracting a site specific optical depth that in turn can be used in the H.E.S.S. simulation algorithms.

4.2.1 Solving the LIDAR equation

The LIDAR equation 4.1 can be simplified by setting the calibration constants $O(R)$ and $\kappa(\lambda)$ to unity and by omitting the wavelength and size dependence:

$$P = P_0 \frac{c\tau}{2} \frac{A}{R^2} (\beta) \exp^{-2 \int_0^R (\sigma) \mathrm{d}r} \tag{4.4}$$

The LIDAR response is usually (e.g. Klett, 1981) reported as the the range-

corrected power defined as follows:

$$S(r) = \ln[R^2 P(r)] \tag{4.5}$$

One could use the difference between the range-corrected signal of a stable reference altitude (r_0) and r in order to eliminate the LIDAR constant (Klett, 1985):

$$S - S_0 = \ln \frac{\beta}{\beta_0} - 2 \int_{r_0}^{R} \sigma(r) d(r) \tag{4.6}$$

The differentiation of Eq. 4.6 with respect to LIDAR's range yields:

$$\frac{\mathrm{d}S}{\mathrm{d}r} = \frac{1}{\beta} \frac{\mathrm{d}\beta}{\mathrm{d}r} - 2\sigma \tag{4.7}$$

In the following sections the main inversion techniques will be briefly discussed.

Slope Method

Equation 4.7 can be easily solved if one assumes a homogeneous atmosphere over the range of the LIDAR. This assumption removes the range dependence from both extinction and backscatter coefficients as both optical parameters are considered to be constant over the whole measurement range:

$$\sigma = -\frac{1}{2} \frac{\mathrm{d}S}{\mathrm{d}r} \tag{4.8}$$

Thus, in the case of a homogeneous atmosphere, the extinction coefficient can be found directly by plotting the corrected signal as a function of range. This method has the merit of being simple and less intensive computationally than any other inversion method. It can be applied in highly turbulent atmospheres where the fractional gradient of backscatter corresponds to small signal variations (Rocadenbosch et al., 1998):

$$\frac{1}{\beta(r)} \left| \frac{\mathrm{d}\beta(r)}{\mathrm{d}r} \right| \ll 2\sigma \tag{4.9}$$

This approximation does not hold, however, for atmospheres possessing smaller optical depths where inhomogeneities may lead to a fractional gradient of backscatter that is comparable with $-2\sigma(r)$. Indeed, if the slope method is applied within an

inhomogeneous medium (e.g. dense clouds or smoke) it often yields a positive slope for $S(r)$ that in turn defines a non physical, negative extinction coefficient (Evans, 1984).

Backward Inversion

In the most realistic case where $\mathrm{d}S/r \neq 0$, the LIDAR equation 4.1 can be solved analytically if one makes an a priori assumption for the relation between aerosol extinction and backscatter coefficients. Traditionally, a power law relation is assumed:

$$\beta_a = B\sigma_a^k \tag{4.10}$$

where k depends on the wavelength of the LIDAR and the aerosols' optical properties and B is, in the simplest case, a proportionality constant. This relation holds well for water fogs (with $k = 1$, $C = 0.05\ sr^{-1}$) and research for different aerosols indicates that k lies between 0.67 and 1 (Klett, 1985).

By differentiating Eq. 4.6 with respect to range and taking into account Equations 4.4 and 4.10 one gets:

$$\frac{\mathrm{d}S}{\mathrm{d}r} = \frac{k}{\sigma}\frac{\mathrm{d}\sigma}{\mathrm{d}r} - 2\sigma \tag{4.11}$$

Equation 4.11 is special type of nonlinear differential equation (i.e. Bernoulli) and has the following solution (Klett, 1981):

$$\sigma(r) = \frac{\exp\left[(S - S_M)/k\right]}{\sigma_M^{-1} + \frac{2}{k}\int_r^{r_M} \exp\left[(S - S_M)/k\right]\mathrm{d}r'} \tag{4.12}$$

where S_M and σ_M are the corrected signal and extinction coefficient respectively corresponding to the maximum inversion range r_M. The novelty of Klett's inversion was to select the calibration coefficient at the furthest point of the LIDAR's signal path (r_M), as opposed to the closest (r_0), which had been used until then (forward inversion), yielding a stable solution. At the far end, the extinction is dictated by Rayleigh scattering and thus is easier to predict and the signal-to-noise ratio is small. The error on the chosen σ_M becomes less important for descending values of r as the integral term in Eq. 4.12 increases. Furthermore, when r decreases the extinction

coefficient is defined as the ratio of increasingly greater numbers, thereby converging towards a representative value. One should not forget, however, that both k and σ_M cannot be determined accurately as they depend on the aerosols' optical characteristics and composition, which are unknown. However, if these parameters were known, the LIDAR would not have been needed. In addition, by assuming a constant value of k (and B in the case of backscatter inversion), we accept that both aerosol size distribution and chemical composition remain constant within the LIDAR's range.

Modern LIDARs, such as Leosphere's ALS450XT, use inversion algorithms that discriminate between Rayleigh and aerosol scattering and assume a backscatter to extinction ratio that is itself a function of r:

$$\beta_{a+m}(r) = B(r)\sigma^k_{a+m} \tag{4.13}$$

where, as already defined, a and m correspond to the aerosol and molecular parts of the the optical coefficients and k is set to unity.

The total extinction coefficient can be written as the sum of the aerosol and molecular attenuation:

$$\sigma = \sigma_a + \sigma_m \tag{4.14}$$

The backscatter signal registered by the LIDAR is a result of an elastic process and therefore the backscatter coefficient can be expressed as:

$$\beta = P_a(180^\circ)\sigma_a + P_m(180^\circ)\sigma_m \tag{4.15}$$

where P denotes the phase function which is defined as the ratio of the energy scattered per unit solid angle at 180° to the average energy scattered per unit solid angle in all directions ($\beta/4\pi$) (van de Hulst, 1957; McCartney, 1976). Thus, by definition the phase function equates with the backscatter to extinction ratio for molecular or aerosol scattering. Rayleigh theory predicts a constant backscatter to extinction ratio:

$$B_m = \frac{\beta_m}{\sigma_m} = \frac{3}{8\pi} \tag{4.16}$$

In contrast, the relevant ratio in the case of aerosol scatterers for the LIDAR's wavelength is variable and can be expressed as a function of the aerosol size distribution and chemical composition as defined by the complex index of refraction. A short derivation of the backscatter to extinction ratio is provided below due to its importance in validating and correcting the LIDAR's signal.
The Mie backscatter cross section coefficient can be expressed in terms of backscatter efficiency as (Gobbi and Barnaba, 2002):

$$\sigma_b(r, \lambda, m) = \pi r^2 Q_b(x, m) \tag{4.17}$$

where r, m, x are the aerosol's radius, complex refractive index and size parameter respectively. The same relationship holds for the extinction cross section, which according to Mie theory can be expressed (e.g. Cachorr and Salcedo, 2001):

$$Q_{ext} = \frac{2}{x^2} \sum_{n=1}^{\infty} (2n+1)[Re(a_n + b_n)] \tag{4.18}$$

where the Mie scattering coefficients a_n and b_n are expressed as Ricatti-Bessel functions of x and $m \cdot x$. For aerosols of a given density distribution, the backscatter and extinction coefficient can be calculated as follows (Gobbi and Barnaba, 2002, e.g.):

$$\beta_a = \int_0^{\infty} \sigma_b N(r)(d)r = \int_0^{\infty} Q_b N \pi r^2(r)(d)r \tag{4.19}$$

A plethora of analytical functions has been devised for the simulation of aerosol size distributions (i.e. power law, modified gamma, generalised and lognormal distribution). The lognormal distribution is ideal for covering the full range of aerosol sizes. In addition, two or three lognormal distributions can be used to identify aerosol components of different origin as each component is allocated with an individual median radius, standard deviation and number density (Ackermann, 1998):

$$n_i(r) = \frac{N_{tot}\mu_i}{\sqrt{2\pi} \ln \sigma_i r} \exp\left(\frac{-\ln^2 (r/r_{m,i})}{2 \ln^2 \sigma_i}\right) \tag{4.20}$$

where N_i is the number density of the component
σ_i and $r_{m.i}$ are the standard deviation and median radius of the distribution
and μ_i is the normalised particle concentration defined as the ratio of N_i over the total number of particles per unit volume $N_{total} = \sum_{i=1}^{n} N_i$.

Thus, the important backscatter to extinction ratio can be computed if the size distributions and the complex refractive index for each aerosol component are known, in terms of the relevant efficiencies (e.g. Ackermann, 1998):

$$B_a = \frac{\int_0^\infty \sum_{i=1}^n \beta_i \mathrm{d}r}{\int_0^\infty \sum_{i=1}^n \sigma_i \mathrm{d}r} = \frac{\int_0^\infty \sum_{i=1}^n Q_{bsc}(r, m_i, \lambda)\pi r^2 n_i(r)\mathrm{d}r}{\int_0^\infty \sum_{i=1}^n Q_{ext}(r, m_i, \lambda)\pi r^2 n_i(r)\mathrm{d}r} \tag{4.21}$$

In practice, one can identify the variability of the prevailing aerosols in terms of both size distribution and chemical composition and apply Mie theory to derive the extinction and backscatter properties over a large sample of different size distributions and refractive indeces within the predetermined range. By fitting the obtained results with an analytical curve a functional relationship between backscatter and extinction can be estimated (Gobbi and Barnaba, 2002):

$$B_a \approx f[\sigma_a(r)] \tag{4.22}$$

The LIDAR differential equation 4.7 can be written to account for the difference between the atmospheric backscatter and extinction due to Rayleigh (molecular) and aerosol (Mie) scattering with the aid of equations 4.14 and 4.15:

$$\frac{\mathrm{d}S}{\mathrm{d}r} = \frac{1}{\beta_{a+m}} \frac{\mathrm{d}\beta_{a+m}}{\mathrm{d}r} - 2(B_a^{-1} - B_m^{-1})\beta_m \tag{4.23}$$

The trick is again to find the right transformation function that would bring Eq. 4.23 to a Bernoulli form. Klett defined the new signal variant as:

$$S' - S'_c = S - S_c + \frac{2}{B_m}\int_r^{r=r_c} \beta_m \mathrm{d} - 2\int_r^{r=r_c} \frac{\beta_m}{B_a}\mathrm{d}r \tag{4.24}$$

that leads to a generic expression of the LIDAR equation after setting the backscatter coefficient at the far end of the LIDAR's path ($r = r_c$)(Klett, 1985; Gobbi and Barnaba, 2002):

$$\beta_a(r) + \beta_m(r) = \frac{\exp(S' - S'_c)}{\left[\beta_c^{-1} + 2\int_r^{r=r_c} \frac{\exp(S'-S'_c)\mathrm{d}r}{B_a}\right]} \tag{4.25}$$

This expression would permit the use of an analytical function that correlates the backscatter coefficient with the extinction magnitude, chosen from best available

local atmospheric data, to improve the generic assumptions made by the LIDAR's manufacturer in order to extract more representative optical depth tables that are used in simulating the H.E.S.S. telescopes' response.

4.3 Validation of the ALS 450 XT LIDAR

4.3.1 ALS 450 XT First Results

The new LIDAR was installed at the H.E.S.S. site at the end of April 2007. The main concern of the operation of any instrument comprising of a powerful light source at the H.E.S.S. site is its interference with the sensitive photomultiplier tubes (PMTs). Preliminary tests upon installation indicated that if the LIDAR is co-pointed with the telescopes there is not a detectable increase in the telescopes' trigger rate. As before the LIDAR was incorporated within the H.E.S.S. data acquisition (DAQ), measurements were taken with the LIDAR pointing at the zenith. Inevitably after a few days, the LIDAR beam crossed the field of view of the telescope with alarming results. Indeed, on May the 13^{th} an almost two-fold increase on the telescopes' trigger rate was observed due to the coincident operation of the LIDAR. The sharp increase in the registered trigger rate as soon as the LIDAR is turned ON is clearly shown in Figure 4.10. The laser beam is actually mapped into the sensitive H.E.S.S. cameras as Figure 4.11 demonstrates. Although this is a very accurate way to calibrate the new LIDAR, it posses an immediate threat for the sensitive PMTs in addition to interfering with the detected signal. It was decided, therefore, that until the LIDAR is fully incorporated within H.E.S.S's DAQ, it was to be used only in dusty conditions at the end of a night's observation.

At this stage (May 2007) we had only a few days of LIDAR data indicating very clear atmospheric conditions. In order to test the new LIDAR's response, various simulations were performed with the aid of MODTRAN (see Section 4.4). The vertical atmospheric transmittance was estimated for the LIDAR's wavelength 355 nm by the use of the standard tropical density profile coupled with desert and tropospheric aerosol models (see Fig. 4.12). For the tropospheric model the default value of visibility has been selected (i.e. VIS=50 km), while in the more

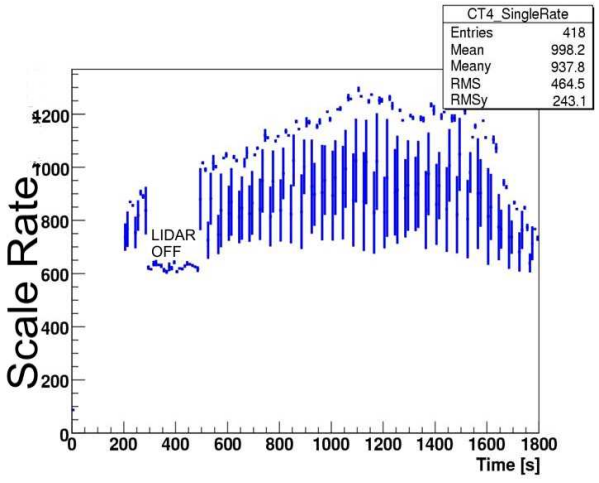

Figure 4.10: Trigger rate as measured by telescope CT4 during LIDAR testing. The rate drop between $200-500$ s corresponds to the LIDAR's being switched off.

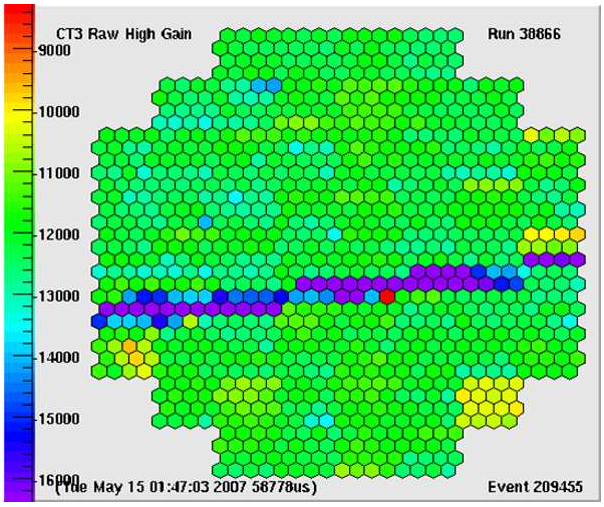

Figure 4.11: A snap-shot of the CT-3 camera response while the LIDAR was operational. The LIDAR's beam is evident in the camera.

representative desert aerosol model the visibility was set by the prevailing surface wind speed. Figure 4.13 presents the monthly summary of the surface wind speeds for May 2007. The wind speed daily average on the 13^{th} of March was ~ 3.3 ms^{-1}.

A special program was written by the author to calculate atmospheric transmittance for altitude bins of 30 m instead of the 1 km that is the MODTRAN default binning value within the troposphere. The atmospheric transmission due to molecular scattering only has also been included. The altitude profile of the atmospheric transmittance as dictated by the LIDAR's extinction values is in very good agreement with the output of the default for the H.E.S.S. site desert aerosol model scaled for the prevailing wind speed, a fact that gives a first indication of the LIDAR's performance. However, the performance of the ALS 450 XT LIDAR should be checked under dusty conditions where the atmospheric corrections become relevant (see also Section 4.4.2).

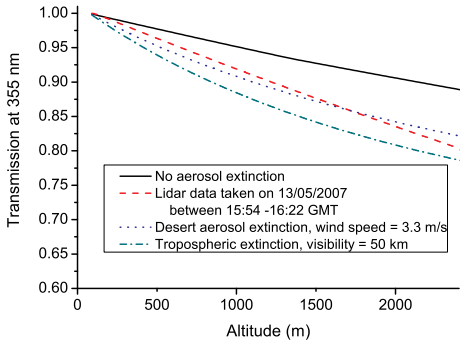

Figure 4.12: MODTRAN Vertical atmospheric transmittance vs LIDAR measured transmittance.

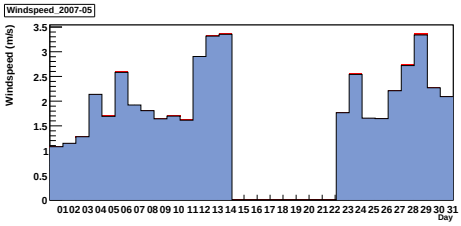

Figure 4.13: Distribution of surface wind speed at the H.E.S.S. site as registered by the weather station.

4.3.2 ALS 450 XT LIDAR Validation Under Dusty Conditions

The Durham group has devised active atmospheric corrections for data taking under the presence of low-level aerosol populations that were based chiefly upon the cosmic-ray trigger-rate dependence on atmospheric clarity while the CT25K LIDAR was used to identify high density of aerosols (e.g. Nolan et al., 2008; Brown et al., 2005*a*; Aye et al., 2003) (see Section 4.3.3). It is evident the new ALS 450 XT LIDAR, operating at the Cherenkov relevant wavelength of 355 nm and an expected maximum range of 15 km (as opposed to CT25K values: 905 nm and 7.5 km), needs to be extensively tested under dusty conditions before being incorporated within the atmospheric correction scheme.

The opportunity for LIDAR testing was provided during dust events between $11^{\text{th}} - 18^{\text{th}}$ of September 2007 while observing the microquasar LS 5039. In order not to risk any interference between LIDAR and the telescopes' cameras, the LIDAR tests were performed at the end of each night's observation period with the LIDAR pointing at 20°, to match the mean observing angle, for one hour period. The LIDAR's output during a run obtained on the dustier night (i.e. 13^{th} of September) in comparison with that obtained on a relatively clear night together with the relevant measurements of TOMS aerosol index is presented in the Figures 4.14.

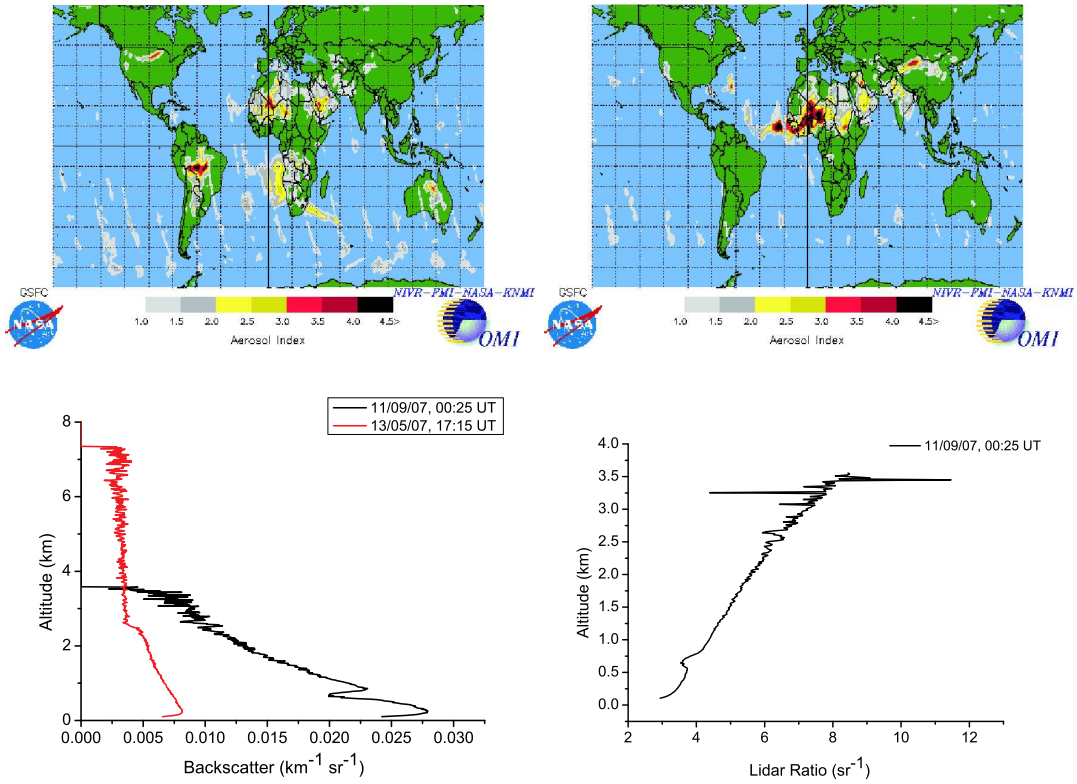

Figure 4.14: Upper panel. TOMS global aerosol index distribution Left: 13/09/07. Right: 13/05/07 (TOMS, 2008). Lower panel: The altitude profile of the backscatter coefficient as measured by the LIDAR during the relevant periods.

Figure 4.14 reveals the following problems with the operation of the ALS 450 XT LIDAR under dusty conditions:

- the cut-off of the backscatter coefficient (and LIDAR ratio) at approximately 3.5 km above the H.E.S.S. site (see 4.14, lower panel) , and
- the characteristically low LIDAR ratio (see 4.14, lower panel, right).

The following analysis was performed by the author in an effort to identify how the LIDAR malfunction related to the observed effects.

The low cut-off problem

The LIDAR's raw signal has been checked, to account for any software malfunction in the derivation of the backscatter coefficient, and it was verified that above $\sim$ 3.5 km

it began to oscillate around zero. For the sake of comparison, the backscatter profile from a clear run has been also plotted. The cut-off is present in every backscatter profile within the period of the dusty measurements.

The LIDAR's PMT was checked for abnormal fluctuation since a maximum fluctuation of $\sim 16\%$ of the LIDAR's PMT was observed between runs taken at the beginning of September 2007. As PMT voltage calibration is not provided within the software, this could lead to mis-interpretation of the LIDAR's return signal. However, during the dusty data taking period (i.e. $11^{\text{th}} - 18^{\text{th}}$ of September 2007) the maximum deviation of the PMT driving voltage was 2.4% and for the dustier night of 11^{th}, for which most simulations were performed (see Section 4.3.3), was $< 0.5\%$ and thus could be safely ignored.

Then the LIDAR's auxiliary files were scanned in an effort to identify each parameter used for the raw signal derivation. In other words, one needs to pin-point the different parts forming the LIDAR equation (see Section 4.2). The results showed a severe drop of the laser nominal output value as a difference of a factor of five in the relevant calibration coefficients was observed between measurements taken on 13/05/07 and 11/09/07. This observation was communicated to the LIDAR's manufacturer. The drop of the laser output has been verified after remotely completing a series of calibrations tests under their instructions. In addition, updated software, allowing for the remote control of the PMT's driving voltage, was supplied.

Thus, as in the case of the CT25K LIDAR, the laser power output is too low to access the nominal altitude range (i.e. $0 - 15$ km). In the following analysis only backscatter profiles up to an altitude of 3.5 km will be considered as the LIDAR's hardware malfunction was not identified at that stage.

The low LIDAR ratio problem

The calculated transmission, based on the extinction coefficient provided by the ALS 450 XT LIDAR's software, is shown in Fig. 4.15. In the same figure, two MODTRAN-calculated transmission profiles for a desert aerosol model with a wind speed of 4.5 m/s and a pure molecular atmosphere, together with the transmission based on the LIDAR data on the 13/05/07, have been also plotted. The LIDAR im-

plied transmission suggests a clear atmosphere and conflicts with both the H.E.S.S. registered cosmic-ray trigger rate (see Fig. 4.17) and satellite measurements (see Fig. 4.14). Indeed, a drop of 50% in the trigger rate corresponds to a 10% decrease in transmittance. Moreover, the application of the LIDAR-derived transmittance to cosmic ray simulations yielded a trigger rate that exceeds the observed value by 500% (Nolan, 2008).

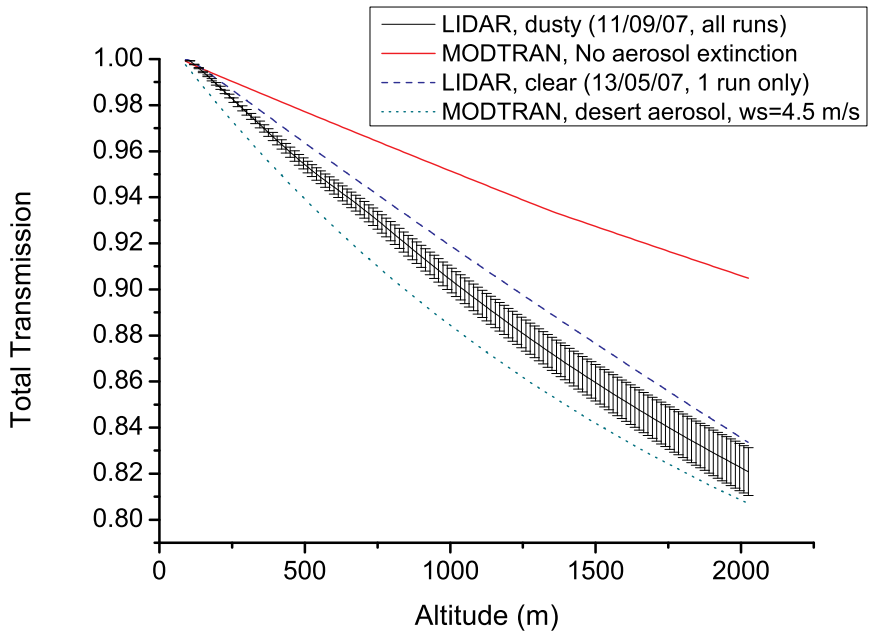

Figure 4.15: MODTRAN-calculated atmospheric transmittance vs LIDAR measured transmittance on 13/05/07 and 11/09/07.

The derivation of the erroneous extinction coefficient is based upon the backscatter measured profile and the assumed LIDAR ratio. A method of checking the validity of the measured backscatter profiles is by calculating the backscatter ratio (Gobbi and Barnaba, 2002):

$$B_R = \frac{\beta_{total}}{\beta_m} = 1 + \frac{\beta_a}{\beta_m} \tag{4.26}$$

Thus, the backscatter ratio is a measure of the aerosol contribution on the measured backscatter. The calculated backscatter ratios for the nights of 13/05/07 and

11/09/07 are presented in Fig. 4.16.

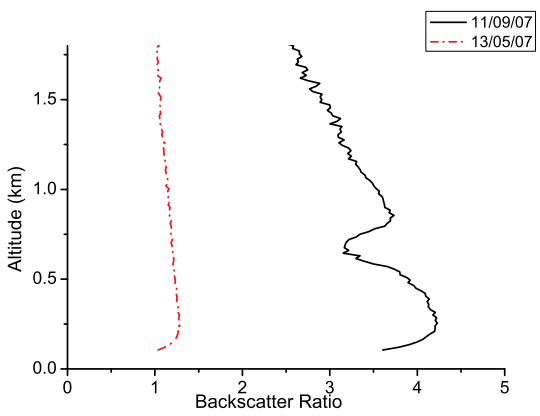

Figure 4.16: Comparison of the backscatter ratio as measured by the ALS 450 XT LIDAR on 13/05/07 and 11/09/07.

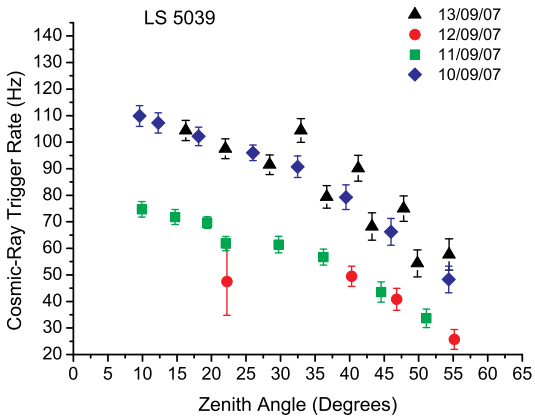

Figure 4.17: Cosmic ray trigger rate vs zenith angle during the observation of LS5039 in September 2007.

The backscatter contribution due to aerosols on the night of 11/09/07 is shown clearly in Fig. 4.16 whereas the ratio value for 13/05/07 indicates a molecular−dominated atmosphere with ratios very close to unity. This can be independently verified from satellite measurements during the relevant periods. Indeed, a closer look at Fig. 4.14 (i.e. upper panel) reveals that the aerosol index had an average value of $A_I =\sim 2.5$ for the 11^{th} of September while the aerosol index for the 13^{th} of May approaches zero indicating an aerosol-free atmosphere.

The LIDAR ratio, on the other hand, during the dust storm data-taking is characteristically small (i.e. see Fig. 4.14 lower panel). The average value of $\sim$ 6 sr^{-1} lay outside all reported bounds (e.g. Ackermann, 1998; Barnaba et al., 2004). Moreover, the presence of non-absorbing UV aerosols, as indicated by the low LIDAR ratio, should be excluded from both H.E.S.S. and satellite data. Specifically, during the observation of LS5039 under the dust episodes, a 50% reduction on the cosmic-ray trigger rate was observed (as shown in Fig. 4.17). In addition, the strong positive TOMS aerosol index is a clear indication of UV absorbing aerosols (TOMS, 2008).

Thus, while the backscatter measured profile agrees with satellite measurements the LIDAR ratio assumption is erroneous leading to meaningless extinction profiles.

In the next section a more realistic LIDAR ratio will be calculated in an effort to derive transmission values in agreement with the observed trigger rates.

4.3.3 Correcting the LIDAR's signal

The LIDAR ratio has already been discussed and formulated via Eq. 4.21. It involves two quantities that depend both on aerosol size distribution and chemical composition. Aerosols of the same composition have a common refractive index and their size dispersion can be characterised by a lognormal distribution. Since the atmosphere contains different aerosol components, one must research on the variability of the local aerosol species on both size distribution and refractive index.

The soil composition of Namibia is presented in Fig. 4.18 while the air mass trajectories ending on and above H.E.S.S site (i.e. ground level, 250 and 500 m) at 02:00 UTC on 11/09/07 are provided in Fig. 4.19.

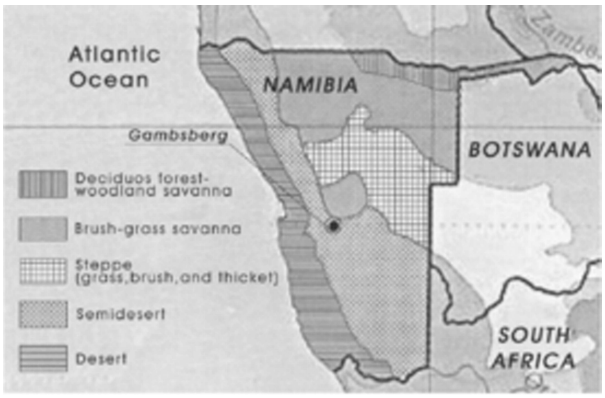

Figure 4.18: The soil composition of Namibia (Esposito et al., 2003).

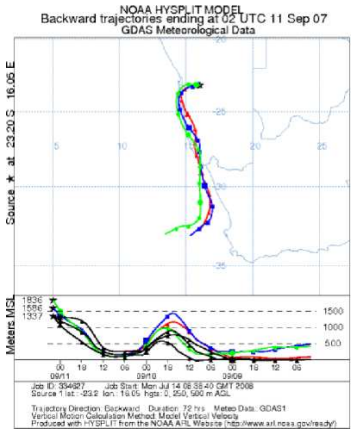

Figure 4.19: Three day backward trajectories for air masses arriving over the H.E.S.S. site in Namibia on 11 of September 2007 at 17:00 UTC (Draxler and Rolph, 2003; Rolph, 2003).

Namibian aerosol dust originates mainly from the desert lands and has been identified by the GOCART (i.e. Global Ozone Chemistry Aerosol Radiation and Transport) model as one of the ten main sources of dust globally (Taylor et al., 2002). It is a mixture of different kind of materials (sodium, calcium, silicon, aluminium

and sulphur). In general, desert aerosols consist of a background model irrelevant to the local soil composition and a component representative of soil erosion under high wind speeds (Ackermann, 1998; Kneizys et al., 1996). The aerosol size distribution has been monitored during the AERONET campaign via ground based LIDARs for about a year (Privette et al., 2005). The inverted aerosol size distribution for May 2001 is presented in Fig. 4.20. According to this, the size distribution of desert aerosols can be described by the nucleation (Aitken) and the large (accumulation) mode. Since both modes correspond to minerals their refractive index should be identical. Furthermore, Fig. 4.19 shows that the low altitude air masses are mainly arriving from the the land above the coast line.

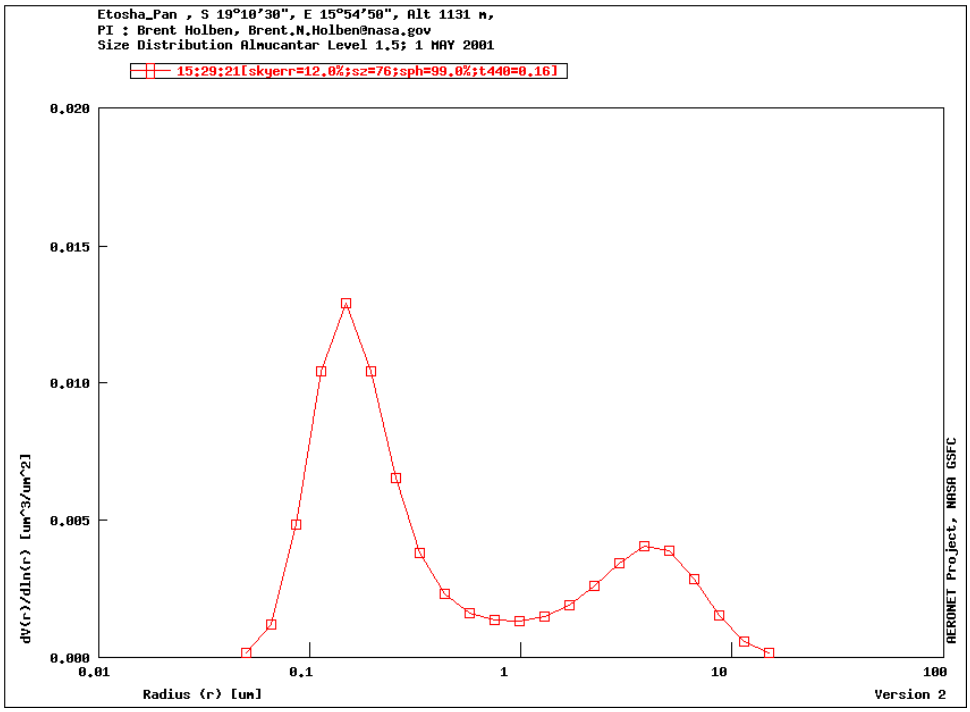

Figure 4.20: Size distribution of aerosols present in Etosha Pan site for May 2001 measured during the AERONET campaign via a ground based LIDAR. Unfortunately more recent data was not available from this site.

A quick review of the literature revealed that a relatively recent and very thorough work on the analytical derivation of the LIDAR ratio, for desert aerosols and elastic LIDAR operating at 355 nm, has been performed by Barnaba et al. (2004). This method was first introduced in order to facilitate the inversion of single wave-

length LIDAR's response operating at 532 nm (Barnaba and Gobbi, 2001). According to this method the dispersion of the aerosol size distribution was taken into account by adopting two lognormal distributions, namely $R_1 = 0.02 - 0.08$ nm, $\sigma_1 = 1.5 - 2.1$ and $R_2 = 0.3 - 1.5$ nm, $\sigma_2 = 1.5 - 2.0$. As discussed previously, the modes correspond to mineral aerosols and thus their refractive index would possess common variability ($m_r = 1.50 - 1.55$ and $m_i = (-0.008) - (-0.01)$) (d'Almeida et al., 1991; Gobbi and Barnaba, 2002). Finally, the fluctuation of the normalised number concentration was assumed (i.e. $N_1/N_1 + N_2$: $93 - 98$ and so $N_2/N_1 + N_2$: $2 - 7$).

Mie theory was implemented for the computation of the backscatter and extinction coefficients with optical parameters and refractive indices within the selected range. In order to account for all possible combinations, 20,000 different size distributions were generated by a random variation of their parameters between the imposed bounds and the relevant extinction and backscatter coefficient were calculated. Finally, the analytical relationship between the backscatter and extinction coefficient was obtained by a high-order polynomial fit on the resulting dispersion of the extinction versus backscatter coefficient (Barnaba et al., 2004):

$$\begin{aligned} \log(\sigma_a) &= 40.06 + 132.75x + 185.504x^2 + 139.9882x^3 + 61.273x^4 + \\ &\quad 15.58723x^5 + 2.13661x^6 + 0.121828x^7 \end{aligned} \tag{4.27}$$

This expression was used in order to invert the LIDAR's backscatter profile into extinction. In order to test the corrected LIDAR's response, simulations were performed with the aid of MODTRAN (see Section 4.4). The vertical atmospheric transmittance was estimated for the LIDAR's wavelength 355 nm by the use of the standard tropical density profile, which best represents the Namibian atmosphere (see Section 4.4.2), coupled with desert aerosol models representing clear and dusty skies (i.e. WS = 4.5 m/s and 22.5 m/s respectively, see Fig. 4.21). The difference between the LIDAR-derived extinction and extinction derived by using the backscatter profile in conjunction with the analytically derived LIDAR ratio is evident in Fig. 4.21.

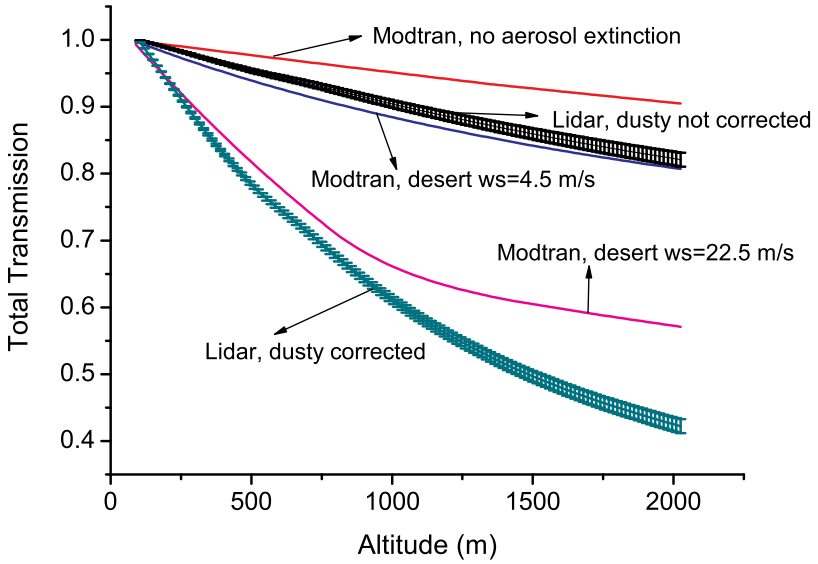

Figure 4.21: Comparison of the corrected LIDAR transmission with various MODTRAN models.

In order to verify the validity of this process, one has to apply the LIDAR inferred atmospheric model to the simulated cosmic-ray trigger rate and seek agreement with the observed trigger rate. The MODTRAN program was used to simulate the atmospheric transmission that best matches the LIDAR results. The desert aerosol model was selected for the boundary layer (i.e. 0-2 km above the H.E.S.S. site). The wind speed was used as tuning parameter to match the LIDAR-derived transmission. By increasing the wind speed, the density of aerosols within the boundary layer increases, yielding lower atmospheric transmittance. Thus the wind speed is used to modify aerosol density and does not represent the actual wind speed on the site (Brown et al., 2005*b*). The results are presented in Fig. 4.22, which shows that the LIDAR measurements agree with a desert aerosol model with a wind speed of 26 ms^{-1}. The run numbers correspond to the corrected LIDAR response on the night of 11/09/2007 and the default atmosphere currently used by the H.E.S.S. simulations (Brown et al., 2005*a*). It was later realised by the author that the wind speed modulation has an effect on both size distribution and chemical composition on the MODTRAN aerosol formulation (see Section 4.4). A more efficient treatment

of the MODTRAN code will be presented in Section 4.4.2.

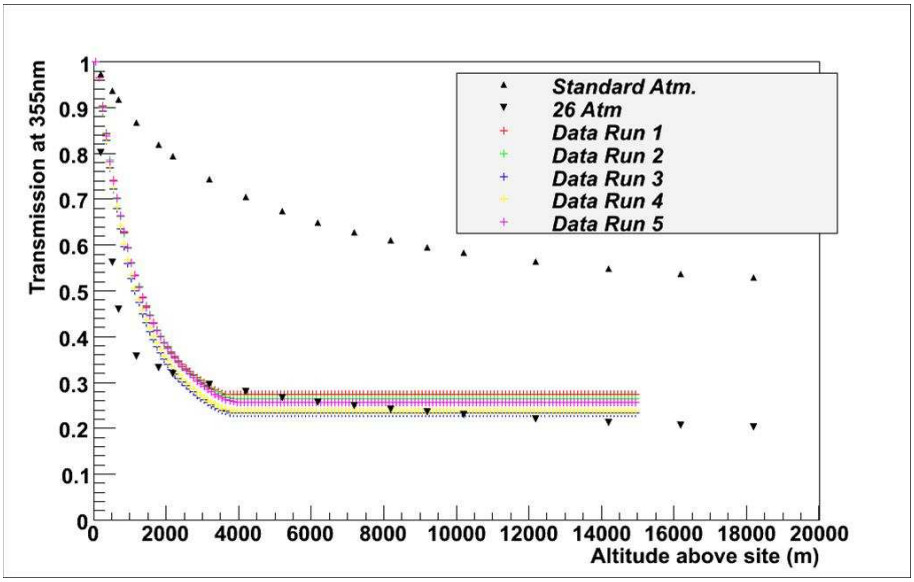

Figure 4.22: Matching the LIDAR response with MODTRAN desert aerosol model. Data Run $1-5$ correspond to to the atmospheric transmittance calculated by the relevant backscatter profiles for LIDAR runs on the 11^{th} of September 2007.

A first check on the LIDAR's corrected transmission was achieved by plotting the transmission probability against the observed cosmic-ray trigger rate (see Fig. 4.23). The correlation between the array trigger rate and transmissivity is a strong indication that the the correction technique is valid. This model has been applied to a set of CORSIKA cosmic-ray simulations covering the zenith angle range of observations (i.e. $0-60$ degrees) (Nolan, 2008). The surviving Cherenkov light has been fed to the telescope array simulation program, yielding the simulated cosmic-ray trigger rate appearing in Fig. 4.24. Figure 4.24 argues for a first order agreement between observed and simulated trigger rates. One has to keep in mind, however, that the confidence in the new LIDAR can be restored only after its operation at the nominal laser output values. Indeed, it is hard to quantify the uncertainties arising from the use of the LIDAR outside its operational specifications. In addition, the LIDAR range is limited at ~ 4 km providing only limiting information for the transmission probability of the Cherenkov photons which are produced in average 10 km above the H.E.S.S. site.

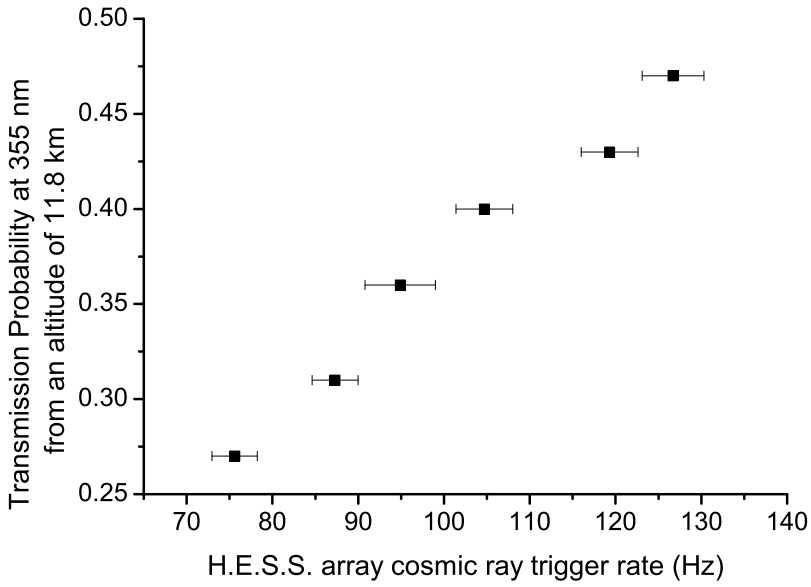

Figure 4.23: Corrected LIDAR's transmission profile versus array trigger ray. Data provided by Nolan (2008).

4.4 The MODTRAN Atmospheric Program and γ-Ray Astronomy

MODTRAN is used extensively throughout this thesis to validate both transmissometer and LIDAR responses (e.g. see Figures 3.26, 4.21 respectively) in addition of being a part of the H.E.S.S. simulation chain. It is a radiation transfer algorithm for calculating atmospheric radiance and transmittance that has been developed by the Air Force Research Labs (AFRL) with the aid of Spectral Sciences, Inc (SSI). A full account of this program is given in the MODTRAN 2/3 and LOWTRAN 7 model report upon which this section is based (Kneizys et al., 1996). MODTRAN calculates atmospheric transmittance and background radiance, single-scattered solar and lunar radiance, direct solar and lunar irradiance and multiple-scattered solar and thermal radiance. The measurements are performed for a spectral range $0 - 50,000$ cm^{-1} with the moderate resolution of 2 cm^{-1} FWHM in averaged steps of 1 cm^{-1}. The calculations are performed by the division of the atmosphere in

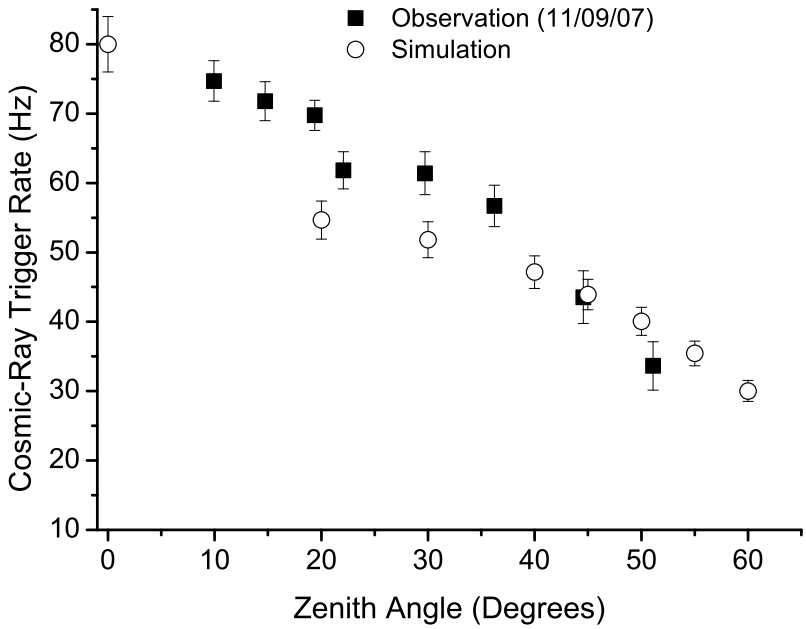

Figure 4.24: Observed and simulated cosmic-ray trigger rate vs zenith angle during the observation of LS5039 in September 2007. Data taken from Nolan (2008).

homogeneous layers whose characteristics are extracted either from internal generic models or by the inclusion of local radiosonde data (Ientilucci, 2007). The effects of both continuum type (i.e. molecular scattering, aerosol absorption and scattering) and molecular line absorption (by the use of a three band absorption model based on pressure, temperature and line-width) are all incorporated within MODTRAN.

The user has the flexibility to choose between the internal standard atmospheres and aerosol, rain and cloud models or provide more representative values overriding the default settings. In the case of γ-ray astronomy observations are limited to cloudless, dry nights. Thus, one is interested in finding the most representative combination of atmospheric and aerosol model starting with the parameters provided.

4.4.1 Standard Atmospheric and Aerosol Models

MODTRAN incorporates six built-in atmospheres each characterised by the relevant temperature, pressure, density and mixing ratios for H_2O, O_3, CH_4, CO and N_2O altitude profiles. The altitude ranges between $0-120$ km and is divided into 50 bins. The mixing ratio of CO_2 is by the user and is set at 365 ppmv for the whole range of atmospheric simulations produced in this thesis. Moreover, new atmospheric constituent profiles comprised of separate molecular profiles for thirteen minor and trace gases are also provided.

The six reference atmospheres for MODTRAN are shown in Table 4.2.

Atmospheric Model	**Location**	**Period**
Tropical	15 N	Annual average
Mid-latitude summer	45 N	July
Mid-latitude winter	45 N	January
Sud-arctic summer	60 N	July
Sub-arctic winter	60 N	January
US Standard	USA	1976

Table 4.2: MODTRAN Default Atmospheric models

In order to efficiently account for the altitude dependence of the aerosols optical properties MODTRAN divides the atmosphere (i.e. $0-100$ km) in to four layers, each containing a different type of aerosols; namely the boundary layer ($0-2$ km), the upper troposphere ($2-10$ km), the lower stratosphere ($10-30$ km) and the upper stratosphere ($10-30$ km). The relevant layers for γ-ray astronomy are the boundary layer and the upper stratosphere. In the boundary layer, the user can choose between four generic aerosol models (rural, urban, maritime and desert). Within the boundary layer, the optical characteristics and the refractive index are taken as altitude independent. Thus, only the aerosol concentration changes. The total aerosol number is dictated by the visibility parameter:

$$VIS(km) = \frac{\ln(50)}{\sigma_{\lambda_{550}} + \sigma_{mol}} \quad \frac{1}{km} \tag{4.28}$$

where σ_λ, $\sigma_{mol} = 0.01159$ km^{-1} are the aerosol and molecular extinction coefficients at 550 nm respectively. Thus, in MODTRAN the term VIS refers to the surface meteorological range (MOR, see also Section 5.5.1). VIS takes default values for each aerosol model that can be overwritten by the user. For moderate to low visibilities ($VIS = 2 - 10$ km), the aerosols are well mixed within the boundary layer and thus the aerosol vertical profile is constant. For VIS values between $23 - 50$ km the vertical aerosol profile follows faithfully the exponential decrease of the total number density of air molecules.

In the next sections, the effect of atmospheric and aerosol model selection in the Cherenkov light density will be discussed.

4.4.2 Importance of Atmospheric Modelling

The first thorough work on the effect of different atmospheric profiles on the Cherenkov light density was undertaken by Bernlöhr (Bernlöhr, 2000). Each MODTRAN reference atmosphere (see Section 4.4.1) has been used in conjunction with 2000 vertical CORSIKA simulated gamma ray showers for the wavelength range $300 - 600$ nm. The transmission of the Cherenkov light was calculated using the rural aerosol model with a surface meteorological range VIS of 23 km. Figure 4.25 shows the lateral density of Cherenkov light as a function of the core distance for the simulated γ-ray showers arriving at a detector of an altitude 2.2 km. In the extreme case, a difference of 60% is observed for the Cherenkov photon density close to shower axis between the tropical and the antarctic winter standard atmosphere. For latitudes near the H.E.S.S. site, a seasonal fluctuation of $15 - 20\%$ is evident (see Fig. 4.25) and has been included in energy calibrations of the H.E.S.S. array.

The fluctuation of the Cherenkov photon yield for different atmospheric profiles can be explained in terms of the refractive index. Different atmospheric profiles can be seen as different profiles of refractive indices. Since both the Cherenkov emission and the angle of emission depend on the index of refraction the amount of Cherenkov photon yield will vary. As an example, for a profile that possesses a higher temperature within the first two atmospheric layers ($0-10$ km) the maximum Cherenkov emission is more likely to be at higher altitude compared to one having a

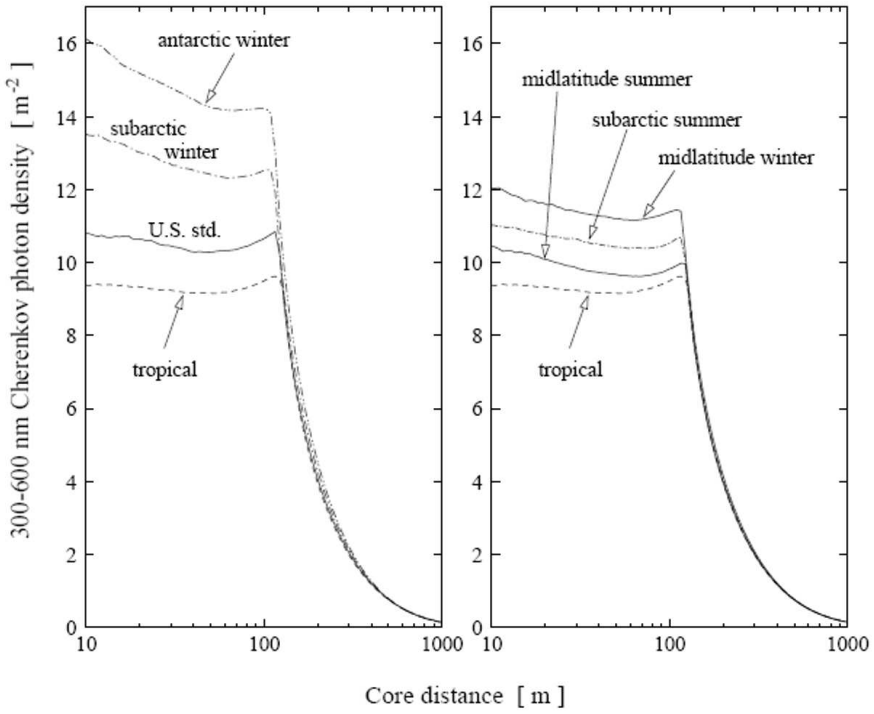

Figure 4.25: Average Lateral density of Cherenkov photons for 2000 CORSIKA simulated γ-ray showers of 100 GeV. Extracted from Bernlöhr (2000).

lower temperature. Indeed, for the same altitude, a higher temperature corresponds to higher atmospheric density (i.e. higher refractive index), and thus to a higher Cherenkov emission probability. Consequently, a higher temperature profile forces the maximum of Cherenkov emission to elevated altitudes.

The atmospheric model for the H.E.S.S. site was selected based on one year's radiosonde (i.e. radio-sounding) measurements performed in Windhoek, Namibia. Figure 4.26 shows the radiosonde measurements, taken at midnight throughout 1999, together with the reference pressure profiles provided within the MODTRAN program (see 4.4.1). The tropical model (annual average) fits the data well. MODTRAN provides the flexibility of incorporating actual radiosonde readings for a maximum of 50 altitude bins. Thus, local radiosonde measurements at the H.E.S.S. site may be used in conjunction with MODTRAN to provide a more localised atmospheric model.

The atmospheric transmission of Cherenkov light is modelled by the adaptation

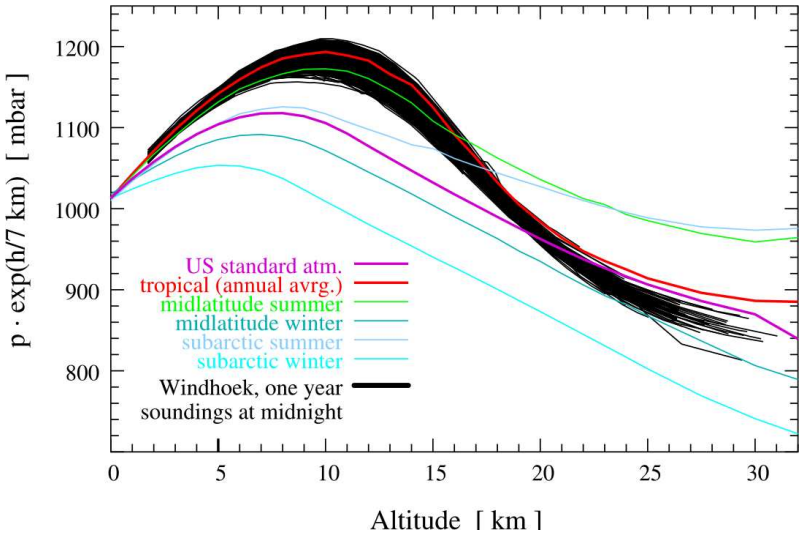

Figure 4.26: MODTRAN built-in pressure profiles compared with radiosonde readings taken throughout 1999 at Windhoek, Namibia (Osborne et al., 2002).

of MODTRAN's desert aerosol model at a default wind speed of of 10ms^{-1} for the mixing layer, whilst the tropospheric extinction model is used for the upper troposphere. Thus, Cherenkov light extinction fluctuations are mainly dictated from the aerosol density variation within the boundary layer. The confinement of the aerosols within the boundary layer is supported by the old (CT25K) LIDAR's backscatter profiles retrieved during its three years of operation (i.e. March 2004 − April 2007). The selected extinction model is adequate for measurements under clear atmospheric conditions usually to be found on the H.E.S.S. site. However, H.E.S.S. telescope runs taken under moderate to high concentration of low-level dust are usually identified by their low trigger rate and excluded from further analysis. The Durham group has developed an active atmospheric calibration method that has been successfully applied to PKS 2155-304 and H2356-309. A brief description for the method will be given below followed by some suggestions of improvements (Spangler, 2008; Brown et al., 2005b,a) :

- The Corsika program is used to simulate the air showers induced by cosmic-ray particles.

- The MODTRAN default atmospheric model is modified by changing the wind speed (i.e. $0 - 30\text{ms}^{-1}$) on the mixing layer producing a series of different optical depth tables . The wind speed is used to modify the aerosol density and does not reflect the actual wind speed on the site.

- MODTRAN tables are used to filter the Cherenkov light produced via the simulated cosmic-ray showers. The transmitted light is fed into the H.E.S.S. array simulation program and the relevant trigger rate is extracted.

- A wind speed is associated with each night's observations by requiring agreement between simulated and observed cosmic-ray trigger-rate.

- Finally, the atmosphere with the selected wind speed is applied to a large set of γ-ray simulations leading to the derivation of the corrected parameters (i.e. energy, effective area and mean-scale parameters).

The assumption that wind speed relates only to the aerosol number density is not a valid one. A closer look at desert aerosol model reveals that MODTRAN utilises two different size distribution formulations to describe the background and dust storm conditions (Kneizys et al., 1996). The parameters of the size distributions used in the background and dust storm desert aerosols models are given in Table 4.3:

Model	**i**	N_i **(cm^{-3})**	**log** (σ_i)	$\mathbf{R}_i$ $(\mu\mathbf{m})$
	1	997	0.328	0.0010
Background	2	842.4	0.505	0.0218
	3	7.10×10^{-4}	0.277	6.24
	1	726	0.247	0.0010
Dust Storm	2	1,140	0.770	0.0188
	3	1.78×10^{-1}	0.438	10.8

Table 4.3: Parameters used in the background desert and desert dust storm aerosol models (Kneizys et al., 1996).

The wind speed acts as a model selector modifying the optical characteristics of the aerosols. Moreover, the elemental concentration of desert aerosols (i.e. Ca, Si, S, Fe, Cl) can vary as a function of the wind speed (Kushelevsky et al., 1983). Thus, the use of a high wind speed, as dictated by the matching of simulated versus measured cosmic-ray trigger-rate, for observations on a dusty but non-windy night could lead to unrealistic atmospheric models. The active calibration could use the surface meteorological range (MODTRAN parameter: VIS) as opposed to the wind speed (MODTRAN parameter: WSS) and the value of the wind speed can be set to the actual value provided by the weather station. Figure 4.27 demonstrates the difference between the used and suggested method obtained by requiring the coincidence in transmittance between the wavelength range $360 - 550$ nm for at least one wavelength bin. The selection of both wavelength range and the vertical transmission path (0.55 km) was driven by the transmissometer's characteristics.

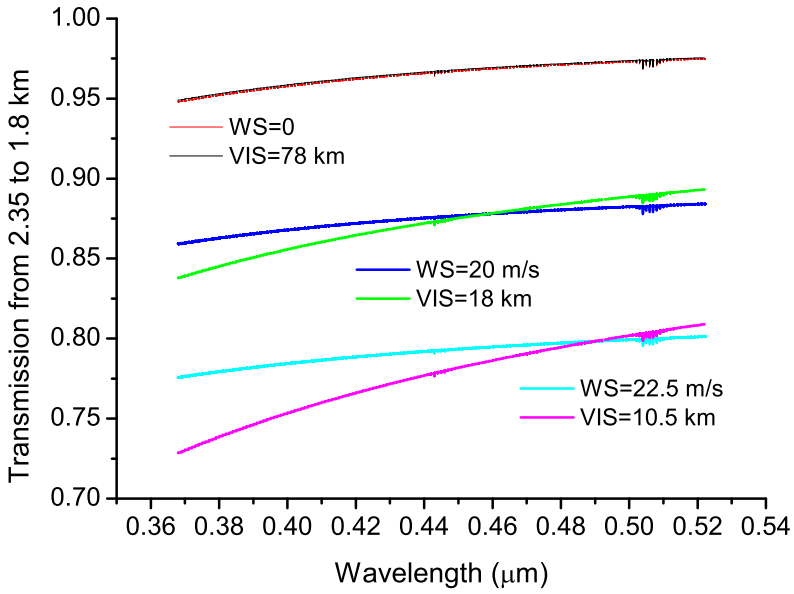

Figure 4.27: Comparison between visibility and wind speed as model selectors.

For clear atmospheres (high visibilities and low wind speeds) only the background model is invoked and the transmittance profiles are inseparable. However, atmospheric calibration is necessary only under dusty conditions. It is evident that as the wind speed increases, the dust storm model comes in to play leading to an gradually increasing the difference between the transmission profiles (see Fig. 4.27).

The observed difference can be justified by the difference in the number of large particles in mode 3 (see Table 4.3).

4.5 The Status of Atmospheric Monitoring

This Chapter marks the end of the first part of this thesis, which was concerned with the atmospheric monitoring of the H.E.S.S. site. Simulations of a stand-alone H.E.S.S. telescope, under different atmospheric assumptions, were used to quantify the atmospheric effect on the telescope's performance. Specifically, the simulations used the same atmospheric model with different aerosol boundary layer scaling to calculate the difference on stand-alone telescope's effective sensitive area response. It was seen that for low energies the attenuation of the signal becomes significant, a fact that, at this time, supported the use of a transmissometer.

The DNT was later installed and tested. The MODTRAN atmospheric code was adopted to simulate its performance with positive results. However, the DNT's inherent altitude constraint at 550 m necessitated its incorporation with the CT25K LIDAR for the derivation site-specific atmospheric transmission tables. That was proven to be impossible, mainly due to the CT25K low power, but also because of the DNT's 910 nm LED unreliability.

The CT25K, after an operation of three years, has ceased to work due to a problem identified in the receiver. The incapability of the old LIDAR to derive meaningful optical depths, coupled with the installation of the new one a few days later, rendered the possibility of costly repairs pointless.

The much awaited ALS 450 XT LIDAR was tested under low-level dust conditions with disappointing initial results. Considerable effort was dedicated by the author to understand the fine art of interpreting the elastic LIDAR response while operating outside specifications - a fact reflected upon in the theoretical section. The author identified hardware and software malfunctions rendering the immediate incorporation of the ALS 450 XT within the atmospheric monitoring scheme impossible. Specifically, the incapability of the new LIDAR to penetrate aerosol layers at altitudes higher than ~ 3.5 km was attributed to the LIDAR's laser out-

put operating at much lower power than specified. More importantly, it has been shown that the assumption of the manufacturer lidar-ratio was erroneous. With the aid of analytical back trajectories and satellite images, a proper functional relationship between the backscatter and extinction profiles was selected and the corrected results have been favourably compared against MODTRAN models. In addition, the correlation between the LIDAR's corrected transmissivity with the cosmic-ray trigger-rate has been demonstrated.

The manufacturer has restored the laser output at the nominal level. The ALS 450 XT currently covers the atmosphere above the H.E.S.S. site up to the height of the Cherenkov radiation production. In addition, the manufacturer equipped the LIDAR with a basic list of realistic backscatter-to-extinction ratios under the assumption of different aerosol models. Thus, the LIDAR provides optical depth tables than can, in theory, be directly incorporated within the H.E.S.S. analysis scheme. Moreover, the methodology described for the derivation of realistic daily lidar-ratios can be applied to minimise the LIDAR uncertainties.

The LIDAR, however, has yet (May 09) to be incorporated within the H.E.S.S. DAQ. This is due to its possible interference with the telescopes' PMTs if pointed at the wrong direction during run time. Its inclusion within the DAQ is expected soon, at which point the LIDAR's response will be checked against the active atmospheric calibration scheme based on the cosmic-ray trigger-rate, preferably with the adoption of suggestions provided in Section 4.4.2.

An operational LIDAR will also provide the motivation to update the Namibian transmissometer (DNT) as a direct comparison between the DNT and the ALS 450 XT is now possible. In what follows, the adaptation of the DNT for daylight operation leading to its transformation into a competitive aviation transmissometer will be discussed.

Chapter 5

Durham's High Level Transmissometer (DHLT)

In this chapter we discuss the development of and first results from the High Level Transmissometer that has been manufactured at Durham University.

5.1 Motivation and Prior Art

5.1.1 The Durham's Night Transmissometer

The creation of the Durham's High Level Transmissometer (DHLT) was based on the successful deployment of a similar instrument in Namibia that has been fully operational for two years (as described in section 3.4).

The constant operation of the DNT allowed its comparison with standard atmospheric monitoring devices such as the Vaisala CT25K Ceilometer also operating on site. The agreement between the DNT and Vaisala's Ceilometer is evident in Figure 5.1. This favourable comparison with Vaisala's LIDAR, considered as one of atmospheric market's standard instruments, built our confidence to explore the DNT's day-time capabilities.

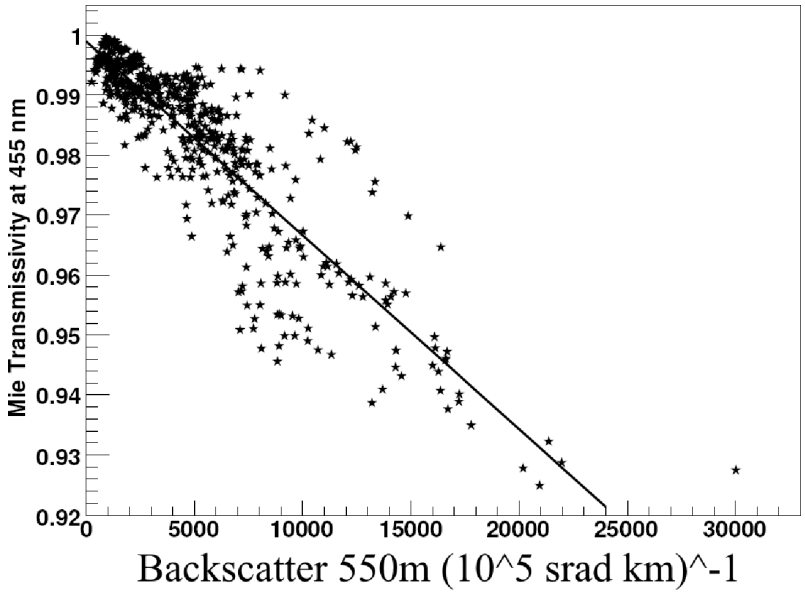

Figure 5.1: Correlation between transmissivity (T) and backscatter (Bs) measured for the first 550m above the H.E.S.S. site from Durham's transmissometer and Vaisala Ceilometer respectively. The linear fit is $T = (0.999 \pm 0.099) - (3.23 \pm 0.004) \times 10^{-6} \times Bs$. *(Courtesy of Denise Spangler).*

5.1.2 Motivation for Durham's High Level Transmissometer (DHLT).

Due to the nature of γ-ray Astronomy, our transmissometer needs to operate only at night, where the battle between the signal and noise can be won relatively easily. Following the success of the DNT, we built a day-light transmissometer prototype which incorporates all the advantages of the night version, but can be operated during the day, with the aspiration of promoting it into the vast aviation market.

The measurement of visibility at airports is a vital factor in aviation safety. Visibility can be defined as a direct function of the extinction coefficient (see Section 5.5.1) . The latter can be measured either directly, by the use of transmissometers, or indirectly via forward scatter sensors.

Forward Scatter Sensors

In contrast to transmissometers, forward scatter sensors only measure the amount of the light scattered by aerosols at a small solid angle. The extinction coefficient (σ) is estimated by the assumption of a light scattering function of the prevailing aerosols. It has been proven, however, that different aerosol distributions having the same value of σ may exist (van der Meulen, 1992). In addition, the salinity of aerosols may vary, leading to changes in their size distribution. For scattering angles between 30° and 35° the scattering functions lead to the same result (for a wavelength range 400 - 1000 nm) for most aerosol types. Thus, σ can be derived from the following formula:

$$\sigma = c\iota(\phi, \Omega) \tag{5.1}$$

where:
$\iota(\phi, \Omega)$ denotes the relative amount of light scattered at an angle ϕ in the forward direction and observed within the solid angle Ω, and c is the calibration constant

Forward scatter sensors cost less than transmissometers and are easier to maintain and install. Moreover, due to their compact design, they can be positioned on a tall mounting. Thus forward scatter sensors can be mounted at the level of pilot's eyes when approaching the end of the runway, which for big planes can be as high as 5 metres. That is not possible with transmissometers which, due to stability issues, are usually mounted at a maximum height of 2.5 m above ground level.

On the other hand, due to the indirect nature of the scatter measurement, forward scatter sensors cannot produce accurate results under all weather conditions. Specifically, these instruments have been proven to work better under fog, snow and (less frequently) under rain. However, it is not clear whether they could produce measurements of sufficient accuracy under sand-storms or smoke (Utela, 2002). Thus, the response of a forward scatter sensor is usually calibrated against a transmissometer under weather conditions most likely to occur for the specific site.

The DHLT has the aspiration to fill in this gap in the airport industry by providing a transmissometer that can accurately measure visibility under all weather conditions, incorporating the low cost and flexibility only found until now in forward scatter sensors.

5.2 Project Strategy

The author, appointed to work part-time on and carrying the main responsibility for this project, constructed an action plan in order to achieve the project's principal objective, namely to draw a license agreement with an industrial partner:

1. develop a daylight-operating prototype quickly, without particular regard to cost, in order to demonstrate that, in principle, an instrument could be built that would operate during the day and over the required distances,
2. test and optimise the prototype,
3. calibrate the prototype and validate its performance by estimating its combined uncertainty, thereby realising its strengths and weaknesses and
4. advertise the instrument's innovative characteristics, performance and price in order to identify interested potential distributors.

In addition to developing quickly a daylight working prototype, one should identify, and if possible develop, ways of reducing the costs of the instrument, this being a major element in fulfilling the requirements of a commercial instrument.

In what follows an account will be given of the author's effort to meet the first three requirements set by this action plan. The last requirement of the action plan was commissioned to RTC North (McStea, 2006), who performed market research by contacting possible licensees.

All in all, the author has been responsible for the algorithms used to perform the transmission and MOR calculations, the optical design, all data analysis, error minimisation, instrument calibration and liaison with Durham's University Electronic and Mechanical workshops and RTC North (see also Chapter 1).

5.3 Hardware

The basic design of the Durham transmissometer involves the use of an LED-based transmitter and a detecting camera, with suitable software for locating the LED in

camera's field of view and measuring its intensity.

5.3.1 The light transmitter

The Namibian transmissometer employs an array of LEDs operating at different wavelengths. Our first modification to this design was to use a single super-bright broad-spectrum LED (capable of producing a typical luminous flux $\Phi = 80$ lm) as the light source (Lumileds, 2005). This follows the recommendations of the International Civil Aviation Organisation (ICAO), which notes that the usage of monochromatic light sources may lead to errors under some weather conditions (ICAO, 2005). The main optical and electrical characteristics of the selected Luxeon© III Star LXHL-LW3C are listed in Table 5.1. In addition, the LED's typical emission spectrum and spatial radiation pattern are provided in Figures 5.2 and 5.3 respectively. It is worth noticing that Luxeon's super bright LED was initially offered in cool white at a colour temperature of 5500 K. Thus, its emission spectrum (as shown in Fig. 5.2) was expected to deviate from the spectral power distribution of the standardised incandescent lamp (Wyszecki and Stiles, 1982), which has a colour temperature of 2700 K, and is required for the visibility measurement (see Section 5.5.1). This problem was rectified by the acquisition of a warm white Luxeon LED (3000 K colour temperature) that become available later (see Section 6.9.1).

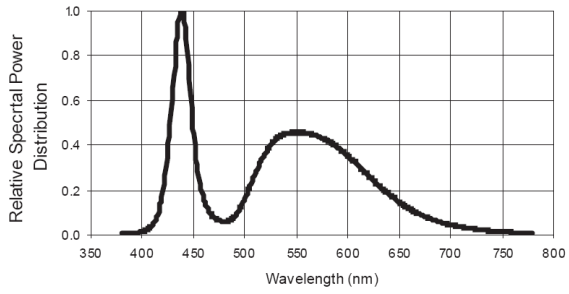

Figure 5.2: Typical cool white spectrum of Luxeon III Star LED at 1 A test current and junction temperature $T_J = 25°C$ (Lumileds, 2005).

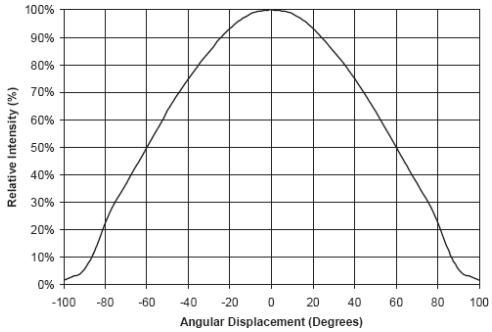

Figure 5.3: Representative spatial radiation pattern for Luxeon III Star LED at 1 A test current and junction temperature $T_J = 25°C$ (Lumileds, 2005).

Typical characteristics of the Luxeon III Star LXHL-LW3C LED				
Flux		Optical		
Luminous Flux (lm)	Drive Current (A)	Colour Temperature CCT (K)	Total Included Angle (degrees)	Viewing Angle (degrees)
65 80	0.7 1.0	5500	160	140
Electrical Characteristics				
Drive Current (A)	Forward Voltage (V)	Dynamic Resistance (Ω)	Temperature Coefficient of V_f (mV/°C)	Thermal Resistance Junction to Case (°C/W)
0.7	3.70	0.8	-2.0	17

Table 5.1: Typical characteristics of the Luxeon III Star cool white LED. Drawn from the Luxeon manual (Lumileds, 2005).

The LED (see Figure 5.5) is mounted in a polycarbonate lens providing a beam of 3° FWHM. In front of the LED's optics sits a diffuser in order to smooth both its lateral profile and the effect of its central obstruction (see Figures 5.4, 5.5 and 5.6). A control system for the LED that would provide a stable current independent of temperature was designed at Durham and a suitable PCB produced (Moore, 2008), shown in Figure 5.6 (a circuit diagram can be found in the Appendix B.2). This can be programmed to operate the LED under a wide range of currents (i.e. $35\% - 100\%$) to provide for better calibration and to allow the transmissometer to be used over a wide range of distances. A photodiode is employed to monitor the intensity of the LED, and the drive characteristics and temperatures of the LED and its associated electronics are monitored. The stability of the LED current and temperature can be used for quality assurance of the data, while the photodiode's signal is used for the active calibration of the instrument (see Section 5.6.5).

The transmitter is driven using RS232, as the baselines required by the aviation

industry are small, typically $25 - 70$ m. However, the instrument in Namibia is operated via a licence-free radio connection, and this possibility exists for the new instrument. The Namibian transmitter is also solar-powered for use in its remote location, and again this remains an option (Le Gallou, 2005).

Figure 5.4: The light transmitter. The controller system is towards the top of the enclosure and the power supply is at the bottom right. The LED is located behind the large, square diffuser.

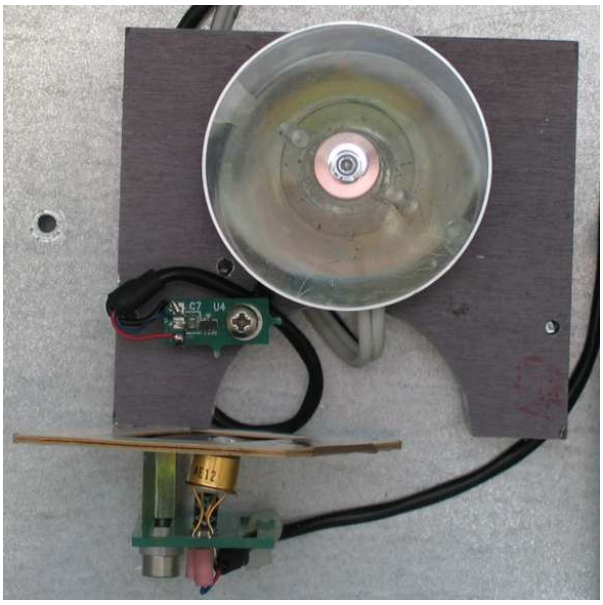

Figure 5.5: A closer look at the LED's optics. The photodiode - now located behind the diffuser (see in Figure 7.2)- and the temperature gauge are also clearly identifiable.

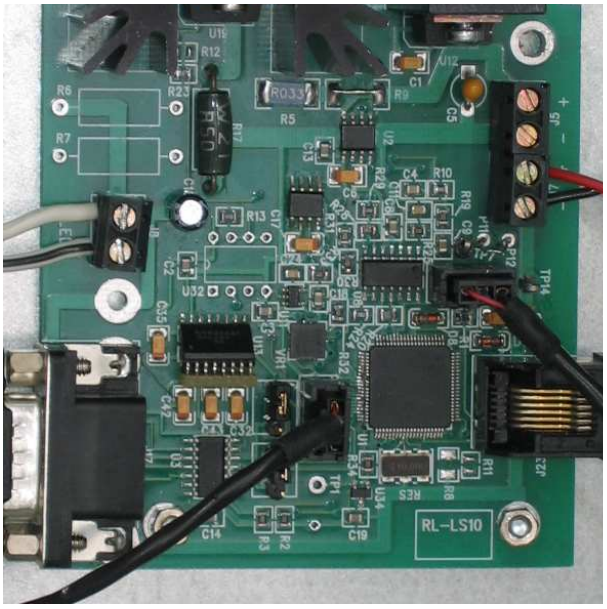

Figure 5.6: A closer look at the PCB.

5.3.2 The light receiver

The light receiver (see Figures 5.7 and 5.8) is based around the monochrome uEye CMOS camera manufactured by IDS (Imaging Development Systems). The camera (see Figure 5.9) is equipped with a light sensitive $1/3''$ sensor with rolling shutter and has a resolution of 640×480. It comes with a C-Mount that allows for a wide field of view when equipped with a suitable lens, providing for simple and robust alignment. Specifically, two lenses with focal lengths of 16 mm and 105 mm have been used to give a field of view that varies from 6.50° to 0.50° across respectively. Even with the bigger lens, the field of view is more than adequate to prevent problems due to misalignment.

The camera is driven using Arcom's Apollo SBC (Single Board Computer) via a USB 2.0 cable. The Apollo is an EBX format, high functionality PC-compatible processor board based around the $855GME/ICH4$ chipset (Arcom, 2005). The selected version includes an 1.6 GHz M Celeron processor, 512 Mb of memory, a 40 Gb hard disc drive and offers all standard features and connectors found on a

Figure 5.7: The light receiver. One can clearly identify the Apollo SBC with its power supply and hard disc, the camera equipped with the 16 mm lens and a simple temperature monitoring device.

Figure 5.8: The light receiver with the lid closed. The heat sink was used in the initial stages of development. The CMOS camera, located at the bottom right of this photograph, was later relocated to a separate box to maintain temperature stability.

Figure 5.9: The camera equipped with the big lens ($f = 105$ mm) in its separate box.

PC motherboard (see Figure 5.10). It is running under license free SUSE 9.3 Linux.

This camera has the further advantage of being considerably less expensive than the CCD camera used in the original instrument, and immediately contributes to a reduction in manufacturing costs.

Both the camera and the transmitter are enclosed by two identical enclosures that meet IP66/67 standards of ingress protection. The receiver's box was equipped with a big contact heat sink (see Figure 5.8) in order to resolve heating issues during the hot summer days. After exhaustive tests, which included the creation of a controlled air flow throughout the receiver, it was decided that the camera should be totally isolated from the receiver's other instrumentation (see Fig. 5.9).

The transmitter and receiver are both mounted in steady bases (manufactured in the Physics Workshop at Durham) that allow easy mechanical alignment.

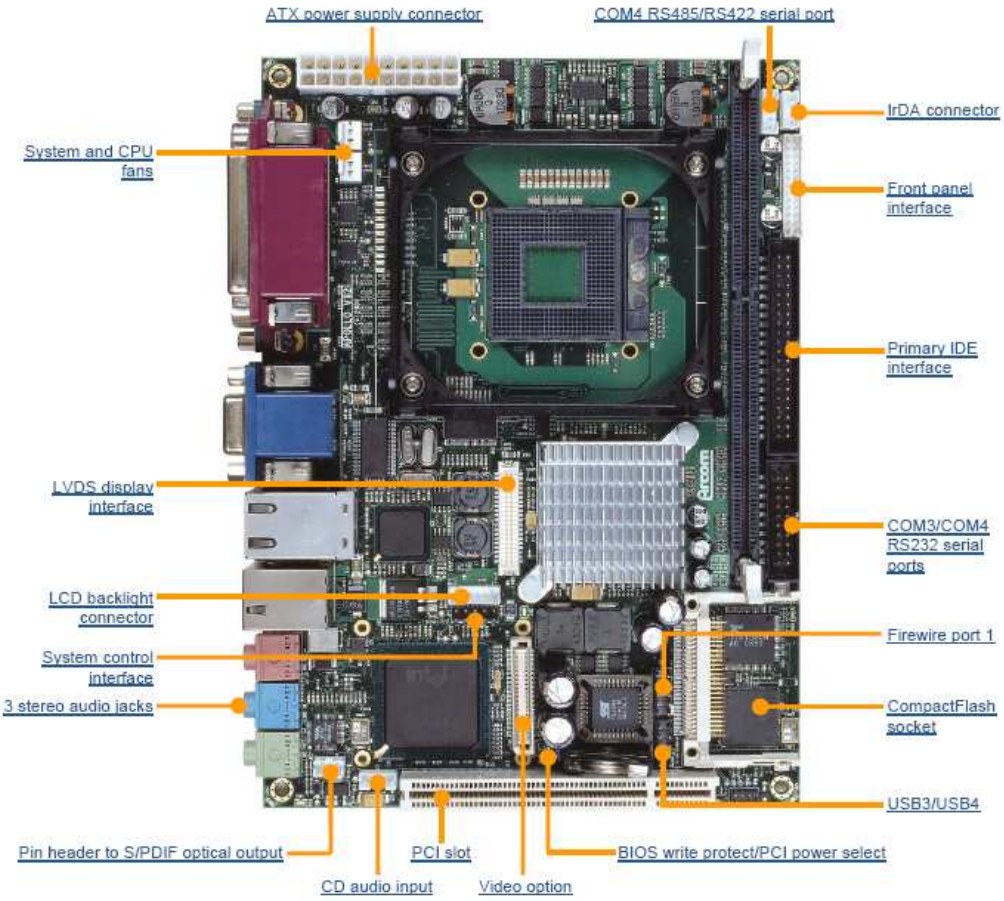

Figure 5.10: Apollo 'at a glance'. Taken from its technical manual (Arcom, 2005).

5.4 Software

5.4.1 Measurement algorithm

The program that operates the transmissometer (dlgmainview.cpp) is based on the licence-free code that drives the monochromatic CMOS camera. It is responsible for synchronising the operation of the LED with the camera in order to take exposures optimised for the dynamic range of the camera. It also measures the background intensity by two independent methods to allow for an accurate determination of the observed LED intensity. In the first method, the observed intensity of the LED

and luminous background is calculated from the picture taken with the optimised exposure time by summing the pixel values of the 5×5 pixel square centred around the brightest pixel. The intensity of the background is then calculated by summing the values of the pixels located at a distance between 10 and 20 pixels from the centre of the brightest spot. The observed LED intensity is calculated by subtracting the normalised average values. In the second method, the intensity of the background is calculated by taking a dark frame of 5×5 pixels. By subtracting this value from the overall intensity calculated from the ON picture, a second value for the observed LED intensity is derived.

The operational algorithm can be described as the sum of the following steps:

- the LED is switched ON,
- after a short delay, an exposure is taken by the CMOS camera with an exposure time that is believed to be typical of transmissometer's baseline and site of operation,
- the picture taken is analysed in order to locate the brightest array of pixels (of size 3×3) and determine its intensity,
- this maximum intensity is required to be between 170 and 230 ADUs (i.e. Analog-to-Digital Unit). If this condition is not satisfied a loop of exposures with successive corrected exposure times is initiated until the intensity criteria are met,
- the observed intensity ($R_l + R_B$) of the LED and luminous background is calculated from the picture taken with this optimised exposure time by summing the pixel values of the 5×5 pixel square centred around the brightest pixel. The intensity of the background is calculated by summing the values of the pixels located at a distance between 10 and 20 pixels from the centre of the brightest spot. The observed LED intensity (R_1) is calculated by subtracting the normalised average values. (Hereafter, this method of extracting the background intensity from the CMOS ON frame is referred as Method A),
- the LED is switched OFF,

- after a delay, optimised to take into account the short term variation of the background intensity, an OFF exposure is taken having exactly the same exposure time as the ON exposure,
- the intensity of the background is now calculated by a dark frame of 5×5 pixels. By subtracting this value from the overall intensity (R_l+R_B) calculated from the ON picture a second value (R_2) for the observed LED intensity is calculated. (Hereafter, this method of inferring the background intensity from the difference between the ON and OFF CMOS frames is referred as Method B),
- the process continues until any desired length.

The output of the transmitter's photodiode when the LED is OFF is constantly monitored. This is used to discriminate between day/night conditions and to switch the program to send the data to the relevant day/night folders.

5.4.2 Data Structure

The PCB has the ability to monitor many parameters that can be used to better assess the measured LED intensity. Specifically, the monitored quantities, in addition to the observed LED intensity, include:

- day and time of the measurement,
- values of the current and voltage that drive the LED (I_{LED}, V_{LED}),
- photodiode signal that measures the LED's direct transmission,
- temperature of the PCB and LED optics,
- coordinates of the brightest pixel.

The data-files are written in ASCII format. Part of a typical file is listed below:

```
‘‘-------------------
Mon Feb 26 14:37:02 2007
14:37:35 4 197.449 198.076 24.96000 262 260 201.469   4.020 201.469   3.394 0.991 8.970 13.2 11.7 2.484 0.641
14:37:41 5 198.633 198.974 24.96000 262 263 202.429   3.796 202.429   3.454 0.991 8.970 12.7 11.7 2.489 0.636’’
```

The columns are: "time, Intensity(ON-OFF) 1st method, (ON-OFF) 2nd method, exposure time, X coordinate of the brightest pixel, Y coordinate of the brightest pixel, Intensity ON, Intensity OFF 1st method, Intensity ON, Intensity OFF 2nd method, LED current, LED voltage, ON board temperature, OFF board temperature, photodiode voltage (LED ON), photodiode voltage (LED OFF)"

The stability of the LED current and temperature can be used for quality assurance of the data while the photodiode's signal is used for the off-line calibration of the instrument (see Figure 5.24). Moreover, the coordinates of the centre of the light spot are traced to allow for the prompt alignment between receiver and transmitter.

The author developed a purpose-built readout program, based in Root, that provides a processing suite capable of handling the relatively large amount of discrete data provided by the instrument. These data are used to calculate transmittance and visibility values and the program is able to represent graphically any usable combination of calculated and monitored quantities. This program will be presented in Section 5.7.4, after the introduction to the mathematical methods for the calculation of both transmittance and visibility.

5.5 The calculation of visibility

The term visibility is generally used to define the greatest distance that a prominent object can be seen and identified by unaided, normal eyes. Thus, it is a complex psycho-physical phenomenon depending mainly on the atmospheric extinction coefficient (σ). While σ can be measured objectively, visibility is also affected by subjective factors caused by differences in individual visual perception and interpretative ability. Moreover, visual perception is governed by different physical mechanisms during day and night time. The relative sensitivity of a normal observer at various wavelengths (i.e. luminous efficacy) is shown in Figure 5.11. The observed difference is due to the fact that day vision (photopic) involves the fovea centralis (located at the central part of the eye's retina) consisting of cones, while night vision (scotopic) involves rods (peripheral part of the retina) that are absent from the fovea.

The cones are responsible for light-adapted vision. Figure 5.12 shows that cones

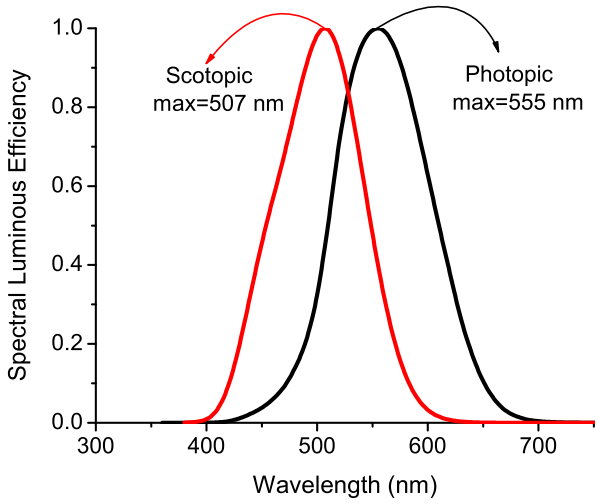

Figure 5.11: Relative sensitivity curve for the C.I.E. Standard Observer. *The data files for this graph were adopted from Wyszecki and Stiles (1982).*

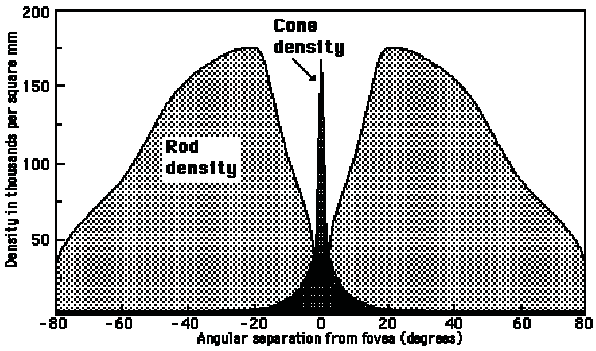

Figure 5.12: Density curves of coned and rods on the eye's retina. Taken from Williamson and Cummins (1983).

are very closely packed within the fovea centralis. Thus, this region of close-packed cones provides eye's highest visual resolution. Moreover, cones are responsible for colour perception as their total number of 6-7 million can be discriminated into red (64%), green (32%) and blue (2%). Cones are, therefore, responsible for both colour vision and the highest visual resolution.

On the other hand, rods are both more numerous and more sensitive to light than the cones. A typical retina consists of 120×10^6 rods which are distributed in the retina as shown into Figure 5.12. Even though rods are absent from the fovea, their density increases rapidly at a short angular distance from it, occupying a large area of the retina. Due to their light sensitivity rods are much better motion detectors than cones. The domination of rods in the peripheral vision explains its sensitivity to light.

Photopic vision is active for luminances greater than 3 cdm^{-2} while scotopic vision dominates for luminances lower than 0.01 cdm^{-2} (Palmer, 2003). For light levels between photopic and scotopic visions, both cones and rods are simultaneously active. The derivation of a composite spectral response for the mesopic (i.e. in-between) region is difficult due to both the different spectral and light level sen-

sitivities between the cones and the rods and is a topic of current research (Orreveteläinen, 2005).

5.5.1 Practical Estimation of Visibility

The confusion related to the measurement of visibility for aeronautical purposes is reflected in the plethora of visibility definitions. Indeed the aeronautical-related visibility can be defined (and therefore reported), in the following ways:

- Meteorological Optical Range (MOR) is the length of the path in the atmosphere required to reduce the luminous flux in a collimated beam from an incandescent lamp, at a colour temperature of 2700 K, to 0.05 of its original value, the luminous flux being evaluated by means of the photometric luminosity function of the International Commission on Illumination (CIE) (metre, m or kilometre, km) (WMO, 1992),

- Visibility for aeronautical purposes (VIS-AERO), is the greater of:
  a) the greatest distance at which a black object of suitable dimensions can be seen and recognised when observed against a bright background; b) the greatest distance at which lights in the vicinity of 1000 candelas can be seen and identified against an unlit background (ICAO, 2000; Červená, 2005).

- Runway Visual Range (RVR) is the range over which the pilot of an aircraft on the centre line of the runway can see the runway markings or the lights delineating the runway or identifying its centre line (WMO, 1995).

To add to this confusion MOR and VIS-AERO are often forecasted interchangeably (AMOSSG, 2006).

MOR is directly related to the atmospheric extinction coefficient and does not depend on the time of the observation (day/night). It is close to an observer's estimation of visibility during the day (i.e. visibility by contrast: see next section). The latter depends on the observer's acuity and the object observed but in practice

the contrast threshold is fixed at 0.05. The mathematical relation between the MOR and extinction coefficient can be found from equation 3.2 by requiring a transmission coefficient T of 5%:

$$T(d) = \left(\frac{I_0}{I}\right) = 0.05 = e^{-\sigma(MOR)} \Rightarrow MOR = \left(\frac{\ln(\frac{1}{0.05})}{\sigma}\right) \tag{5.2}$$

Even though MOR can be used accurately for day-time estimation of visibility, during the night MOR underestimates the visibility because the observer's perception of light sources increases. That leads to the ICAO's definition of aeronautical visibility. According to this definition VIS-AERO depends, in addition to the atmospheric transparency, on the intensity of the light source (1000 Cd) and the background luminance. The difference between VIS-AERO and MOR increases for low values of visibility and background luminance (AMOSSG, 2006).

The RVR takes into account the dedicated runway lights, used to guide the pilots, which have an average intensity of 10000 Cd. The average height of a pilot's eye-level in an aircraft above the centre line of the runway is 5 m. It should be noted that for larger aircraft this height could exceed 10 m. In practice, RVR is calculated for a height of 2.5 m above the runway. RVR, therefore, depends on the atmospheric extinction coefficient, runway lighting and background illuminance. The difference between the three different expressions of visibility and its variations between day/night is demonstrated in Figures 5.13, and 5.14 respectively.

Daylight Visibility

Daylight visibility involves seeing an dark object against the bright sky background. When a black object is viewed from a distance through an illuminated atmosphere the observed contrast decreases and image illuminance is attenuated. Contrast luminance is defined by Koschmieder (Koschmieder, 1924) as:

$$C = \frac{L_o - L_h}{L_h} \tag{5.3}$$

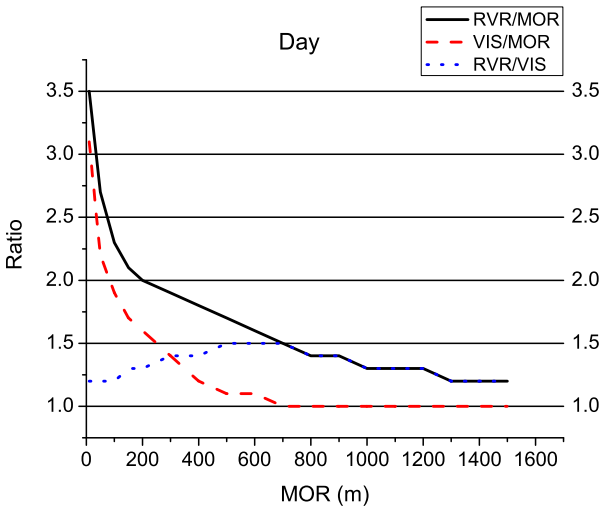

Figure 5.13: Ratios of RVR/MOR, VIS/MOR and RVR/VIS are plotted as a function of MOR during the day. *The data files for this graph were adopted from AMOSSG (2006).*

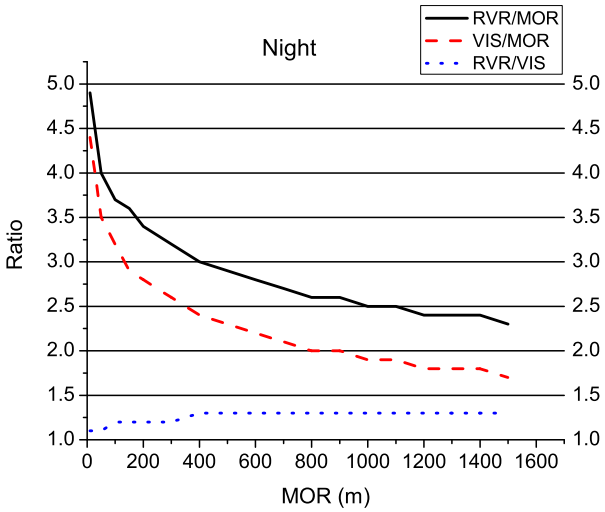

Figure 5.14: The same ratios as in Figure 5.13, are plotted against MOR during the night . An intensity of 10000 Cd and 5000 Cd for side and axial runway lighting have been considered. *The data were taken from AMOSSG (2006).*

where:

L_o is the luminance of the object

L_h is the luminance of the horizon sky.

The contrast transmittance can be defined:

$$Contrast\ Transmittance = \frac{C}{C_o} \tag{5.4}$$

where:

C is the apparent contrast at a given distance

C_0 is the initial contrast observed at a very close distance (thus, eliminating the atmospheric effect).

By adopting a contrast detection threshold for the human eye and assuming that contrast and radiometric transmission are the same, MOR can be calculated from transmissometer's measurements via the Beer-Bouguer transmission equation 5.2

(Farmer, 2001*b*):

$$\frac{I}{I_o} = \frac{C}{C_0} = e^{-\sigma x} \tag{5.5}$$

The luminance of a perfectly dark target is by definition $L_o = 0$ that gives a contrast of $C = -1$ (the negative sign indicates that the target is darker than its background). The value of the contrast ratio threshold viewing this target is assumed to be 0.05 for aeronautical purposes (a value of 0.02 is adopted in meteorology). By substituting these values into equation 5.5 and expressing the extinction coefficient in terms of the transmissometer's measurements, one gets the visual range or MOR:

$$MOR = \frac{R \ln(0.05)}{\ln \frac{I}{I_0}} \tag{5.6}$$

where R is the transmissometer's baseline.

The MOR calculated in this way is very close to an observer's estimation of visibility during the day. The latter depends on the visual acuity of the observer and on the contrast of the object observed (see Section 5.5.1). These parameters are set by definition to 0.05 and -1 respectively.

Thus, the daylight visibility is a function of σ which is estimated directly from the transmissometer.

Night-time Visibility

Night-time visibility involves the distance at which a runway light of a known intensity can be seen. Under prevailing artificial lighting conditions the general form of Allard's law (Allard, 1876) can be expressed as:

$$E_t = \frac{I \exp\left[-\int_0^V \sigma(x)\mathrm{d}x\right]}{V^2} \tag{5.7}$$

where:

I is the intensity of the runway light

E_t is the visual threshold of illumination, which is defined as the smallest illuminance required by the eye to make a point (or small) light source visible (i.e. the observer's sensitivity to the illumination intensity) (ICAO, 2005)

and V is the visual range.

If the extinction coefficient is constant within this range equation 5.7 becomes:

$$E_t = \frac{I_0 exp(-\sigma V)}{V^2} \tag{5.8}$$

One can introduce the transmission factor as calculated by the transmissometer $T = e^{-\sigma R}$ in order to make equation 5.8 more usable (Petitpa, 1982):

$$T^{\frac{V}{R}} = e^{-V} \Rightarrow E_t = \frac{I_0 T^{\frac{V}{R}}}{V^2} \Rightarrow 2\ln V + \ln E_t = \ln I_0 + \frac{V}{R}\ln T \tag{5.9}$$

where:

R is the transmissometer's baseline.

Using the above equation RVR can be calculated by setting the transmissometer's baseline R and light intensity. The standard for aeronautical purposes is R=750 ft and $I_0 = 10,000$ candela. Corrections must be taken into account in order to compensate for the actual transmissometer's characteristics. The visual threshold of illumination also needs to be estimated. The value of this threshold depends mainly on the background luminance (B) against which the point (or small) light source is seen. The background luminance was initially separated into four categories, corresponding to different background conditions ranging from a dark night to a bright day fog, each of which was allocated a constant threshold of illumination as listed in Table 5.2. The recommended stepped function between the illumination threshold and the background luminance is graphically represented in Fig. 5.15. It is evident that the illumination threshold ranges over three orders of magnitude between extreme background conditions (night to bright day fog) whereas for adjacent steps it varies by one order of magnitude. In practice, modern transmissometers monitor constantly the background luminance (B), and E_T is approximated by the analytical expression of the continuous curve intersecting the steps in the middle (see Fig. 5.15) (ICAO, 2005):

$$log(E_T) = 0.57\log(B) + 0.05[\log(B)]^2 - 6.66 \tag{5.10}$$

Table 5.2: The steps of the visual threshold of illumination under different background conditions (ICAO, 2005).

Condition	Threshold of illumination (lx)	Background luminance (cd/m^2)
Night	8×10^{-7}	≤ 50
Intermediate	10^{-5}	$51 - 999$
Normal day	10^{-4}	$10^3 - 12 \times 10^3$
Bright day (sunlit fog)	10^{-3}	$> 12 \times 10^3$

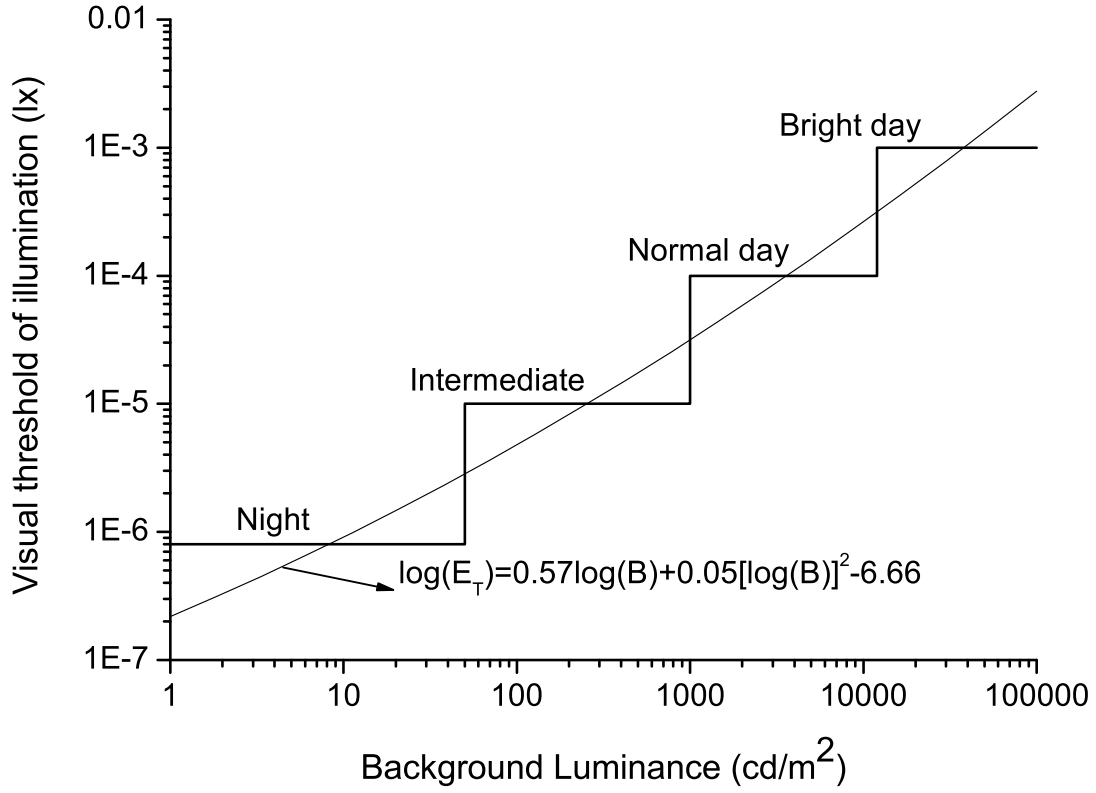

Figure 5.15: The variation of the visual threshold of illumination (E_T) as a function of the the background illuminance (B). The recommended values for the illumination threshold under different background conditions have been adapted from ICAO (2005).

Thus, for the calculation of the RVR one needs only three parameters; namely: the transmittance factor (or MOR), the luminous intensity of the runway lights (I)

and the background luminance (B). The last can be determined by the provision of an extra background luminance monitor.

5.6 System Performance

5.6.1 Eliminating Background Intensity

A very important aspect of DHLT is that the background intensity is calculated by two independent methods. These methods have been proven to work in Namibia where only night-time observations are taken. In order to deal with the high-intensity background associated with our day prototype more effectively, we devised a black shield around the transmitter's window. Figure 5.16 shows the variation of the relative difference between the values obtained by the different methods during a relatively bright day. The percentage difference is very small and illustrates the reliability of the device.

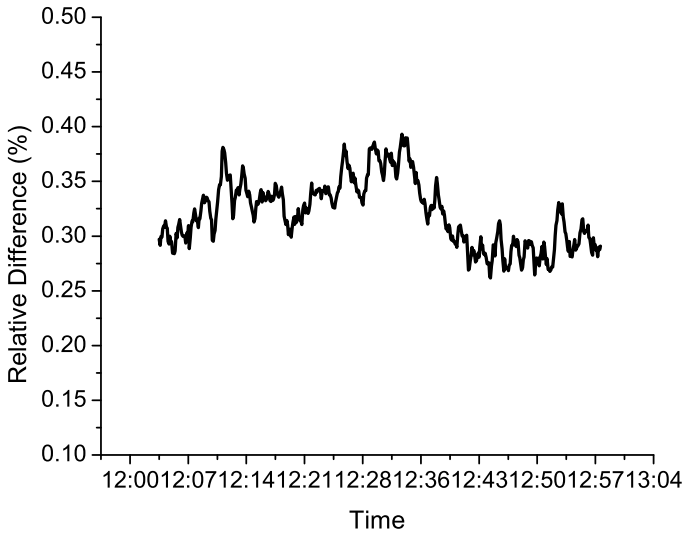

Figure 5.16: Percentage difference between values of visibility measured with the DHLT, calculated by using the two different methods (outlined in Section 5.4.1). The difference is very small, and illustrates the comparability of the two methods.

5.6.2 Averaging-Time Optimisation

Each individual transmissometer reading suffers from the statistical fluctuation that is inherent in any photon counting method. This uncertainty can be limited by averaging over a large number of measurements. However, the presence of meteorological interference between the transmissometer's transmitter and receiver units (e.g. a fast moving fog front) could also lead to rapidly fluctuating irradiance measurements. Thus, one needs to find the optimum averaging time that gives a transmissometer signal that is both steady and sensitive to swift changes in the atmospheric transparency. This objective was tackled by calculating the 95% confidence interval as a function of averaging time under stable atmospheric conditions (see Figure 5.17). The individual measurements used had already been corrected for small variations of the source's intensity (see Section 5.6.5). Figure 5.17 convince us that using an averaging time greater than two minutes will not lead to a significant improvement of the measurement's accuracy.

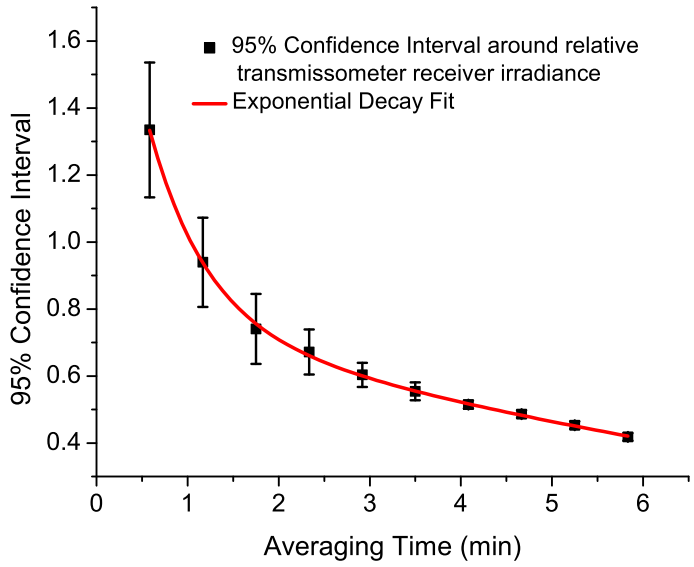

Figure 5.17: 95% confidence interval around the mean CMOS irradiance plotted against signal averaging time for the DHLT.

5.6.3 Spot Size Optimisation.

The light signal from the transmitter is registered in CMOS photodiodes (pixels) where the received light is translated into electrons. For the DHLT characteristics, a baseline of 45 m, aperture 2 mm and camera focal length of 105 mm, the LED produces a spot of 15 pixels radius within the camera's field of view. Analysis of the full spot size would produce adequate statistics, but suffer from charge overflow from the brightest pixels located at the spot's centre, thereby increasing the signal variation. One needs to find the optimum size that gives the golden mean between statistics and the signal's standard deviation. For this purpose, both the mean value of the spot intensity and its standard deviation have been plotted for a wide range of pixel apertures from squares 9 to 169 of side (see Figures 5.18, 5.19 respectively).

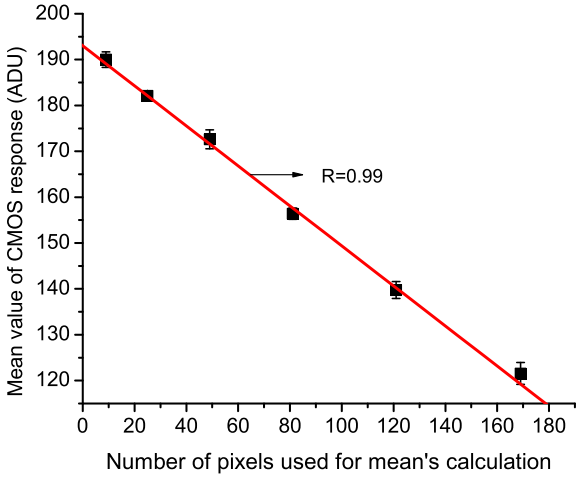

Figure 5.18: The mean value of the measured intensity of DHLT is plotted against the number of the pixels used for its calculation.

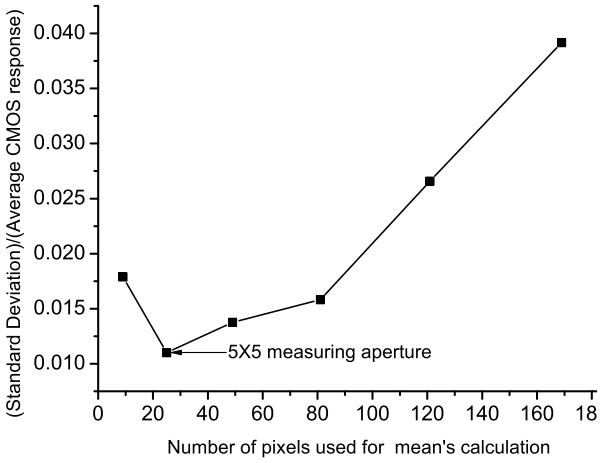

Figure 5.19: The ratio of the standard deviation over mean intensity of the DHLT (i.e.:$\frac{\text{SD}}{\text{MeanInt}}$) is plotted against the number of pixels used for the calculation of the mean intensity.

Figure 5.19 shows that a 5×5 measuring aperture minimises the standard deviation over the measured intensity ratio, yielding the most consistent measurements. Therefore, a square, centred in the brightest pixel, of side 5 pixels is used.

5.6.4 Window Material Selection

The original transparent plastic window that covered both transmitter and receiver (see Figure 5.8) had a very low transmittance value ($\sim 60\%$) that could have restricted the transmissometer's performance under low visibility conditions. This issue was addressed with the provision of a new glass window for the receiver unit. The new glass material allows for a very good transmittance value of $(87.5 \pm 0.61)\%$, as recent tests revealed (see Figure 5.20). This measurement was taken in the morn-

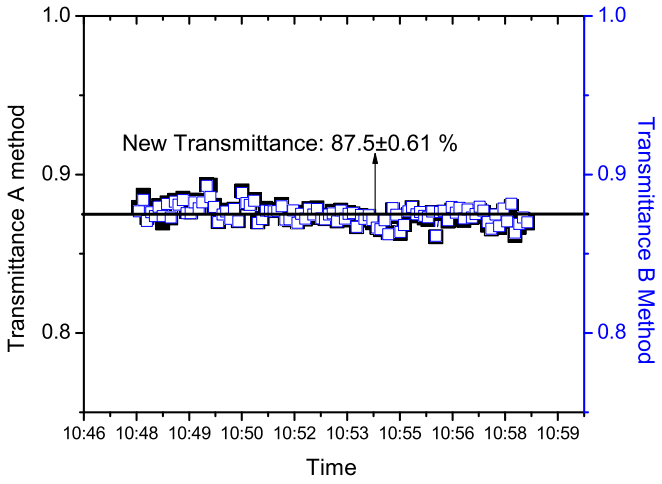

Figure 5.20: New glass window transmittance.

ing of a relatively bright day. It is worth noticing the good agreement between the different methods of estimating background lighting conditions (the black and blue points representing Method A and Method B respectively are hardly distinguishable. For the definition of Methods A and B see Section 5.4.1).

5.6.5 Calibration and Linearity Tests

Due to the complexity and the psycho-physical nature of visibility, there is no standard test method for assessing visibility sensors. Since a "standard atmosphere" (in which a transmissometer can be checked) does not exist, one must look at the consistency between measurements under the assumption of steady atmospheric conditions.

Table 5.3: Calibration Constants for Durham's High Level Transmissometer

Instrument Used	Measured Quantity	Accuracy
Bosch DLE 150 laser finder	$R = 44.50m$	3 mm
Longman Vernier Caliper	Aperture=4.00mm	0.05 mm

In order to calibrate our instrument, we need to estimate the LED's irradiance that would have been registered by the CMOS camera if the intervening atmosphere between transmitter and receiver was transparent. In practice, the calculation of I_0 is performed under clear atmospheric conditions and visibility above 30 km. For the visual estimation of visibility, Penshaw Monument, which stands (well in front of the background) on a hill approximately 30 km from the Physics Department, is used (see Figure 5.21). The calibration is currently performed on the roof of the Physics Department. Pre-calibration consists of the following steps:

- clean all optical components and windows,
- set up the units and measure the distance between them with a laser finder,
- verify that the light spot sits at the centre of the receiver's field of view,
- warm-up the LED for a few minutes to get a stable temperature (the LED is powered by a temperature-stabilised constant current generator) and
- select an appropriate exposure time (i.e. 18 ms) for the calibration aperture in order to give a signal at the high end of the CMOS range.

The calibration coefficient calculated for the distance and aperture (as shown in Table 5.3), is 219.23 ADUs (or 12.12 $\frac{ADU}{ms}$) with a standard deviation of 0.31%.

The DHLT operated under fixed distance and aperture. The above measured quantities and uncertainties can be used for the calculation of an expanded uncertainty of I_0 should one wish to perform calibration runs at other distances.

The linearity of the instrument has been verified by using calibrated neutral density filters with optical densities 0.04, 0.3, 0.8, 1 and 1.5 to provide known trans-

Figure 5.21: The view from the roof of the Physics building on a clear day. Penshaw monument is easily identified against the background.

mittance check points. Figure 5.22 shows how the measured transmittance compares with the theoretically calculated values.

Figure 5.22 shows the linear response of the receiver and gives us a first clue about the accuracy of the instrument. Ideally, the calibration process needs both more check points and longer calibration runs. Winter weather conditions, combined with the effort to keep the temperature variation of the CMOS camera to an acceptable range, did not allow the usage of a wider combination of ND filters. The standard deviation associated with the calibration coefficient calculation (i.e. 0.31%) will be used in a first attempt to calculate instrument's accuracy (see Section 5.7.3).

The LED can be programmed to operate under a wide range of currents (i.e. $35 - 100\%$). Figure 5.23 shows the linear response of the CMOS camera over a wide range of LED intensities.

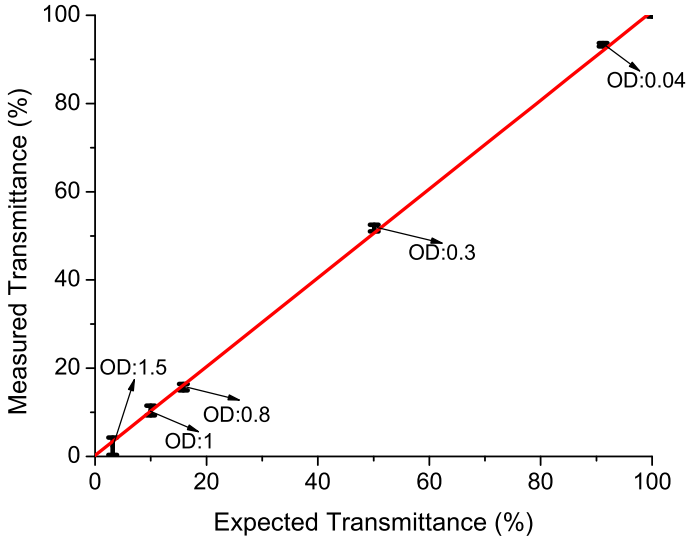

Figure 5.22: Measured transmittance of the DHLT versus neutral density filter-derived checkpoints, from a density of 0.04 to 1.5. The linear fit to the data reveals a small non-linearity correction.

Active Calibration

A particularly important and innovative feature of the DHLT is the active calibration system we have devised. Variation of the light source's brightness constitutes the major source of uncertainty in any transmissometer. Traditional transmissometers use a pre-calibrated light source, whose drift is calculated as a function of accumulated source usage and various other calibration factors, so that a passive correction may be applied to the raw transmissometer readings. In DHLT, the photodiode provides the means for continuous monitoring of the LED's brightness, which enables us to take into account any LED fluctuation in real time. Figure 5.24 shows the percentage deviation from the mean value of the observed LED intensity before and after the correction. It is worth noticing that even after the photodiode's voltage correction, a fluctuation of 1.5% is still evident in the registered signal (see Figure 5.24). This fluctuation originates from the photodiode's half-hour warm-up time and should be taken into account, especially in the calibration process.

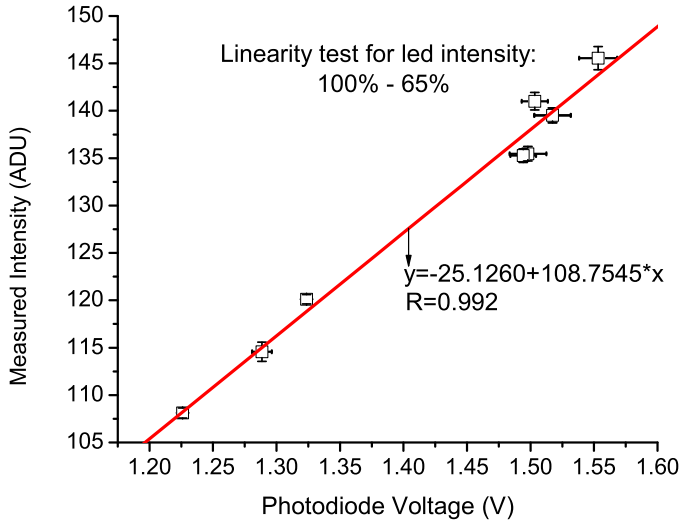

Figure 5.23: Measured LED intensity versus applied LED voltage, showing the good linear response of the CMOS camera.

5.7 Durham's High Level Transmissometer Uncertainty Estimation

In this section, known sources of uncertainties that limit the performance of DHLT will be discussed. A mathematical method, used to quantify the effects of these sources, will be also presented.

5.7.1 Uncertainties Associated with the Receiver Unit

The light receiver is based around the monochrome uEye CMOS camera, manufactured by IDS (Imaging Development Systems). The camera is equipped with a light sensitive 1/3" sensor with rolling shutter and has a resolution of 640×480 (see also 5.3.2). The most prominent characteristic of the camera is its dynamic range of 62 dB. The *d*ynamic *r*ange (dr) of a CCD/CMOS image sensor is defined as the ratio of the camera's maximum pixel capacity over the fluctuation of the camera's read-out noise (i.e. $\mathrm{dr} = 20 \log \frac{\text{full well capacity}}{\text{RMS read-out noise}}$) (Martinez and Klotz, 1998). Thus, a dynamic range of 62 dB represents a ratio between the saturation pixel output signal and the read-out noise of 1258:1. The camera is equipped with an

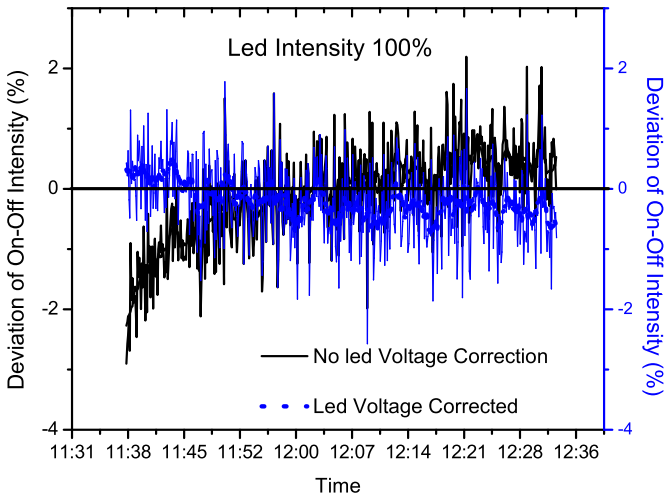

Figure 5.24: The percentage deviation of the LED intensity from its mean value before and after calibration using the photodiode. Our calibration system ensures that data are usable almost as soon as the transmissometer is switched on.

8-bit "on-chip" digitiser that allows for 256 levels of grey. That limits the camera resolution to an ideal transmittance level of $T = 1/256 = 0.0039$, which in turn puts a lower limit to the measured MOR (for a baseline of 44.5 m) at 24 m. For an industrial instrument, this resolution can be improved easily by using a sensor possessing higher level of both linear range and digitisation. It was decided therefore to base the theoretical estimation of the receiver's uncertainty to an alternative camera, namely the C-Cam Technologies BCi4-U-M-20 (C−Cam Technologies, 2006), which had been originally selected to equip the final version of DHLT (i.e. the development of the industrial version of the DHLT began one year latter, after securing a PIPSS grant at which time the ATIK-16 CCD camera possessing better characteristics than the BCi4-U-M-20 at a comparable price was selected; see Section 6.5.1). The BCi4-U-M-20 possesses a linear dynamic range of 68 dB (2750:1) -that can be extended to 100 dB (10^5:1) for limited exposures- which is coupled with a 12 bit converter offering 4096 levels of grey. Performing the same calculations for the aforementioned sensor and a 44.5m baseline gives:

$$T = \frac{1}{4096} = 0.00024 \qquad \text{and} \qquad \text{MOR=15.9m} \tag{5.11}$$

for transmittance and meteorological range resolutions respectively. The use of 14 and 16 bit digitisers, readily available on the market, can improve the above resolutions drastically.

A list of possible sources of uncertainties that will limit the performance of any selected camera is provided below:

1. Temporal Noise:
   - read-out noise,
   - thermal noise,
   - pixel photon shot noise, and
   - MOS Device Noise.
2. Fixed pattern (spatial) noise

A short discussion on the nature of the listed sources of error, along with the techniques used to control and eliminate them, will be the focus of the next subsections.

Temporal Noise.

Read-out Noise. To produce an image from the electrons deposited in each sensor's photodiode requires the charge of each photodiode to be measured and converted into a digital value. This read-out process is never perfect and an uncertainty is produced each time a digitised signal is sent to the computer. The origin of this noise is partly due to the CMOS amplifier (the amount of charge in each photodiode is too small to be measured without amplification) and noise at the output level. The main source of error on the CMOS camera is the pixel reset noise (kTC). This noise is produced each time a capacitance C is reset to a given voltage via a resistance R. In CMOS sensors, R is provided by the reset transistor and C is the total capacitance in the input node.

In order to reduce the reset noise, the CMOS KAC-9618 sensor applies correlated sampling, and contains a CMOS active pixel array consisting of 488 rows by 648 columns. This active region is surrounded by 8 columns and 8 rows of optically

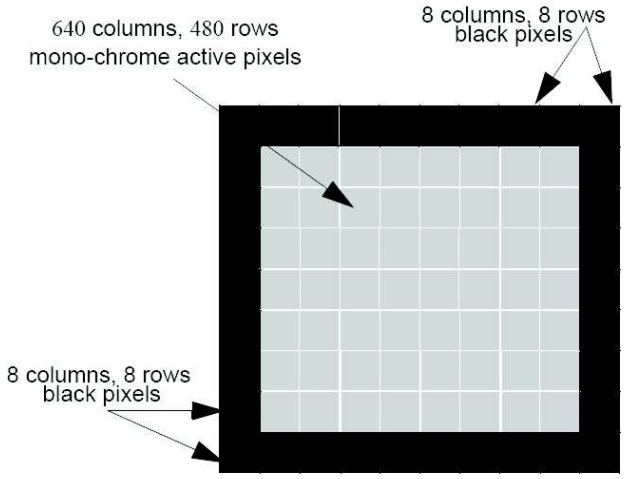

Figure 5.25: CMOS Active Pixel Sensors of the KAC-9618. Taken from sensor's manual (KODAK, 2007).

shielded (black) pixels as shown in Figure 5.25. At the beginning of a given integration time, the on-board timing and control circuit will reset every pixel in the array, one row at a time, as shown in Figure 5.25. Note that all pixels in the same row are simultaneously reset, but not all pixels in the array.

At the end of the integration time, the timing and control circuit will address each row and simultaneously transfer the integrated value of the pixel to a correlated double-sampling circuit and then to a shift register as shown in Figure 5.26. Once the correlated double-sampled data have been loaded into the shift register, the timing and control circuit will shift them out, one pixel at a time, starting with column "a". The pixel data are then fed into an analogue video amplifier, where a user programmed gain is applied and the analogue value of each pixel is digitised.

With this "CCD-like" correlated sampling, the RMS temporal noise of the pixel output averaged over all pixels in the array is reduced to:

$$\text{Read-out Noise} = 4 \text{ ADUs} \tag{5.12}$$

according to the sensor's manual. This value will be used in order to calculate an expanded uncertainty in transmittance, and, therefore, in MOR. The aforementioned value also implies that, in low visibility conditions, the largest noise component is

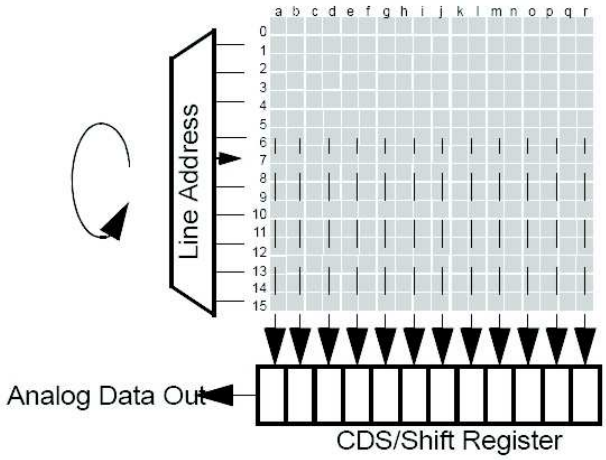

Figure 5.26: Sensor's addressing scheme. Excerpt from the KAC-9618 sensor manual (KODAK, 2007).

due to the reset transistor noise.

Dark Current. Dark noise originates from the accumulation of heat-generated electrons on the CMOS sensor. The dark current possesses the following characteristics, which facilitate the elimination of dark noise (Klotz, 1998):

- it is a reproducible phenomenon: in identical temperature and exposure time conditions, a given sensor accumulates the same amount of electrons with a narrow statistical dispersion,
- it is quasi-proportional to the integration time and
- It strongly depends on the CMOS sensor temperature. Its intensity increases by a factor of 2 if the sensor's temperature is increased by 6 °C.

The DHLT applies the standard "astronomical technique" for reducing this background noise: namely, two images are taken with the LED switched ON and OFF respectively, under the same temperature and exposure time conditions. By subtracting the latter image, which contains background and thermal charge, from the former, this noise is almost eliminated. However, one can never be totally clean of thermal electrons, as they obey a Poisson distribution. In our case, each pixel

generates 130 ADUs, at a temperature of 25 °C, and the representative exposure time is 18 ms; thus, the number of the thermal ADUs to remove is 2.34. However, its uncertainty cannot be removed:

$$\text{Dark Signal RMS} = \sqrt{2.34} = 1.53 \text{ ADUs} \tag{5.13}$$

Other Sources of Temporal Noise Other noise sources in the pixel include photon shot noise and the MOS device noise. The values for both these temporal sources of noise have been incorporated in the calculation given for the readout noise (see equation 5.12). Thus, the overall temporal noise can be given by adding in quadrature the readout noise with the dark current noise:

$$\text{Temporal Noise} = \sqrt{4^2 + 1.53^2} = 4.28 \text{ ADUs} = 0.11\% \tag{5.14}$$

Pixel Photon Shot Noise Pixel photon shot noise originates from the differences of the arrival time of photons to the sensor. The process of photon detection obeys Poisson statistics, which means that the Signal-to-Noise Ratio (SNR), corresponding to a detection of an average number of photons (N), is:

$$SNR = \sqrt{N} \tag{5.15}$$

That limits the SNR whenever signals close to saturation level are detected.

MOS Device Noise MOS Device Noise originates from both thermal and flicker ($1/f$) noise of the MOS transistors. Thermal noise is controlled by limiting the bandwidth of the amplifier. On the other hand, $1/f$ noise is highly suppressed via rapid double sampling.

Fixed Pattern (Spatial) Noise (FPN)

FPN refers to a non-temporal spatial noise generated by the non-ideal nature of the components. These might include mismatches in the pixels and variation in column amplifiers. The spatial noise can be divided into pixel-FPN and column-FPN. The former originates from variations in the in-pixel transistors whereas the latter comes from analogous dispersion in the column amplifiers (Turchetta et al., 2003). After

the analogue value of each pixel has been converted into digital data, the CMOS sensor corrects for bad pixels in order to suppress FPN noise.

In practice, the total spatial noise in the dark, at a temperature range between 20-80 °C, can be found by root-sum-square summation of the offset FPN (0.1%) and the Dark Signal Non-Uniformity (DSNU) RMS value from figure 5.27 (both provided in the sensor's manual).

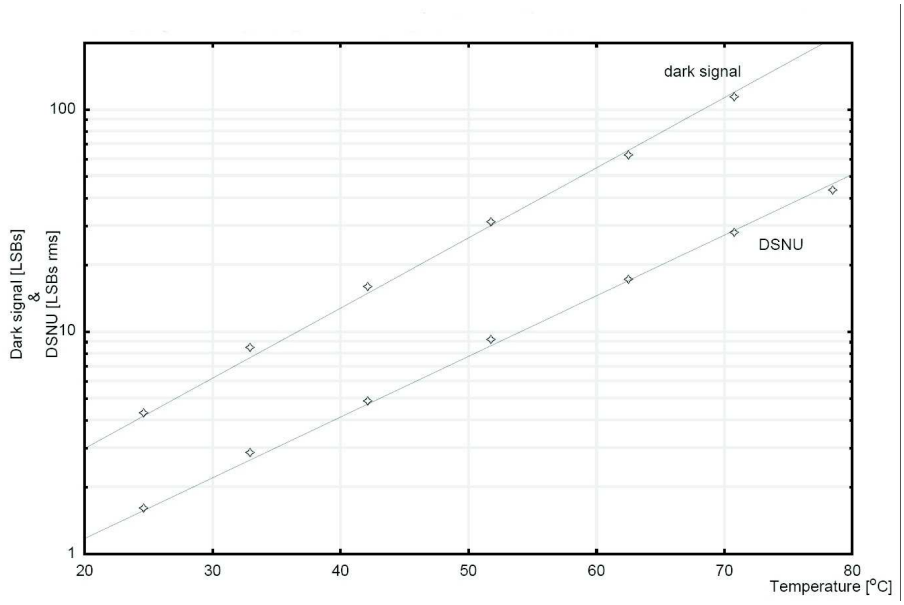

Figure 5.27: Dark signal and dark signal non-uniformity versus temperature. Taken from the sensor's manual (KODAK, 2007).

From the Figure 5.27 we can extract the RMS value of the DSNU is 1.74 ADUs for an exposure time of 33 ms. Since the typical exposure of Durham's transmissometer receiver is 18 ms, the spatial noise at a temperature of 25 °C is:

$$\text{Spatial Noise} = \sqrt{(FPN)^2 + (DSNU)^2} = \sqrt{0.1^2 + (1.74\frac{18}{33}\frac{100}{4096})^2} = 0.1\% \quad (5.16)$$

Overall Camera Noise

The overall noise from the camera's components can be calculated by root-sum-square summation of temporal and spatial noise:

$$\text{Camera Noise} = \sqrt{0.1^2 + 0.11^2} = 0.15\% \quad (5.17)$$

5.7.2 The Transmitter's Uncertainties

The DHLT light transmitter is based around a single super-bright LED (80 lm). It is powered by a steady-current and temperature-independent generator (see Section 5.3.1). As fluctuations of the LED's intensity could lead to direct misinterpretation of transmittance, and thus MOR, its intensity is constantly monitored by a photodiode. The photodiode's output voltage is used for the calibration coefficient correction in the read-out level (see Section 5.6.5). This correction, however, reduces but does not eliminate the fluctuations caused by the photodiode's half-hour warm-up time. Indeed, a variation of 1.5% (reduced from 3%) is evident in the corrected data (see Figure 5.24). During the DHLT calibration, sufficient warm-up time was allowed; this, combined with the new window material, reduced drastically the uncertainties previously calculated.

A purpose-built PCB, manufactured in Durham, is used to monitor the LED's properties. Specifically, the LED and electronic board temperatures, in addition to the LED's supplied voltage and current, are monitored (see Section 5.3.1). This provides a handy tool for quality control, as results associated with abnormal behaviour of the LED can be easily eliminated. The associated uncertainty of the data (after being corrected for the photodiode voltage and checked for abnormalities) is reflected in the standard deviation of the measured signal and the offset deviation of known transmittance points. In the next section, the uncertainties associated with the calibration process, together with a combined uncertainty estimation, will be provided.

5.7.3 Calibration and Combined Uncertainty Calculations

The transmissometer equation (5.6) implies that the precision of MOR is limited by the precision of the transmittance and baseline measurements. As seen in Table 5.3, the DHLT's baseline is estimated via a laser finder at a very high precision in comparison with the estimation of transmittance. Thus, only the uncertainty of transmittance needs to be calculated. In order to calculate an uncertainty associated with the transmittance measurement, one must combine the relative uncertainty of

the calibration coefficient with the uncertainties associated with both raw transmissometer readings and overall camera noise, according to the equation:

$$T = \frac{I_0}{I} \Rightarrow \frac{\sigma_T}{T} = \sqrt{(\frac{\sigma_I}{I})^2 + (\frac{\sigma_{I_0}}{I_0})^2 + (\text{Cam Noise})^2} \tag{5.18}$$

An additional term, namely $F_{source} = f(t)$, was used within the above equation to take into account the expected variability of the constant source as a function of time. Durham's transmissometer uses a pulsing LED, the output of which is constantly monitored and used for active calibration of data. Therefore, there is no need to pre-calibrate the LED.

The relative uncertainty associated with the calibration coefficient is 0.31%. A typical value of the relative uncertainty, associated with the raw transmissometer readings, is 0.70% whereas the camera's overall noise equals 0.15% (see 5.7.1). Substitution into equation 5.18 gives:

$$\frac{\sigma_T}{T} = 0.78\% \tag{5.19}$$

The above relative uncertainty might be used only as a baseline as equation 5.18 cannot quantify all the possible sources contributing to the transmissometer's uncertainty. A list of possible sources of error in transmissometer readings is provided below:

- on very windy days, instability of the transmitter's/receiver's mounting can cause erratic jumps of the light spot within the CMOS field of view,
- relative reduction of transmittance due to contamination,
- atmospheric conditions between transmitter and receiver not being representative of the local air mass and
- fluctuations in the transmitted light intensity due to optical turbulence.

A more realistic evaluation of the error associated with the transmittance measurement could be achieved by the comparison of the corrected transmissometer measurements (using the fit of Figure 5.22) with the theoretical expected values (see Figure 5.28).

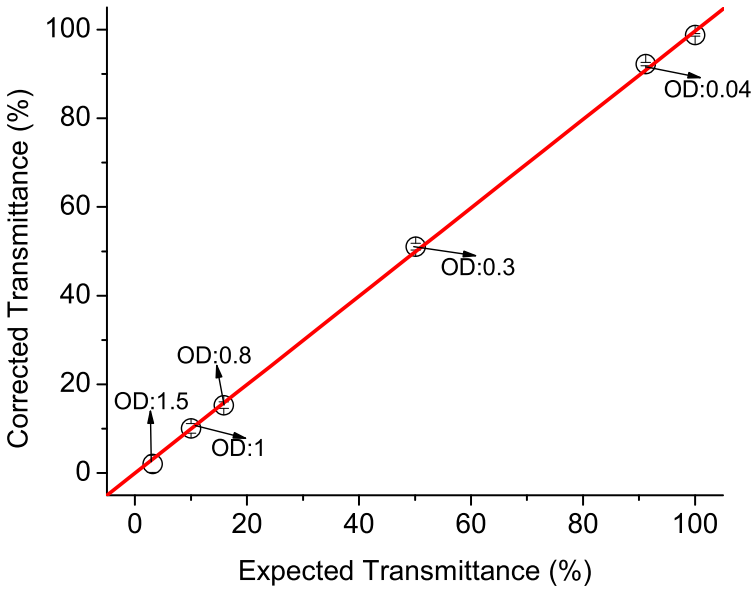

Figure 5.28: Corrected transmittance compared with theoretical expected values.

Graph 5.28 implies a typical deviation from the expected transmittance of 0.84%. Thus, for an estimation of the relative overall uncertainty associated with the transmittance measurement, one should quadratically add the combined uncertainty (provided in equation 5.19) to the typical deviation from the theoretically estimated transmittance:

$$\left(\frac{\sigma_T}{T}\right) = \sqrt{0.78^2 + 0.84^2} = 1.15\% \tag{5.20}$$

The error in the transmittance factor T is usually expressed as (van der Meulen, 1992):

$$\sigma_T = \alpha + \beta T \tag{5.21}$$

where:

α is the transmissometer's offset due to a systematic error related either with calibration or with the electronics, and β is the relative decrease of the measured transmittance due to the contamination effect.

The accepted values in the market today are $\alpha = 1\%$ and $\beta = 5\%$ (van der Meulen, 1992). Durham's Transmissometer is regularly cleaned and the receiver's window

can be equipped with a wiper similar to the one used in our Namibian model. Thus, we can safely set the constant $\beta = 0$ whereas $\alpha = 1.15\%$ is given in equation 5.20.

In order to translate this value into relative error of MOR, one must differentiate the transmissometer equation (van der Meulen, 1992):

$$MOR = \frac{Rln(0.05)}{ln(\frac{I}{I_0} = T)} \Rightarrow \frac{\sigma_{MOR}}{MOR} = \frac{1}{ln(T)} \frac{\sigma_T}{T} \tag{5.22}$$

From the above equation is obvious that MOR is limited by both the resolution of the transmittance measurement and transmissometer's baseline (R). Figure 5.29 shows the percentage variation of MOR as a function of the transmittance factor. The exponential increase of the relative uncertainty associated with the MOR measurement sets the limits on both sides of the MOR range.

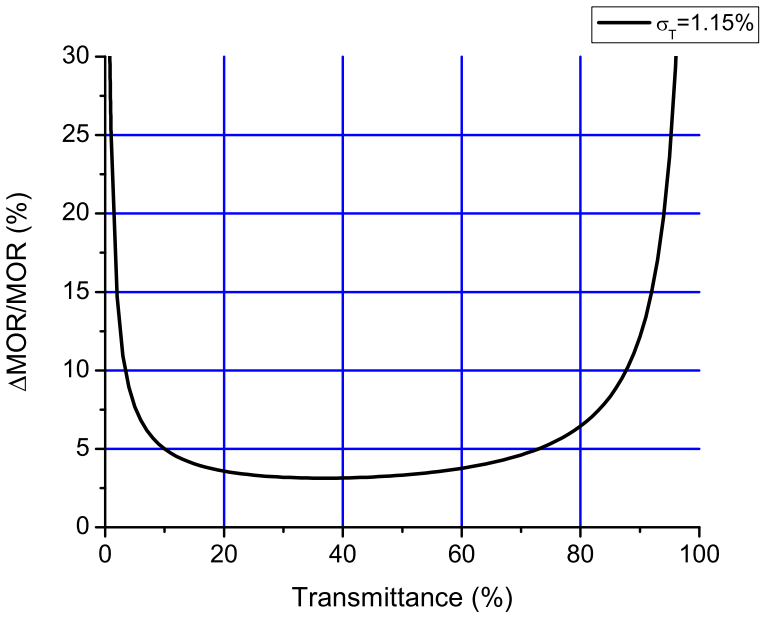

Figure 5.29: Percentage error of measured MOR as a function of 1.15% error in transmittance.

The baseline of the transmissometer is currently limited to 44.5 m by the dimension of the roof of the Physics Department where it is currently installed. As the range of MOR measurements is also limited by the transmissometer's baseline (see Equation 5.6), the operational range of the DHLT has been calculated as in Equation 5.22 for three baselines, by the adoption of camera with 12-bit resolution

and 72 dB dynamic range. In addition to the 44.5 m baseline currently in use, the transmissometer's operational range calculations (based on a 1.15% relative transmittance error) have also included baselines of 12 and 75 m, the most commonly used in aviation industry today. Specifically, in Figures 5.30, 5.32 and 5.31, the operational range of the transmissometer has been calculated for a baseline of 12 m, 44.5 m and 75 m respectively, providing that an error of 5%, 10%, 15% and 20% was accepted.

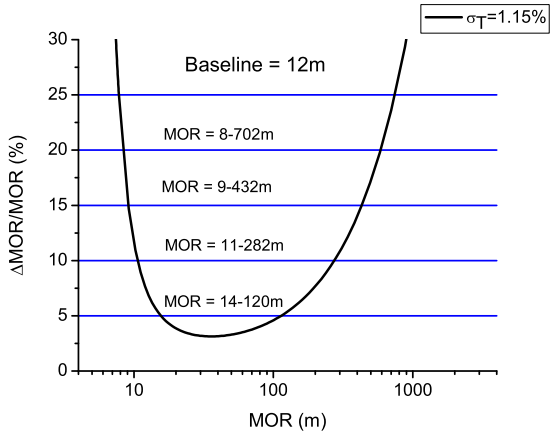

Figure 5.30: Relative error in the determination of MOR as a function of MOR for a baseline of 12 m.

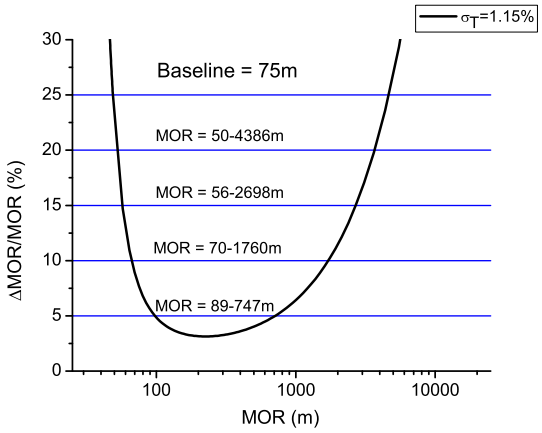

Figure 5.31: Relative error in the determination of MOR as a function of MOR for a baseline of 75 m.

The MOR range of the DHLT within which the accuracy is better than 20% is also provided in Table 5.4 for the sake of convenience.

Table 5.4: Durham's High Level Transmissometer Performance.

Baseline (m)	Operational Range (m)	Accuracy
12.0	8 – 702	Better
44.5	29 – 2603	than
75.0	49 – 4386	20%

Thus, the DHLT's operational range varies, depending on the selected baseline, from 7.8 m to 4.4 km with accuracy better than 20% over the whole field range.

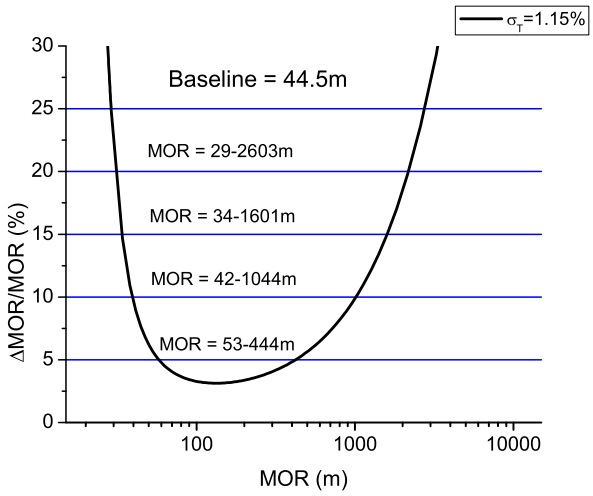

Figure 5.32: Relative error in the determination of MOR as a function of MOR for a baseline of 44.5 m.

Table 5.5: Visibility Sensor Manufacturer Specification. Taken from (Crosby, 2003)

Manufacturer	Sensor	Operational Range	Accuracy
Aanderaa Instruments A/S	Model 3340	20 m – 3 km	< 20%
	Model 6000	20 ft – 10 miles	±10%
Belfort Insrtument	Model 6100	20 ft – 10 miles	±10%
	Model 6230	17 ft – 30 miles	±10%
Biral, LTD	Model VF-500	3 m – 16 km	±5%
EnviroTech Sensors	Model SVS1	20 m – 16 km	±10%
Optical Scientific, Inc	Model OWI-130	1 m – 3 km	±20%
Qualimetrics	Model 6364-E	10 m – 32 km	±10%
Vaisala,	Model	10 m – 10 km	±10%
Inc	PWD21	10 km – 20 km	±15%

The above stated accuracy can be improved by:

- the use of a wider linear dynamic range. If the full 100 dB range of the camera (under limited exposure) is to be used, a 14-bit digitiser would be necessary,

- the improvement of the calibration process, with the use of ND filters that have been recently calibrated to a high degree of accuracy, and
- the temperature stabilisation of the transmitter/receiver units.

The DHLT's calculated uncertainty of 20% is in good agreement with today's market expectations for the similarly priced forward scatter sensors (see Table 5.5). However, it should be noted that the present work is an effort to evaluate the potentials of a prototype under constant revision and testing. Therefore, the claimed uncertainties should be treated as a guideline. Any firm claim on a visibility sensor's accuracy must be backed up with hundreds of hours worth of data under various weather conditions, and, most importantly, must be checked against a reference visibility sensor.

5.7.4 Read-out Program and Data Quality Control

As discussed in Section 5.4.2, the transmissometer data is directed to ASCII files. These files are immediately available to the user. The output update rate is 7 seconds and can be reduced by 2-3 sec if required. That provides, to the experienced user, a handy tool for sorting out problems very quickly.

For the proper analysis of the data the Root script ReadTranstest.C must be invoked. This program reads the data-file, makes the necessary calculations and plots the results. Root is not installed into the transmissometer's computer due to space limitations. However, the transmissometer's computer can be operated remotely since it is connected to the local network. That allows for quick access to the data.

The read-out program initially employed on the DHLT was very similar to the one used in the Namibian transmissometer. Figure 5.33 shows a typical plot from the Root script. In this example, the transmittance factor has been plotted against run number for the calibration run obtained using the filter with optical density 0.04. The measured transmittance is very close to the expected value of 0.91. However, Figure 5.33 also reveals that time data are difficult to handle within Root.

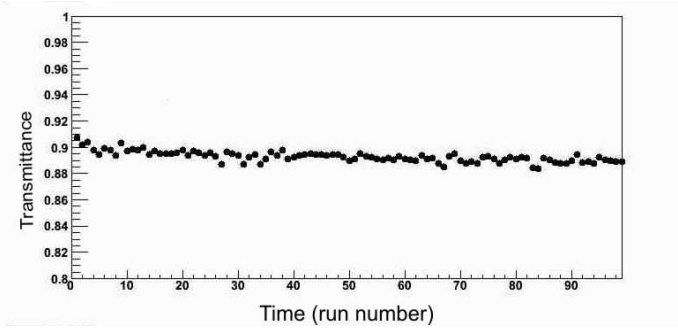

Figure 5.33: Transmittance measured during the calibration run using an ND filter (OD=0.04). The DHLT frequency is 0.14 Hz

In order to both improve the usage of time and to facilitate quality control of the data, a new read-out program was written. The transmissometer's data, including raw transmissometer readings and monitored quantities, are now plotted against time within the same sheet. A typical output screen is presented in Figure 5.34. Closer inspection reveals a correlation between the sudden drop of transmissometer ADU counts with the re-location of the Y-coordinate of the brightest camera spot (i.e. LED image). The first and second image in the first row represent the raw transmissometer signal as a function of time using methods A and B for background elimination respectively. The first image in the second row shows the variation of the Y-coordinate of the brightest pixel as a function of time. In this example, a gust of wind is probably responsible for the vertical oscillation that resulted in this drop in digital counts. Therefore, the circled data should not be taken into account for transmittance/MOR calculations.

5.7.5 "Teething" Problems and Preliminary Results

The DHLT has been operational between January 2006 and September 2007. At the beginning of its operation some "teething problems" were addressed. Specifically, in the original design the camera was located in the same cabinet as the Single Board Computer (SBC), power supplies and other supporting electronics, as shown in Figure 5.7. That led to an unacceptable variation in camera's temperature.

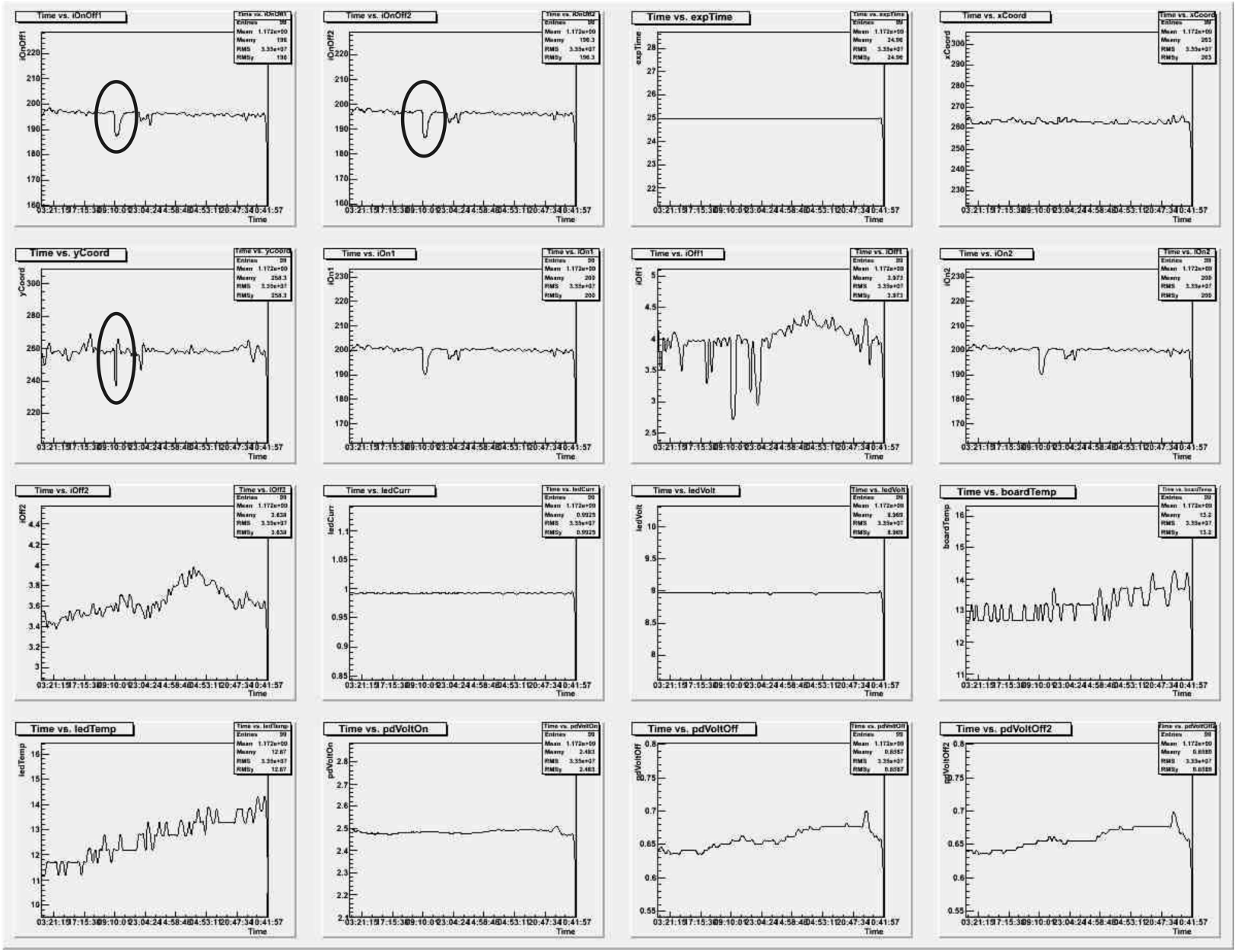

Figure 5.34: Part of the new read-out program's output. See text for discussion.

Moreover, during the hottest summer days, the temperature of the CMOS sensor reached its maximum limit of 50°C. This problem was firstly tackled by mounting a big heat-sink at the receiver's window (see Figure 5.8). Although that helped to stabilise the camera's temperature its value remained at unacceptable levels so the camera was isolated in a separate cabinet (see Figure 5.9).

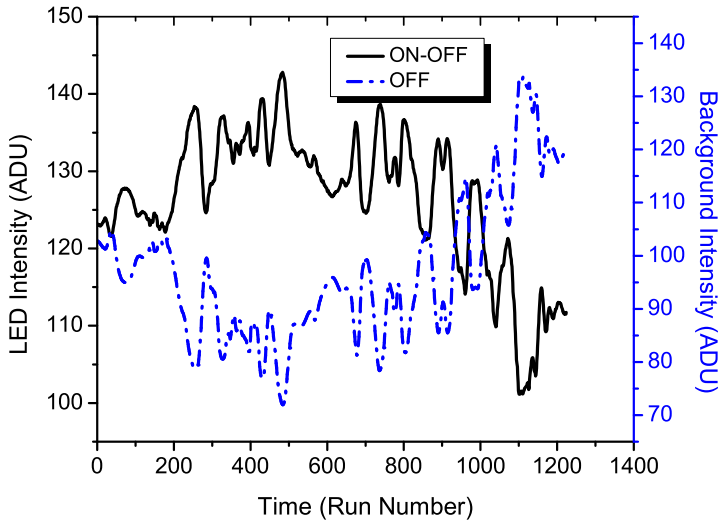

Figure 5.35: The anti-correlation between LED (ON-OFF) and background (OFF) signals.

Another problem was the alarming anti-correlation that was sometimes found between the receiver's measured LED and background intensities (see Figure 5.35). After exhaustive testing of the equipment it became clear that a bug in the software was responsible for this behaviour. Namely, in order to maximise the camera's dynamical range, a loop over optimised exposure-times is initiated until the value maximum intensity is between $170 - 230$ ADU (as discussed in Section 5.4.1). This value had been calculated as the mean of the brightest 5×5 cluster of pixels. It became clear that whenever this mean intensity settled close to the upper limit of 230 ADU, the brightest pixel had already saturated (i.e. its intensity exceeded 255 ADU) and that in turn led to the observed anti-correlation between the LED's and background's measured intensities. This problem was rectified by using only the brightest pixel for the exposure-time loop and the cluster of 5×5 for the calculations

of the mean LED intensity, removing the problems as Figures 5.36 and 5.37 testify.

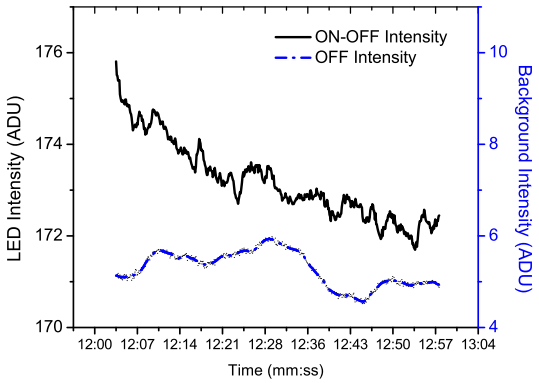

Figure 5.36: LED and background intensities plotted against time.

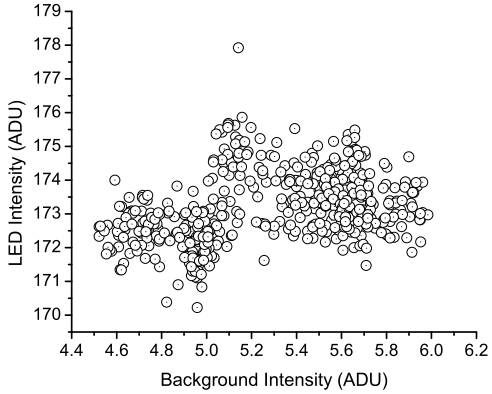

Figure 5.37: LED intensity plotted against the background Intensity.

Moreover, under very bright conditions the background intensity can be as high as $\frac{1}{2}$ of the signal, thereby limiting the dynamical range of the CMOS sensor (see Figure 5.35). That triggered the manufacture of the black shield around the receiver's window (see 5.6.1). This, combined with the use of a much smaller aperture and a camera equipped with a 105mm focal length lens (as opposed to the 16mm lens used originally) drastically lowered the background intensity level as shown in Figures 5.36 and 5.37.

After addressing these "teething problems", the instrument was tested under different weather conditions. Figures 5.38 and 5.39 show typical values of the visibility over day and night respectively.

5.7.6 Conclusions and Future Directions

The Durham γ-ray group has manufactured working day-light transmissometer prototype, based on a CMOS camera, at a construction cost of £1 k. Prior art aviation transmissometers utilise photodiodes as photo sensors requiring a very accurate alignment between transmitter and receiver units (see also Section 6.1). Thus, they are mounted on rigid bases at a maximum height of 2.5 metres above the ground to allow for good mechanical stability (e.g. Telvent, 2008). According to the RVR

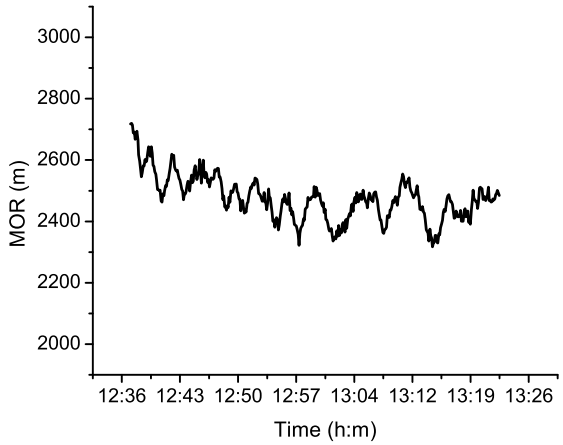

Figure 5.38: Day-time visibility measured with the Durham transmissometer

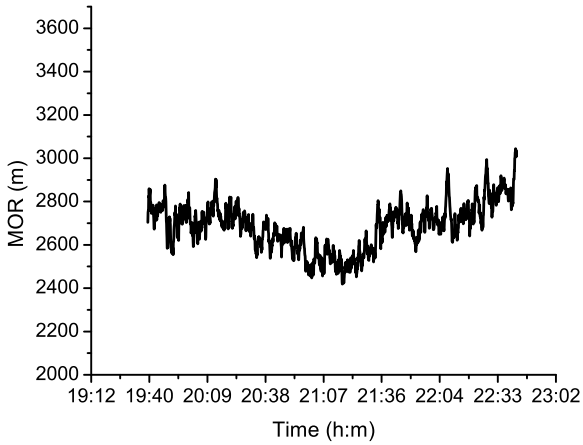

Figure 5.39: Night-time visibility measured with the Durham transmissometer.

definition visibility sensors should be mounted at the height of the pilot of an aircraft on the centre line of the runway (see Section 5.5.1). For larger aircraft, this point is 5 metres above the ground. As the alignment of our transmissometer is not so critical due to its wide field of view, stability is much less of a problem making a 5 m height easily attainable, and this could provide a clear advantage over existing products.

The DHLT performance has been established. Specifically,the DHLT resolution in transmittance is 1.5% leading to an 20% uncertainty in the MOR determination within the DHLT operational range as dictated by the selected baseline 5.7.3. Although this is an acceptable value for similarly priced forward scatter visibility sensors (see Table 5.5), the best attainable resolution of today's cutting-edge transmissometers is 0.005% yielding an accuracy of 1% over the whole MOR range (e.g. Telvent, 2008). Thus, a drastic improvement on the DHLT resolution is needed in order to reach the level of the required accuracy in the transmittance measurement. The thorough estimation of the DHLT's combined uncertainty suggest that the following changes can be made in order to optimise the DHLT's resolution:

- use a CCD sensor possessing much higher dynamic range and lower noise than the uEye CMOS;
- thermally stabilise both the LED and the light detector;

- use more accurate neutral density filters for calibrating the DHLT;
- optimise the measurement algorithms for maximum signal to noise under a broad range of visibilities.

The suggested changes are expected to increase the DHLT's construction cost. The overall DHLT cost, however, will be minimal in comparison to the price of a typical aviation transmissometer of £ 50 k. In addition, the cost of the suggested hardware and software changes can be counterbalanced by the use of simple microprocessor-based technology with an embedded control program rather than a complete PC to control the system.

Regional Technology Centre (RTC) North Ltd. were commissioned to undertake research to assess the potential market for the novel DHLT. It was not until a matter of days before the end of the grant period that we gained some strong interest from Aeronautical and General Instruments Ltd. (AGI) in Dorset, which came about via the market research. The author demonstrated the transmissometer to them, and they performed a technical assessment with positive results. AGI are particularly interested in the airport applications, and see the Durham instrument as a potential replacement for the transmissometer which they manufacture currently and is coming to the end of its useful design life. As a result, AGI and Durham University drew up a license agreement to pursue future development of the instrument. The work has already started as part of a technology transfer between Durham University and AGI and is the subject of the following chapter.

Chapter 6

The long road from γ-ray site atmospheric monitoring to the aviation market

In this chapter we discuss the steps taken so far in order to transform the DHLT prototype (as described in Chapter 5) into an automatic Runway Visibility Range (RVR) sensor capable of meeting both the high standards set by the aviation authorities and being competitive within the demanding airport market. This work is being funded under the PPARC (now STFC) Industrial Programme Support Scheme (PIPSS).

6.1 Generic Design Considerations for Aviation Transmissometer

The principal transmissometer designs currently used in the aviation industry are shown in Fig. 6.1. The simplest transmissometer configuration is shown Fig. 6.1-I and consists of a light transmitter and receiver separated by a set baseline (b). The transmitter unit utilises a light source (i.e. tungsten-halogen [e.g. AGIVIS (AGI, 1990)], xenon flash lamp [e.g. Revolver transmissometer (Telvent, 2008), MITRAS transmissometer (Vaisala, 1995)] or a high intensity white LED [e.g. LT31 trans-

missometer (Vaisala, 2004), 5000-200 extended MOR transmissometer (MTECH, 2008)]). The light source is frequency modulated either mechanically via choppers or, more recently, electronically, to optimise the transmissometer's reliability (i.e. LT31). A lens is utilised to collimate the light beam to a divergence of a few milliradians, defined by the size of the light source or field stop used and the focal length of the lens. The light beam passes into the atmosphere through a transparent window of high transmissivity. The light is collected by the receiver and focused via a lens on to an aperture, having a size determined by the light beam's divergence angle, for the efficient removal of the off-axis scattered light. Finally, the surviving photons are directed to the detector, which usually consists of a photodiode fitted with a photopic response filter.

The alternative arrangement illustrated in Fig. 6.1-II has the benefit of containing both the light source and light detector, accompanied by the relevant electronics, in one unit, while a passive retro-reflector is located in the opposite unit, thereby doubling the transmissometer's operating baseline. The transmitted and reflected beams are discriminated within the active transmissometer unit via a beam splitter (see Fig. 6.1-II). A beam splitter can also be used in the double-ended transmitter unit to create a reference beam for controlling the light source output.

Although aviation transmissometers are conceptually simple instruments, the strict accuracy requirements (see Section 6.2) necessitate very fine optical alignment between the light transmitter and receiver components, making transmissometer construction challenging. The alignment should be preserved under strong winds, temperature fluctuations and climatic changes affecting the soil under the transmissometer's installation site. It is worth noting that the alignment preservation becomes crucial under severe weather conditions where RVR is expected to be low and, therefore, needs to be measured with the highest accuracy (Canton and Wetherell, 1995). Thus, conventional transmissometers should be mounted in concrete bases of exemplary rigidity. These mountings not only increase dramatically the transmissometer's installation cost but constitute a threat to aviation safety. These safety concerns are usually addressed by placing the transmissometers 120 m away from the runway centre line whose visual range needs to be determined (ICAO, 2005).

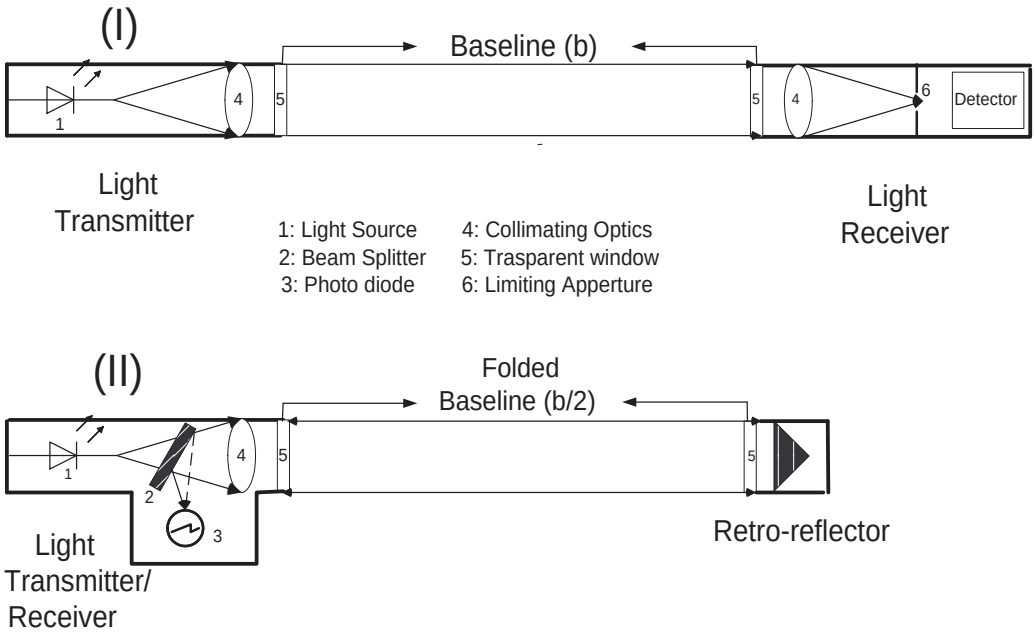

Figure 6.1: Schematic diagrams of the single (II) and double (I) ended transmissometer designs used in aviation industry today.

Thus, an additional source of error is introduced that would be more prominent in areas of localised weather (e.g. coastal or mountainous locations) where an accurate determination of RVR is most needed (Canton and Wetherell, 1995). The cost of a runway closure due to faulty RVR readings exceeds, in an average USA airport, $ 1 million per hour according to official Federal Aviation Administration (FAA) estimations (Canton and Wetherell, 1995).

The main deviation of Durham's solution to the prior-art transmissometer design is the replacement of the receiver's photodiode with a CCD sensor. The spatial information of the light spot is retrieved in each measurement cycle and the coordinates of the brightest pixel/centroid are determined. Thus, any small physical shift of the transmissometer's mounting would be translated in to a corresponding shift of the brightest pixel/centroid within the CCD sensor field of view. The disadvantage of using a CCD sensor as opposed to a photo-diode is the restricted modulation frequency of the light source (i.e. a few Hz). This can cause problems in rejecting the background noise especially in cases where the visibility fluctuates rapidly. This problem has been resolved by implementing an additional method of extracting

the background noise from the same CCD frame that is used for the atmospheric transparency calculation (i.e. see Section 5.4.1).

6.2 Requirement for the Durham Transmissometer

The work described in Chapter 5 was a 'proof-of-concept' for the daylight operation of Durham's patented technique. In order to translate this successful technique into a viable commercial product, the following marketing specification has to be met (Clark, 2008):

1. Reliable components that minimise the instrument's uncertainty budget are required. Specifically, the daylight prototype resolution in transmittance of 1.5% should be minimised to a value approaching 0.005% in accordance with the ICAO recommendations (ICAO, 2005) (see Section 5.7).

2. The selected photo detector should possess a linear photopic response in order to provide a ±1% accuracy for MOR. In order to achieve the required accuracy an automatic window contamination compensation system must be included (see Chapter 7).

3. The lifetime of the selected light source must exceed 50,000 hours and the MTBF of the selected photo-detector must be greater than 20,000 hours.

4. The external equipment should remain operational within a temperature range of −40 to 60°C, humidity up to 100% and wind speeds up to 60 m/s,

5. The relevant environmental requirements for the internal system are: temperature between 10 and 35°C, relative humidity up to 60%.

6. The frequency of the transmissometer should be optimised at 1 Hz.

7. The transmissometer should possess a quick alignment mechanism. The alignment time should be less than 10 min.

8. The transmissometer's software must be modified according to AGI specifications and tested for safety by the Safety Regulatory Group before embedding into a microprocessor system for commercial manufacture.

9. The production cost of the transmissometer should not exceed £8000.

10. An innovative solution for automatic calibration without the need of user intervention would be a desirable feature if achievable within the cost target of £8000.

It has been decided that AGI, being an expert in transmissometer manufacture, would be responsible for construction of the transmissometer's housing in accordance with the marketing requirement specification (i.e. items 4 and 5). In terms of software, Durham would be responsible for re-writing the software in Visual Basic under Windows, as opposed to the C^{++} and Root software used in the daylight prototype, in order to assist AGI in complying with the Safety Regulatory Group requirements (i.e. item 8).

Therefore, the subject of the following sections is the work undertaken between October 2007 and May 2009, on both software and hardware, in an effort to meet the requirements set by this challenging list.

6.3 Action Plan

Careful planning of the work needed to fulfil the set requirements could be the most decisive step towards its success. The author, being fully responsible for this project, constructed the following action plan. This will dictate the presentation of the content of this and the following chapter.

1. Select the transmissometer's light detector and establish its theoretical maximum resolution in transmittance (see Sections 6.5.1 and 6.6.1).
   The first consideration should be meeting the accuracy requirement in the transmittance measurement throughout the assessed RVR range of 50 to 2000m. The minimum transmittance that can be measured is limited by the dynamic range of the selected light detector (see Section 5.7.1). Thus, the first priority

should be the acquisition of a CCD detector offering a theoretical resolution in transmittance in accordance with the ICAO (i.e. 0.005% (ICAO, 2005)). In addition, the selected camera should operate within the environmental limits set for the transmissometer's internal systems (see item 5 of Section 6.2).

2. Evaluate the transmissometer's optimum baseline based on the calculated transmittance resolution (see Section 6.6.2).
   The optimum baseline, needed to calculate the transmissometer's performance in MOR/RVR, depends on the light detector resolution. Thus, the analysis for selecting the transmissometer's optimum baseline should directly follow the calculation of the minimum transmittance that can be measured by the instrument.

3. Alter the software of the old transmissometer prototype (see Section 6.7.1) in order to:

   - meet the single baseline specification (Modulation of both CCD exposure time and the LED's driving current as presented in Section 6.7);
   - permit online analysis of the data in compliance with aviation industry standards. (Migration from C^{++} and Root to the aviation industry accepted Visual Basic standard offering online data analysis).

4. Evaluate the performance of the transmissometer prior to constructing the new transmitter unit (see Section 6.8).
   Test the new CCD detector together with the accompanying software in conjunction with the old transmitter. The result will highlight the required level of accuracy for the new transmitter unit. It is worth noticing that the design of transmitter unit, although more complicated in comparison with the design of the receiver unit, is based on the prior art and therefore the accuracy can be estimated more easily.

5. Construction and optimisation of the new transmitter unit (see Section 6.9.2).
   The stability of the light source will be ensured via the implementation of a light output monitor feedback loop that utilises a sensitive RGB photodiode.

The light transmitter will be equipped with a Peltier device that will be modulated via a temperature feedback loop to drive the light source at a steady temperature (see Section 6.9.3).

6. Test the new transmissometer and resolve any instabilities in order to meet the long term stability requirements (see third requirement of Section 6.2) prior to the field test (see Section 6.12.2).

7. Finally, Chapter 7 will be dedicated to the ongoing project work:

   - Durham's novel window monitoring unit.
   - A novel idea for the automatic calibration of the new transmissometer.
   - Photopic response calibration.

6.4 Trasnmissometer Configuration Under Testing

The transmissometer was constantly under revision and numerous hardware and software solutions had been tested until reaching its final optimised stage. For the sake of clarity, therefore, a table relating the instrument's configuration to the results obtained throughout the project is provided in Table 6.1.

Description	**Software**	**Hardware Receiver**	**Hardware Transmitter**	**Tests**
Old transmitter-new receiver **ATMX-I**	Brightest-pixel Centroid (small aperture)	ATIK-16 135 mm lens	DHLT transmitter (see Section 5.3.1)	Sections 6.6 6.8
Telescope Based, Centroid Algorithm **ATMX-II**	Centroid (small aperture)	**In Lab**: ATIK-16 135 mm lens **Outside**: ATIK-16 Sky-Watcher Manfrotto	Sky-Watcher and Manfrotto PCB control	Section 6.10
Telescope Based, Threshold Algorithm **ATMX-III**	Background based threshold (large aperture)	**In Lab**: ATIK-16 135 mm lens **Outside**: ATIK-16 Sky-Watcher Manfrotto	Sky-Watcher and Manfrotto DAQ/PC control Light output control	Sections 6.11 6.12
Telescope Based, Final **ATMX-IV**	Background based threshold (large aperture)	**In Lab**: ATIK-16 135 mm lens **Outside**: ATIK-16 Sky-Watcher Manfrotto	Sky-Watcher and Manfrotto DAQ/PC control Light output control LED temperature control	Section 6.13

Table 6.1: Configuration of the Durham's Aviation Transmissometer (ATMX)under Testing. It was necessary to use a 135 mm lens in the laboratory to avoid saturating the CCD since the transmitter and receiver were necessarily close together.

6.5 Receiver

6.5.1 ATIK-16 CCD camera

The Achilles heel of the old DHLT working prototype, which limited its accuracy to 20%, was the use of a CMOS camera with a modest dynamic range coupled with an 8-bit digitiser. That limited the camera's resolution to a theoretical transmittance level of T= 0.0039 (as discussed in Section 5.7.1). In addition, the camera's dynamic range (i.e. 62 dB or 1258:1) could never have been fully explored, as the ADC offered 256:1 resolution at best. Furthermore, the old design did not allow for camera cooling, making dark current a dominant source of noise during periods of very low visibility (requiring measurements to have unusually long exposure times) and high temperature, thereby limiting the camera's dynamic range.

Following thorough market research, the ATIK-16 CCD camera (ATIK Instruments, 2007) was selected over the original 8-bit uEye (see Section 5.3.2, Fig. 5.9) and the later 12-bit BCi4-U-M-20 CMOS cameras. The ATIK-16 camera has an estimated well depth of 55000 electrons per pixel and a read out noise of 10 electrons per pixel (RMS). That gives a dynamic range of 5500:1, which can be fully explored with the aid of the 16-bit converter offering 65536 levels of grey. In addition, the ATIK-16 CCD camera is equipped with a Peltier thermo-electric cooling device capable of maintaining the CCD at 25°C below ambient temperature. As a result, the thermal noise of the new camera is less than 0.1 electron/sec and thus negligible in comparison with the typical (i.e. at 25°C) thermal noise of 130 electrons/sec of the old CMOS camera. However, the temperature of both the CCD camera and the photodiode array responsible for the LED output monitoring should be constantly monitored as the spectral response of both instruments is temperature dependent.

The spectral sensitivity characteristics of the CCD image sensor (ICX429) must eventually be altered in order to closely approximate the CIE photopic luminosity function (see Section 7.5).

The CCD camera was initially equipped with a 135 mm lens for immediate testing. It was later decided to replace the lens with the Sky-Travel telescope (Sky-Watcher, 2007) with a focal length of 400 mm, which offers a better magnification of

Figure 6.2: The new ATIK-16 CCD camera equipped with a 135 mm lens.

Figure 6.3: The ATIK camera mounted in the Sky-Travel telescope.

the LED image (see Section 6.9.1) and is more economical (i.e. £ 99) in comparison with typical camera lenses.

The receiver unit (i.e. the CCD camera equipped with either lens or telescope) is mounted on a photographic tripod. In order to increase the stability of the receiver unit and minimise its alignment time with the transmitter, the Manfrotto geared tripod head, presented in detail in Section 6.10, is used.

Finally, the ATIK-16 CCD sensor should possess a lifetime in excess of 20,000 h in accordance with AGI's requirements (see Section 6.2). It is believed that the lifetime of the CCD sensor will exceed the specification even though it is not common practice for the manufacturers of astronomical CCD sensors to provide official compliance to such a requirement. The degradation of the CCD's performance over long time intervals can be taken into account by the frequent re-calibration between of instrument (see Section 7.4.1).

6.6 Baseline Considerations

In order to construct a competitive aviation transmissometer, one should estimate the optimum baseline length that, coupled with the instrument's transmittance resolution, will dictate the accuracy of the MOR/RVR measurements over the whole range of their assessment. Specifically, one could express the baseline length (R) in

terms of the calculated MOR or RVR (V) and transmissometer's measured transmittance (T_R) as follows (see Equations 5.2 and 5.9):

$$\frac{MOR}{R} \approx \frac{-3}{\ln T_R} \tag{6.1}$$

and

$$R = \frac{V \ln T_R}{2 \ln V + \ln E_T - \ln I} \tag{6.2}$$

From equations 6.1 and 6.2 it is clear that both MOR and RVR measurements depend on the transmissometer's baseline and do not possess a linear relationship with the measured transmittance T_R. That causes a trade-off between the transmissometer baseline and its resolution and dynamic range:

- too short a baseline would require very high resolution in transmittance for determining MOR/RVR with an acceptable accuracy,
- too large a baseline would limit the lower end of MOR/RVR measurement,
- finally, using longer baselines to measure a set range of MOR/RVR would dictate an increase in the transmissometer's dynamic range. In standard transmissometers, that can be achieved by either increasing transmitter's light intensity or by using dual baseline systems (ICAO, 2005). In our case, the linear response of the CCD detector allows the optimisation of the transmissometer's dynamic range by adapting the exposure time.

For the aviation industry, the useful range of MOR assessment is:

MOR: 10 - 2000 m

Therefore one needs to find the optimised baseline for which an acceptable value of accuracy (i.e. 1%) can be attainable within the whole MOR range (the relevant RVR range will be derived in Section 6.6.2). In this work we will try to find the baseline optimised for the transmissometer's resolution in accordance with suggestions and examples within the 'Manual of RVR Observing and Reporting Practices' approved by the *I*nternational *C*ivil *A*viation *O*rganisation (ICAO, 2005) . In order to achieve this, one has to estimate the minimum transmittance that can be detected by the CCD sensor.

6.6.1 Transmittance Resolution Estimation

The resolution of Durham's transmissometer is limited by the noise sources (i.e. read-out noise, photon shot noise, FPN and thermal noise) that have already been discussed in detail (see Section 5.7.1) and, most importantly, by the level of background (stray) light within the measured signal. The methodology for the estimation of a theoretical resolution in transmittance, for the ATMX-I transmissometer equipped with the ATIK-16 CCD, differs from the one presented in Section 5.7 in the following ways:

- the calculation has to be based on the receiver unit, since the baseline length will dictate the design of transmitter. Thus, one should calculate an approximate baseline length before committing the funds for purchasing expensive optical components,
- the new design allows for the constant and independent determination of the read-out and background noise, allowing for the elimination of the systematic sources of noise. One has to take into account, however, the photon noise relevant to both the read-out and background signals, and
- the dark-count noise has a non measurable effect on the signal and spatial noise, but can be eliminated by proper flat-fielding calibration.

The new software, for use with ATIK-16 camera, begins by setting the exposure time of the CCD sensor in order to produce an output signal of 50 kADUs. This signal is comprised of:

$$S_{ON} = S_{LED} + S_D + S_B + b_{ro} + b_{FPN} \tag{6.3}$$

where:
S_{LED} is the signal produced by the LED
S_D is the dark current signal
S_B is the signal induced by the background
b_{ro} is the bias so that the read out noise never drives the A/D input negative (McLean, 1997)

and b_{FPN} is the spatial (non-temporal) noise generated by variations in the pixel to pixel response on the incident light.

The combination of short baseline (dictated by the space limitations in the laboratory) and an ultra bright white LED leads to exposure times, for a signal of 50 kADUs, of the order of 7 ms. The Peltier cooling of the CCD sensor keeps the dark current below a maximum of 0.1 e^-/s. The dark current over the set exposure is:

$$S_D = \frac{0.1 \times 7 \times 10^{-3}}{g} \quad \frac{e^-}{s} \times s \times \frac{1}{e^-} \tag{6.4}$$

where g is the conversion factor:

$$g = \text{full well capacity/levels available} = 55000\ e^-/65536 = 0.84 \quad e^-$$

Thus, the exposure time used does not allow for an accumulation of dark current capable of producing a measurable variation in the detected signal. In addition, the non-uniformities introduced by variation in both quantum efficiency and illumination can be treated by taking flat frames. These consist of exposing the CCD camera to a uniform field of light for the same period as was used to acquire the signal. Under uniform illumination, the CCD reveals the pixel to pixel variations in sensitivity, enabling their correction. Flat frames require suitable dark frames for the background subtraction. Thus, in addition to removing various efficiency inconsistencies, flat dark-subtracted frames will add a small photon-induced noise that needs to be evaluated. For this work, we will consider the photon-induced noise as negligible. Finally, as noted above, the exposure time used does not allow for a measurably large accumulation of dark current. In addition, the combination of both small aperture and minimal exposure time did not allow for a measurable background signal under different lighting conditions. For the sake of completeness, however, a 30 ADU background signal will be considered to account for possible restriction of the dynamic range during brighter conditions. Taking into account a 250 ADU bias of the CCD camera, equation 6.3 becomes:

$$S_{ON} = S_{LED} + 0 + 30 + 250 + 0 \tag{6.5}$$

The total noise in the ON image, measured in ADUs, is:

$$\sigma_{ON} = \frac{1}{g}\sqrt{\sigma_{LED}^2 + \sigma_B^2 + \sigma_{RO}^2} \tag{6.6}$$

where σ_{LED}, σ_B are the photon shot noise of the LED signal and background signal respectively and σ_{RO} is the read-out noise. All errors are expressed in units of electrons (e^-). Both LED and background signals obey Poisson statistics:

$$\sigma_{LED} = \sqrt{49720 \times 0.84} = 204.36 \text{ e}^- \quad \text{and} \quad \sigma_B = \sqrt{30 \times 0.84} = 5.02 \text{ e}^- \tag{6.7}$$

The camera's read out noise has been measured in the lab for the centroid pixel and for a 15×15 array of pixels, centred at the centroid pixel, as follows:

$$\begin{aligned} \text{Mean Intensity}_{1\times1} &= 270.5 \quad \text{with SD} = 11.3 \quad \text{and} \\ \text{Mean Intensity}_{15\times15} &= 251.5 \quad \text{with SD} = 0.74 \end{aligned}$$

where all measurements are expressed in ADUs.
The combined noise associated with the ON signal is (6.6, 6.7):

$$\sigma_{ON} = \frac{1}{0.84}\sqrt{204.36^2 + 5.02^2 + 11^2} = 243.71 \quad \text{ADUs} \tag{6.8}$$

In order to subtract the bias and the background noise from the signal an OFF frame is taken having exactly the same exposure as the ON frame, with the light source's shutter switched OFF. The intensity of the OFF signal is:

$$\mathrm{S_{OFF}} = \mathrm{S_D} + \mathrm{S_B} + \mathrm{b_{ro}} + \mathrm{b_{FPN}} = 30 + 250 + 0 = 280 \quad \text{ADUs} \tag{6.9}$$

The uncertainty with which this background signal can be calculated is:

$$\sigma_{OFF} = \frac{1}{g}\sqrt{\sigma_B^2 + \sigma_{RO}^2} = \frac{1}{0.84}\sqrt{5.02^2 + 11^2} = 12.09 \quad \text{ADUs} \tag{6.10}$$

By subtracting the background (OFF) frame from the ON frame one can extract the signal produced by the LED itself:

$$\begin{aligned} \mathrm{S_{ON-OFF}} &= (\mathrm{S_{LED}} + \mathrm{S_D} + \mathrm{S_B} + \mathrm{b_{ro}} + \mathrm{b_{FPN}}) - (\mathrm{S_D} + \mathrm{S_B} + \mathrm{b_{ro}} + \mathrm{b_{FPN}}) \\ &= \mathrm{S_{LED}} = 49.720 \quad \text{ADUs} \end{aligned} \tag{6.11}$$

The noise related to the LED signal, however, will be increased in comparison with the ON signal because the subtraction process involves taking into account a larger number of e^-:

$$\sigma_{LED} = \sqrt{\sigma_{ON}^2 + \sigma_{OFF}^2} = 244 \quad \text{ADUs} \tag{6.12}$$

The resolution (i.e. signal to noise ratio) of the CCD camera can be calculated at the set ON intensity of 50000 ADUs as below:

$$SNR_{ON-OFF} = \frac{49720}{244} = 203.77 \tag{6.13}$$

In order to optimise the CCD resolution one can use the common method of averaging several ON and OFF images (Berry and Burnell, 2005). The current aviation practice dictates that transmissometer readings should be averaged over one minute periods (ICAO, 2005). The updating frequency of Durham's transmissometer permits for 30 ON and 30 OFF frames in a minute. The noise of the averaged frames can be calculated from the following formula:

$$\bar{\sigma} = \frac{\sigma_{ON} + \sigma_{OFF}}{N} = 2.85 \quad \text{ADUs} \tag{6.14}$$

The signal to noise ratio for the averaged frames has now increased to 17445 giving an exemplary transmittance resolution of 0.0057%. This value is in good agreement with the minimum transmittance value of 0.005% required by the ICAO, and can be further improved by taking more ON than OFF frames.

One should not forget that the above estimated resolution was based on the CCD sensor alone, without considering errors caused by contamination of the transmitter/receiver optics, weather phenomena causing forward scattering towards the receiver etc. On the other hand, all calculations were performed under a pre-set exposure of ~ 7 ms that is adequate for a $50,000$ ADU signal to be produced in the CCD sensor during a clear day; the CCD sensor currently allows for a maximum 256 ms exposure, corresponding to very low visibility. Initial testing of the ATMX-I (i.e. old transmitter unit in combination with the new CCD sensor) proved that the old LED was able to produce a $50,000$ ADU signal even when the sensor was sitting behind a neutral density filter ($OD = 3$). Thus, even in situations where visibility is reduced by a factor of 10^3 in comparison with an "average clear" day, one will

be able to use the whole dynamic range of the camera. It is therefore possible for the powerful Durham technique, based on the excellent linearity of the CCD sensor over exposure time, to improve drastically the resolution in MOR/RVR measurements offered by today's transmissometers (ICAO, 2005). In order to both verify and quantify this improvement, we need to proceed in the manner of Section 5.7.3 following the completion of the transmitter unit.

6.6.2 Baseline Calculation vs MOR and RVR

In order to calculate the accuracy of the MOR (meteorological range) measurement for the ATMX-I transmissometer within the useful range $10 - 2000$ m, as a function of MOR itself, one has to use Equation 5.22. Equation 6.1 allows the MOR to be expressed in baseline multiples. Thus, by plotting the relative error in MOR (%) as a function of MOR itself, translated in baseline multiples, we can estimate the optimum baseline that gives a relative error of MOR of less than 1% within the whole range of the MOR range (see Fig. 6.4).

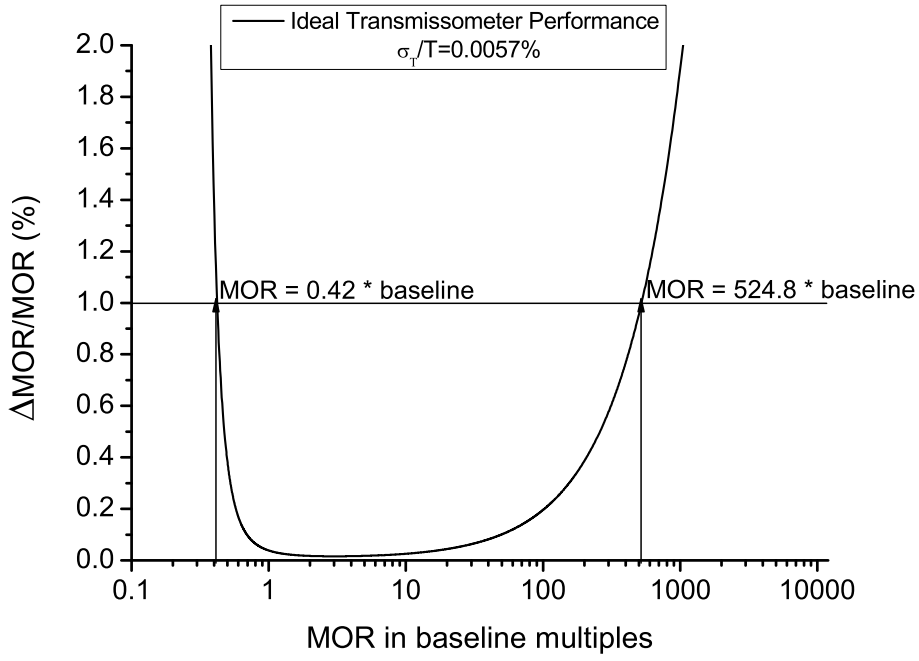

Figure 6.4: Relative MOR error due to the ATK-16 CCD sensor resolution in transmittance.

According to Figure 6.4, a single baseline of ~ 24 m will be adequate to cover the

full MOR range of $10 - 10000$ m. One has to take into account, however, that this calculation was based on optimal performance of the CCD sensor (as calculated in the previous section) providing an order of magnitude calculation for the baseline. That will enable us to set the optical requirements for the transmitter unit.

A similar baseline optimisation can be performed when the visual range needs to be expressed as Runway Visual Range (RVR). Before attempting to calculate the transmissometer's maximum operational baseline in terms of RVR, one needs to translate the MOR operating range (i.e. 10 - 2000 m) into an RVR range. The derivation of meteorological range (MOR) involves seeing dark objects during the day. The contrast of these objects with the background against which the viewing takes place is assumed to be fixed at 0.05. Thus, the visual range by day is assumed to be independent of the background luminance and viewing angle (ICAO, 2005). The RVR is a better way to report visibility as it can be accurately calculated for both daytime and nighttime conditions. It is defined by the distance over which a pilot (who flies just above the centre line of the runway) can identify runway markers or runway lights (as discussed in Section 5.5.1). For the same reason, this calculation is more involved than the MOR, as it takes into account the intensity of the runway lights (I) and the visual barrier of illumination (E_T) over which an "average - sighted" pilot could discriminate a small runway light. This relates to the background luminance against which the light is viewed and it is usually defined as $E_T = 10^{-4}$ lx and $E_T = 10^{-6}$ lx on a normal day and night respectively (see Table 5.2 and Fig. 5.15 of Section 5.5.1). In order to understand better the relationship between MOR and RVR, the ratio of RVR over MOR (i.e. $\frac{RVR}{MOR}$) is plotted against MOR by setting the runway lights at 10000 cd and discriminating between a day and a night runway-light based RVR calculation (i.e. $E_T = 10^{-4}$ lx and $E_T = 10^{-6}$ lx).

Figure 6.5 provides the means for translating MOR into RVR values. During the night, an extreme MOR value of 10 m corresponds to an RVR value of 50 m. During the day, MOR (Kosschmieder's law) would be greater than RVR (Allard's law) at the high end of the MOR range and, therefore, the reported RVR is by definition equal to MOR (see Section 5.5.1). Thus the aviation industry's useful range for the RVR assessment is:

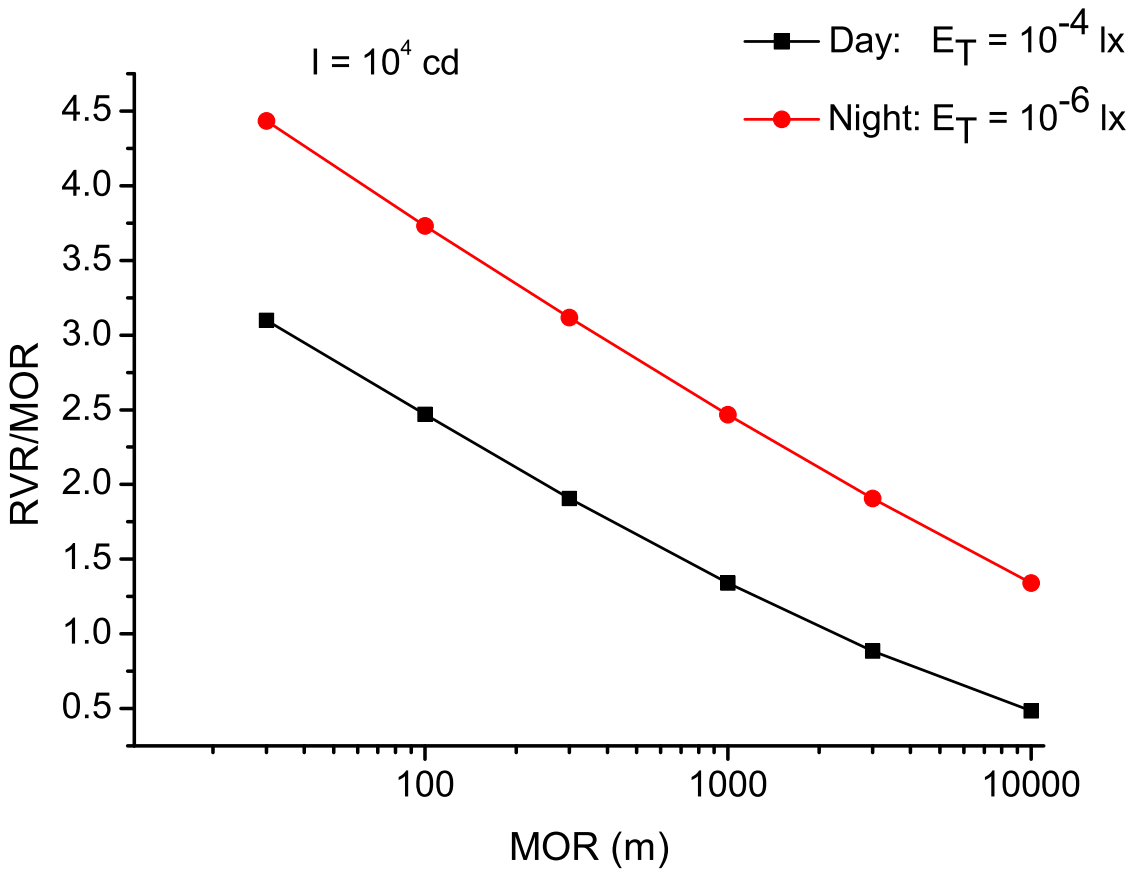

Figure 6.5: The connection between RVR and MOR. The values used for the intensity of the runway lights (I) and the visual barrier of illumination (E_T) for day and night conditions respectively are also shown in the graph. Based on ICAO requirements (ICAO, 2005).

RVR: 50 - 2000 m

Equation 6.2 can be used to relate the transmissometer's maximum baseline length (i.e. R_{max}) to the transmittance resolution (i.e. $t_{R_{max}}$):

$$R_{max} = \frac{V \ln t_{R_{max}}}{\ln E_T + 2 \ln V - \ln I} \tag{6.15}$$

where:

I is the intensity of the runway light

E_T is the illuminance threshold (i.e. the observer's sensitivity to the illumination intensity)

V is the visual range

and $t_{R_{max}}$ is the minimum transmittance that can be accessed by the transmissometer.

Equation 6.15 allows for the calculation of the maximum baseline length that should be used to assess the low RVR limit of 50 m using a transmissometer with 0.0057% resolution in transmittance. Thus, by fixing the luminous intensity at $I = 10000$ cd, and discriminating between diurnal and nocturnal conditions, by setting E_T to 10^{-4} lx and 10^{-6} lx respectively, it is possible to plot the maximum baseline needed for accessing the minimum RVR point of 50 m as a function of the transmittance resolution for the day and night cases as shown in Fig. 6.6.

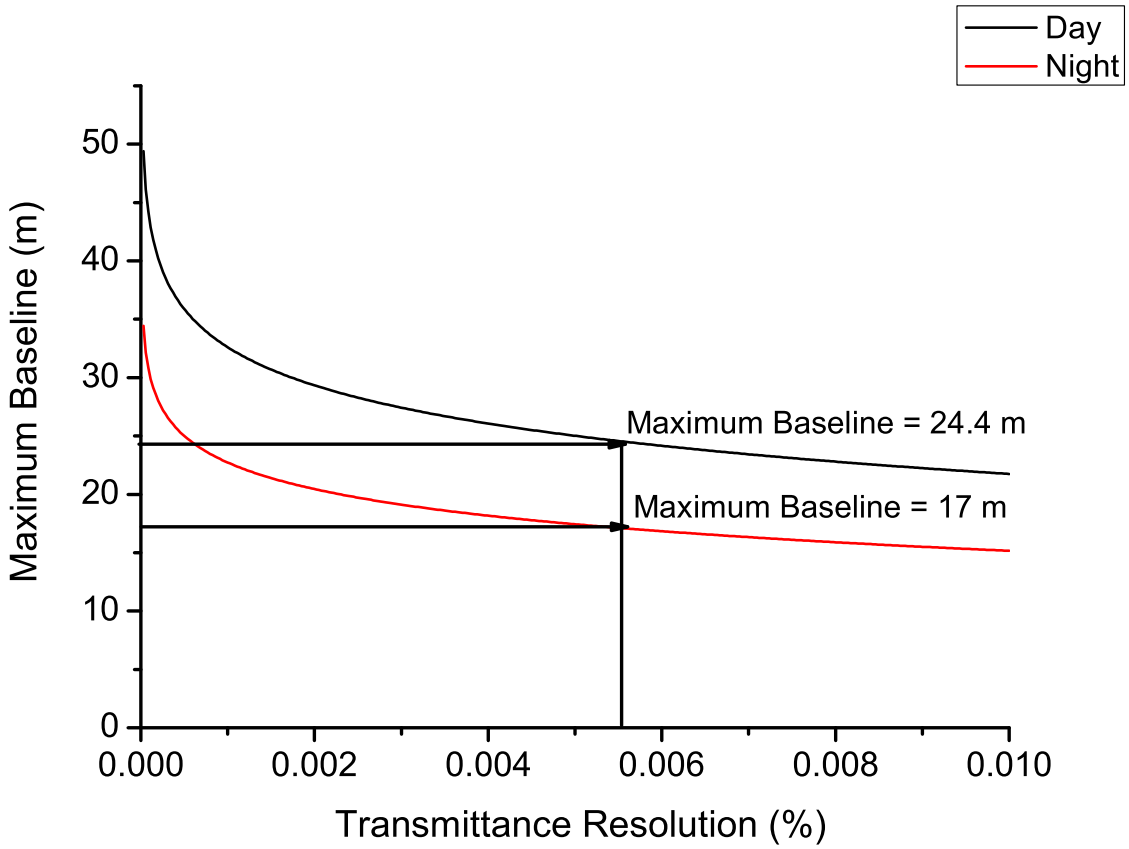

Figure 6.6: Maximum baseline of the ATMX-I as a function of the sensor's resolution in transmittance.

According to Figure 6.6 the baselines capable of accessing the whole RVR range, with an accuracy better than 1%, will be:

$$R_{day} = 24.4 \text{ m} \quad \text{and} \quad R_{night} = 17 \text{ m}$$

During the day time, baseline calculations based on either MOR or RVR are compatible, but the baseline length will be dictated by the night-time conditions.

6.7 Software Considerations

The DHLT camera was driven via a C^{++} program provided by the manufacturer that was altered in order to synchronise transmitter and receiver units and extract the beam's intensity. The analysis of the data was performed off-line with the aid of Root: the standard analysis software for high energy physics, but completely unknown to the world of industrial atmospheric physics. For the new transmissometer it was decided to re-write the software, initially using Visual Basic, in order to comply with the industry's accepted standards. In addition to the alterations dictated by the incorporation of the new parts (CCD camera, LED, photodiode etc), the ATMX-I's algorithm differs substantially from the old one (see Section 5.4.1). The old algorithm, used with minor alterations in both the DNT and DHL transmissometers, already described in Sections 3.4.2 and 5.4.1 respectively, was based on producing a signal between 2/3 and 1/3 of the camera's dynamic range by altering the exposure time whenever the signal dropped outside this region. The overall resolution in transmittance was dictated therefore by camera's:

1. dynamic range (mainly limited by its well depth, read-out noise and digitiser), and

2. resolution in exposure time.

In order to achieve the best possible accuracy in the transmittance measurement (see also Section 6.6.1), the signal-to-noise ratio should be optimised under different weather conditions. The light output of the LED source can be controlled by the forward current driving the LED. Indeed, the considerable increase of the power of LED outputs, witnessed in the $\sim$ 3 years since the completion of the Namibian transmissometer, has been mainly achieved by increasing the forward current (see Table 6.2). The disadvantage of using high-current driving LEDs is the increase of power consumption leading to a higher junction temperature (the ambient tem-

perature and system's thermal resistance being the same) (Pinter and Sarakinos, 2008). The higher junction temperature degrades both the LED's light output and life expectancy. The novelty of the new software, therefore, consists of controlling the driving current, in addition to the exposure time, in order to maximise both the signal-to-noise ratio and the LED's performance.

Preliminary tests of the ATMX-I, for a 20 m baseline, proved that in a clear atmosphere (visibility $\geq$ 30 km) only 35% of the maximum driving current is required to produce a 40 kADU signal (i.e. $\sim 2/3$ saturation level) at a 4 ms exposure. Hazy conditions were simulated by the use of different neutral filters with optical densities ranging from 0.1 to 3. It was shown that a near-optimum signal can be achieved even when the transmittance has been reduced to one hundredth of its original value.

The new software was evaluated under these initial tests and its logic is presented in Figure 6.7. It starts by trying to produce an optimum signal (i.e. 2/3 saturation level) with a 35% driving current. The excellent linearity of the CCD sensor over exposure time (see Figure 6.20) allows for the evaluation of the optimum exposure (i.e. time needed to produce optimum signal) based on the 1 ms exposure step. If the predicted exposure time lies above one half of the maximum exposure (i.e. $1/2 \times 240 = 120$ ms) then the driving current is switched to 100%. The signal is allowed to drop below the optimised region down to 5σ of the noise level only when both maximum exposure and driving current values have been reached.

6.7.1 The brightest-pixel based measuring algorithm problem

The ATMX-I CCD sensor's excellent resolution revealed a serious drawback of the technique employed in the DHLT instrument (see Section 5.4.1), which was based on the determination of the brightest pixel. According to this technique, the intensity measurement was based on extracting the counts of the pixels located on a suitable-sized square centred on the brightest pixel. The first results from the incorporation of the ATIK-16 camera with the brightest-pixel algorithm are shown in Figures 6.8 and 6.9.

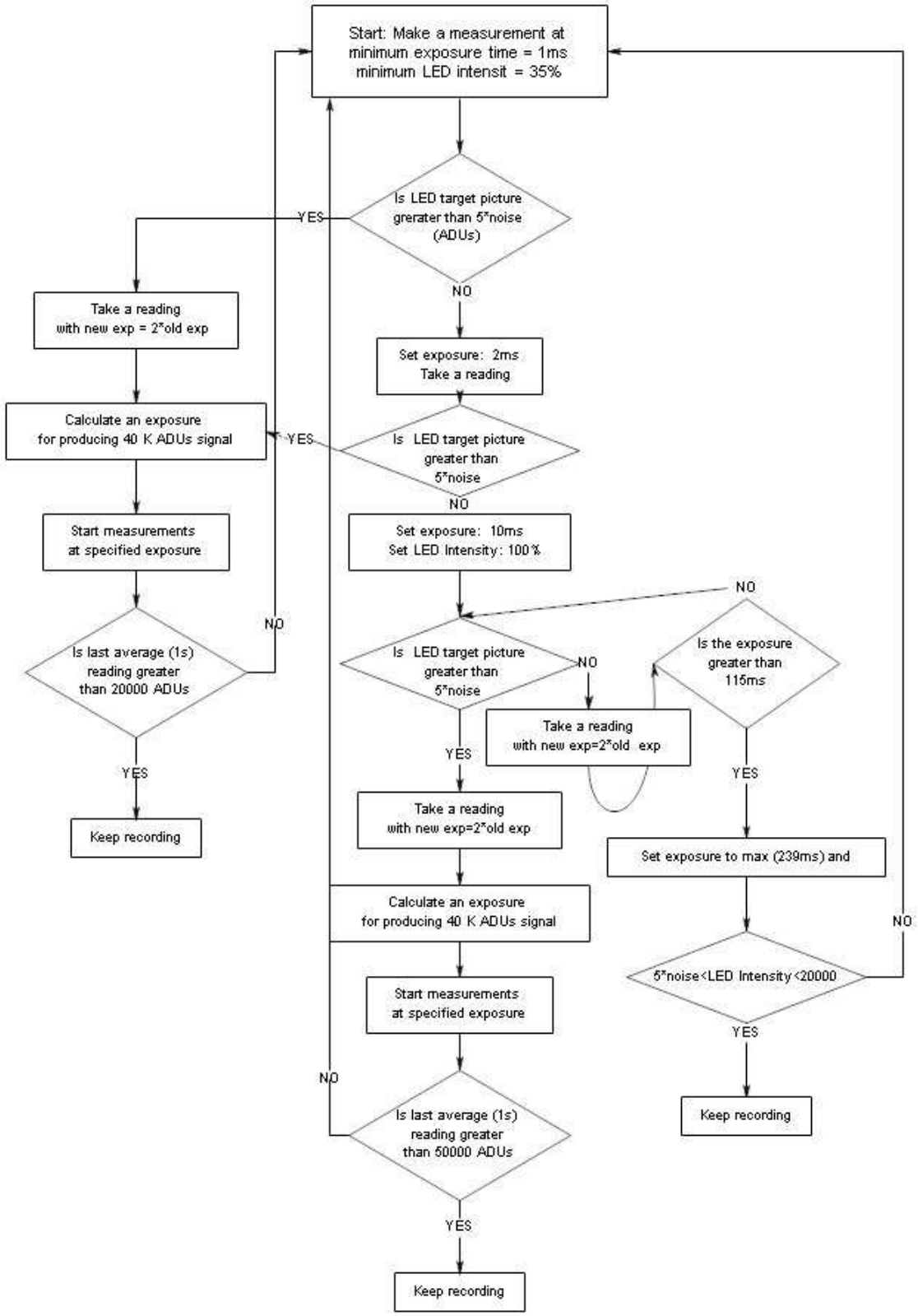

Figure 6.7: Flow chart of the software responsible for the control of the ATIK-16 CCD exposure time and the LED driving current control.

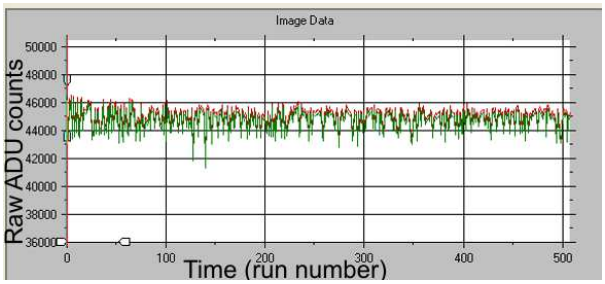

Figure 6.8: Fluctuation of the LED signal (i.e. ON-OFF) during a calibration run.

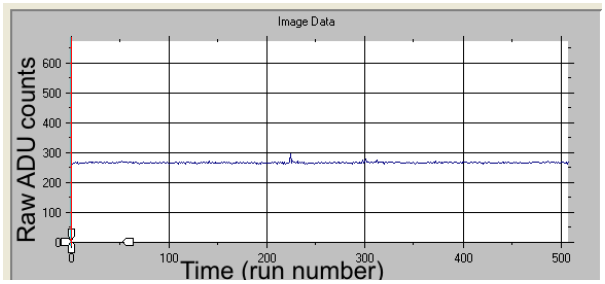

Figure 6.9: Fluctuation of the read-out noise (i.e. OFF) for the same calibration run.

The plot in Figure 6.8 suggests a signal variation in excess of 2000 ADUs - one order of magnitude higher than the expected value - while read-out noise was very stable throughout the measurement (see Figure 6.9). At first it was thought that the ON-OFF fluctuation might be the cause of inaccuracies in determining the exposure time (read-out noise being independent of exposure time). For the measurement in discussion, the exposure time has been set to 7 ms, a value that lies suspiciously close to the exposure resolution of 1 ms. After constructing a monitor that contains both the visual and numerical representation of the LED's light spot on the camera (see Figure 6.10) it became clear that the brightest pixel could be located anywhere within the spot. Thus, the normalised mean intensity measuring 7×7 pixels square, centred on the brightest pixel, may not be representative of the light spot (as Figure 6.10 clearly demonstrates). Thus, the measuring algorithm was re-written to incorporate a centroid algorithm that is the subject of the following Section.

6.7.2 The Centroid Algorithm

The ability to locate the centre of an object's image (as registered by a CCD camera) with sub-pixel accuracy is a vital requirement in many fields (see, e.g., (Ares and Arines, 2004)). In astronomy one is interested in discriminating between sources mapped into a digital image and determining their relative position. In adaptive optics the wavefront measurement methods (e.g. Shack-Hartman wavefront sensor) depend on the ability to measure the displacement of the spots formed by dividing

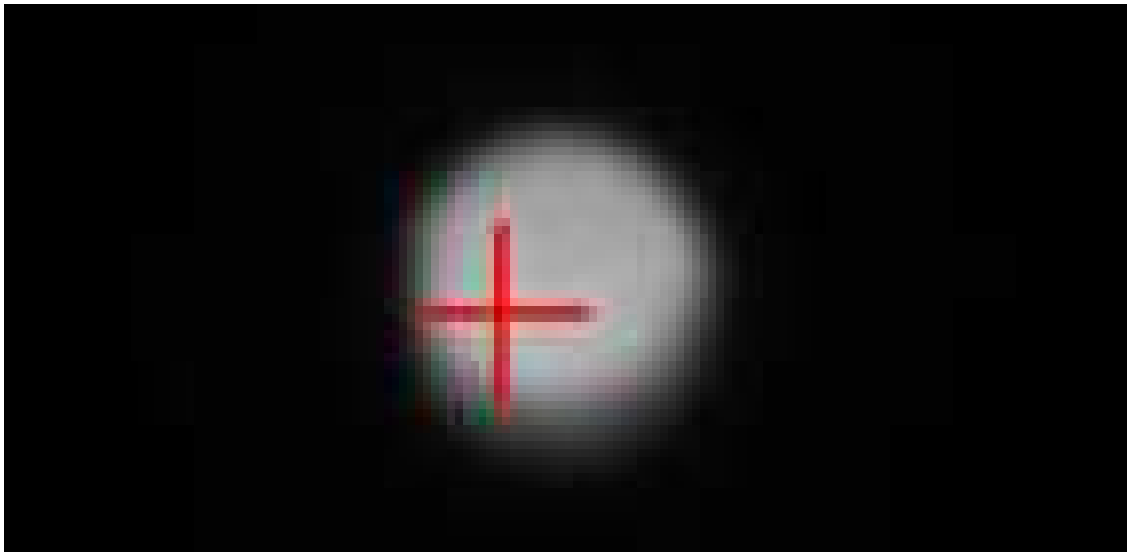

Figure 6.10: Image of the LED as seen by the ATIK-16 CCD sensor. The cross identifies the brightest pixel, which happens to be located away from the centre. Thus, the aperture fixed at this pixel might include background pixels, in which case the light spot intensity will be underestimated.

wavefront via a lenslet array (Baik et al., 2007). In image analysis, basic image processing techniques (e.g. geometric transformations to restore a distorted image) require the knowledge of the location of common characteristics within images (Morgan et al., 1989). There is, therefore, a healthy literature concerning the application and limitations of centroid algorithm variations (e.g. see Stone (1989) for a comparison of centroid algorithms used in astronomy).

The centroid algorithm in our application is designed for optimum speed in an effort to maximise the instrument's frequency. The brightest pixel is located and a square window, that includes the whole LED spot, is constructed. The length of this window for the current experimental set-up is 50×50 pixels but the optimised length will eventually be dictated by the final combination of optics, aperture and baseline. A typical histogram of the intensity distribution of this 50×50 pixel image is presented in Figure 6.11.

The grey level histogram (Figure 6.11) has a clear bimodal distribution. Indeed, the combination of very small apertures, bright LED and flexible exposure time

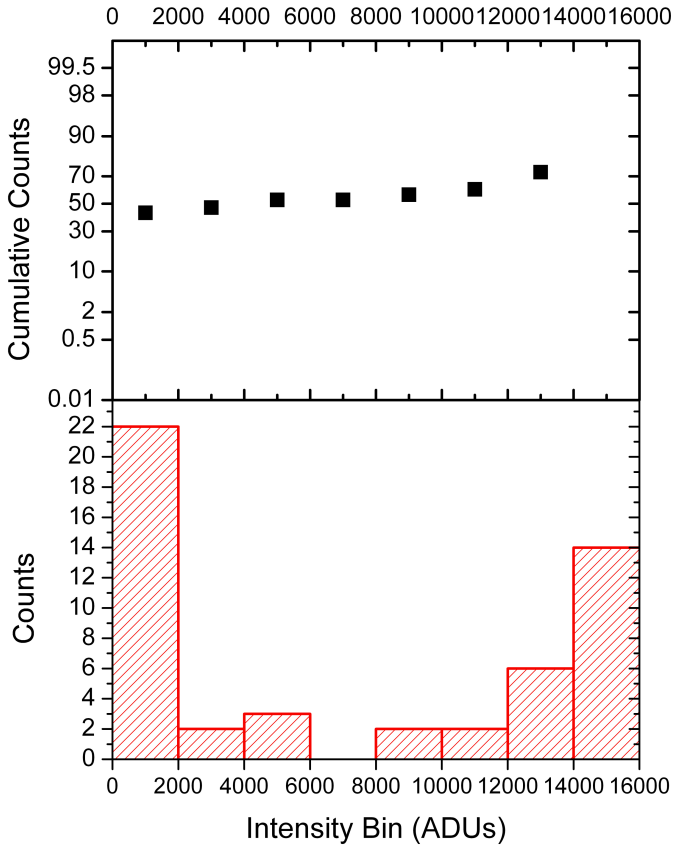

Figure 6.11: Typical histogram of the intensity distribution of the image of the LED recorded by the ATIK-16 camera used in analysis.

allows for a clear discrimination between the LED signal and background under different weather conditions. The typical histogram of the digital image suggests that there is no overlap between background and signal pixel distributions. Thus, a threshold value can be easily determined from the image histogram as the valley between the two dominant modes (i.e. $T = I(i,j)_{max}/2$). One can now retain only the pixels with values greater than a half of the brightest pixel while eliminating the rest of the pixels by the following semi-thresholding process (Haralick and Shapiro, 1992):

$$I(i,j) = \begin{cases} I(i,j) & : \quad I(i,j) \geq T \\ 0 & : \quad I(i.j) < T \end{cases} \tag{6.16}$$

where:

I(i,j) is the grey level intensity at (i,j) and $T = I(i,j)_{max}/2$

Finally, the centroid (x_c, y_c) can be calculated from the following equations (Baik et al., 2007):

$$x_c = \frac{\sum_{i=x_0-L/2}^{x_0+L/2} \sum_{j=y_0-L/2}^{y_0+L/2} I_{ij} \times x_i}{\sum_{i=x_0-L/2}^{x_0+L/2} \sum_{j=y_0-L/2}^{y_0+L/2} I_{ij}} \tag{6.17}$$

$$y_c = \frac{\sum_{i=x_0-L/2}^{x_0+L/2} \sum_{j=y_0-L/2}^{y_0+L/2} I_{ij} \times y_i}{\sum_{i=x_0-L/2}^{x_0+L/2} \sum_{j=y_0-L/2}^{y_0+L/2} I_{ij}} \tag{6.18}$$

where:

$I_{i,j}$ (or I(i,j)) is the intensity (ADUs) of the pixel located at the ith column and jth row

x_0, y_0 are the coordinates of the brightest pixel and

L is the length of the square aperture used (i.e. $L = 50$ pixels for the current experimental setup).

This simple centroid algorithm replaced the brightest-pixel algorithm ensuring that the measuring box is always centred at the estimated centroid as opposed to the brightest pixel centering (see Fig. 6.10). Thus, by eliminating the fluctuation introduced by the inclusion of background pixels into the signal due to the measuring aperture's off-centring, the transmissometer's signal variation (i.e. RMS) has been brought down to less than 200 ADUs; a value in excellent agreement with the statistical uncertainty in the photon count (i.e. $\sqrt{counts} = 216$ ADUs).

The implementation of this simple centroid determination algorithm should yield sub-pixel accuracy (i.e. 0.01 pixels (Carlson, 1999)), which is more than sufficient for our application. It has been shown (Cao and Yu, 1994; Ares and Arines, 2004) that the centroid variance can take the following form:

$$\sigma_{x_c}^2 = \frac{\sum_{i=0}^{L} \sigma_N^2 x_i^2}{\langle I_t \rangle^2} = \frac{\sigma_N^2}{\langle I_t \rangle^2} \left(\frac{L^3 - L}{12} \right) \tag{6.19}$$

where:

σ_N^2 is the noise variance, and

$\langle I_t \rangle$ is the mean of the total intensity

In deriving this equation the following assumptions were made (Ares and Arines, 2004):

- the covariance of error fluctuation between pixels is negligible (uniform spatial pixel response), an assumption that is justified by both the number of pixels within signal's aperture (of length L) and the flat fielding correction,
- the signal is contaminated by an additive Gaussian noise that possesses zero mean and a variance of σ_N^2, and that
- the average centroid position is centred on the signal window.

Equation 6.19 implies that the uncertainty in the centroid determination is proportional to the area of the signal window and inversely proportional to the signal to noise ratio. In our case, the software has revolved around optimising the signal-to-noise ratio (see Section 6.7) and the optimised sub-aperture length is $L = 7$ pixels (see Fig. 6.18).

An alternative method of validating the centroid algorithm is by Gaussian fitting the marginal distribution of the LED spot image:

$$P_{xi} = \sum_{j=x_0-L/2}^{x_0+L/2} I_{ij} \tag{6.20}$$

$$P_{yj} = \sum_{i=y_0-L/2}^{y_0+L/2} I_{ij} \tag{6.21}$$

In Figure 6.12 the 3-d intensity distribution of the LED projection into the camera is presented. The average marginal distribution (i.e. $\bar{P}_{xi} = \frac{P_{xi}}{L+1}$) of the

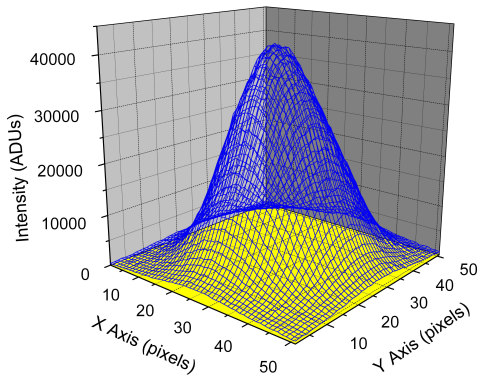

Figure 6.12: Three dimensional plot of the LED intensity distribution.

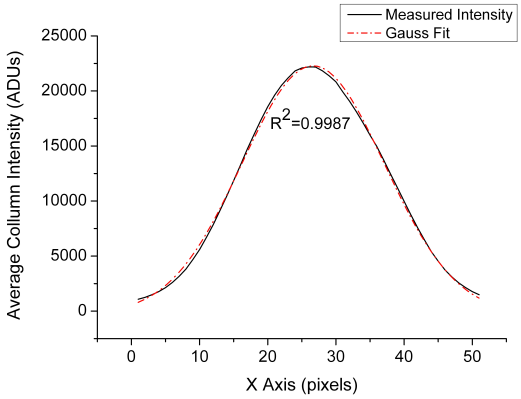

Figure 6.13: Average marginal sums distribution (along columns of Fig. 6.12) and its Gaussian fit.

same LED image along the x-axis is shown in Figure 6.13. It is clear that the signal faithfully follows a Gaussian distribution, yielding a value of 26.648 for the centroid's x-coordinate. The analytically calculated value (i.e. Equation 6.17) was $x_c = 26.697$, thus the same within the integer pixel accuracy demanded by our application. The Full Width Half Maximum (FWHM) of the distribution is $\sim$ 21 pixels leading to a maximum signal aperture of 7×7. This selection is mainly driven by the limited $8-$bit resolution over exposure time. One could use a 50×50 aperture that would account for the whole signal leading to a more accurate derivation of its intensity. However, that would limit the dynamic range of the instrument. In the following section (i.e. 6.7.3) we will investigate diffusers providing a "top-hat" intensity distribution that allow for more of the signal to be used without limiting the sensor's dynamic range.

6.7.3 Hardware optimisation of the ATMX-I transmitter

The first tests of the new camera suggested that the LED produces a CCD signal with an almost perfect Gaussian distribution (see Figure 6.13). The width (FWHM) of this distribution will set a limit the size of the aperture than one may use in order to retrieve the LED's intensity. In general, the diameter of the LED image on the CCD can be calculated from the camera's optical characteristics by the following

equation:

$$\Phi_{img} = \frac{\Phi_{target} f}{d\sqrt{x^2 + y^2}} \tag{6.22}$$

where: $\Phi_{img}, \Phi_{target}$ are the diameters of the LED image (in pixels) and the transmitter's aperture respectively (cm)
d is the distance between transmitter-receiver
x,y are the CCD pixel sizes in the relevant direction (i.e. $8.6\mu\text{m} \times 8.3\mu\text{m}$), and
f is the focal length of the camera's lens.

The measurement of the LED intensity, after the light has travelled a distance d, consists of averaging values from neighbouring pixels located at the top of the signal distribution. One should aim, therefore, to produce a signal having a "top-hat" distribution, in order to minimise the uncertainty budget. That is, to bring the standard deviation of these average values to the level of the read-out noise fluctuation.

The LED beam can be diffused and shaped by using the novel Thorlab diffusers (ThorLabs, 2008). Due to their special design, these engineered diffusers can be used to control the shape of the LED projection and slightly modify the LED's Gaussian intensity distribution towards a "top-hat" profile.

As our application implements square-aperture photometry, the ED1-S20 diffuser was selected due to its square scatter shape with an 20° flat region. Initial tests were encouraging.

The first test of the ED1-S20 diffuser consisted of mounting it at the exit of the ATMX-I transmitter unit, on the top of the DHLT's diffuser (see Fig. 5.4). The first results are presented in Figures 6.14, 6.16 and 6.15, 6.17 for the new and old diffuser respectively. It is clear that the addition of the ThorLabs ED1-S20 diffuser resulted in a smoother "top-hat" intensity distribution. This is more evident if one compares the equi-intensity plots: the new diffuser (see Fig. 6.16) eliminates the structure seen in Figure 6.17.

The ThorLab diffuser allows for a wider sampling of the intensity distribution. In order to find the optimum aperture size, one should plot the extracted average value and its related uncertainty (RMS) as a function of the number of pixels used for these calculations.

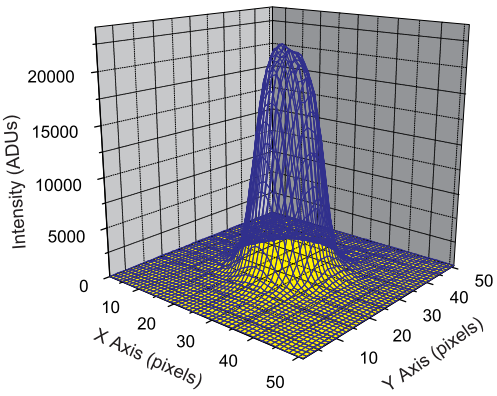

Figure 6.14: Three dimensional plot of the LED intensity distribution with the Thorlab engineered diffuser.

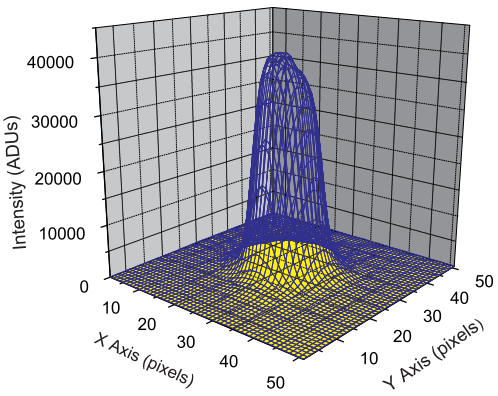

Figure 6.15: Three dimensional plot of the LED intensity distribution with a typical diffuser.

Figure 6.18 calls for the use of either a 7×7 or an 11×11 pixel aperture. It is worth noticing that the intensity can be measured with a minimum uncertainty of 40 ADUs, a value which is comparable with the read-out noise fluctuation (i.e. 11 ADUs). The completion of the ATMX-II transmitter unit will dictate an analogous procedure for the calculation of the instrument's optimised aperture.

6.8 First Linearity Tests

In order to get a first idea of the transmissometer's performance it is necessary to check the measured transmittance against known transmittance points provided by neutral density filters. This process was performed for the old DHLT prototype (see Section 5.6.5). The new software, optimised for maximum signal-to-noise ratio, dictates a different approach as the measured signal has to be normalised for both exposure time and the driving current under which the measurements were taken. In order to derive the relevant normalisation procedures, the linearity of the CCD camera over exposure time and driving current needs to be investigated.

All tests have been performed using the ATMX-I on the roof of the Physics department. The receiver-transmittance distance was fixed at 20 m under clear and

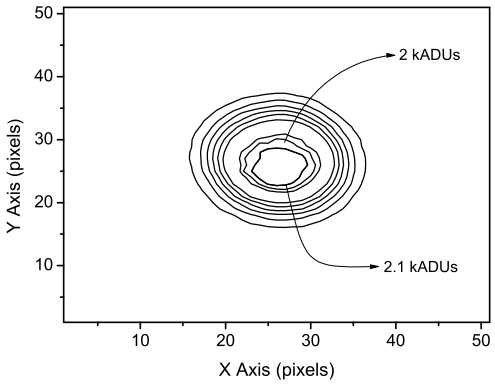

Figure 6.16: The equi-intensity plot of the LED image with the Thorlab engineered diffuser.

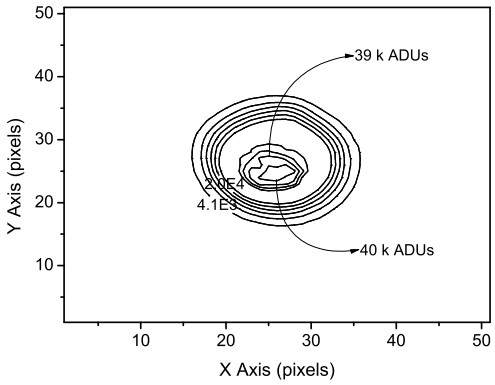

Figure 6.17: The equi-intensity plot of the LED's beam image with a typical diffuser.

stable atmospheric conditions with visibilities in excess of 30 km.

6.8.1 Driving Current Normalisation

In order to determine the camera response under different LED light outputs, the LED was driven with a DC current ranging from $35-100\%$ of its maximum capacity. The results are illustrated in Figure 6.19. Each point was calculated as the average of 20 measurements and the relevant standard deviation is illustrated by the error bars.

As ATMX-I transmitter was operating without the aid of a monitoring photodiode, the driving current modulation could not have been used to optimise the LED's image signal-to-noise ratio. Indeed, even though a linear trend is evident in Figure 6.19, the precision is not sufficiently adequate to allow the use of the full range of the driving current as a tool for optimising the LED's image signal-to-noise ratio. This becomes more evident for the extreme value of the LED driving current, where an increase of 65% corresponds to almost a 100% increase of the relative LED light output. Thus, the new software uses only two extreme settings of current (i.e. 35% and 100%), thereby maximising the instrument's dynamic range. By default the 35% setting is used and a switch to the LED's maximum output occurs only when

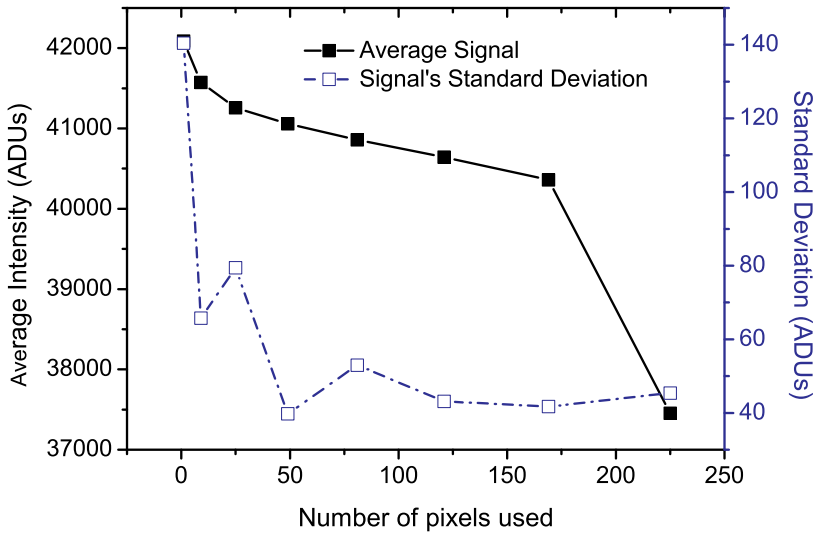

Figure 6.18: Average LED intensity and its uncertainty as a function of the measuring aperture size used, for the ATMX-I instrument with ThorLabs ED1-S20 diffuser.

the prevailing atmospheric conditions prevent the detection of an optimised signal. These measurements are normalised to the 35% level according to Equation 6.23:

$$C_I = \frac{\text{CCD counts at } 35\%}{\text{CCD counts at } 100\%} \Rightarrow \text{Normalised Counts} = C_I \times \text{Measured Counts} \quad (6.23)$$

The normalisation factor (C_I) is determined whenever a re-calibration (switch between the extreme current settings) of the transmissometer occurs. In our case, C_I=1.98 with a relative uncertainty of 0.9%. Following a re-calibration, time is allowed for the LED's temperature stabilisation.

6.8.2 Linearity over exposure time

CCD sensors are nearly perfect linear detectors with a linearity often better than 0.01% (Martinez and Klotz, 1998). That means that there is a linear relationship between the number of electrons produced by the light arriving in each pixel (input signal) and the digital value stored for this pixel (output value) (Howell, 2000). It was due to this high linearity, over a wide range of different light inputs, that CCD

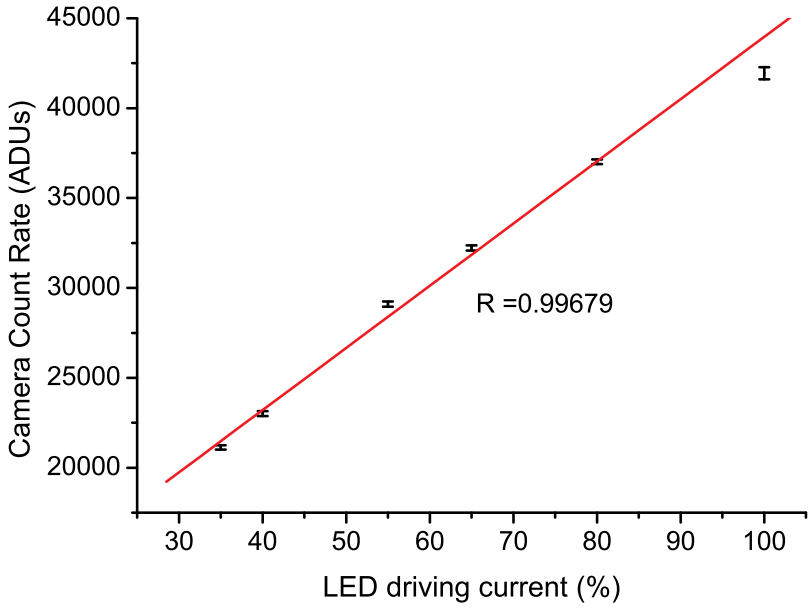

Figure 6.19: Camera response under different driving LED currents.

sensors swiftly replaced photographic plates, revolutionising astronomical observations (Ferrero et al., 2006).

The expected CCD linearity over the exposure time was verified by plotting the camera measured counts over an exposure range of 60 to 100 ms. This exposure range was achieved by the use of a neutral density filter (O.D. = 1) and a default forward current of 35%. The results are shown in Figure 6.20. As in the case of the driving current linearity, a set of twenty measurements has been taken for each exposure check point and the error bars denote the standard deviation. The number of measurements used, common to both normalisation procedures, has been selected as the mid-point of the expected optimum transmissometer's frequency (i.e. $\sim$ 1Hz), taking into account the ICAO recommendation for 1 min averaging time in reporting visibility values.

The linear relationship of the CCD response over exposure time is apparent in both Figures 6.20 and 6.21. Indeed, the linear equation resulting from the least-squares fit to the experimental data (see 6.20) can be used as a measure of the non-linearity of the CCD sensor:

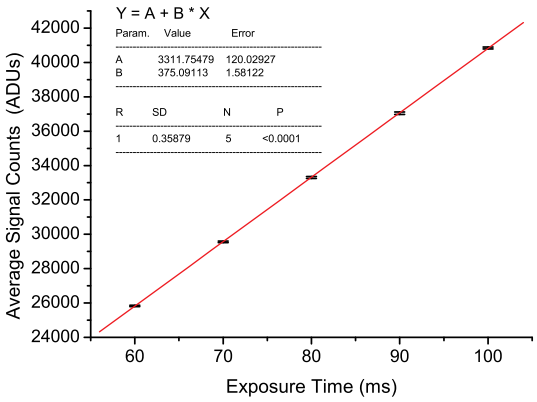

Figure 6.20: The ATIK-16 CCD's near perfect linearity over the range of the exposure tested

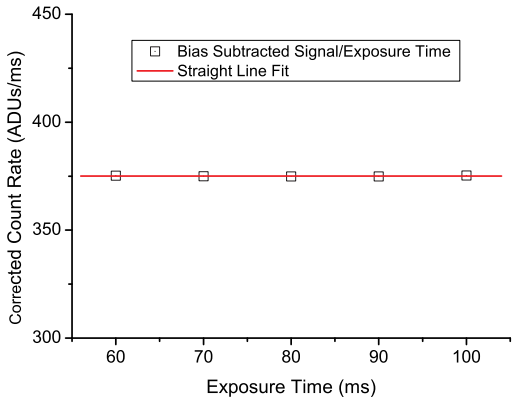

Figure 6.21: The CCD's count rate vs exposure time.

$$C_{lin} = \frac{\text{Maximum Deviation}}{\text{Maximum Signal}} \times 100 \Rightarrow C_{lin} = \frac{(N_{meas} - N_{exp})_{max}}{(N_{exp})_{max}} \times 100 \qquad (6.24)$$

where:

C_{lin} is the non linearity correction, N_{meas} is the measured counts and N_{exp} is the expected counts

One can use the linear equation to compute the expected counts for each exposure time and then find the maximum deviation from the experimentally determined counts. In our case, the maximum deviation (21.3 counts) occurs at the maximum signal (40842 counts) leading to non-linearity correction of only $\sim 0.05\%$.

A different method that can be used to verify the extent of the CCD's non-linearity is by plotting the CCD's count rate (measured counts/exposure time) as a function of the exposure time (see Figure 6.21). Deviation from this ratio, that should be constant for a linear CCD sensor, yields the non-linearity correction with the aid of parameter α:

$$N_{meas} = N_{exp}(1 + \alpha C_{exp}) \qquad (6.25)$$

The α parameter can be determined by fitting a straight line to the count rate data determined by dividing the bias subtracted counts over the exposure time (i.e.

$\frac{N_{meas}-N_{bias}}{t}$):

$$\alpha = \frac{B}{A^2} \tag{6.26}$$

where:

B is the slope and A is the y-intercept of the corrected count rate fit.

The straight-line fit in Figure 6.21 yielded an α value of 0.02×10^{-6}. Thus, even at the maximum signal of 40 kADUs the non-linearity correction is:

$$C_{lin} = \alpha N_{exp} \times 100 = 0.08\% \tag{6.27}$$

According to these results the deviation from linearity is so small that a non-linearity correction is not necessary even for the highest intensity values. Thus, the CCD's near perfect linearity, over the measured range of data values, justifies the usage of the exposure time in order to increase the transmissometer's dynamic range in transmittance.

The linearity tests revealed, however, a problem with the CCD sensor. The bias level of ~ 3311 ADUs (i.e. y-intercept of the linear fit on Figure 6.20) was unexpectedly high in comparison to the read-out noise level of ~ 250 ADUs. This abnormal bias level limits the CCD's usable dynamic range and points out a malfunction of the CCD electronics. This malfunction also explains why the CCD's sensor linearity was validated for a moderated range of exposure times (i.e. $60 - 100$ ms). While waiting for the problem to be resolved, the vendor released the new ATIK-314E camera offering a 16-bit resolution in exposure time and possessing superior noise characteristics than the ATIK-16 camera. It was decided to upgrade to ATIK-314E for reasons that will be discussed in Section 6.11.1. Thus, the calculated linearity for exposures times between $60 - 100$ ms can provide a good estimation of the ATIK-314E performance over the whole range of the exposure values utilised in the measurement of atmospheric transmissivity.

6.8.3 Neutral Density Filter Test

After the determination of the normalisation coefficients one can check the linearity of the whole ATMX-I instrument. Five neutral density filters with optical densities 0.1, 0.3, 0.5, 1 and 2 have been selected for this test. In addition to linearity verification, the ability of the new software to produce an optimum signal over a wide range of transmittances will be put to the test.

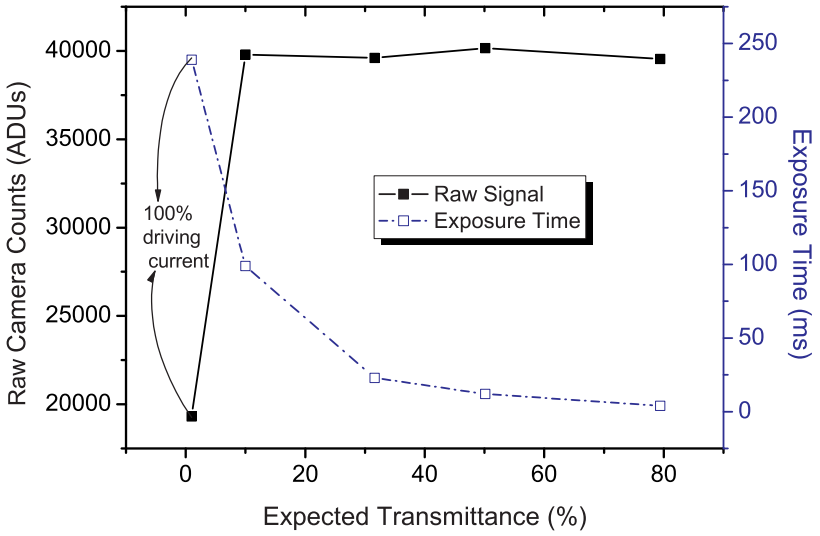

Figure 6.22: Camera response to different filters before normalisation. The exposure time is modulated to produce a 40 kADU signal in all but the foggiest conditions (i.e. OD=2). For transmittance lower than 1% the both LED driving current and CCD exposure are set to their maximum values.

The raw results of the test are presented in Figure 6.22. By examining this graph, one can verify that the algorithm is able to produce a signal very close to 40 kADUs, for all but the filter with optical density 2, by altering the exposure time. When the filter OD= 2 is used, simulating a transmittance of 1%, the algorithm switches the LED driving current to 100% and sets the exposure value to the maximum usable value (i.e. 239 ms). Thus, even at 1% transmittance, the signal-to-noise ratio is very good and the dynamic range of the instrument is extended from 20 kADUs down to

a just detectable signal (5× read-out noise: $\sim 1,200$ ADUs).

In order to examine the linearity of the ATMX-I configuration of the transmissometer, the raw values must be normalised for both driving current and exposure time. The linearity test over exposure time has been undertaken by the use of a filter with optical density of 1 (see Fig. 6.20). The raw values, therefore, obtained under a specified exposure time and driving current, need to be compared with the relevant values (i.e. same driving current and exposure time) that the CCD is expected to register when sited behind an OD = 1 filter. This normalisation of the raw signal, at the 1% transmittance level, can be achieved with the aid of the following comparative coefficient κ:

$$\kappa = \frac{\text{Raw Signal}}{\text{A+B exposure}} \times C_I \tag{6.28}$$

where:

A, B are the constants calculated by the linear least-square regression (see Fig. 6.20) and

C_I is the driving current normalisation factor (see Equation 6.23).

Finally, the measured transmittance can be calculated from the following equation:

$$T = \frac{\kappa \text{ with filter}}{\kappa \text{ without filter}} \times 100 \tag{6.29}$$

The comparison of the measured transmittance against the filter-derived transmittance checkpoints is shown in Figure 6.23

In this case, the linearity of the transmissometer can be found directly by the deviation of the slope of fitted line from the ideally expected value of 1. The linear fit yields an excellent non-linearity correction, ranging between 0.17 and 0.33%. This value is less than half of the value calculated for the old prototype. It is expected that the use of the telescope-based transmitter (see Figure 6.26) providing a more focused beam, in conjunction with recently acquired ThorLabs diffuser, will minimise further the transmittance uncertainty. One has to take into account, however, that at this level of accuracy the uncertainty introduced by the calibration of the neutral

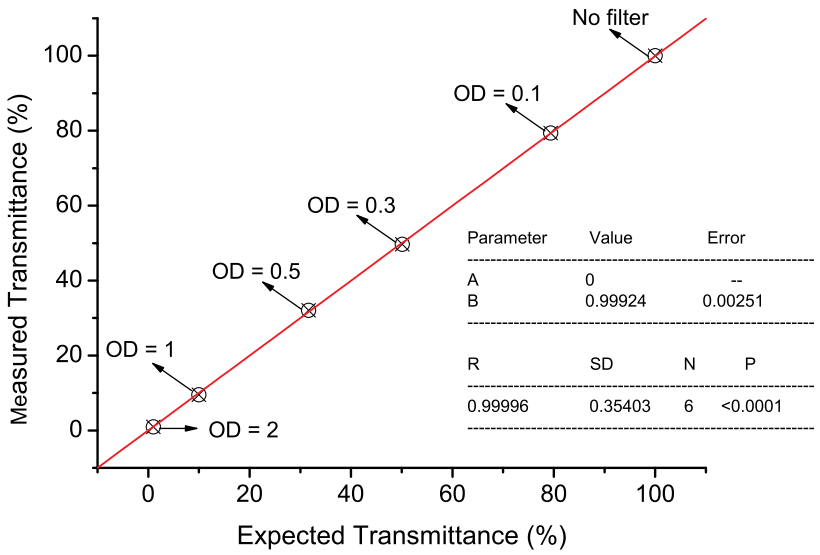

Figure 6.23: Measured transmittance of the ATMX-I versus neutral density filter-derived checkpoints, from a density of 0.1 to 1.0. The linear fit to the data reveals a very small non-linearity correction.

density filters may be the limiting factor in transmittance resolution.

One has to note that the new software was built and tested by using the DHLT transmitter unit in conjunction with the ATIK-16 CCD sensor (i.e. ATMX-I). The construction of the first transmitter, based on the Sky-Watcher telescope (i.e. ATMX-II), was completed during April 2008 (see Figure 6.26). Thus, the optimisation of the software based on the telescope transmitter optics will be the next logical step.

6.9 The Telescope-Based Transmitter Unit

6.9.1 Transmitter Parts

The S9706 Hamamatsu Photodiode

In the DHLT transmissometer a simple photodiode (IPL's 10040 (IPL, 2000)) was used to monitor fluctuations of initial beam intensity (see Figures 5.4, 5.5). The old

design suffered from the following major issues:

- limited resolution of the photodiode dictated by the 10-bit digitiser of the transmitter's micro-processor,
- the photodiode was simply mounted at an angle of $\sim 20^{\circ}$ to the LED. There was no means of extracting and guiding a known portion of the initial LED beam into the photodiode,
- there was no cooling of the photodiode. That limited the photodiode's dynamic range on hot days, and
- the two light monitoring devices (photodiode, camera) had different spectral responses.

An integrated solution requires changes in both instrumentation and design. A new photodiode array, namely a Hamamatsu S9706 digital colour sensor, was therefore purchased. This encapsulates three built-in registers that allow for simultaneous measurement at 615, 540 and 465 nm wavelengths respectively (RGB colours) (Hamamatsu, 2007). In addition to the higher 12-bit resolution, the new photodiode's RGB spectral sensitivity allows for better matching with the final camera's spectral response.

In order to monitor the beam's initial intensity more effectively, a beam splitter in conjunction with guiding optics (fibre optic guide) is used. In addition, the photodiode is located in an isolated compartment within the transmitter's control box (see Fig. 6.27), and is equipped with a Peltier cooling device. The cooling will keep the dark count noise at acceptable levels regardless of the ambient temperature fluctuations while the photodiode feedback loop will drive the light source towards a fixed intensity value (see Section 6.9.3).

LEDs

The ATMX-I transmissometer employed a white super-bright (80 lm @ 1A) Luxeon-III LED. Brief market research revealed successors offering a $\sim 70\%$ increase in typical luminous flux. This is particularly important, especially during very bright

days where the LED's maximum light output will set the signal to noise ratio and, therefore, determine the instrument's resolution.

In addition to the enhanced luminous flux, the selected white LED should possess an emission spectrum approximating the emission of the CIE standard illuminant A (Section 5.5.1). The super-bright LED that best matches this criterion is the warm white (i.e. 3000 K colour temperature) Luxeon L2K2 MWW4 (Lumileds, 2007), which was selected to equip all of the transmissometer's later versions (ATMX-II,III,IV). The L2K2 warm and neutral white LED emission are provided in Figures 6.24 and 6.25 respectively. As expected, the emission spectra of the warm white LED approximates better the spectral power distribution of the standardised CIE Illuminant A (Wyszecki and Stiles, 1982).

Finally, according to the manufacturer the L2K2 LED has an expected life span of 50,000 h, when driven at 1 A with 70% lumen maintenance. In our application the LED's emission is constantly monitored. Moreover, the LED temperature is kept to a minimum via an innovative Peltier coupling, and thus the LED's lifetime is expected to exceed the specification required (see Section 6.2).

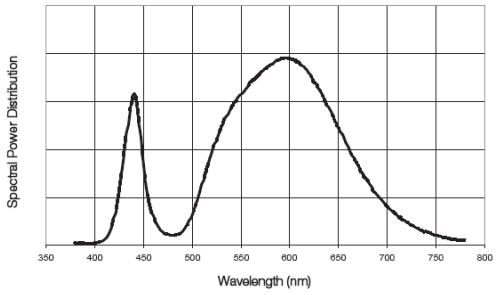

Figure 6.24: Typical warm white spectrum of Luxeon K2L2 LED at 1 A test current and junction temperature $T_J = 25°\mathrm{C}$

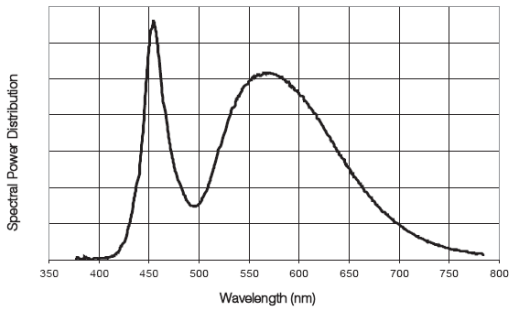

Figure 6.25: Typical neutral white spectrum of Luxeon K2L2 LED at 1 A test current and junction temperature $T_J = 25°\mathrm{C}$

6.9.2 Telescope-Based Transmitter Construction

It was decided to base the transmitter unit for the ATMX-II and subsequent instruments on the Sky-Travel 80 mm refractor telescope (Sky-Watcher, 2007). A Sky-Watcher auto-focuser will be responsible for LED focusing. The construction of

Typical characteristics of the L2K2-MWW4-11-BU00 LED				
Flux		Optical		
Luminous Flux (lm)	Drive Current (A)	Colour Temperature CCT (K)	Total Included Angle (degrees)	Viewing Angle (degrees)
100 130	1 1.5	3000	160	140
Electrical Characteristics				
Drive Current (A)	Forward Voltage (V)	Dynamic Resistance (Ω)	Temperature Coefficient of V_f (mV/°C)	Thermal Resistance Junction to Case (°C/W)
1	3.72	0.6	-2.0	9

Table 6.2: Typical characteristics of the Luxeon L2K2 warm white LED. Drawn from the Luxeon manual (Lumileds, 2007).

the final transmitter is underway (April 2009) and the status of our building efforts is illustrated in Figures 6.26 and 6.27.

The telescope's eye-piece has been replaced with a custom-made aluminium LED enclosure. The LED has been directly mounted at the the centre of the copper heat sink covered by an aluminium shroud, and is equipped with a variable rate fan system (see Figure 6.27, lower panel: left). The heat sink is attached to the LED holder which is directly mounted on the telescope (see Fig. 6.26). The photodiode is located on a separate isolated unit within the transmitter's control box (see Fig. 6.27, lower panel: right). The connection between the LED and the photodiode is achieved via an optical fibre.

The telescope-based transmitter unit has been under constant revision until reaching its final stage (ATMX-IV, April 2009). For the sake of simplicity and practicality, the telescope-based transmitter was originally controlled by the DHLT PCB (see Figure 5.6, Appendix B.2). As described earlier, it was quickly proven that

Figure 6.26: The ATMX-II light transmitter unit.

the DHLT photodiode needed to be replaced as its resolution was not compatible with the ATIK-16 sensitive CCD camera. In order to use the S9706 photodiode a separate PCB with its own small microcontroller (see Appendix B.3 and Fig. 6.27, lower panel: right) was manufactured by the Durham University Electronic Workshop (DUEW) (Moore, 2008). As the optimisation of the transmitter's frequency dictated major changes on the PCB firmware, attainable only by the DUEW and thus delaying the project, the author decided on the replacement of the main PCB controller by a laptop and a data acquisition board (see Fig. 6.27). The benefits of such a solution are listed below:

1. The implementation of the "PCB-free" solution allows full control over the transmitter's hardware and software leading to elimination of unnecessary measurement delays in controlling the LED via the PCB originally designed for night transmissometer (i.e. background free) operation.

2. It allows for an easier implementation of a closed-loop system to maintain the light output on a constant level.

3. Finally, the implementation of a computer controlled transmitter would dras-

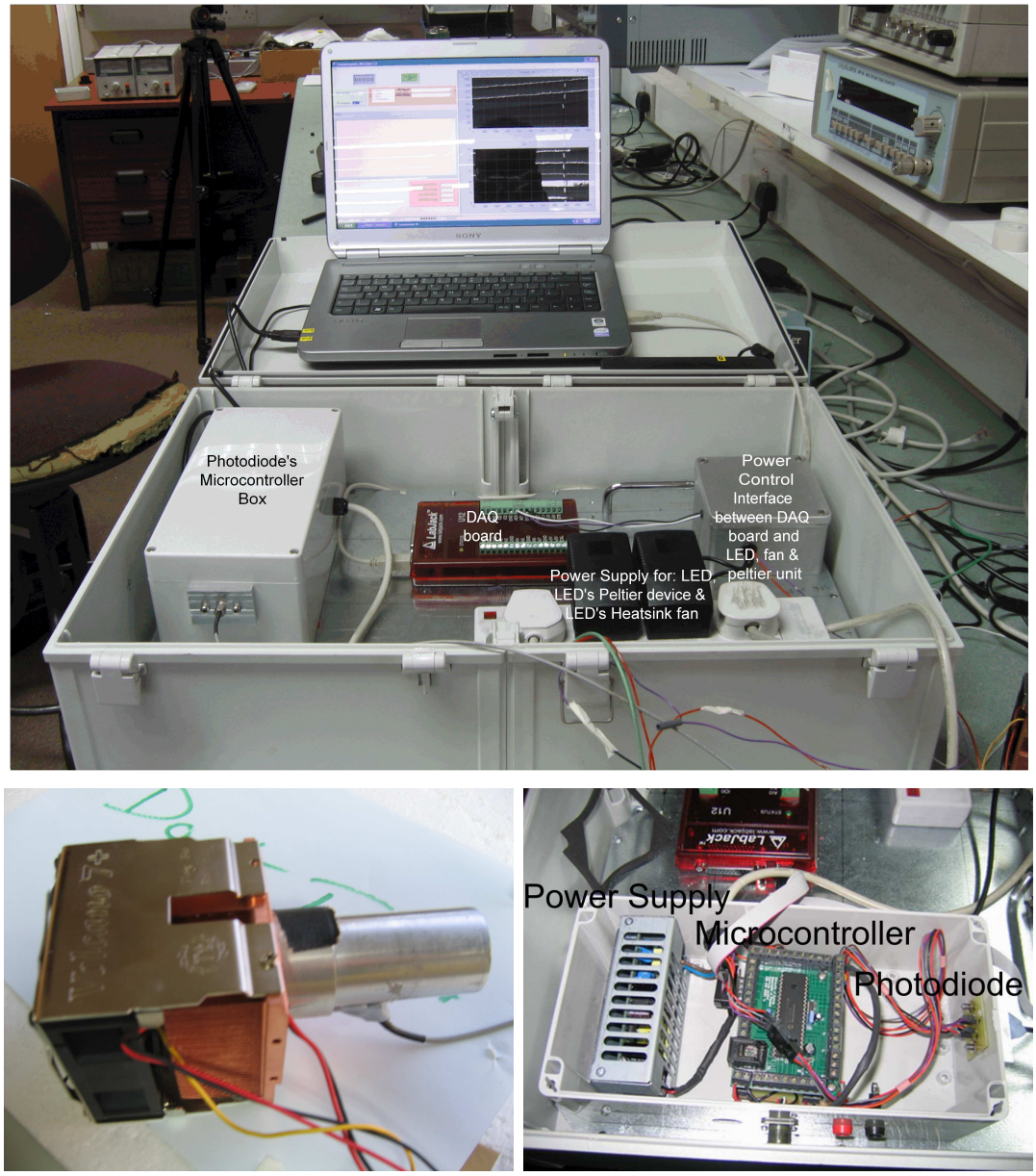

Figure 6.27: Upper Panel: The new transmitter's control box. Lower Panel Left: The custom LED holder attached to the heat sink. Right: The photodiode with the purpose built microcontroller and its power supply.

tically reduce its development time.

The migration of the old PCB transmitter controller to the laptop/DAQ solution was completed in December 2008 allowing for the full hardware and software TMX control for the first time. That made possible the construction of a thermally stable LED source, which is the subject of the following section.

6.9.3 The Durham Thermally Stable LED Source

Background Theory

LED emission intensity depends on junction temperature. In general, an LED's emission intensity decreases exponentially with increasing temperature according to the equation:

$$I = I_0 \exp^{-\frac{T}{T_c}} \tag{6.30}$$

where:
I_0 is usually taken as the LED intensity at a junction temperature of 25 °C and
T_c is the LED's characteristic temperature, which describes its temperature dependence (Schubert, 2003).

This can be attributed to the increase of both non-radiative recombination and surface recombination following an increase in the LED's temperature. Equation 6.30 is empirical and does not provide a theoretical connection with the underlying physical processes. Indeed, the degradation of the light intensity of the white Luxeon K2 LED, used in our application, as a function of its junction temperature is almost linear throughout the LED's operating temperature range, as shown in Figure 6.28. In addition to significant light intensity degradation, the wavelength of emitted radiation will shift towards higher values with increasing LED temperatures. Specifically, the dominant emitted wavelength is inversely proportional to the semiconductor's effective energy gaps, and these become slightly smaller with increasing temperature (Mroczka and Parol, 1993). Thus, in the case of the Durham transmissometer, where stability of the LED light source is imperative for a correct estimation of transmittance, efficient temperature compensation is needed. In our application the LED intensity must be kept near maximum over a wide range of ambient temperatures in order to optimise the resolution in transmittance. Before discussing the details of the novel LED light source which allows us to achieve this, a brief description of the prior art will be given.

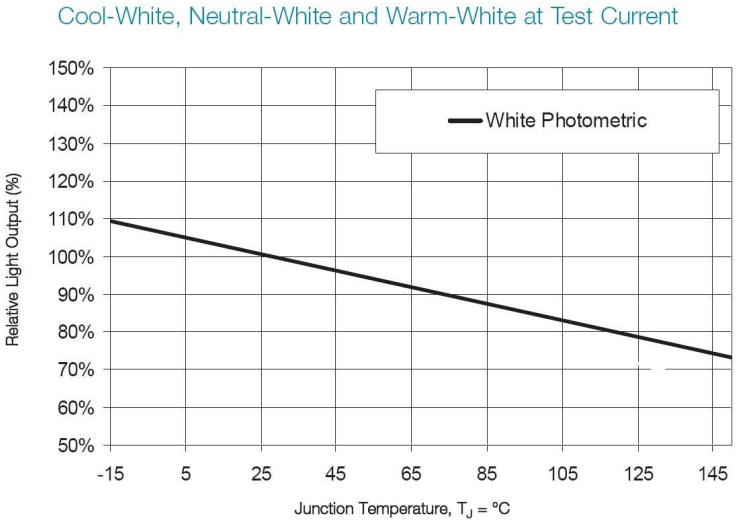

Figure 6.28: Relative light intensity as a function of Luxeon K2 white LED junction temperature.

Prior Art

A quick search through patents and the internet revealed the following methods for producing a stabilised LED-based source:

- Temperature control method: The LED junction temperature is determined by measuring the board temperature and the LED's forward voltage and current and applying the equation:

$$T_j = T_B + \theta_{JB} I_{\text{LED}} V_f I_0 \tag{6.31}$$

where:

θ_{JB} is the junction to board thermal resistance in °C/W

By using the manufacturer's LED-specific temperature plot (e.g. Fig. 6.28), an intensity value consistent with the new temperature is calculated. This is used as feedback to drive the LED towards a stable intensity value. Such a solution is disclosed in U.S. Pat. No. 6,717,559 granted to (Weindorf, 2004). The invention is used for backlighting Liquid Crystal Displays (LCD). An alternative method based on sensing the ambient temperature is described in

U.S. Pat. No. 6,693,394. This invention uses an ambient temperature sensor connected to a regulator for adjusting the current flow to the LED in response to the measured ambient temperature (Guo and Russel, 2004). Both solutions require complex circuits encapsulating thermo-sensitive sensors. In addition, the temperature gradient between these sensors and the LED could lead to compensation errors (Bera et al., 1993).

- Light Output Method: According to this method the light output is measured via a photodiode and this information is used to modulate the driving current of the LED. The problem with the naïve implementation of the light sensor feedback is that as the LED temperature increases its luminous intensity decreases, resulting in operating the LED at higher currents, which in turn increase LED's dissipated power and, thus, temperature. Our method, which allows an effective "photodiode-feedback" without the aforementioned problems, is the subject of the next section.

Description of the Transmissometer's temperature stabilised light source

In our application the LED intensity must be kept near maximum over a range of ambient temperatures (i.e. 10 and 35°C, see Section 6.2) in order to optimise the resolution in transmittance. This is achieved by maintaining the LED at a low temperature via the coupling of the LED with a Peltier device, which is also connected to a copper heat-sink supported by a fan. This solution provides an optimised thermal path for the heat dissipation from the LED, in comparison with prior art, and ensures maximum LED brightness operation over the whole temperature range. For best results, a feedback loop implementing a temperature sensor can be used to drive the Peltier device towards a steady LED temperature. The small fluctuations of the LED's junction temperature are compensated via a light output monitor feedback employing a thermally stable photodiode, which is coupled to the LED by means of an optical fibre. The photodiode is located in a separate box fully shielded from background light (see Fig. 6.27). The thermal noise of the photodiode is kept into a minimum via a second Peltier device. The photodiode can be kept at a constant temperature by regulating the Peltier's device driving current as described above.

A schematic view of the light transmitter operation is provided in Figure 6.29.

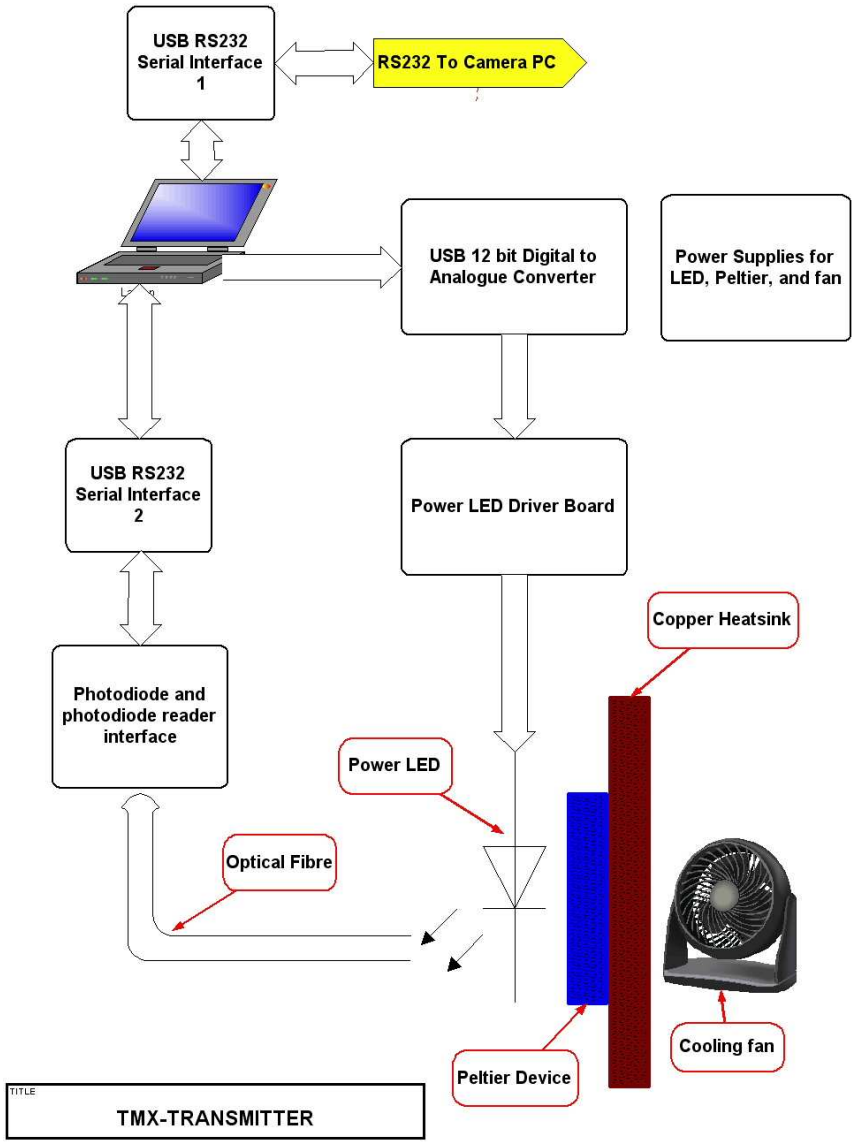

Figure 6.29: Operation of the transmitter unit implemented in the ATMX-III and IV transmissometers.

The purpose of the transmitter is to maintain a constant light output from a high power LED. The operation of the transmitter can be described as the sum of the following steps:

1. A PC running a bespoke application provides the processing to maintain the light output at a constant level,

2. the user sets the desired intensity level using the application,

3. a nominal voltage value is set by the PC via the 12 bit DC converter to produce a luminous output from the LED. Part of this output is being directed through an optical fibre into an isolated and thermally stable photodiode. The photodiode has a 12-bit resolution and is capable of registering LED intensity via three different RGB colour sensors (i.e. at λ = 615, 540 and 465 nm respectively),

4. the PC requests the reading from the photodiode and compares it against the set reading, and finally

5. an adaptive algorithm sends a correction value to the D/A converter to adjust the light output to maintain a constant level.

6.10 Transmitter Design Optimisation

6.10.1 Achieving quick alignment and Resolving stability issues under strong winds

Preliminary tests of the first telescope-based transmitter (i.e. ATMX-II) revealed that its alignment with the receiver unit had become increasingly difficult, counteracting the higher resolution offered by the magnified LED spot. The alignment time sometimes exceeded 10 min, a period considered as a maximum by the current aviation industry standards (in Section 6.2).

The Manfrotto geared tripod head (see Fig. 6.30) was selected in order to both minimise the alignment time and increase system's stability. The head offers precise geared movement in 3 directions, namely pan, tilt and levelling (i.e. side-to-side tilt). It incorporates a quick release camera plate system and is suitable for both transmitter and receiver units. It also incorporates a unique feature that allows the instant disengagement of the gears and rough positioning of the transmitter/receiver unit by hand, followed by instant re-engagement for ultra-precise final alignment (Manfrotto, 2008). After the alignment fine-tuning, the head mounts in place offering exemplary stability for both transmissometer units (i.e the centroid of the LED's

image is located with ±1.5 pixel accuracy, even under windy conditions, as shown in Figures 6.31 and 6.32).

Figure 6.30: The Manfrotto 410 geared head (Manfrotto, 2008).

The incorporation of the 410 Manfrotto geared head into the ATMX-II and subsequent transmissometers reduced the length of the alignment procedure to less than five minutes. In addition, the three dimensional plot of the LED spot revealed a more precise alignment in comparison with that achieved without the geared head over a 20-25 min period.

Testing the ATMX-II transmissometer's stability under strong winds

The 'windy test' was performed on 31/03/08. The test took place on the roof of the Physics Department, with clear skies (i.e. visibility greater than 30 km), for a baseline distance of 25 m and at a height of approximately 1.8 m. In the vicinity of the transmissometer set up there is a weather station installed originally to support astronomical observations. It offers information about the temperature, wind speed and rain fall. At the time of the test the average wind speed was 35 mph while occasional gusts of over 45 mph were registered.

The stability of the geared head was checked by plotting the centroid coordinates during the course of a typical measurement (see Figures 6.31, 6.32).

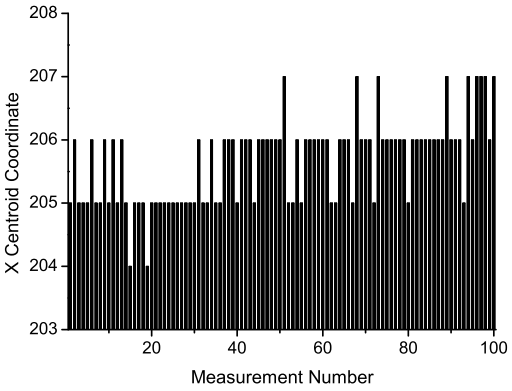

Figure 6.31: Variation of the x centroid coordinate as a function of time in the ATMX-II under windy conditions. Maximum deviation is 3 pixels

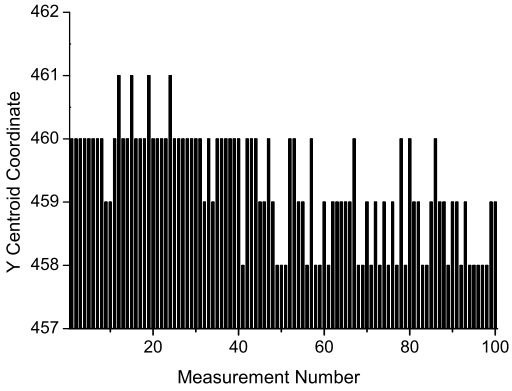

Figure 6.32: Variation of the y centroid coordinate as a function of time in the ATMX-II under windy conditions. Maximum deviation is 3 pixels.

The biggest deviation of the mean centroid position (460,205) is 3 pixels in both directions. The uncertainty in estimating the centroid is about one pixel itself. Thus, the Manfrotto 410 geared head offers acceptable stability even when tested under strong, gusty winds.

Testing the ATMX-II resolution under strong winds exceeding 40 mph

After establishing the stability of the the ATMX-II transmissometer we took this opportunity to estimate the 'real-life' resolution of the new instrument under strong winds.

We have two tools at our disposal in order to produce small but detectable changes in the LED output: either by altering the LED's driving current or by using a neutral density filter. The resolution achievable by neutral density filters is dictated by the filter with optical density 0.04 providing a $\sim 8.8\%$ difference in transmittance. On the other hand, one can scale the driving current in 1% steps offering an average resolution in transmittance of 0.98% (min: 0.65%, max 1.35%). Thus, for testing the new system's resolution under the worst case scenario (strong winds coupled with the use of a diffuser) the driving current was increased with 1% steps from 63% to 70% of its maximum. The results are shown in Figure 6.33.

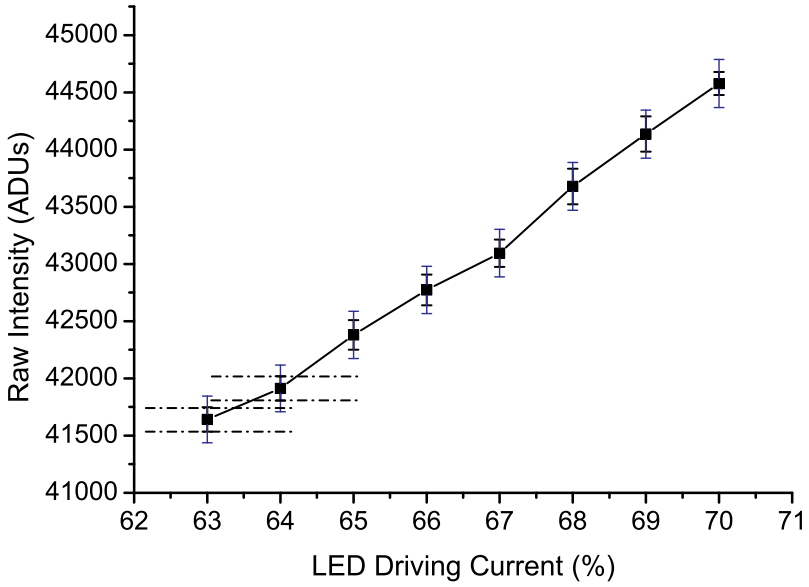

Figure 6.33: Registered raw intensity for different LED driving currents in the ATMX-II under windy conditions.

In Fig. 6.33, the standard deviation of each point - corresponding to the average value of 10 measurements - is denoted with the black error bars whereas the expected Poisson noise of the measured signal is identified by the blue ones. According to Fig. 6.33 the smallest change in transmittance (i.e. 0.65%) is registered when increasing the driving current from 63 to 64%. Thus, Figure 6.33 suggests that the smallest achievable change in the LED output (i.e. for driving currents of 63 and 64%) can be clearly identified by the camera lying outside the bounds formed by the measurement uncertainty. One might also note that the standard deviation of the measurements exceeds the value quoted on Fig. 6.38. That can be easily explained by statistics as in the resolution test each check point corresponds to 10 measurements in comparison with the 30 needed for the diffuser test. Indeed, a second test was performed at the end of the resolution test for the nominal values of driving current and baseline (i.e. 35% and 25 m respectively). In this case the signal has been extracted as the average of 30 neighbouring measurements (see Fig. 6.34).

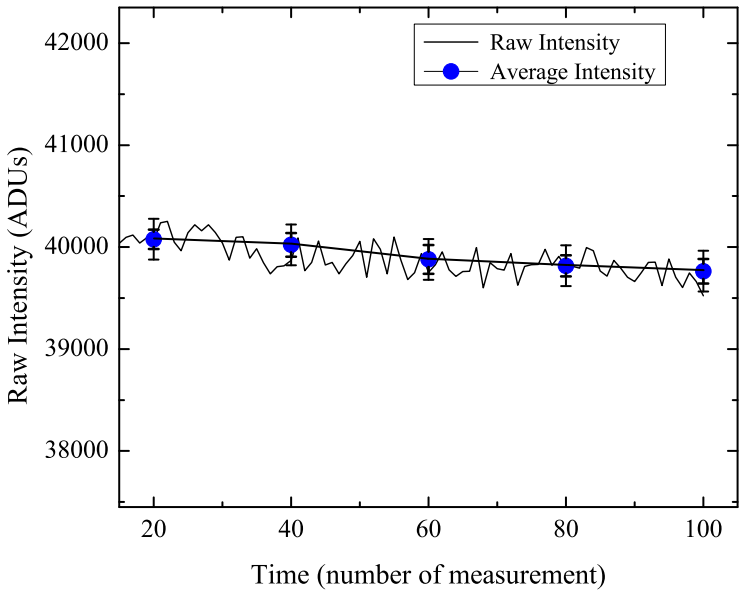

Figure 6.34: Variation of the CCD registered intensity in the ATMX-II under clear atmospheric condition and gusty winds of 45 mph.

Thus, RMS decreases from 133.4 to 78.4 ADUs for signals computed as the average of 10 and 30 single measurements respectively. The theoretical relation between the calculated RMS is:

$$\sigma_{10} = \sigma_{30}\sqrt{3} \tag{6.32}$$

The theoretically derived value for σ_{30} is 77.11 ADUs, therefore within the measuring uncertainty, essentially identical with the experimentally derived value of 78.4 ADUs (i.e. the difference between theoretically and experimentally derived values is only 1.6%).

6.10.2 Re-examining the use of a diffuser on the ATMX-II system

The telescope-based ATMX-II transmitter allowed for a very detailed mapping of the LED spot, revealing potential problems with the use of the ThorLab diffuser

described earlier in Section 6.7.3. The diffuser is used in order to produce 'top-hat' signal in an effort to calculate the representative signal's intensity via an increased number of pixels minimising, therefore, the relevant uncertainty. The magnified projection of the LED into the CCD camera revealed the following problems that could potentially compromise the transmissometer's efficiency:

- the construction of the diffuser can be mapped onto the camera, increasing the standard deviation of the extracted intensity,
- the engineered diffuser can potentially lower the efficiency of the camera in detecting small changes in the intensity.

In addition, the use of any diffuser would limit:

- the LED output,
- the transmissometer's operating frequency, as the use of a larger aperture for extracting the signal's intensity will increase the processing time.

In order to quantify the effect of the first list of potential problems on the extracted signal, one has to define an optimised measuring aperture for the new system with and without diffuser and compare their relevant standard deviations. This procedure has been performed already for the ATMX-I unit (see Section 6.7.3). The transmissometer's software allows the control of the measuring aperture by altering n that is related to the aperture length by:

$$\text{Aperture Size} = 2 \times \text{n} + 1 \tag{6.33}$$

For the new system optimisation, n is allowed to increase between 1 and 6 leading to six measuring apertures ranging from 3×3 to 13×13 pixels. The optimised measuring aperture is determined as the aperture that yields the minimum standard deviation over average signal ratio.

Both tests were performed under identical atmospheric conditions and system configurations. The mean value of each different aperture used was extracted as the average of 30 measurements, for both cases, taking into account the suggested

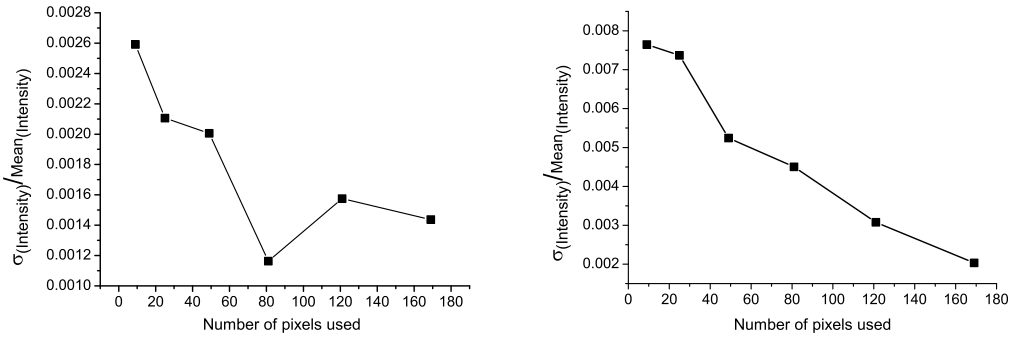

Figure 6.35: The standard deviation of the mean value of the measured intensity over the mean intensity is plotted against the number of the pixels used for its calculation (measurement performed with ATMX-II under strong winds). Left Panel: ATMX-II equipped without diffuser. Right Panel: ATMX-II equipped with ED1-S20 diffuser.

1 min average in reporting the transmittance/visibility value according to the current aviation industry consensus.

Figure 6.35 suggests the use of square measuring apertures with sides 6 and 4 pixels for the measurements with and without diffuser respectively. One might notice that the test with diffuser terminates at n=6 (13×13 pixels aperture) possibly before the minimum ratio has been reached. The culprit is the processing time approaching the download time limiting the ATMX-II's operating frequency.

These results offer a first insight on the ATMX-II's accuracy. The standard deviation of the average value of 30 measurements are 75 and 60 ADUs for optimised aperture tests (i.e n=6 and n=4) with and without diffuser respectively, giving the slight advantage to the no-diffuser solution. Both values lie well below the expected photon induced noise of $\sim$ 200 ADUs. In order to determine the set-up that yields the minimum uncertainty a thorough test was performed.

6.10.3 Comparison between different configurations for the ATMX-II

The comparison tests were performed on the 1/04/08 under windy conditions (i.e. 30-35 mph). The experimental setup was similar with the one described in Section

6.10.1 (i.e. baseline = 25 m, visibility > 30 km).

In order to better visualise the projection of the LED into the CCD camera during the tests both vertical and horizontal histograms of the registered LED intensity have been plotted while the colour map of the intensity is shown in the middle of each graph (see Figures 6.36, 6.37).

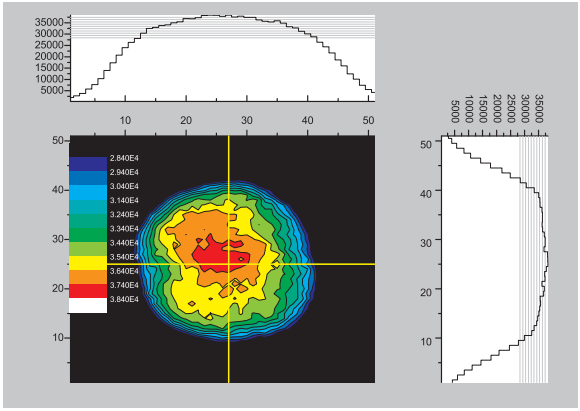

Figure 6.36: Detailed profile of the LED spot with diffuser.

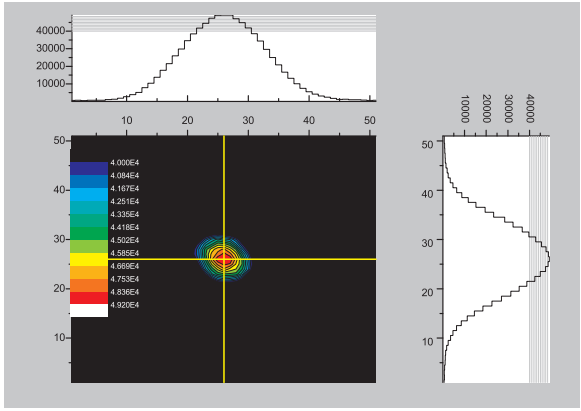

Figure 6.37: Detailed profile of the LED spot without diffuser.

The almost perfect Gaussian fit of the intensity histograms presented in Fig. 6.37 argue for a set-up without diffuser, however one should remember that the use of the diffuser allows the sampling of more pixels, leading to a reduced uncertainty. The data from both tests were plotted and the relevant standard deviation is shown in Fig. 6.38.

Figure 6.38 shows the typical variation around the mean intensity over 30 measurements for the new instrument and the best value attained for the same system with the addition of a diffuser (the typical standard deviation is 78.4 ADUs). The results are very similar and suggest that taking out the diffuser would give a slightly more responsive system for less cost.

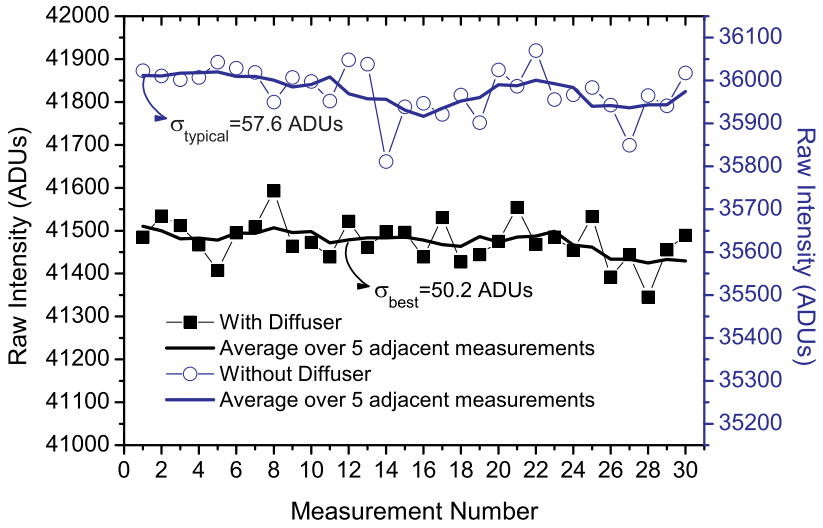

Figure 6.38: Comparison of intensity variation retrieved with and without diffuser.

6.11 The Threshold-Based Algorithm

6.11.1 The limitations of the ATIK-16 Camera

After the software and hardware optimisation of the ATMX-II it became apparent that its performance in terms of resolution and frequency is limited by:

- The 1 minute RMS values being one order of magnitude higher than the physical limitation of 13 ADUs dictated by the CCD read-out noise.
- The 5 seconds full frame download time of the used CCD sensor (ATIK Instruments, 2007)

As both limitations are directly related to the CCD sensor performance (i.e. resolution in transmittance is limited by the CCD 8-bit dynamic range over exposure time) the author searched for a CCD sensor offering higher performance while meeting the strict manufacturing budget set in Section 6.2. In the next section the reasoning behind the selection of the final instrument's design and components, as dictated by the manufacturing budget of £ 8000, will be discussed. Furthermore, the compromises, induced by the budget-driven selections, in terms of accuracy in

transmittance will be measured. It will be seen that one should be constantly aware of the CCD - and electronics - market, as even a one year difference between equally priced components may correspond to a performance increase capable of simplifying the measuring algorithm which in turn greatly improves the instrument's resolution.

6.11.2 Motivation for the threshold-based Measuring Algorithm

In the beginning of the project, the set manufacturing budget (see 6.2) dictated the purchase of the ATIK-16 CCD camera (see Section 6.5.1) equipped with a 16 bit converter offering a wide dynamic range of 65536 levels of grey. The limiting factor is set, however, by the 8 bit dynamic range over exposure time. The proven linearity of the CCD camera over exposure time (see Fig. 6.20) suggests the use of the exposure time alone is sufficient to cover the whole transmittance range without sacrificing accuracy. However, the limited resolution over exposure time of the current CCD camera is extended, in order to cover the whole transmittance range, by the following:

- increasing the LED driving current at low visibility conditions, and
- extracting a value for the intensity of the whole LED induced spot from a small measuring window located near the top of the intensity distribution.

Both methods result in a reduction of the accuracy in measuring the atmospheric transmittance. Indeed, modulating the driving current results in the LED's temperature instabilities compromising the ATMX-II's accuracy. As a light output control was not installed in the ATMX-II, a nonlinearity of 4.5% of the CCD response over different LED driving currents was observed (see Fig. 6.19).

In the same manner, the use of a small measuring window fixed at the top of the intensity distribution would yield a representative value for the whole LED intensity without sacrificing much of the CCD's dynamic range. Specifically, the measuring algorithm begins by setting a proper exposure time leading to a brightest pixel value of ~ 40000 ADUs. Thus, if one uses a small measuring aperture around

the centroid of the intensity distribution (7×7, or 11×11), accounting for $\sim 5\%$ of the whole light spot, the average intensity value would be $\sim$ 38500 ADUs (i.e. allowing the exploration of the full dynamic range) in comparison with an average value of $\sim$ 25500 ADUs obtained by the use of $\sim 80\%$ of the light spot. The use of a small measuring window leads to uncertainties (i.e. 1 min variation of measuring transmittance) of $\sim 90-130$ ADUs, one order of magnitude higher than the physical limitation of 13 ADUs dictated by the CCD read-out noise (see Fig. 6.45).

Fortunately, a few weeks after the completion of ATMX-II instrument (i.e. May 2008), an upgraded model of the CCD camera, namely the ATIK-314E, became available conveniently priced at £ 784. This camera offers a 16-bit dynamic range over exposure time with a 1 μs steps in comparison with the 8-bit range coupled with 1 ms resolution offered by its predecessor, the ATIK-16. The use of the new CCD camera would allow a more precise determination of the LED intensity by integrating over all 'signal containing' pixels. In addition to the enhanced dynamic range over exposure time the new camera offers:

- a USB-2.0 performance leading to a 1.6 s full-frame download time (i.e. the relevant period for the current camera is 5 s), and
- a read out noise of 4 e^-, a vast improvement in comparison with the 13 e^- read-out noise of the CCD camera in use.

Thus, the use of the new CCD camera would offer a more accurate transmissometer that would be able to operate at higher frequency.

The delivery of the ATIK-314E CCD camera, however, was much delayed due to the customised software needed to achieve the 1 μs resolution in exposure time. Thus, it was decided to implement the background threshold based algorithm, which would be used for the ATIK-314E camera, in the ATIK-16 camera while awaiting the new one. The implementation of the optimisation of this new background algorithm into the ATIK-16 camera will be the subject of the following Sections.

6.11.3 Implementation of threshold-based measuring algorithm

The simplest and quickest way to implement the new measuring algorithm is by setting a threshold based on the value of the background corrected brightest pixel intensity. In this manner, all pixels are scanned but only those exceeding the threshold value are selected for analysis. A simple test was devised to determine the optimum threshold. Firstly, the threshold has been increased from 5% to 70% of the brightest pixel intensity with an initial step of 5% followed by 10% steps. All measurements have been taken over a 1 min measuring period. The results are shown in Figure 6.39. The effect of threshold on both measured intensity and the number of pixels used for this calculation is presented. As expected, an increase in the selecting threshold yields higher values of intensity that has been averaged over a smaller number of pixels. Figure 6.39 suggests that the compromise between statistics and intensity is achieved for a threshold value of $\sim$ 25%. Thus, for determining the optimum threshold value, a new test was performed covering the threshold range $13\% - 30\%$ with a 1% resolution around the expected optimum of 25%.

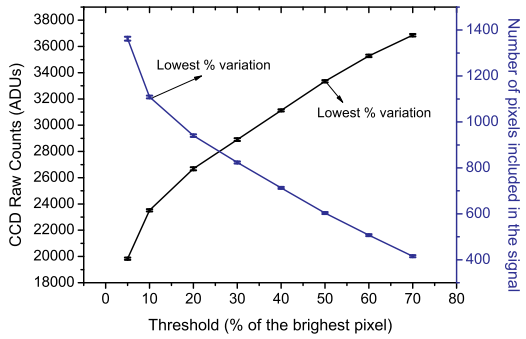

Figure 6.39: The effect of the threshold selection on LED intensity and the number of pixels used for its calculation.

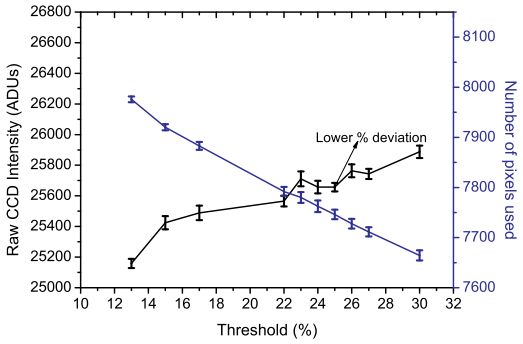

Figure 6.40: The effect of the threshold selection on LED intensity and the number of pixels used for its calculation.

Figure 6.40 confirms that the optimum threshold value is 25%. The variation of a typical 1 min intensity measurement is shown in Fig. 6.41. The standard deviation of $\sim$ 28 ADUs approaches the limit imposed by the read-out noise of

13 ADUs (without taking into account the other electronics). The fluctuation of the number of pixels exceeding the set threshold during the measurement is also shown in Fig. 6.40. The expected anti-correlation between the determined intensity and the number of pixels used in the determination should not be present within the 9.4 pixels RMS of the fluctuation. That is more evident in Fig. 6.42 where least-square regression gives a small anti-correlation of $r^2 = 0.11$ which is not statistically different from no correlation.

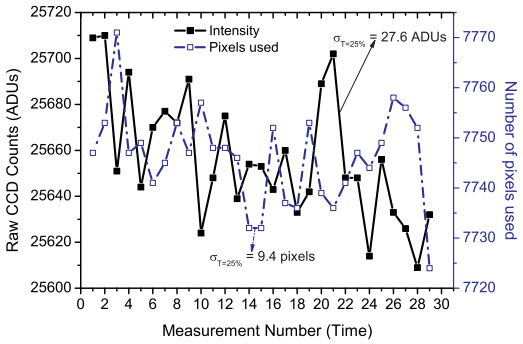

Figure 6.41: Variation of the LED intensity for a typical 1 min measurement at a fixed threshold of 25%. The variation of the numbers of pixels used in each intensity measurement is also shown.

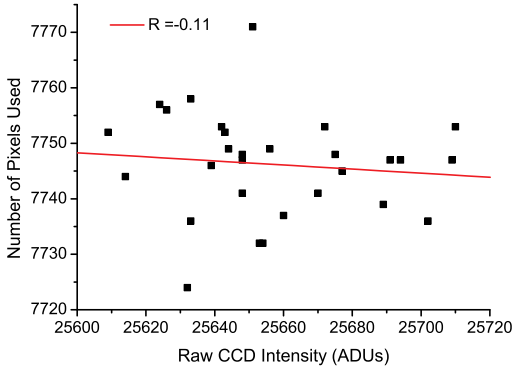

Figure 6.42: LED measured intensity versus the numbers of pixels used in the determination at a fixed threshold of 25%.

6.11.4 Optimisation of the threshold-based measuring algorithm

The new measuring algorithm works by a setting a threshold based on the brightest pixel of the LED's light spot. This method was implemented for the sake of simplicity in order to provide a quick comparison between the different measuring approaches, namely using a measuring window of 7×7 pixels as opposed to using 75% of the signal, corresponding to thousands of pixels. The implementation of the new method brought the standard deviation of the signal averaged over 30 measurements (i.e. 1 min measurement interval) down to 30 ADUs from an average value of $\sim$ 110 ADUs

(see Section 6.10.3). The Achilles heel of this simple algorithm, however, is that it depends solely on the value of the brightest pixel, which might vary considerably. A better statistical method was devised based upon the mean and the standard deviation of the background intensity:

- the OFF image is scanned and the mean intensity and its variation are calculated (<IOFF>, $\sigma_{\rm OFF}$), and
- The ON image is scanned and all pixels with values lying 5σ above the background average value are integrated to derive the signal's mean intensity:

$$\begin{aligned} x_i > \text{Threshold} &= < \mathrm{I_{OFF}} > + 5\sigma_{\rm OFF} \quad \text{and} \\ \text{Signal} &= \frac{\sum_{i=1}^{N} x_i}{N} \end{aligned} \tag{6.34}$$

  where x_i is the ith pixel and N is the number of pixels that satisfy Equation 6.34.

By setting the threshold at 5σ above the average noise counts we make certain that only signal containing pixels will be used in extracting the signal value. Indeed, the probability that a background pixel will lie above a range of 3.290σ is only 0.1%. The assumption behind this evaluation is that both background and signal's registered counts are well approximated by a Gaussian distribution. That is a valid assumption, however, since even the smallest background rate registered by the camera, namely a background due to read-out noise of 250 ± 30 ADUs, is large enough that the Poisson distribution (expected for both signal and background) is well approximated by a Gaussian.

The next logical step entails the use of distance cuts in conjunction with the threshold method currently used. The use of an 'astronomical'-like algorithm to identify the LED's projected light-spot borders starting from either the brightest pixel or the centroid is also under consideration. Such a code can be used to control stepping-motors for the automatic alignment of the transmissometer, or, if that is proven to be economically inefficient, to warn the user of a requirement for manual re-alignment.

The benefits of using this stable measuring algorithm as opposed to a fixed (9×9 or 13×13) pixel aperture are listed below:

1. Optimum transmittance resolution.

   The typical standard deviation for the average intensity value over $1-$ min reporting intervals has been brought down to read-out noise fluctuation that sets the physical limit on the attainable transmittance resolution (i.e. ~ 18 ADUs, see Figure 6.43). The daily fluctuations of the one minute intensity values, under controllable atmospheric conditions within the lab, will be presented in Section 6.12.

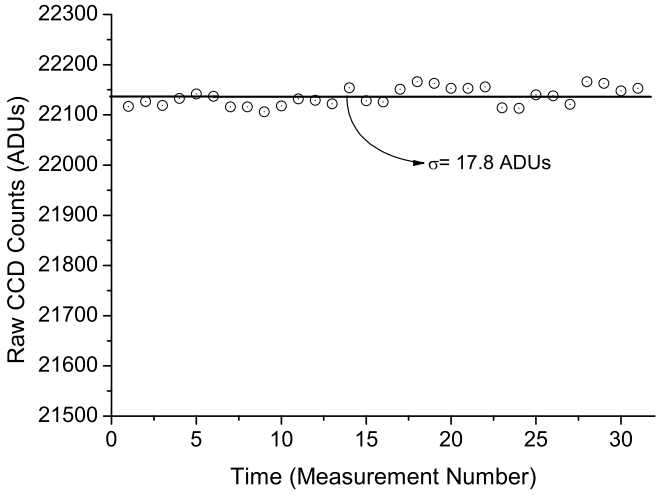

Figure 6.43: Variation of the LED intensity for a typical 1 min measurement by using the background optimised threshold.

2. Minimal signal fluctuation related to the brightest pixel's displacement.

   The small aperture algorithm was very sensitive to vibrations of the LED light beam primarily caused by gusty winds. Temperature variations and earth movement can also cause misalignment between receiver and transmitter in the long term. Indeed, the use of small measuring window (e.g. 9×9 pixels for a system without diffuser, see Section 6.10.2) to calculate the intensity of the whole LED induced light spot assumes a symmetric and homogeneous light

beam. In order to better visualise the LED induced light spot onto the CCD camera, under windy conditions, one could plot the profiles of the intensity along the orthogonal lines crossing the brightest pixel (or centroid) followed by the relevant 2-d colour diagram of the light spot. A grey scale 2-d representation of the light spot has also been plotted followed by its 3-d schematic. This three-fold visualisation allows us to take a snap-shot of the light spot and examine the symmetry and homogeneity of its intensity distribution. In addition, the alignment of the instrument, under windy conditions, can also be checked. A quick comparison of the one, two and three dimensional intensity distributions, obtained under extreme weather conditions (see Figures 6.44), with those obtained under moderate wind (see Fig. 6.37) convinces us that symmetry is not preserved for winds approaching the top end of the external environmental specifications (see Section 6.2). For a more quantitative comparison, the RMS of the measurements performed under extremely windy conditions for two set-ups with and without the ED1-S20 diffuser, has been calculated and their typical fluctuation corresponding to 1 min data taking is shown in Fig. 6.45. The results obtained without the diffuser possess the greater variation (i.e. $\sigma = 216.3$ ADUs) over the whole range of different set-ups tested, whereas the relevant RMS value for measurements taken with the diffuser is 168.8 ADUs. That seems to be in conflict with the results obtained in Section 6.10.3 yielding smaller fluctuations for the ATMX-II without a diffuser. A closer look at the data, in the case of the set-up without diffuser, convinces us that the measured 1 min fluctuation has been magnified by the abnormal intensity minima corresponding to the second, seventh and fifteenth measurement number respectively. Indeed, the plot of the variation of the brightest pixel coordinates over the same period revealed a perfect correlation as each intensity minimum corresponds to a jump of the brightest pixel coordinates (see Fig. 6.45). A displacement of the brightest point by just one pixel corresponds to a 2% difference on the registered intensity. One has to discard these pixels (3 out of 20) in order to bring the intensity variation to an acceptable level (i.e. from 216.3 to 110.5 ADUs, see Fig. 6.45) in accordance with

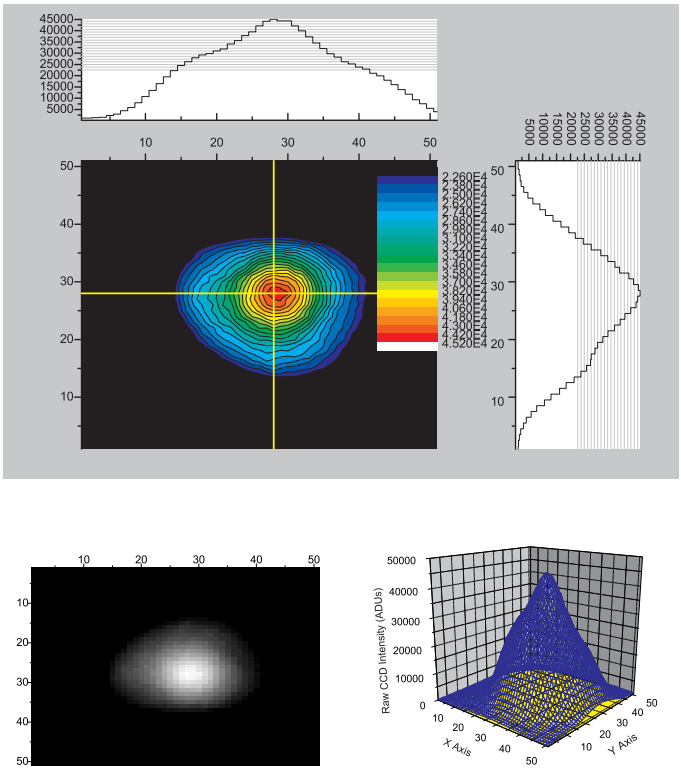

Figure 6.44: Three-fold visualisation of the light spot for LED coupled with optics without the ED1-S20 diffuser under windy conditions: Horizontal and vertical intensities profiles and colour map, grey map and 3-d light spot intensity profile.

results presented in Section 6.10.3. The background threshold-based measuring algorithm was tested, under the same conditions, yielding 1-min intensity and brightest pixel coordinates fluctuation shown in Figures 6.43 and 6.46 respectively. These figures argue for a non-correlation between the brightest pixel coordinate and the intensity measured. The maximum deviation in intensity is 0.2% an order of magnitude better than the small-aperture algorithm. Thus, the background threshold-based algorithm provides optimum resolution independent of the brightest pixel (centroid) displacement even under extreme weather conditions.

The stabilisation of the ATMX-III transmissometer implementing the background based algorithm and leading to the first long term tests will be the subject of Section 6.12.

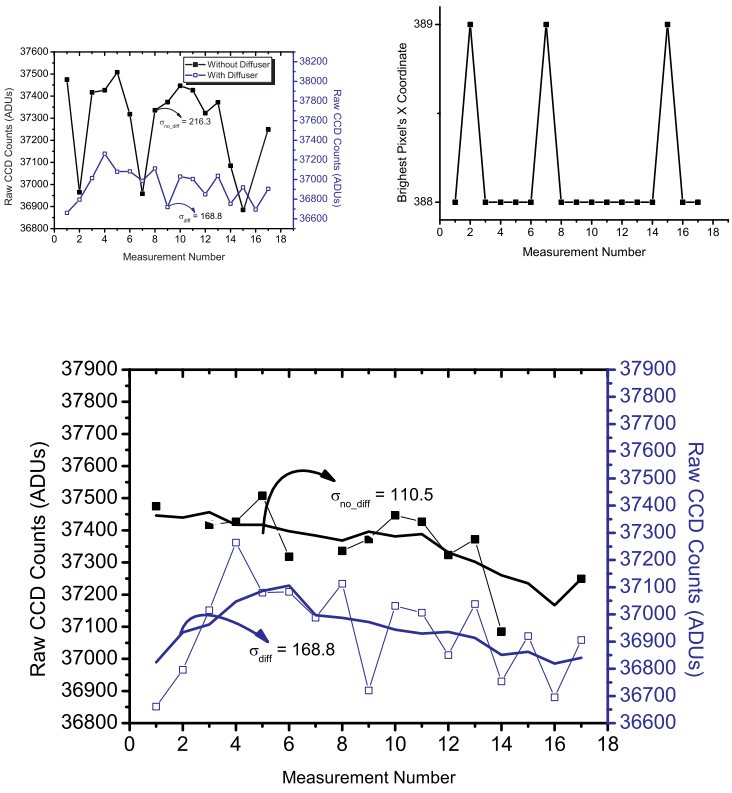

Figure 6.45: Upper panel: Right: CCD raw counts for measurements taken with LED and optics with and without the ED1-S20 diffuser using the ATMX-II. Left: Plot of the X brightest pixel coordinate during the same measurement. Lower panel: CCD registered intensity after filtering out abnormal brightest pixel position.

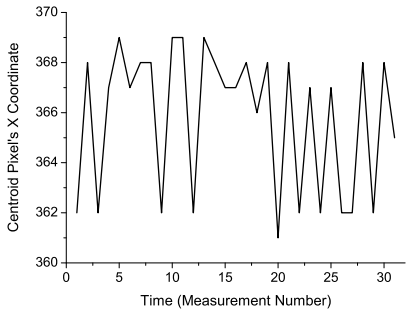

Figure 6.46: Plot of the brightest pixel X coordinate during the measurement shown in Fig. 6.43.

6.12 ATMX-III Stability Tests

6.12.1 Preliminary test inside the laboratory

Upon completion of the light output feedback loop construction, which entailed replacing the PCBs with a laptop and a data acquisition board (see Section 6.9.3), the system has been subjected to short-term tests both inside and outside the lab in order to evaluate its stability. A preliminary test was performed by requesting a stable photodiode light output level, for the green photodiode's sensor, of 3500 ADUs. In order to check the performance of the light source under sharp thermal changes, the LED was subjected to a heat gun operating between segments 85-107 of the measuring period shown in Fig. 6.47. The photodiode's response at the RGB wavelengths over the full 350 measurement cycle is presented in the upper panel of Fig. 6.47. During these tests, the L2K2 warm white LED (see Table 6.2) had been temporarily replaced by the Luxeon© III Star LXHL-LW3C (see Table 5.1), originally used in the DHLT prototype, due to earlier equipment failure. In contrast to the warm white L2K2 emission spectrum (i.e. 3000 K CCT, see Fig. 6.24), the cool (i.e. 5500 K CCT) LXHL-LW3C LED's spectral power distribution possesses a narrow emission peak at $\sim$ 435 nm followed by a secondary much wider peak at $\sim$ 550 nm (see Fig. 5.2). The agreement between the expected and measured emission spectra has been checked by extracting the normalised intensity values at the RGB wavelengths from Figure 5.2 (i.e. 0.29 at 615 nm, 0.45 at 540 nm and 0.16 at 465 nm) and comparing the R/G, B/G and B/R ratios with the relative RGB intensities registered during the short tests presented in Figures 6.47 and 6.48 (see Table 6.3). The agreement between expected and measured relative intensities is excellent, taking into account that the experimental error in extracting the normalised intensity from Fig. 5.2 can be as high as 12.5% around 465 nm due to the limited resolution in wavelength ($\pm$1 nm) combined with the very narrow emission peak at $\sim$ 435 nm.

The ability of the transmitter's controlling algorithm to produce a stable light output, even under accute ambient temperature changes, has been verified by forming the normalised histograms of the green photodiode's sensor amplitudes presented

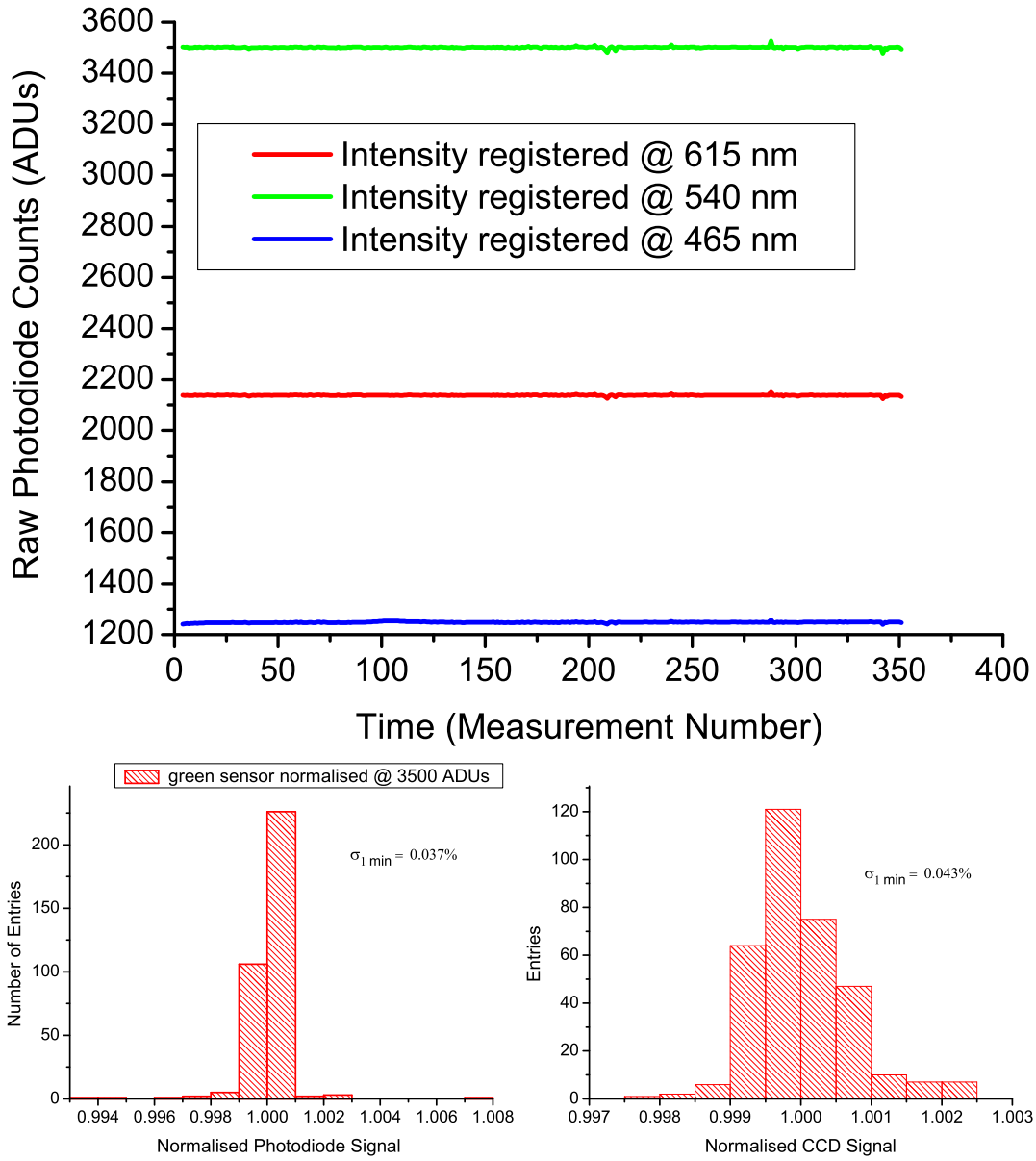

Figure 6.47: Upper Panel: Short term variation of the photodiode's signal from its green, red and blue sensors. A heatgun was applied to the LED between measurements 85-107. Lower Panel. Left:Mean normalised amplitude distribution of the photodiode's green (controlled) signal over the 350 measurement cycle. Right:Mean normalised amplitude distribution of the CCD signal over the 350 measurement cycle.

in Fig. 6.47 (i.e. lower panel, left). The typical RMS over a 1-min measurement cycle is 0.037%. Thus, the accuracy of the method is essentially limited by the photodiode's 12-bit serial output, leading to an ideal resolution of 0.024%. For

Ratio	Expected	Measured		Average Deviation
	From Fig. 5.2	From Fig. 6.47	From Fig. 6.48	(%)
R/G	0.644	0.611	0.625	0.4
B/G	0.355	0.357	0.350	1.0
B/R	0.552	0.583	0.560	3.5

Table 6.3: Comparison between the expected and measured intensity distribution at RGB wavelengths

this reason, the stability of the light transmitter has been simultaneously checked against the more sensitive 16-bit camera. Figure 6.47 (i.e. lower panel, right) shows the mean normalised response of the CCD camera yielding the more realistic 0.043% 1-min instability for the light-source. It should be noted, however, that maintaining a steady light output (i.e. independent of the LED temperature fluncuations) at 540 nm can not secure stable emission spectra over longer periods. Indeed, LED emission temperature depends strongly on junction temperature; not only do temperature variations introduce changes in LED intensity, but the wavelength of the emitted radiation shifts towards higher values with increasing LED temperature. The effect of the the LED's spectral drift with temperature became apparent during the long-term stability tests (see Section 6.12.3) leading to the implementation of an additional temperature feedback loop (see Sections 6.9.3, 6.13). The resolution of teething problems related to the newly-built ATMX-III instrument that allowed for these long-term stability tests will be the subject of the next section.

6.12.2 Short-term test outside the laboratory and teething problem resolution

A longer test was performed on the roof of the Physics Department on October 28th 2009. The intensity level was set at 4000 ADUs (using the green sensor photodiode) for 1530 measurement cycles, corresponding to 3 hours from 15:14 UT to 18:13 UT. The variation of the RGB photodiode sensor signal over this period is shown in Fig. 6.48.

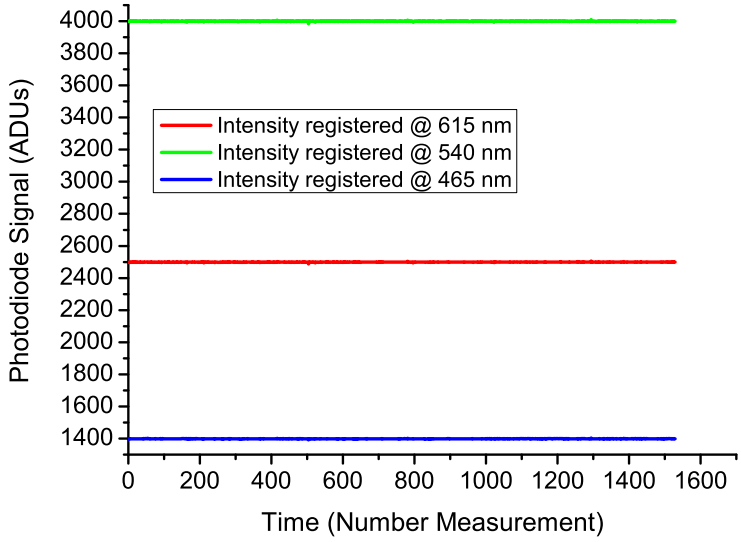

Figure 6.48: Variation of the photodiode's RGB sensors for the 3h test.

Figure 6.48 revealed a problem with instantaneous erratic readings that are present as the lines appearing simultaneously in the three wavelength channels. The problem has been identified as the erratic fluctuations of the D/A output. The implementation of a low pass filter stabilised the D/A output resolving the problem. However, conducting uninterrupted test for periods longer than $\sim$ 3 h has proved difficult due to frequent CCD sensor stalls and PC resets. The CCD malfunction was attributed to the frequent transmission of broken data packages between the transmitter and the receiver. The implementation of a simple check-sum secured transmission of complete packages only. The frequent PC reset problem was related to the erratic fluctuations of the mains supply probably caused by the intermittent use of the Physics Department elevator. The acquisition of the Smart-UPS (APC, 2006) secured the PC's uninterrupted operation. These changes allowed for long-term stability tests that will be the subject of the next section.

In order to evaluate the mid-term stability of the ATMX-III transmitter from the collected data (see Fig. 6.48), one could filter out the erratic measurements and proceed in the manner of Section 6.12.1. The distribution of the photodiode's registered amplitudes at 540 nm is given in Fig. 6.49 and the relevant plot for the CCD's registered signal is provided in Figure 6.50.

The width of the distribution in Fig. 6.49 corresponds to a FWHM fluctuation of

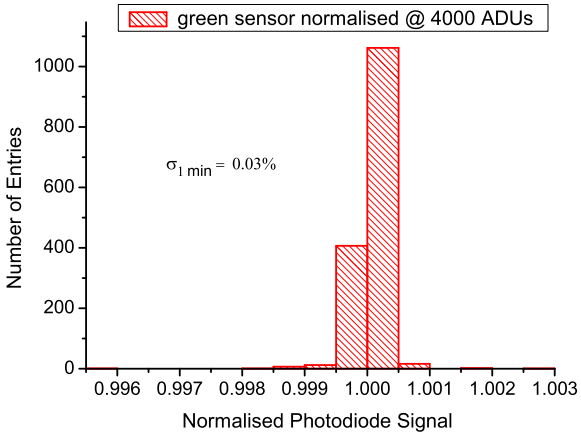

Figure 6.49: Mean normalised amplitude distribution of photodiode's green (controlled) signal over the 3 h test.

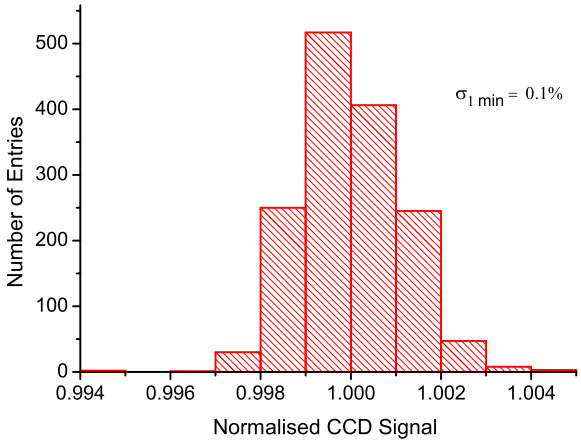

Figure 6.50: Mean normalised amplitude distribution of CCD signal over the 3 h test.

1.5 ADUs arguing that upgrading into a higher serial output dynamic range (i.e. 14-16 bit) is the only way to improve the transmitter's accuracy. This is also supported by the fact that the RMS of photodiode's green sensor distribution, obtained by using all available data, is equal to the typical fluctuation over the 1-min averaged data (i.e. $\sim 0.3\%$).

The stability of the ATMX-III over the short 3 h test is presented in Figure 6.50. The RMS has been calculated using the data registered by the CCD sensor and their 1-min average values (see Table 6.4). The richer structure appearing in the histogram of Figure 6.50 can be explained in terms of the higher sensitivity of the 16-bit CCD camera. The measured typical RMS over the 3 h measurement is four times larger that the one calculated for the green photodiode response, a deviation not observed in the shorter-term stability test (see Section 6.12.1). The possibility of spectral shift over the short time test was checked by plotting the normalised histogram of photodiode's red sensor response (see Fig. 6.51). The RMS of this distribution is 0.04% showing a very stable LED signal at 615nm. The observed difference can be explained, therefore, by the fact that the baseline of this test has been set to the nominal value of 25 m and the test was performed under real (i.e. out of the lab) conditions. Thus the CCD responds, in addition to the LED luminous output, to visibility. The stability of the configuration ATMX-III has been

tested under short term tests yielding acceptable results. In the next section the ATMX-III's mid- and long term stability will be established.

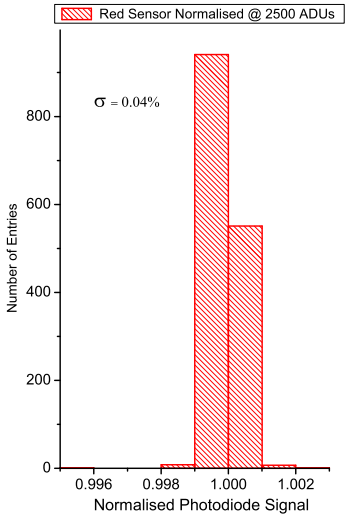

Figure 6.51: Mean normalised amplitude distribution of photodiode's red (uncontrolled) signal over the 3 h test.

6.12.3 Long Term tests

The software and hardware changes described in the previous Section allowed for a smooth transmissometer operation free of stalls, resets and spurious readings. In order to establish the long-term stability of the transmissometer, a three day test was conducted between 14^{th}-19^{th} January 2009. The test was performed inside the lab at a baseline of ~ 5 m to exclude fluctuation due to atmospheric changes. The time variation of the CCD signal and background measurements are shown in Fig. 6.52.

Figure 6.52 shows the expected independence between CCD signal and background. It also reveals a periodic fluctuation of signal between diurnal and nocturnal conditions. In order to evaluate the effect of this diurnal/nocturnal variation the histogram of the CCD's registered signal amplitude has been plotted in Fig. 6.53.

The peaks corresponding to the maximum/minimum amplitudes registered during nocturnal/diurnal conditions are clearly identifiable. The diurnal/nocturnal fluctuation occurs despite the implementation of the feedback output loop that se-

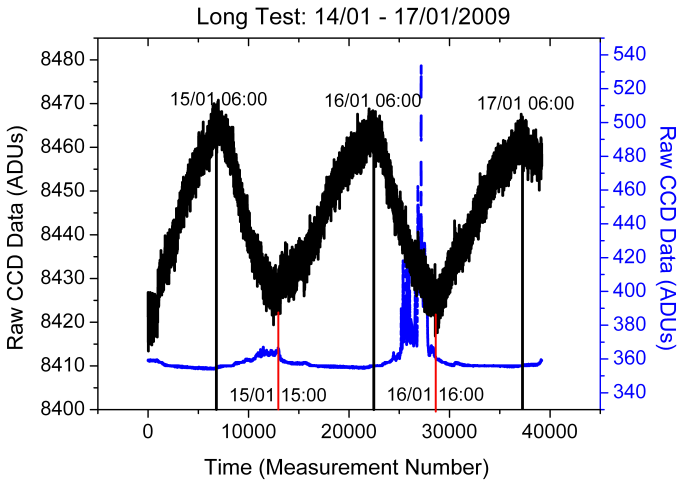

Figure 6.52: Variation of the CCD registered signal and background over the 3 day test of the ATMX-III system.

cures a constant emission at 540 nm independent of temperature changes. This can be explained by the fact that a temperature rise of the LED's junction temperature will result in a decrease of the light intensity followed by an increase in the peak emission wavelength and usually an increase in the spectral bandwidth (Murtaza and Senior, 1994). The spectral bandwidth change is much smaller compared with the white LED bandwidth so its effect can be safely neglected. Thus, securing a constant LED emission at 540 nm cannot guarantee the optical source output stability due to the spectral shift associated with temperature fluctuations. The magnitude of the spectral shift is quantified by the temperature coefficient of spectral shift (i.e. $K_s = \Delta\lambda_D/\Delta T_J$) and its value is usually provided within the specification of monochromatic LEDs (i.e. ranges from 0.04 to 0.09 nm/°C between green and amber for Luxeon K2 LEDs Lumileds (2007)). The spectral emission of the warm-white LED, for a driving current of 1 A and junction temperature of 25 ° C, has been presented in Fig. 6.24. The dependence of its spectral drift can not be defined by a single coefficient and the effect of this drift on the LED measured intensity will also depend on the CCD spectral sensitivity (see Figures 7.11 and 7.12).

The stability of the ATMX-III transmitter was evaluated over 1-day and$\sim$ 3-day (65 h) periods. For the estimation of the ATMX-III instability the RMS of the

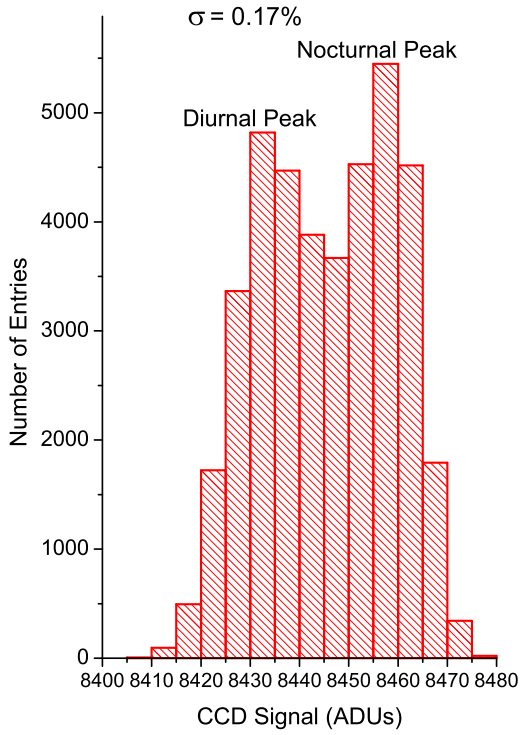

Figure 6.53: Amplitude distribution of CCD signal over the 3-day test.

distributions, formed by the individual and the 1-min averaged measurements, has been calculated (see Table 6.4). As a thermocouple has not been implemented in the ATMX-III transmitter, one can try to correct for the effect of temperature variations shown in Fig. 6.53 by seeking for correlation between the CCD registered signal and the red sensor photodiode signal. The time variation of the CCD signal and photodiode's red sensor is plotted in Fig. 6.54 and indicates a clear anti-correlation between the CCD and red-photodiode registered signals. The CCD signal can be plotted as a function of the photodiode's red signal output and fitted with a straight line to yield the linear fit coefficients (see Fig. 6.55). These coefficients can in turn be used to produce a corrected histogram of the 3-day CCD intensity variation taking into account photodiode's red channel fluctuation. The corrected histogram of the CCD signal variation over the 3-day stability test is provided in Figure 6.56.

Thus, by indirectly correcting the transmissometer signal for temperature variations, via the photodiode's signal at 615 nm, the transmissometer instability, over 1 and 3-day periods, has been reduced by $\sim 42\%$. The alternative method of control-

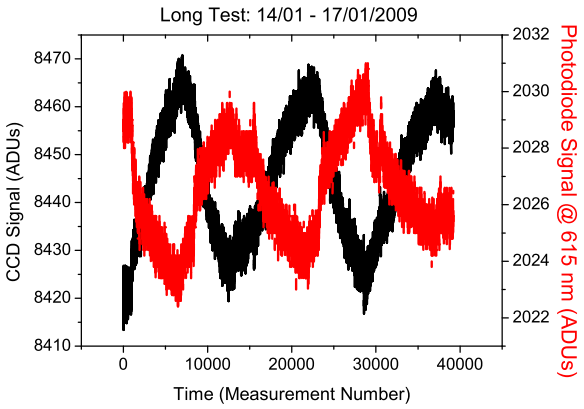

Figure 6.54: Variation of CCD and red sensor photodiode signal during the 68 h test

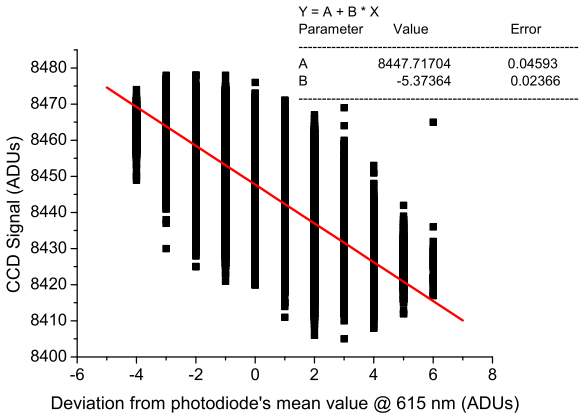

Figure 6.55: CCD 1-min average signal as a function of the photodiode's red sensor deviation from its mean value during the 3 day test

ling the LED intensity by fixing photodiode's red channel response and correcting the transmissometer signal for the green sensor fluctuation has been also tested, yielding increased values for the transmissometer's daily instability (i.e. 0.36% prior to 0.14% after correcting for photodiode signal fluctuation at 540 nm).

Thus, corrections based on the red channel of the photodiode yield an acceptable daily transmissometer fluctuation of 0.1% but suffer from the following side effects:

- A magnification of the 1-min signal variation due to the photodiode's limited resolution, and
- the assumption that any fluctuation of the red photodiode sensor is related to a temperature fluctuation.

Indeed, the application of the red-sensor linear fit coefficients (see Fig. 6.55) to the raw transmissometer data over 1 minute yields a typical RMS fluctuation of 0.6%, thus limiting the transmissometer's resolution by more than one order of magnitude (i.e. 0.043%, see Section 6.12.1). For this reason, the red channel correction does not improve the 1-min averaged data (see Table 6.4). Moreover, any atmospheric fluctuation within the laboratory (relative humidity) will produce a signal variation independent of the photodiode's response yielding additional sources of error for the linear coefficient estimation.

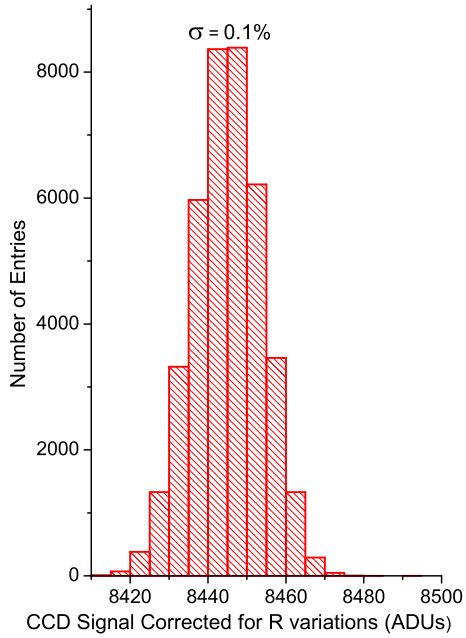

Figure 6.56: Red signal corrected amplitude distribution of CCD signal over 3 days.

These results underline the necessity to thermally stabilise the LED, in addition to its spectral light output stabilisation, an aim which was achieved towards the completion of this thesis (i.e. May 2009). The preliminary results on the performance of the final incarnation of Durham's transmissometer (ATMX-IV) will be the subject of the next section.

6.13 ATMX-IV Tests

The construction of the temperature feedback loop started after reaching a state of a stabilised transmissometer (i.e. capable of operating for more than a month without failure or spurious readings) to allow for a more efficient component-by-component debugging. As the author is currently working (May 2009) towards the implementation of an accurate and stable temperature compensation algorithm, a more simplistic method has been devised to allow the inclusion of the final transmissometer version (i.e. ATMX-IV) results within this thesis. The LED has been directly mounted to a Peltier unit and is equipped with the K-novus (Novus, 2007) thermocouple providing a temperature resolution of 0.1 °C. The temperature read-

ings are used to switch the Peltier unit on/off, setting the LED temperature to a full oscillation within the 1-min measurement interval. Specifically, the simplistic algorithm switches the Peltier unit on at the beginning of the measurement, driving the LED towards lower temperatures.When the LED temperature drops below a predetermined level (i.e. 10 °C) the Peltier unit is switched off. This causes the LED temperature to oscillate around the fixed temperature with max/min temperature values of ±1.5°C. The period of the LED's temperature oscillation is approximately 1-min (see Fig. 6.57) allowing for very stable 1-min intensity values.

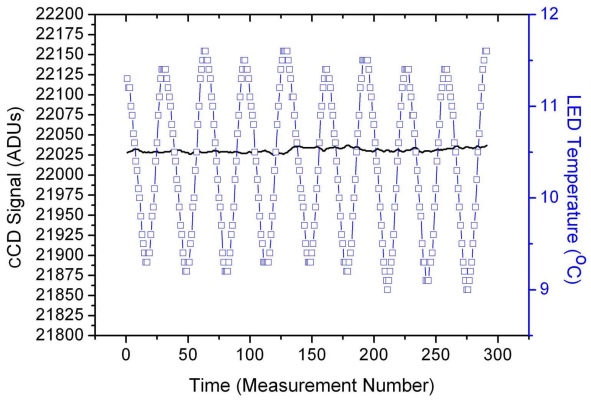

Figure 6.57: Time variation of the CCD signal and LED temperature.

For this short test photodiode's light output was set at 2500 ADUs and the temperature cut off level to 10 °C. The raw CCD signal varies by as much as 220 ADUs (i.e. 1%) due to the temperature oscillation and its RMS value is 0.15%. However, the 1-min averaged CCD signal possesses a maximum/minimum variation of 12 ADUs, a value comparable to the CCD physical limitation due to read-out noise, yielding an RMS of 0.012%. An initial 2 h test yielded an RMS fluctuation of 0.05% (see Table 6.4). It should be noted, however, that ATMX-IV exemplary stability, proven by the short-term test, has resulted in an instrument very sensitive to the small atmospheric variations more probable to occur during the longer-term tests. A noticeable drop in the stable ATMX-IV signal was present each time one of the observers entered the lab to check the progress of the longer test. It eventually became apparent that the ATMX-IV was responding to the increased water vapour intro-

duced by the testers' hot beverages. The ATMX-IV exemplary resolution allowed us, for the first time, to disentangle minor atmospheric differences within the laboratory over the small baseline of ~ 5 m. Thus, in order to determine the mid and long term stability of Durham's transmissometer final version (i.e. ATMX-IV) one has to make use of a standardised air tunnel in accordance with airport transmissometer specifications (Clark, 2008).

A more sophisticated algorithm allowing for a linear temperature compensation via the Peltier driving current is currently being devised. It is expected that the temperature oscillation can be limited to ± 0.1°C. The advantages of the LED's stable light output at 540 nm and temperature control are:

- Optimum resolution in transmittance, which is reduced only by the CCD's electronic noise fluctuation,
- elimination of the magnification of 1-min RMS error associated with the R-channel based correction, and
- an extended MTBF for the thermally stable LED.

When compared with the ATIK-16, the ATIK-314E exhibits an electronic noise fluctuation which is lower by a factor of ~ 3. Consequently, its incorporation into the ATMX-IV is expected to improve the instrument's resolution in measured transmittance and bring it down from its current value of 0.012% to below the industry standard of 0.005%.

The results from the short-term, middle-term and long-term stability tests of the ATMX-III configuration together with the preliminary stability results of the latest ATMX-IV are provided in Table 6.4.

6.14 Conclusions

An innovative transmissometer prototype has been manufactured providing an optimum resolution in transmittance of 0.0057% in accordance with the specification described in 6.2. Different hardware and software solutions have been checked in order to achieve optimum transmissometer performance. Specifically, while we had

Instability of the ATMX-III and preliminary results of the ATMX-IV (%)		
	ATMX-III	
	Uncorrected	R-channel Corrected
All Data 1-min average Short (3 h)	0.11 0.08	NA NA
All Data 1-min average Mid (24 h)	0.17 0.14	0.11 0.13
All Data 1-min average Long ($\sim$ 3 days)	0.17 0.14	0.10 0.15
	ATMX-IV	
	Temperature Modulated	
1-min average Resolution (20 min)	**0.012**	
1-min average (2 h)	**0.05**	

Table 6.4: Collective results of the short, middle and long stability tests on ATMX-III and preliminary short test of ATMX-IV performance

.

already designed a system to provide a stable *current* independent of temperature, once the measurement resolution had been improved, it became clear that some temperature control of the transmitter unit's LED was necessary in order to provide a stable *light* output. We have therefore designed our own temperature-controlled LED, based around a Peltier device, 12-bit temperature sensor and a photodiode and two feedback loops. The green sensor of the photodiode is utilised in a feedback

loop in order to drive the white LED towards a steady light output at its peak wavelength of emission. Moreover, the temperature sensor is used to drive the LED's Peltier unit towards a fixed temperature. The combination of the background based measurement algorithm with the innovative thermally stable device lead to 1-min signal fluctuation of 0.012%, a value comparable with the ATIK-16 CCD physical limitation (i.e. 13 e^- at 25 $^\circ C$).

The instrument's specification states the visual range (i.e. MOR) is to be assessed between 50 and 100m with an accuracy of 1% or better. The author has calculated that a 24 m baseline is required to provide this accuracy on the basis of the transmittance resolution. Thus, the instruments exemplary resolution in transmittance allows for a single baseline to cover the full visual range, thereby limiting the transmissometer's production cost (see requirement specification item 10 in Section 6.2).

The linearity of the newly-configured transmissometer has been tested using neutral density filters (see Fig. 6.23). The non-linearity correction ranges from 0.17% to 0.33%, less than half the value calculated for the earlier prototype. Further modifications are expected to improve this even more, but in any case at this level of accuracy the uncertainty introduced by the calibration of the neutral density filters is likely the limiting factor.

The original transmissometer was driven via a C^{++} program, and analysis was performed offline using RooT. In order to comply with industry standards (i.e. item 8 in Section 6.2) , all the control software has been re-written in Visual Basic by group technician Dave Allan. The author was responsible for improving the transmissometer's measurement algorithms. Specifically, the LED driving current in the transmitter, together with the CCD exposure time, are both now controlled in order to optimise the signal-to-noise ratio while minimising power consumption and increasing the life expectancy of the LED. In addition, the algorithm used for the determination of the brightest pixel in the camera field of view has been greatly improved in order to provide greater accuracy in a shorter time, and thereby increase the measurement frequency of the instrument to 1 Hz in accordance with the commercial requirements (item 6 of specification in Section 6.2) .

The newly-designed transmitter unit incorporates a small telescope to allow for better concentration of light at the receiver unit and more consistent identification of the centroid of the light spot. This made the alignment increasingly difficult, such that alignment time sometimes exceeded the 10 minutes that is normally regarded as the maximum by the aviation industry. The author implemented geared tripod heads, which reduce the alignment process to less than 5 minutes meeting the instrument's specification (see item 7 of Section 6.2). An additional benefit of the use of geared heads has been that the transmissometer also shows improved stability in high winds. Under wind speeds of over 45 mph, the position of the centroid of the LED image in the CCD frame was found to vary by just ± 3 pixels.

Control of the original transmitter unit was accomplished via a PCB manufactured at Durham's electronic workshop. This meant that changes to the transmitter control system often required changes to the PCB that could only be accomplished by the electronic workshop technicians. Since several design changes to the transmitter unit were required, the author decided to migrate the system to a computer/datalogger solution which permitted the full control over transmitter's software and hardware. This lead to the elimination of unnecessary measurement delays caused by controlling the LED via the PCB, enhancing the instrument's frequency. An additional benefit was the easier implementation of the LED's light output and temperature feedback loops leading to a thermally stable LED.

In order to meet the 1% visual range accuracy requirement (see item 2 of Section 6.2), it is imperative that the contamination of the windows of both transmitter and receiver are monitored. All the obvious designs for accomplishing this task are subject to current patents, and in any case have deficiencies. The author has completed an innovative design for the monitoring of window contamination which addresses many of the problems inherent in the prior art (see Chapter 7). The unit will be constructed by the engineers at AGI, and will also form part of the final patent on the device.

Finally, ideas concerning the automatic calibration of the transmissometer, in accordance with item 10 of the specification, will also be presented in the next chapter.

Chapter 7

Open ATMX-IV Design Issues

This chapter will focus on three design issues important for the future operation of the transmissometer. The first is the elimination of potential errors caused by contamination of the transmissometer's outer optical surfaces. The existing techniques used for minimising the contamination rate of aviation transmissometer windows and compensating for it, in systems where the window transparency is being (directly or indirectly) monitored, will be presented. Different methods for eliminating the effects of window contamination, without being in conflict with patented techniques, will be discussed.

Secondly, a method for the automatic calibration of Durham's transmissometer, similar to the forward scatter technique used in Vaisala's LT31 (Vaisala, 2004) , will be presented. The transmissometer can be equipped with a secondary CCD camera for detecting high and stable visibility conditions required for its calibration. Under these conditions, the secondary camera's visibility measurement can be used to automatically calibrate the transmissometer making the need of user intervention obsolete. An automatic way to check, and if necessary correct for, the transmissometer's linearity, will be also presented.

Lastly, the methodology asserting the transmissometer photopic response will be addressed. The required photopic response can be achieved either by a broadband photodetector equipped with a specialised filter, to adjust its spectral response to the photopic function (V_λ), or by multi-channel detectors and software scaling. The merits and disadvantages of each solution will be discussed in detail.

The chapter will conclude with a comparison of the ATMX estimated accuracy to the performance of the most common aviation transmissometers in use today.

7.1 Optical Fouling and ATMX-IV Performance

The fouling caused by the contamination of the transmissometer's external protective windows is considered one of the most important sources of error in determining the atmospheric transmittance (ICAO, 2005). Specifically, the transmittance value registered by a typical transmissometer possesses an average fractional error (σ_T/T), due to the external transmissometer windows' fouling alone, of 1%. The optimum fractional error in transmittance, primarily consisting of electrical noise, has already been estimated at 0.0057% (see Section 6.6.1). Thus, the combined relative uncertainty in transmittance (i.e. $\sigma_T/T = \sqrt{1^2 + 0.0057^2} \simeq 1\%$) will be dictated by the error introduced from the optical contamination. These extreme relative error values in transmittance can be translated into a relative error in terms of the extinction coefficient or the MOR via the equation (as proven in Section 5.6.5):

$$\frac{\Delta\sigma}{\sigma} = \frac{\Delta\mathrm{MOR}}{\mathrm{MOR}} = (1/\ln T)\frac{\Delta\sigma}{\sigma} \tag{7.1}$$

In addition, the MOR can be conveniently expressed in terms of baseline (R) multiples via the transmissometer equation (see Equation 5.6):

$$\frac{MOR}{R} = \frac{\ln(0.05)}{\ln T} \tag{7.2}$$

By using equations 7.1 and 7.2 one can plot the relative error associated with the MOR measurement as a function of the MOR itself expressed as baseline multiples (see Fig. 7.1).

Figure 7.1 suggests that the elimination of the errors introduced due to the window contamination yields a transmissometer operational range, within which the MOR is determined with accuracy better than 1%, of $10 - 12,619$ m assuming an optimised baseline of 24 m (see Section 6.6.2). An allowance of 1% uncertainty in the determination of the window's transparency corresponds to a degraded transmissometer's operational range of $20 - 643$ m, which fails to cover the whole MOR

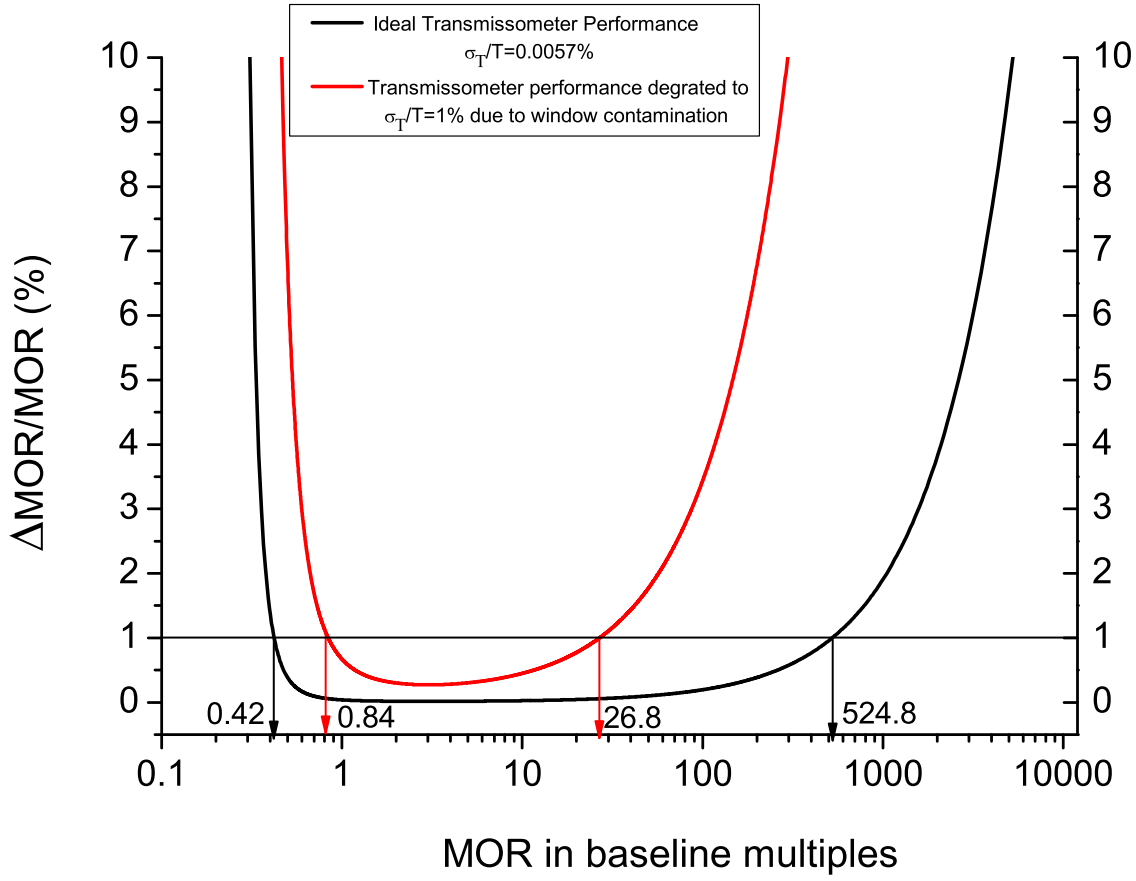

Figure 7.1: Relative MOR error due to the transmissometer's electronic noise (0.0057%) in comparison with the relevant fractional error introduced by optical fouling. Allowing 1% relative transmittance error due to fouling (i.e. the typically accepted value) drastically reduces the transmissometer's operational range.

range ($10-10,000$ m) with the required accuracy. It is imperative, therefore, to minimise the uncertainty introduced via the window contamination by both reducing the contamination rate and determining its effect in the determination of atmospheric transmittance by constantly monitoring the protective window's transparency.

7.2 Prior Art for Window Designs

7.2.1 Reducing Window Contamination

Weather protective enclosures are used in every known transmissometer device and offer adequate protection from errors caused by the deposition of precipitation on the external surface windows. In order to avoid forward scatter errors, the receiver's field of view is typically set to match the transmitter's aperture (ICAO, 2005). Thus, the length of the protective hood is limited by this small field-of-view requirement and by stability problems introduced with increasing wind-exposed surface.

Even though weather hoods offer adequate protection against precipitation deposition on a transmissometer's external windows, they cannot prevent dust, fine particles and insects from entering the transmissometer's measuring area, resulting in misinterpreted measurements. The standard solution to minimise contamination due to dust and fine particles is to circulate air in front of the outer windows. As an example, Vaisala's LT31 (Vaisala, 2004) employs a fan to create an air curtain in front of the transmissometer's outer windows, thereby forcing wind-driven particles towards the ground. An alteration of this technique is to be found in MTECH's 5000-200 transmissometer, which delivers heated and filtered air to both the inner and outer surfaces of the transmitter's window (MTECH, 2008). The manufacturer claims that this is enough to eliminate any window contamination, making the need for compensation obsolete. However, due to eddies in the airflow, a small proportion of the dust particles will reach the instrument's windows, affecting the transmissometer's measurements (Engel and Heyn, 2005). Thus, the cleaning of the external windows is a necessity and constant monitoring of the window transparency in between maintenance intervals is the only way to approach the ideal transmissometer performance (see Fig. 7.1). In the next Section, some techniques for prolonging the maintenance cycle and monitoring the window's transparency will be presented prior to the introduction of the suggested Durham technique.

7.2.2 Monitoring Window Contamination

The standard method of determining transmissivity consists of alternating the examined material between a light source and a light detector. A calibration factor is first determined by measuring the light intensity for the uninterrupted light beam. Then the selected material is introduced between the light transmitter and receiver and its transparency is calculated as the ratio of the measured value to the calibration factor. This straightforward technique cannot be implemented in the case of a transmissometer, however, as its protective environment should remain permanently sealed.

European patent specification EP1300671 (Rakoczy and McGuinness, 2004) describes a double-ended transmissometer, both units of which are equipped with rotating external windows. The windows are divided in six equal portions, five of which can be used, in turn, for the visibility measurement while one portion is obscured and used as a reference clean window. The contamination of the operational windows, on both transmitter and receiver, can be determined by co-instantaneously replacing them with the reference ones and compare the resulting calibration value with the values registered with the operational windows prior to the exchange. In this way the maintenance period of the external window is extended and a contamination factor can be applied to correct the measured light intensity. This technology is currently applied to TELVENt's Revolver transmissometer (Telvent, 2008). The disadvantages of such a solution are summarised below:

1. The visibility measurement must be interrupted,
2. the window contamination correction between calibrations can only be applied off-line and is based on short measurement in order to avoid contamination of the reference window,
3. a realignment is needed after each contamination check, and
4. frequently moving parts in front of the light beam may limit the MTBF of the transmissometer.

Another method of determining the window contamination is by monitoring

the total internal reflection of the transmissometer's windows (Saari, 1998). This method utilises a pair of optotransmitters (5, 6 in Fig. 7.2) and optoreceivers (7, 8 in Fig. 7.2) within each of the transmissometer's separate enclosures (i.e. transmitter/receiver: 1, 2 in Fig. 7.2). The light produced by the sources 5 and 6 is

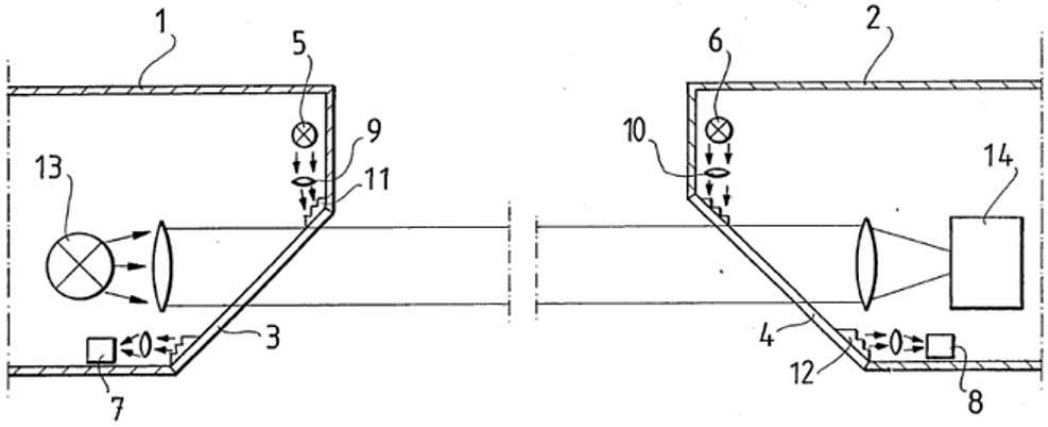

Figure 7.2: Schematic representation of contamination monitoring via the 'total reflection' method, as disclosed in patent U.S. 4794266. See text for a full explanation of the components

collimated and directed to the relevant prism matrix (11, 12) in order to obtain a total internal reflection within the windows' boundary surfaces. In the case of a contaminated outer window surface, a portion of the transmitted light will be scattered off by an amount determined from the readings of the photodiodes(7, 8) measuring the remaining intensities of the totally reflected light beams. In this way a contamination factor is deduced that can be used for the on-line correction of the light transmission measured via the transmissometer's photodiode (14). This method offers on-line monitoring of the window's contamination without the need to interrupt the transmission measurement. However, the determination of the windows' transparency is measured indirectly and the transmission correction is based on predetermined empirical look-up functions relating the intensities of the total reflected light rays with changes in the transmitted light intensity caused by contamination of the receiver's/transmitter's windows.

A refined method offering direct on-line monitoring of the transparency of the transmissometer's windows is disclosed within the Patent Specification GB 2410795 (see Fig. 7.3). The arrangement presented in Fig. 7.3 enables two light beams,

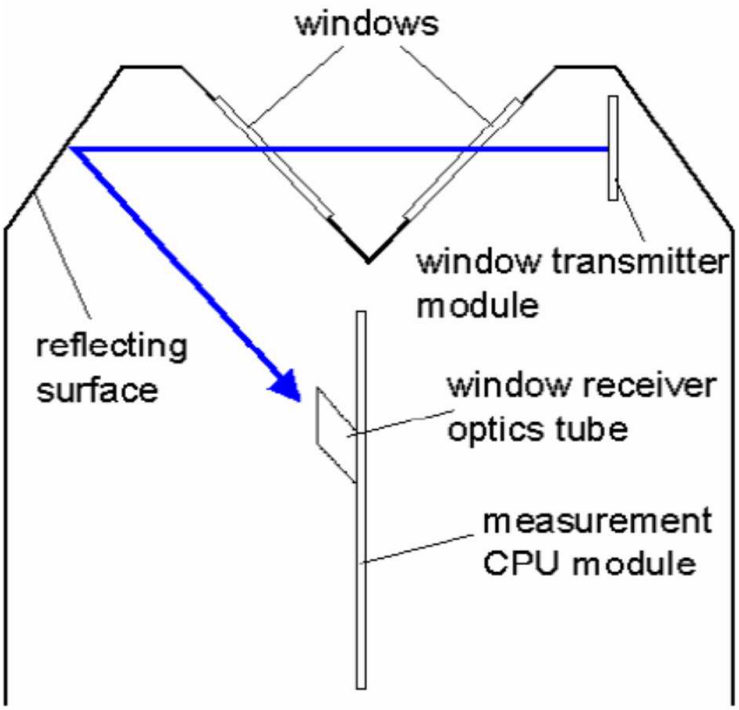

Figure 7.3: Direct measurement of window transparency based on the V-shaped window design. Extracted from Patent Specification GB 2410795.

orthogonal to each other, to cross the same part of the window, allowing for the monitoring of the window transparency while the atmospheric transmittance is being measured. The blue line in Figure 7.3 represents the light path of the window transparency measurement, while the light transmitter can be placed behind one of the windows. The light beam used for the atmospheric transmission measurement is directed through the window towards the receiver with its optical axis forming an angle of 45° with the window's surface. While this design seems to eliminate the disadvantages present in the previous methods, it is based on the crucial assumption that the contamination is uniformly distributed at both windows as only one is, in fact, used for the atmospheric transmission determination.

This technique, along with other innovative solutions, such as the automatic re-calibration of the transmissometer via a forward-scatter device, is implemented

in Vaisala's LT31 transmissometer (Vaisala, 2004) that comprises one of the most complete instruments offered by the aviation industry today.

7.3 Durham Window Monitoring Units (WMU)

The suggested Durham designs for the direct online monitoring of the transparency of the transmissometer's outer windows are introduced with the objective of eliminating the disadvantages of the prior art without infringing any of the known patented techniques.

7.3.1 The 'L-shape' WMU Design

Working with colleagues from Durham University Advanced Instrumentation Group (AIG) an initial WMU design was devised; the 'L-shape' WMU design, which is schematically presented in Fig. 7.4. The presented design has been sketched for the transmissometer's transmitter unit with the telescope shown as the cylindrical tube (i.e. 97 mm) being protected by an outer enclosure (see Fig. 5.4 for an example). According to this design, the telescope and enclosure tubes form an L shape. A semi-silvered mirror has been attached to the telescope's exit window forming a 45° angle. The main LED beam crosses the telescope's exiting window and 90% of its intensity is reflected by the semi-silvered mirror towards the transmissometer's receiver unit. The remaining 10% of is transmitted through the semi-silvered mirror onto a photodiode to determine the combined window and mirror contamination. The calibration (transmitted) and the main (reflected) beams follow different light paths but the absorption due to the light transmission through the mirror can be easily calibrated out. The telescope's exiting window and mirror will be both protected by the same hood. In addition both units are utilised for the atmospheric and window transparency measurements so any contamination effect on each unit will be taken care of. Thus, the 'L-shape' WMU design does not suffer from the 'equal window contamination' of the secondary window' assumptions present in Vaisala's patented 'V-window' design.

One should notice, however, that the coating has to be applied on the exterior

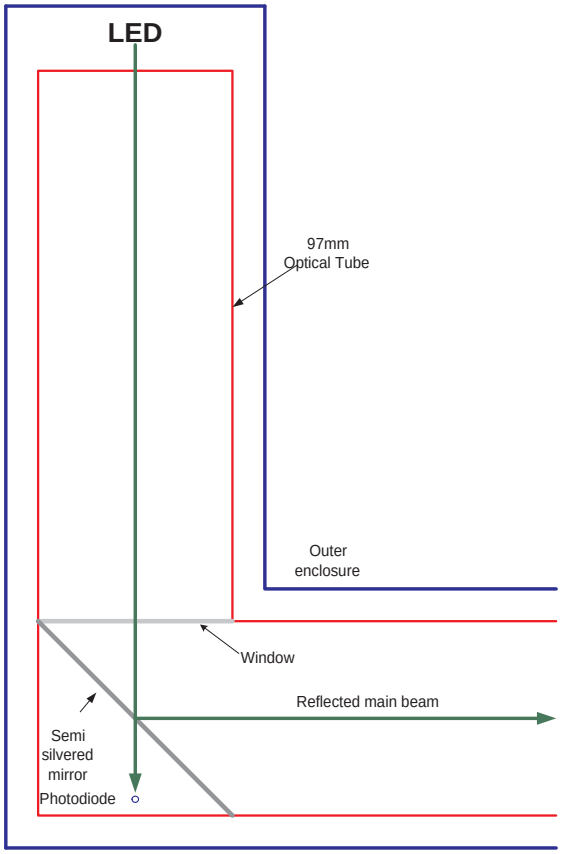

Figure 7.4: Schematic illustration of Durham's 'L-shape' Design

of the semi-silvered mirror or a 'double entry' of the reflected beam onto the semi-silvered mirror will occur. Indeed, in the case of a interior (i.e. protected) coating the LED beam will cross the semi-silvered mirror twice whereas the transmissometer external window will be crossed only once. As the rate of contamination between mirror and transmissometer's external window may not be the same, a valid calculation of the window's contamination would be hard to perform.

Thus, the coating of the semi-silvered mirror will be exposed to the environment requiring frequent cleaning that may, in turn, affect the coating efficiency. Moreover, we need to ensure the stability of the unit (telescope and mirror), which might be challenging with the mirror directly exposed to the elements. Specifically, the alignment of the semi-silvered reflector will be crucial as it is used for both atmospheric and external window transparency measurements. These concerns led to Durham's 'double-mirror' design that is described in the following Section.

7.3.2 The 'double-mirror' WMU Design

The object of the 'double-mirror' design is to provide a WMU, based on the optimised 'L-shape' design, and a method to disentangle the losses suffered due to contamination on the telescope's transparent front window from that on the reflector, thereby eliminating the requirement for the hard-to-justify assumptions which are found in the prior art. The design is schematically presented in Fig. 7.5.

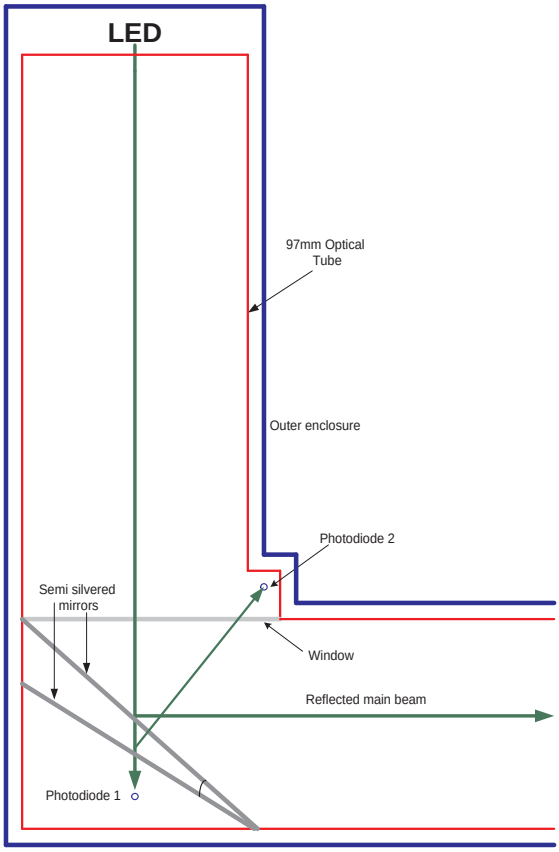

Figure 7.5: Schematic illustration of Durham's 'double-mirror' WMU design.

This design utilises two semi-silvered mirrors, mounted together at a fixed angle (θ, see also Fig. 7.6), having inner, and thus protected, reflective coatings. The primary mirror forms an angle of 45° with the telescope's front window so the emergent beam, responsible for the atmospheric transmittance measurement, is orthogonal to the telescope's axis (see Fig. 7.5). The 'double-mirror' design also utilises two photodiodes, each of which sits behind a protective surface, as shown in Figure 7.5. Photodiode 1 measures the intensity of the light after crossing the telescope's window

and being transmitted consecutively through the two semi-silvered mirrors. Photodiode 2 registers the intensity of the light that, after being reflected from the second semi silvered mirror, is transmitted through the primary mirror into the telescope's outer window. (It is also possible to use a fibre optic in order to simplify the design so only one photodiode may be used). The formation of two distinct optical paths allows the decoupling of the intensity losses due to the telescope's outer window contamination from the losses due to the contamination of the primary reflector. Thus, the 'double-mirror' design allows for the continuous and accurate determination of the contamination of both units utilised in the atmospheric transmittance measurement (i.e. telescope's outer window and primary reflector), thereby providing a means of immediate correction of the measured transmission values. More importantly, the suggested design does not require any a priori assumptions, as is the case in Vaisala's 'V-window' patented design, which assumes uniform fouling between the two plates forming the V-shape (Engel and Heyn, 2005). In addition, the operator can be alerted whenever the level of contamination on any of the exposed optical surfaces reaches a predefined level. The details of the method allowing the determination of the contamination layer of both telescope's outer window and primary reflector will be presented in the following Section.

Determination of the contamination layer thickness

Working with Dr. Andrew Kirby of the Durham AIG, an analysis of the system has been determined. A detailed sketch of the transmissometer's light beam interaction with the optical elements utilised in the 'double-mirror' design is presented in Fig. 7.6. Dust and other contaminants can be accumulated on both the telescope's outer window and primary reflector surfaces, forming contamination layers of thicknesses d_1 and d_2 respectively. Assuming that Bouguer's law is valid for the contamination medium, the intensity of the attenuated beam (I) after crossing the contamination layer of thickness (d) can be expressed in terms of the impinging beam as:

$$I = I_0 \exp^{-d/\lambda} \tag{7.3}$$

where λ relates to the attenuation characteristics of the contaminants and can be expressed as the mean free path, which is the required layer thickness for the initial

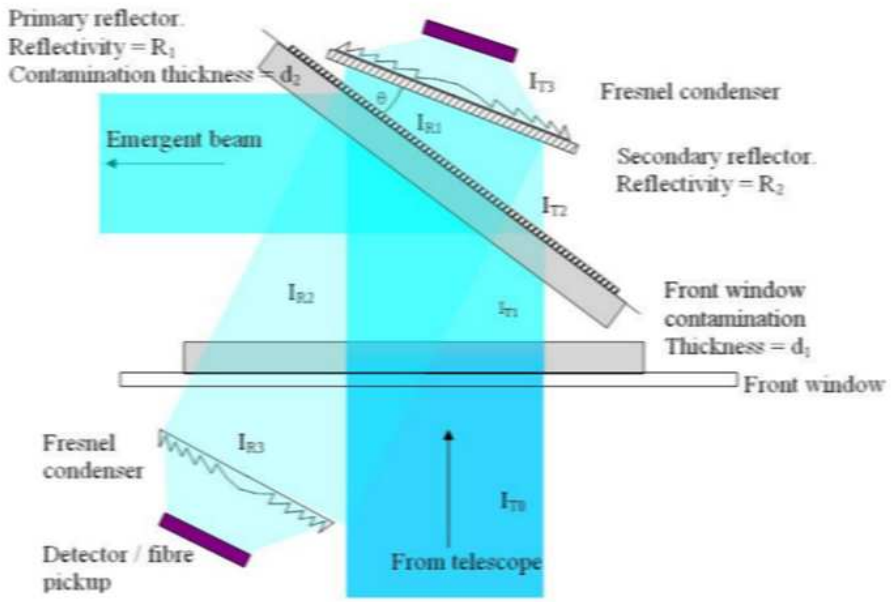

Figure 7.6: Schematic representation of the beam interaction through the Durham's 'double-mirror' WMU design (Kirby, 2008).

beam intensity to be reduced to 36.8% (i.e. $d = \lambda$).

The intensity losses due to the transmission of the LED beam through the transparent optical components (i.e. the telescope's lens and outer window and primary and secondary semi-silvered reflectors) are fixed, and therefore can be easily calibrated out. Thus, absorption through the fixed optical units can be safely neglected, and therefore, the energy of the beam is conserved:

$$\mathrm{R} + \mathrm{T} = 1 \tag{7.4}$$

where the reflectance R is the ratio of the reflected over the incident power, and the transmittance T is the ratio of the transmitted over the incident power.

Equations 7.3 and 7.4 allow the calculation of the beam intensity after its interaction with each of the intervening optical components. The intensity of the light reaching the photodiode sited behind the 'double-mirror' configuration (I_{T3}), has suffered absorption while passing through the contamination layers of telescope's front window and the primary reflector with optical path length of d_1 and $d_2\sqrt{2}$ respectively. In addition, the initial light beam intensity (I_{T0}) emerging from the telescope is transmitted successively through the primary and secondary mirrors by

an amount dictated by the mirrors' respective transmissivities (T_1, T_2). Thus, one can trace the light beam's optical path from the telescope into the first photodiode and assign the following intensity values at each step:

$$I_{\mathrm{T}_1} = I_{\mathrm{T}_0} \exp^{-d_1/\lambda} \tag{7.5}$$

$$I_{\mathrm{T}_2} = I_{T1}(1-\mathrm{R}_1) = I_{T_1}(1-\mathrm{R}_1) \exp^{-\sqrt{2}d_2/\lambda} \tag{7.6}$$

$$I_{\mathrm{T}_3} = I_{\mathrm{T}_2}(1-\mathrm{R}_2) \tag{7.7}$$

where I_{T_1} is the intensity of the light beam emerging from the telescope's front window, and I_{T_2} is the intensity of the light beam transmitted from the primary mirror (see Fig. 7.6).

Thus, the registered intensity (I_{T_3}, Equation 7.7) can be expressed in terms of contamination layer thicknesses and mirror transmissivities (or reflectivities) as:

$$I_{\mathrm{T}_3} = I_{\mathrm{T}_0}(1-\mathrm{R}_1)(1-\mathrm{R}_2) \exp^{-\frac{d_1+\sqrt{2}d_2}{\lambda}} \tag{7.8}$$

The same procedure can be applied to the optical path of the light reflected from the secondary semi-silvered mirror (I_{R_1}) towards the second photodiode, that sits behind the telescope's front window (see Fig. 7.6). Specifically, the light beam reaching the secondary semi-silvered mirror (see Equation 7.6) will be reflected by R_2 (Equation 7.9). The reflected beam will be transmitted back through the primary reflector and its contamination layer (Equation 7.10). Finally, the emerging beam will cross the transparent primary window and its contamination layer before being registered by the secondary photodiode (Equation 7.11):

$$I_{\mathrm{R}_1} = I_{\mathrm{T}_2}\mathrm{R}_2 \tag{7.9}$$

$$I_{\mathrm{R}_2} = I_{R_1}(1-\mathrm{R}_1) \exp^{-d_2/\lambda\left(\cos\frac{\pi}{4}-2\theta\right)} \tag{7.10}$$

$$I_{\mathrm{R}_3} = I_{\mathrm{R}_2} \exp^{-d_1/\lambda\cos(2\theta)} \tag{7.11}$$

The combination of Equations 7.9, 7.10 and 7.11 yields the following expression for the second photodiode's registered intensity:

$$I_{\mathrm{R}_3} = I_{\mathrm{T}_0}(1-\mathrm{R}_1)^2\mathrm{R}_2 \exp^{-\frac{d_1\left(1+\frac{1}{\cos(2\theta)}\right)+d_2\left(\sqrt{2}+\frac{1}{\cos(2\theta-\pi/4)}\right)\sqrt{2}}{\lambda}} \tag{7.12}$$

Equations 7.8 and 7.12 can be conveniently rearranged in terms of the unknown quantities; namely the thicknesses on the contamination layers K_T and K_R on the telescope's outer window and primary semi-silvered mirror d_1 and d_2 respectively:

$$\begin{aligned} K_T = -(d_1 + d_2\sqrt{2}) &= \lambda \ln \frac{I_{\mathrm{T}_3}}{I_{\mathrm{T}_0}(1-\mathrm{R}_1)(1-\mathrm{R}_2)} \\ K_R = -\frac{d_1\left(1+\frac{1}{\cos(2\theta)}\right)+d_2\left(\sqrt{2}+\frac{1}{\cos(2\theta-\pi/4)}\right)\sqrt{2}}{\lambda} &= \lambda \ln \frac{I_{\mathrm{R}_3}}{I_{\mathrm{T}_0}(1-\mathrm{R}_1)^2\mathrm{R}_2} \end{aligned}$$

This system of linear equations can be solved for d_1 and d_2:

$$\begin{aligned} d_1 &= \alpha(K_T - \beta\gamma(K_R - \alpha K_T)) \\ d_2 &= \beta(K_R - \alpha K_T) \end{aligned} \tag{7.13}$$

where:

$$\begin{aligned} \alpha &= \frac{1}{\sqrt{2}+\frac{1}{\cos(2\theta-\pi/4)}/\sqrt{2}-\frac{1}{1+\cos(2\theta)}} \\ \beta &= \frac{1}{1+\frac{1}{\cos(2\theta)}} \\ \gamma &= \sqrt{2}+\frac{1}{\cos(2\theta-\pi/4)} \end{aligned} \tag{7.14}$$

The constants α, β and γ are determined by the geometry of the window monitoring unit (i.e. θ). Thus, one can use equations 7.13 and 7.14 to determine the thickness of the contamination layer, on each of the exposed optical components, from the registered values I_{R_3} and I_{T_3}.

7.4 Automatic Calibration Considerations

A transmissometer measures atmospheric transmittance directly, within the limits of its baseline. By definition, transmittance ranges between $0-1$, corresponding to an MOR/RVR range of 0 to ∞ . The intervening values of transmittance can be

translated to an MOR/RVR value via the relevant equations (e.g. 7.2). The dependence of these equations on transmissometer baseline necessitates the adjustment of the calculated MOR/RVR values to the prevailing visibility on site. Calibration is usually performed under high visibility (i.e. > 10 km), to approximate ideal conditions relating to a transparent (T=100%) atmosphere. Thus, the calibration procedure requires an external input of the independent visual range value (usually estimated by an airport's trained personnel).

Patent specification GB 2,410,7955 (Engel and Heyn, 2005) discloses a method for the automatic calibration of the transmissometer. According to this method, the transmissometer is equipped with a forward-scatter meter that is used for detecting the necessary calibration condition (i.e. visual range > 10 km) and for calculating a calibration factor under this condition. The calibration factor is calculated by translating the visual range registered by the forward-scatter sensor into a transmittance value corresponding to the transmissometer's baseline and subsequently by forming the ratio between the resulting value and the transmissometer's measured value. In addition, the forward-scatter device can detect the presence of precipitation and therefore can be used to activate the air-fan unit only under these conditions (i.e. rain, snow), thereby avoiding the deposition of dust and fine particles due to their recirculation by the air system.

In order to achieve an automatic calibration of the transmissometer, without the need of the trained observer's input, one needs to deploy two independent methods for measuring visibility. In the case of Vaisala's LT31 this is achieved by the use of two visibility sensors. One possibility, still in the process of formation, is to use a secondary camera/video mounted on the side of the receiver unit in order to extract the atmospheric contrast transmittance between two 'black objects' within the camera's field of view. That would allow the use of a plurality of objects/targets, placed at different distances, during the day while during the night the device can be aimed towards the runway centre/edge line lights.

Specifically, a reliable estimate of the visual range can be extracted by capturing with the secondary camera two black objects at different distances together with their background. The black 'object' assumption can be used to simplify the cal-

culation of the contrast transmittance as the object's variation in illuminance is considered negligible over its whole surface:

$$C = \frac{B - D}{B} \tag{7.15}$$

where, B is the observed background illuminance, and D is the observed illuminance of the black object.

By further assuming that contrast reduction is due to illuminance attenuation only, the contrast of a black object at a distance l from the camera can be calculated via the Beer-Bouguer law:

$$C(l) = C_0 \exp^{-\sigma l} \tag{7.16}$$

where σ is the atmospheric extinction coefficient.

The use of two black objects, located at different distances, can be used to eliminate their common inherent contrast (i.e.C_0):

$$\sigma = \frac{\ln C_{l_2} - \ln C_{l_1}}{l_2 - l_1} \tag{7.17}$$

In this way, a value for the atmospheric extinction coefficient, yielding a Koschmieder visual range, can be retrieved from the camera's image by extracting the intensities corresponding to the relevant reference objects and the background. This method assumes the existence of two 'black objects' (i.e. the light reflected by them towards the camera is negligible in comparison with the background radiance) within the camera's field of view. This technique has already been tested, yielding visibility values in close agreement with human observation (Janeiro et al., 2006). The temporal variability of the measured visual ranges was minimal under high visibility conditions due to the reduction of the multiple scattering effects. Thus, this method can be used in parallel with Durham's transmissometer to identify high visibility conditions and, when necessary, to calibrate the transmissometer under these conditions.

This method has already been investigated by (Janeiro et al., 2006), while the US patent 0270537 provides a similar image-based visibility estimation. However, to the extent of our knowledge, this method has never been used before in conjunction with an RVR sensor.

The following potential problems could limit the applicability of the proposed method:

- A suitable landscape might not be available,
- fluctuation of the camera positioning over time necessitates the use of complicated and computationally intensive edge detecting algorithms, and
- the accuracy of this method has not been verified even though it has been the subject of patented research.

Due to the complexity of the suggested method it has been decided that its development does not consist one of the short-term priorities of the project.

7.4.1 Linearity Calibration

The spectral sensitivity of both the camera (see Fig. 7.12) and the S9706 photodiode depends on temperature and will be reduced with ageing. As both detectors are temperature modulated, their response can be safely assumed constant under short and medium time intervals (i.e. days to a few weeks). In order to take into account the photodetectors ageing over longer time intervals, the LED output brightness can be modulated via the LED driving current to provide an automatic re-calibration of the Durham's transmissometer. This procedure can be triggered only under very clear and stable visibility conditions (i.e VIS $>$ 30 km, and RMS cut requesting long periods of exemplary stability) to minimise the atmospheric absorption and fluctuation effects. The following analysis was performed under very clear skies (VIS $>$ 50 Km) using the RGB S9706 photodiode in conjunction with the monochrome ICX429 sensor, in order to test the concept. The brightness of the LED was altered to provide 13 different intensity check points ranging from 74-80% and 94-100% of the LED maximum output with 1% intensity steps. The correlation between the CCD sensor and the photodiode has been checked by using both the photodiode's green and average sensor values (see Figures 7.7, 7.8 respectively).

The evident correlation between the CCD and the photodiode is quantified in Figures 7.9 and 7.10 where the relevant raw readings (i.e. CCD vs. G photodiode,

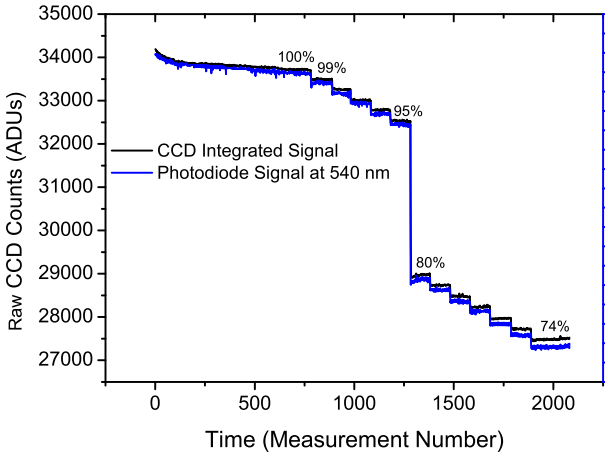

Figure 7.7: ICX429 CCD versus S9706 green photodiode sensor reading for 13 different intensity levels.

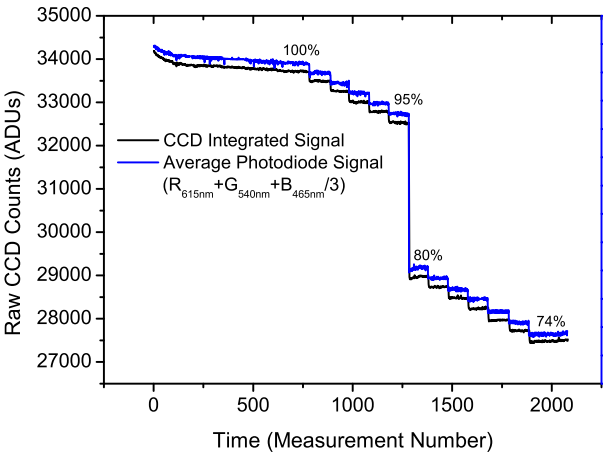

Figure 7.8: ICX429 CCD versus the average reading of the S9706 photodiode's RGB sensors for 13 different intensity levels.

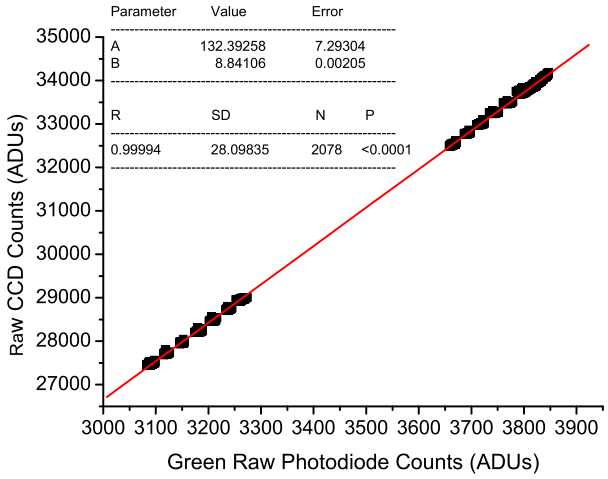

Figure 7.9: Correlation between CCD (ICX429) and the green photodiode (S9706) sensor signal.

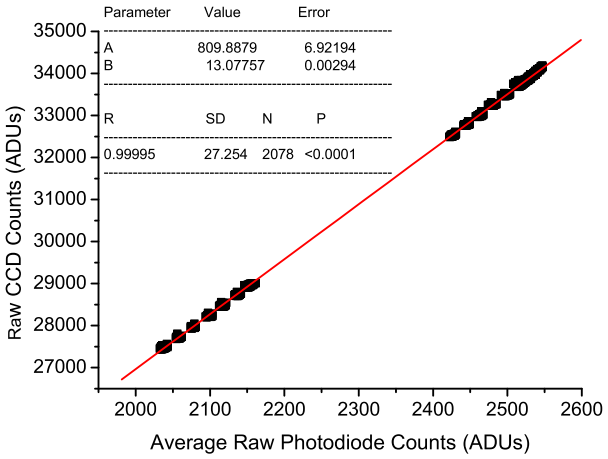

Figure 7.10: Correlation between CCD (ICX429) and the average photodiode (S9706) RGB sensor signal.

CCD vs. RGB photodiode) have been directly plotted against each other. In both cases the slope of the calibration curve is determined with an excellent accuracy (i.e. 0.022% for RGB and 0.023% for G) while the offset between the CCD and photodiode signals is determined more accurately when all photodiodes channels are being considered (i.e. 0.85% RGB and 5% G). Thus, the use of the three available photodiode channels will give more accurate results.

It is expected that the use the ICX205 colour CCD sensor, allowing the direct

comparison between the transmitter/receiver photodetectors, will yield even better correlation with the S9706 photodiode. Thus, re-calibrating Durham's transmissometer, at time-intervals dictated by the good visibility requirement, will yield the means (i.e. linear coefficients) to compensate for any responsivity change affecting the transmissometer. As already discussed, a value for the prevailing visibility must be provided by the operator if the transmissometer cannot detect visibility independently. This method can be also used to inform the operator when the replacement of the photodetectors is necessary, i.e. a predetermined level of efficiency has been reached.

7.5 Photopic Response

The definition of the MOR is based on a traditional incandescent light source with a *C*orrelated *C*olour *T*emperature CCT of 2700 K and a light sensor possessing photopic response (i.e. see Section 5.5.1). LEDs possess higher luminous efficiency, lower power consumption and an extended life time in comparison with traditional light sources, and thus constitute the preferred light source for aviation transmissometers today. For our application the Lumileds K2 warm-white (i.e. ~ 3000 CCT) has been selected (i.e. see Section 6.9.1).

In terms of the light sensor, the ATIK-16 monochrome camera has been used throughout the development of Durham's aviation transmissometer (i.e. ATMX-I to ATMX-IV, Table 6.1). This camera is equipped with the ICX429 CCD sensor, whose spectral sensitivity is presented in Fig. 7.11. A quick comparison with the CIE photopic luminosity function (i.e. V_λ see Fig. 5.11) convinces that a photopic correction filter is necessary for an acceptable matching between the CCD response and V_λ. As the cost of such a purpose-built photopic correction filter is usually greater than of the CCD sensor itself, the author decided to establish the ATIK-16 camera's performance (i.e. linearity, lifetime) and finalise the optical design before committing the necessary funds to produce a photopic filter for the camera's sensor and optics.

Indeed, it was quickly realised that the use of ATIK-16 sensor limited the trans-

missometer to frequencies lower than the specified value of ~ 1 Hz (see Section 6.2) due to the degraded image download speed provided by the USB-1.0 connection. The transmissometer frequency will be optimised via the recently acquired ATIK-314E CCD camera offering USB-2.0 connectivity with sub-second download time. The new camera can be equipped with either monochrome or colour CCD sensor offering the following choices for achieving the required photopic response:

- Photopic Filter

  Although the ATIK-314 camera implements ICX205 CCD sensor, whose spectral sensitivity approximates better the photopic luminosity function (V_λ) than the old one (see Figures 7.12, 7.11 respectively), a closer match is usually required for aviation transmissometers. The level of the required accuracy of matching the CCD sensor response to V_λ is high due to the difference between the LED and illuminant A emission spectra.

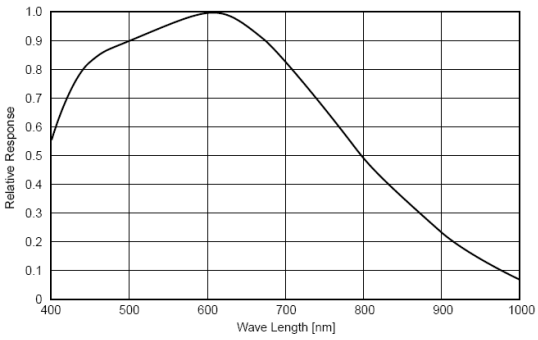

Figure 7.11: Sony ICX429 CCD sensor spectral sensitivity (Sony, 2006).

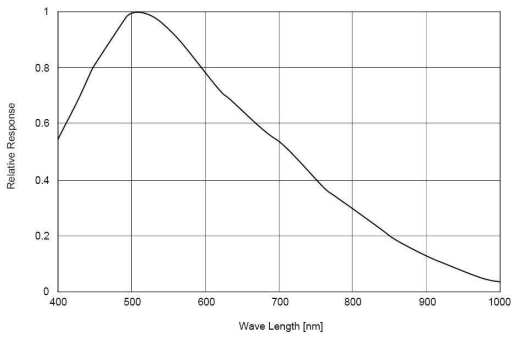

Figure 7.12: Sony ICX205 CCD sensor spectral sensitivity (Sony, 2007).

  The cost of a purpose-built photopic correction filter for the SONY ICX205 sensor is $ 2000 (LUMETRIX, 2005). However, acquiring such a photopic filter does not guarantee a photopic response for the ATIK camera as the filter has been manufactured for a different camera lens than we are using. Thus, buying an 'off the self' photopic filter will be in breach of the Durham transmissometer requirement specification (see Section 6.2)

- RGB CCD and Photodiode Sensors

  A spectroradiometer approach can be used by monitoring the LED's RGB

spectral emission using the Hamamatsu S9706 on the transmitter side and the colour CCD sensor on the receiver. A photopic response can be achieved by scaling the raw values of the LED and CCD RGB pixels to the relevant photopic function factors. Although that would produce a photopic response at the RGB wavelengths the closeness of the photopic approximation to the remaining spectrum has to be checked against a photopic standard. It is initially intended to calibrate Durham's transmissometer against AGI's photopic photodiode, in which case the accuracy will be limited to 2%; a value acceptable by the aviation standards today. It was, therefore, decided to implement the spectroradiometer solution followed by the acquisition of the coloured CCD ATIK-314E camera.

7.6 Conclusions

In this chapter considerable effort was dedicated by the author to the development of an innovative Window Monitoring Unit design that eliminates the disadvantages of the prior art without infringing any of the currently used patented designs (e.g. Vaisala's 'total-reflection' and 'V-window' designs). After considering numerous solutions, and consulting colleagues from Durham's Instrumentation Group, the 'double-mirror' design was produced and a method was devised to allow not only the accurate determination of the losses due to the contamination of the optical components (i.e. telescope's front window and external semi-silvered mirror) but also to associate a contamination thickness layer with each component. Thus, there is no need to make any assumptions about the rate of contamination between the optical parts as is the case for Vaisala's LT31 transmissometer, which assumes uniform fouling between the WMU V−plates, although only one is utilised for the atmospheric measurement (Engel and Heyn, 2005). In addition, there is no need to interrupt the atmospheric measurement in order to allow comparison with calibrated windows or to risk the instruments MTBF via the frequent use of filter wheels (i.e. TELVENT's Revolver transmissometer, see Section 7.2.2).

The WMU for the transmitter unit utilises one LED for both window monitoring

transparency and atmospheric transmittance measurements. That simplifies the WMU design in comparison with competing instruments that require a plurality of light sources (e.g. Vaisala's LT31). In addition, this solution is cost effective, as lot of effort has been placed on the stabilisation of the transmitter's LED (i.e. via light output and temperature feedback loops).

The advantages of Durham's 'double-mirror' design drew a keen interest from AGI. The eligibility of the design has initially been checked with positive results. Moreover, the feasibility of the design has already been evaluated by AGI's engineers and the construction of Durham's WMU is underway (i.e. March 2009). The 'double-mirror' innovative design is expected to be incorporated into the Durham's transmissometer final patent shortly.

Automatic calibration is an attractive option for aviation transmissometer currently to be found only in Vaisala's LT31 instrument. The author suggested an image-based method of measuring visibility via a secondary camera attached to the transmitter unit. Although this method has already been explored (Janeiro et al., 2006), it has never been used in conjunction with an aviation transmissometer (e.g. Vaisala's LT31 auto-calibration is based on a forward-scatter sensor). Even though the complexity of the required image recognition algorithms have put the further exploration of this idea on hold at the present time, it will be explored further at a later date.

Finally, the transmissometer's photopic response will be guaranteed via the combined use of a tristimulus (RGB) CCD (i.e. ICX205) and photodiode sensors. The suggested solution makes the need of a 'photopic filter' obsolete thus minimising the production cost of Durham's aviation transmissometer.

After the completion of these tasks, Durham's aviation transmissometer will be ready for extensive field trials necessary for the instruments validation The transmittance resolution is now 0.0057%, which is very close to the industry standard of 0.005%. The integration of the the new camera into the system, offering a full 16-bit resolution in exposure time while possessing a much lower noise level than the current ATIK-16 camera, will increase the resolution in measured transmittance and bring it down to below the industry standard of 0.005%. Finally, the use of the

innovative 'double-mirror' window monitoring system will guarantee an accuracy of 1% or better for MOR measurements between the range $10 - 12,595$ m for a baseline fixed at 24 m.

The performance of common aviation transmissometers in use today is listed in Table 7.1. The baseline, operational range, stated MOR/RVR accuracy and, where available, the instrument's resolution in transmittance have been extracted from the manufacturers' manuals. The standard method of reporting accuracy in the transmissometer aviation market is by stating compliance with the World Meteorological Organisation (WMO) and International Civil Aviation Organisation (ICAO) guidelines. The WMO/ICAO guidelines specify the desirable accuracy of todays cutting-edge transmissometers and are presented in table 7.2. It is clear that Durham's performance exceeds both WMO and ICAO requirements.

Table 7.1: Transmissometer Manufacturer Specification. Double horizontal lines are used to group transmissometers from the same manufacturer.

Sensor/ Company	Operational Range	Baseline (m)	Accuracy	Transmittance Resolution (%)
AGIVIS	50 m – 100 m		±10 m	
2000	400 m – 800 m	20	±25 m	
(AGI, 1990)	> 800 m		±10 %	
5000-200	25 m – 10 km	50	ICAO/WMO	
(MTECH, 2008)	10 m – 10 km	30	ICAO/WMO	
REVOLVER	10 m – 10 km	10 – 100	Exceeds	0.005
(Telvent, 2008)			ICAO/WMO	
LT31	10 m – 10 km	30	ICAO/WMO	
(Vaisala, 2004)	25 m – 10 km	50	ICAO/WMO	
MITRAS	100 m – 1.5 km	35	ICAO/WMO in	0.02
(Vaisala, 1995)	40 m – 10 km	10 and 200	specific ranges	

All in all, we have built an aviation transmissometer prototype, in accordance with the newest industrial specifications (see Section 6.2), having compatible performance with the most advanced instruments in today's aviation market at a cost of £8000; a reduction by a factor of ~ 5 over the cost of the competitive instruments.

ICAO and WMO desirable resolution for RVR and MOR respectively		
	ICAO Requirement (RVR)	WMO Requirement (MOR)
Operational Range (m)	$50 - 2000$	$25 - 10000$
Resolution	25 m up to 400 m 50 m between 400 and 800 m 100 m above 800 m	50 m up to 600 m 10 % between 600 and 1500 m 20 % above 1500 m

Table 7.2: International Civil Aviation Organisation ICAO (2005) and World Meteorological Organisation WMO (2008) guidelines for the desirable in RVR and MOR measurement respectively.

Chapter 8

Future Work

In this final chapter a short account of future working plans regarding the Durham's aviation transmissometer will be drawn. In addition, the *C*herenkov *T*elescope *A*rray (CTA), which holds the future for the ground based γ-ray astronomy will be briefly presented.

8.1 ATMX Future

We have gone a long way to transform the original DNT, designed to operate only at night with an 20% resolution in transmittance, to an aviation transmissometer in agreement with strict accuracy standards (i.e. see Table 7.2). The Durham transmissometer is easy to align, uses very little power (indeed it can be solar-powered), has an adjustable baseline that can be configured in software, and is lightweight and portable, enabling its use not only in civil airports, at heights exceeding all prior-art aviation transmissometers, but also in tactical military applications, such as remote landing strips. AGI have significant experience in this area, having already supplied systems to the RAF, including RAF Brize Norton, for fixed applications.

At the time of concluding this thesis (May 2009), ATMX is very close to fulfilling all the requirements of the aviation industry (according to Section 6.2), and it is anticipated that it will be complete by October 2009 after the refinements already discussed in Chapter 7. However, in order to satisfy the regulatory requirements for an instrument to be used in airports and military airfields, further improvements,

calibration and testing has to be done jointly with AGI. Most importantly, validation of the instrument requires thorough field trials at an airport.

Thus, the next step will be to get the completed transmissometer to an airport and test it thoroughly. Validation of the instrument requires that these tests occur in the winter conditions between October and April. Field trials are expected to last for six months and will entail a thorough check of the physical integrity of the instrument, regular and careful checks of the downloaded data and, inevitably, refinements to both the hardware and software.

We will also build another device in Durham to help us replicate any problems encountered in the field trial instrument, which will act as a spare in case of any mishap to the transmissometer under test at the airport, and build a further 'cloned' device with AGI so that the knowledge regarding the detailed hardware specifications can be transferred to the company.

Finally, we will work closely with the software engineers at AGI to get the software ready for final production and integration into the commercial instrument. Thus, it is anticipated that Durham's aviation transmissometer to be fully operational in less than a year.

8.2 CTA: the future of γ-ray based astronomy

The third generation of imaging atmospheric Cherenkov telescopes have proven an extremely successful tool for γ-ray astronomy between energies of about 100 GeV to 100 TeV. The *C*herenkov *T*elescope *A*rray (CTA) observatory has been proposed with the aim of an increased performance by a large-scale deployment of proven techniques. The CTA observatory will allow for a full sky coverage consisting of two arrays: a southern hemisphere array, which covers the full energy range from some 10 GeV to about 100 TeV optimised for the investigation of galactic sources and a northern hemisphere array, consisting of the low energy instrumentation (from some 10 GeV to 1 TeV) dedicated mainly to northern extragalactic objects. The design of CTA is currently under consideration. CTA is expected to boost the performance of existing detectors in the following areas:

- Sensitivity: CTA will boost the sensitivity to an order of magnitude higher than any existing instrument (see Fig. 8.1).
- Energy range: CTA aims to cover the energy range from 10 GeV to beyond 100 TeV. Together with FERMI, that will provide a coverage of more than seven orders of magnitude in energy.
- Angular resolution: CTA is expected to have a 5× better angular resolution than current instruments allowing the morphology of extended sources to be resolved.
- Detection Area: CTA increased detection area would dramatically increased detection rates. CTA is expected to boost the number of known γ-ray sources by a factor of about 20.
- Flexibility: CTA consists of a large number of telescopes allowing for simultaneous observation of many objects.

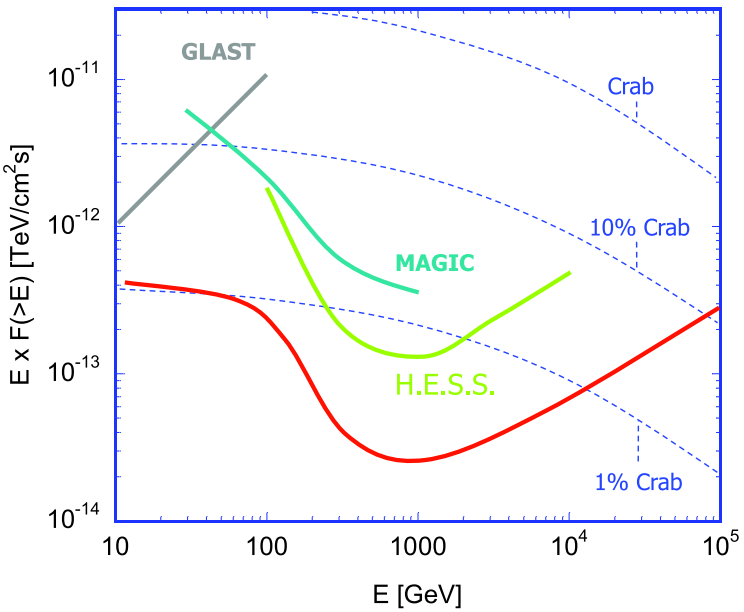

Figure 8.1: Approximate sensitivity for CTA ($5\,\sigma$, 50 hours). The final sensitivity will depend on the configuration of the array. Courtesy of W. Hofmann.

Following the definition of the CTA configuration, the design of atmospheric sensing for CTA will mark the future challenges of the VHE γ-ray group in Durham.

The experience gained by designing instruments for both smaller γ-ray sites and the industry will contribute in meeting the CTA's atmospheric monitoring requirements. In addition, the flat-fielding of the CTA's numerous cameras can be based on Durham's innovative thermally stable light source. In this way a full circle from γ-ray experiments, to industry, and back will be drawn.

Appendix A

Mathematical formulation of the Hillas parameters

The material in this appendix is primarily adapted from (Fegan, 1997). The pixels of a Cherenkov camera image are parameterised angular co-ordinates x_i and y_i and their amplitudes n_i. The following *moments* are then defined as summations over all pixels in the image.

$$\langle x \rangle = \frac{\sum n_i x_i}{\sum n_i} \qquad \langle y \rangle = \frac{\sum n_i y_i}{\sum n_i}$$

$$\langle x^2 \rangle = \frac{\sum n_i x_i^2}{\sum n_i} \qquad \langle y^2 \rangle = \frac{\sum n_i y_i^2}{\sum n_i}$$

$$\langle x^3 \rangle = \frac{\sum n_i x_i^3}{\sum n_i} \qquad \langle y^3 \rangle = \frac{\sum n_i y_i^3}{\sum n_i}$$

$$\langle xy \rangle = \frac{\sum n_i x_i^2 y_i}{\sum n_i} \qquad \langle x^2 y \rangle = \frac{\sum n_i x_i y_i}{\sum n_i}$$

$$\langle xy^2 \rangle = \frac{\sum n_i x_i y_i^2}{\sum n_i}$$

Functions of these moments then define the *spreads* of the Cherenkov image in various directions.

$$\sigma_{x^2} = \langle x^2 \rangle - \langle x \rangle^2 \qquad \sigma_{y^2} = \langle y^2 \rangle - \langle y \rangle^2 \qquad \sigma_{xy} = \langle xy \rangle - \langle x \rangle \langle y \rangle$$

$$\sigma_{x^3} = \langle x^3 \rangle - 3\langle x \rangle^2 \langle x \rangle + 2\langle y^2 \rangle \qquad \sigma_{y^3} = \langle y^3 \rangle - 3\langle y \rangle^2 \langle y \rangle + 2\langle y^3 \rangle$$

$$\sigma_{xy^2} = \langle xy^2 \rangle - \langle x \rangle \langle y^2 \rangle - 2\langle xy \rangle \langle y \rangle + 2\langle x \rangle^2 \langle y \rangle^2$$

$$\sigma_{x^2 y} = \langle x^2 y \rangle - \langle x^2 \rangle \langle y \rangle - 2\langle xy \rangle \langle x \rangle + 2\langle x \rangle^2 \langle y \rangle$$

The Hillas parameters are then defined as specific combinations of the moments and spreads defined above.

$$d = \sigma_{y^2} - \sigma_{x^2} \qquad s = \sqrt{d^2 + 4(\sigma_{xy})^2}$$

$$u = 1 - \frac{d}{s} \qquad v = 2 - u$$

$$w = \sqrt{4(\langle y^2\rangle - \langle x^2\rangle)^2\langle xy\rangle^2} \qquad \tan\phi = \frac{(d+s)\langle y\rangle + 2\sigma_{xy}\langle x\rangle}{2\sigma_{xy}\langle y\rangle - (d-s)\langle x\rangle}$$

$$\text{length} = \sqrt{\frac{\sigma_{x^2} + \sigma_{y^2} + s}{2}} \qquad \text{width} = \sqrt{\frac{\sigma_{x^2} + \sigma_{y^2} - s}{2}}$$

$$\text{miss} = \sqrt{\frac{1}{3}(u\langle x\rangle^2 + v\langle y\rangle^2 - \left(\frac{2\sigma_{xy}\langle x\rangle\langle y\rangle}{s}\right)} \qquad \text{distance} = \sqrt{\langle x\rangle^2 + \langle y\rangle^2}$$

$$\text{azwidth} = \sqrt{\frac{\langle x\rangle^2\langle y^2\rangle - 2\langle x\rangle\langle y\rangle\langle xy\rangle + \langle x^2\rangle\langle y\rangle^2}{(\text{distance})^2}}$$

$$\sigma'_{x^3} = \sigma_{x^3}\cos^3\phi + 3\sigma_{x^2y}\cos^2\phi\sin\phi + 3\sigma^2_{xy}\cos\phi\sin^2\phi + \sigma_{y^3}\sin^3\phi$$

$$\text{asymmetry} = \frac{\sqrt[3]{\sigma'_{x^3}}}{\text{length}}$$

Appendix B

Short Description and Circuit Diagram for the DHLT & ATMX-I, II transmitter's PCB

B.1 Description of the PCB used to control the DHLT & ATMX-I, II transmitter units

The *T*ransmissometer's *T*ransmitter *U*nit (TTU) is based around a single chip flash micro controller from Arizona Microchip (Microchip, 2004). The variant used is the PIC18F8720. All of the program and data storage is contained within this micro controller. The firmware within the micro controller is field upgradeable.

The TTU provides output to a Luxeon white light LED which is the light source for the *T*ransmissometer *R*eceiver (TR). The output is variable in amplitude by commands received from the TR via the RS232/RS485 interface.

Power to the unit is provided by a 9V mains operated power supply, which provides power to U12 a 5V regulator that in turn provides power to most of the electronics. In addition to this U20 + U11 provide a 5V reference source for the A/D converters.

U8-B and U8-D in conjunction with VR1 set the current through the LED. U8-B provides simple feedback to control the current through the LED. U2 is a micro

current sensor to sample the current and provide feedback to the micro controller, which in turn modifies the current in the LED. U8-A is a buffer between the micro sensor and the micro controller.

U8-C monitors the battery voltage which is then sent via the RS232/RS485 interface back to the TR.

U15 and U32 are not used in this configuration.

U34 is a temperature sensor that measures the temperature of the PCB and U4 measure the air temperature around the LED.

U13 is a MAX232 which provides level translation from RS232 to TTL.

U3 is a MAX3086 which provides level translation from RS485/RS422 to TTL

C10, D7, R1 and D8 are the reset circuit for the micro controller.

B.2 Circuit Diagram of PCB used in DHLT & ATMX-I, II transmitters

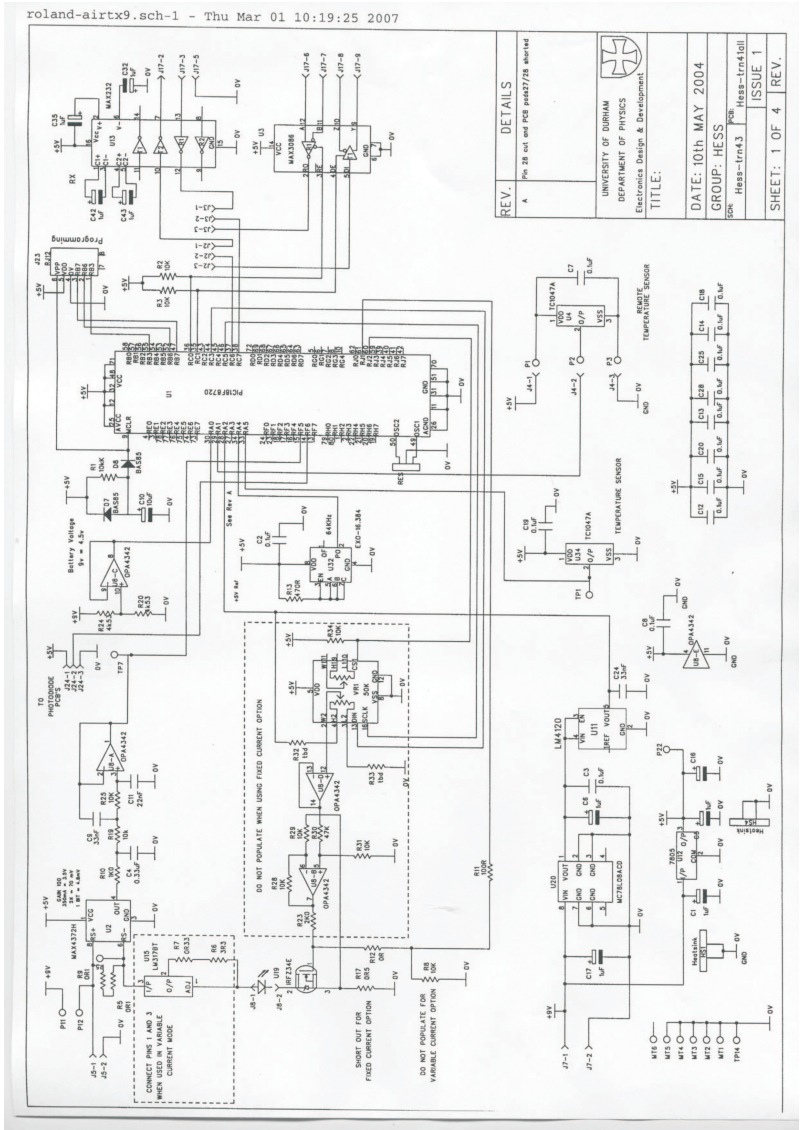

Figure B.1: Circuit diagram of the PCB used to control the DHLT & ATMX-I,II transmitter units (Moore, 2008)

B.3 Circuit Diagram of the secondary PCB used in ATMX-III, IV transmitters

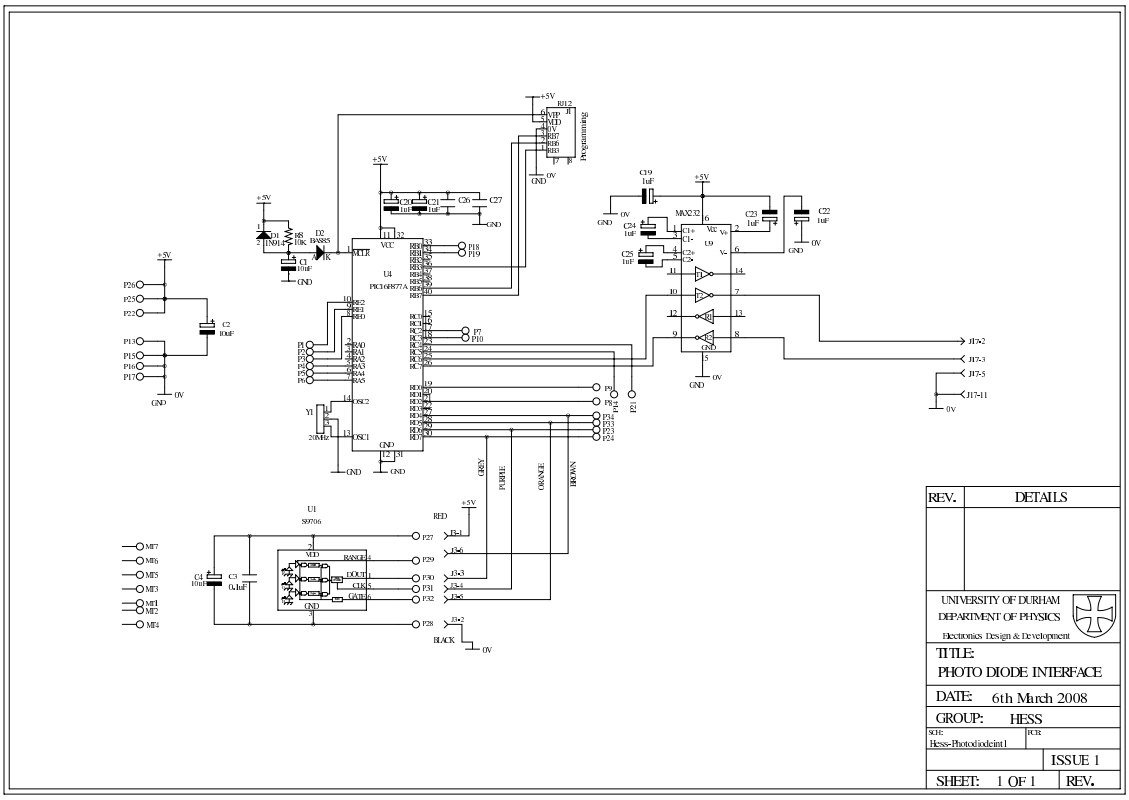

Figure B.2: Circuit diagram of the PCB used to read the S9706 photodiode data on ATMX-III, IV transmitter units (Moore, 2008)

Bibliography

Abbasi R et al. 2008 *Phys. Rev. Lett.* **100**, 101101.

Abraham J et al. 2007 *Science* **318**, 938–943.

Ackermann J 1998 *Journal of Atmospheric and Oceanic Technology* **15**, 1043–1050.

AGI 1990 *AGIVIS 2000 Runway Visual Range Transmissometer System* Aeronautical & General Instruments Ltd Poole, UK.

Aharonian F A and Akerlof C W 1997 *Annual Review of Nuclear and Particle Science* **47**, 273–314.

Aharonian F et al. 2004*a* *Astropart. Phys.* **22**, 109–125.

Aharonian F et al. 2004*b* *Astron. Astrophys.* **425**, L13–L17.

Aharonian F et al. 2006*a* *Nature* **440**, 1018–1021.

Aharonian F et al. 2006*b* *Phys. Rev. Lett.* **97**, 221102.

Allan K 1971 *Prog. Elem. Part. and Cosmic Physics* **10**, 170.

Allard E 1876 *Mémorie sur l'intensité et la Portée des phares* Dunop Paris.

Amenomori M et al. 2008 *Nucl. Phys. Proc. Suppl.* **175-176**, 480–483.

AMOSSG 2006 *Runway Visual Range Forecasting* Aerodrome Meteorological Observing Systems Study Group Exeter, UK. AMOSSG/6-IP/3.

APC 2006 *APC Smart-UPS* American Power Conversion Corporation Rhode Island, USA.

Arcom 2005 *Apollo: Linux Quickstart Manual* Arcom Contron Systems Ltd.

Ares J and Arines J 2004 *Applied Optics* **43**(31), 5796–5805.

Arisaka K, Gelmini G B, Healy M, Kalashev O and Lee J 2007 *JCAP* **0712**, 002.

Armstrong P et al. 1999 *Exper. Astron.* **9**, 51–80.

ATIK Instruments 2007 *ATK-16 CCD Camera* Perseu, Unipessoal L da Iria d Azoia Portugal.

Aye K M 2004 The Effects of Atmosphere Conditions on Gamma-Ray Astronomy, PhD thesis University of Durham, Durham, UK.

Aye K M et al. 2003. Prepared for 28th International Cosmic Ray Conferences (ICRC 2003), Tsukuba, Japan, 31 Jul - 7 Aug 2003.

Baik S H et al. 2007 *Optics & Laser Technology* **39**, 262–267.

Barnaba F and Gobbi G P 2001 *J. Geophys. Res.* **106**, 3005–3018.

Barnaba F et al. 2004 *Atmospheric Research* **70**, 229–259.

Benbow W 2005. Prepared for 7th Workshop on Towards a Network of Atmospheric Cherenkov Detectors 2005, Palaiseau, France, 27-29 Apr 2005.

Bera S C et al. 1993 *IEEE Photonics Technology Letters* **17**(11).

Bergstrahl T and Schroeder C 1952 *Phys. Rev.* **81**, 461.

Berk A et al. 1999 *MODTRAN4 User's Manual* Air Force Research Laboratory Air Force Materiel Command, Hanscom AFB, MA 01731, U.S.A.

Bernlöhr K 2000 *Astropart. Phys.* **12**, 255–268.

Bernlöhr K 2003 *Astropart. Phys.* **23**, 111–128.

Berry R and Burnell J 2005 *The Handbook of Astronomical Image Processing* second edn Wilman-Bell Inc. Richmond, Virginia U.S.A.

Bertone G, Hooper D and Silk J 2005 *Phys. Rept.* **405**, 279–390.

Bird D J, Clay R W, Dawson B R, Gregory A G, Smith A G K and Johnston M 1997 *in* 'International Cosmic Ray Conference' Vol. 5 of *International Cosmic Ray Conference* pp. 349–352.

Blackett P M S 1948 *Phys. Abst.* **52**, 1947.

Brown A M et al. 2005*a*. Prepared for 7th Workshop on Towards a Network of Atmospheric Cherenkov Detectors 2005, Palaiseau, France, 27-29 Apr 2005.

Brown A M et al. 2005*b*. Prepared for 7th Workshop on Towards a Network of Atmospheric Cherenkov Detectors 2005, Palaiseau, France, 27-29 Apr 2005.

Buckley D J et al. 1999 *Experimental Astronomy* **9**(4), 237–249.

C−Cam Technologies 2006 *BCI_4 CMOS Camera* Vector International.

Cachorr R and Salcedo L L 2001 *J. of Electromagnetic Waves and Applications* **5**, 913–92.

Canton J and Wetherell R 1995 *Measuring Runway Visual Range* Teledyne Controls Airport Systems El Segundo, California, U.S.A.

Cao G and Yu X 1994 *Optical Engineering* **33**(7), 2331–2335.

Carlson B 1999 *Investigation of CCD cameras and Image Proccessing Techniques for LAR Surface Measurement* National Research Council of Canada Canada.

Chadwick P M et al. 1999. Prepared for 6th GeV - TeV Gamma Ray Astrophysics Workshop: Toward a Major Atmospheric Cherenkov Telescope, Snowbird, Utah, 13-16 Aug 1999.

Chandrasekhar S 1960 *Radiative Tranfer* Dover Publication Inc. New York.

Chanin N L et al. 1989 *J. Geophys. Res.* **16**, 1,273–1,276.

Chudakov A E, Dadykin V L, Zatsepin V I and Nesterova N M 1967 *in* Y. G Shafer, ed., 'Cosmic Rays and Problems of Space Physics' p. 45.

Clark I 2008. Private communication, Aeronautical & General Instruments Limited (AGI).

Cocconi G 1959 *in* 'Int. Cosmic Ray Conf. (Moscow)' Vol. 2 p. 309.

Cornils R et al. 2003 *Astropart. Phys.* **20**, 129–143.

Crosby J D 2003 *in* '12$^{\text{th}}$ Symposium on Meteorological Observation and Instrumentation' American Meteorological Society Long Beach, California.

d'Almeida G et al. 1991 *in* A Deepak, ed., 'Atmospheric Aerosols' Kluwer Academic Publishers Dordrecht.

Daniel M K 2002 The attenuation of atmospheric Cherenkov photons, PhD thesis University of Durham, Durham, UK.

Distefano C 2009 *Nuclear Physics B - Proceedings Supplements* **190**, 115 – 120. Proceedings of the Cosmic Ray International Seminars.

Draxler R and Rolph G 2003 *HYSPLIT (HYbrid Single-Particle Lagrangian Integrated Trajectory) Model access via NOAA ARL READY Website (http://www.arl.noaa.gov/ready/hysplit4.html)* NOAA Air Resources Laboratory, Silver Spring, MD. accessed on 18/10/2007.

Edlen B 1966 *Metrologia* **2**(2), 71–80.

Engel S and Heyn K 2005 *Measurement of atmospheric transmission and determination of visual range* Vaisala GmbH London, England. UK Patent Application No 2410795 A.

EPIGAP 2004 *LED-Lamp: ELD-910-525* EPIGAP Optoelektronik GmbH.

Esposito F et al. 2003 *Aerosol Science and Technology* **37**, 392–400.

Evans B T N 1984 On the inversion of the lidar equation, Technical report , Defence Research Establisment, Québec, Canada.

Farmer W M 2001*a* *The Atmospheric Filter Effects* Vol. 1 JCD Publishing Winter Park, FL 32789.

Farmer W M 2001*b* *The Atmospheric Filter Effects* Vol. 2 JCD Publishing Winter Park, FL 32789.

Fegan D J 1997 *J. Phys. G: Nucl. Part. Phys.* **23**, 1013–1060.

Feinstein F 2003 *Nucl. Instrum. Meth.* **A504**, 258–261.

Fernald F J 1984 *Applied Optics* **23**(5), 652–653.

Ferrero A et al. 2006 *Metrologia* **43**, 17–21.

Fichtel C E et al. 1975 *Astrophys.J.* **198**, 163.

Frank I and Tamm I 1937 *C. R. Acad. Sci. U.S.S.R.* **14**, 109.

Frost K J and Rothe E D 1962 *IRE Trans. Nuc. Sci.* **9**, 381.

Funk S et al. 2004 *Astropart. Phys.* **22**, 285–296.

Gaisser T K 1990 *Cosmic Rays and Particle Physics* Cambridge University Press Cambridge, UK.

Galbraith W and Jelley J V 1953 *Nature* **171**, 349.

Gillete D A, Blifford Jr I H and Fenster C R 1972 *J. Appl. Meteor.* **11**(106), 977–987.

Gobbi G P and Barnaba F 2002 *in* F Marzano and G Visconti, eds, 'Remote Sensing of Atmosphere and Ocean from Space: Models, Instruments and Techniques' Kluwer Academic Publishers Dordrecht pp. 3–18.

Greisen K 1966 *Phys. Rev. Lett.* **16**(17), 748–750.

Guo S Y and Russel K J 2004 *Temperature Compensation for LED Lighting based on Ambient Temperature* U.S.A. U.S. Patent Application No 6693394.

Guy J 2001 Pulse shape measurements Technical report H.E.S.S. Internal Note.

Halzen F and Hooper D 2002 *Reports of Progress in Physics* **65**, 1025–1078.

Hamamatsu 2007 *Digital Color Sensor S9706* Hamamatsu Photonics K. K. Hamamatsu City, Japan.

Haralick R L and Shapiro L G 1992 *Computer and Robot Vision* Vol. 1 Addison-Wesley, Publishing Company, Inc. U.S.A.

Hartman R C et al. 1999 *Astrophys. J. Suppl.* **123**, 79.

Hillas A M 1985 *in* 'Proc. 19$^{\text{th}}$ International Cosmic Ray Conference (La Jolla)' Vol. 3 p. 445.

Hillas A M 1997 *Nucl. Phys. Proc. Suppl.* **52B**, 29–42.

Houghton J 2002 *The Physics of the Atmospheres* third edn , Cambridge University Press, Cambridge, .

Howell S B 2000 *The Handbook of CCD Astronomy* first edn , Cambridge University Press, Cambridge, UK.

ICAO 2000 *Manual of Runway Visual Range Observing and Reporting Practices* second edn , International Civil Aviation Organization Montreal, Canada. Doc 9328.

ICAO 2005 *Manual of Runway Visual Range Observing and Reporting Practices* third edn , International Civil Aviation Organization Montreal, Canada. Doc 9328.

Ientilucci E J 2007 *Using MODTRAN Predicting Sensor-Reaching Radiance* Chester F. Carlson Center for Imagin Science Rochester, NY, USA.

IPL 2000 *Ten Thousand Series Photodetectors* Integrated Photomatrix Limited Dorset, England.

Janeiro F M et al. 2006 *in* 'Conference on Visibility, Aerosols and Atmospheric Optics, Vienna, Austria'.

Jelley J V 1955 *British Journal of Applied Physics* **6**, 227–232.

Johnson, Davies and Siry 1954 *Rocket Exploration of the Upper Atmosphere* Seaton, M. and Boyd, R. (eds.).

Kirby A 2008. Private communication, Centre for Advanced Instrumentation, Physics Dept., Durham University.

Klett J D 1981 *Applied Optics* **20**(2), 211–220.

Klett J D 1985 *Applied Optics* **24**(11), 1638–1643.

Klotz P M A 1998 *A Practical Guiden to CCD Astronomy* Cambridge University Press Cambridge, UK.

Kneizys F X et al. 1996 *The MODTRAN 2/3 Report and LOWTRAN 7 MODEL* Philips Laboratory Hanscom AFB, MA 01731, U.S.A.

KODAK 2007 *Kodak KAC-9618 CMOS Image Sensor* Eastman Kodak Company Image Sensor Solutions New York.

Konopelko A K 2001 *AIP Conf. Proc.* **558**, 569–573.

Koschmieder H 1924 *Beitr. Phys. Freien Atmos.* **14**(33-53), 171–181.

Kraushaar W L et al. 1972 *Astrophys. J.* **177**, 341.

Kushelevsky A et al. 1983 *Tellus* **35**, 55–64.

Kwok P W, Cawley M F, Fegan D J, Gibbs K G, Hillas A M, Lamb R C, Lewis D A, Macomb D, Porter N A, Reynolds P T, Vacanti G and Weekes T C 1989 *in* 'NATO Advanced Study Institute on Cosmic Gamma Rays and Cosmic Neutrinos' Norwell, Mass.: Kluwer Academic Publishers, 1996 pp. 245–252.

Le Gallou R 2005 *The Transmissometer: description, technical manual and first results* , H.E.S.S. Internal Report.

LeBohec S and Holder J 2002. Prepared for International Symposium: The Universe Viewed in Gamma Rays, Kashiwa, Chiba, Japan, 25-28 Sep 2002.

Leosphere 2005 *Easy lidar - Als 450 XT User's Manual* Leosphere Lidar Enviromental Observations Orsay, France.

Lichti G and von Kienlin A 2008 *Sterne Weltraum* **47N5**, 40–48.

Lidvansky A S 2006 *Radiation Physics and Chemistry* **75**, 891–898.

Longair M S 1999 *High Energy Astrophysics* Vol. 1 Cambridge University Press Cambridge, CB2 1PR.

Ludlow J H, Mitchell W H, Putley E H and Shaw N 1967 *J. Sci. Instrum.* **44**, 694–696.

LUMETRIX 2005 *Digital Photometric Imaging System* Lumetrix Corporation Ontario, Canada.

Lumileds U S 2005 *Power Light Source: Luxeon III Star* Lumileds Lighting U.S. LLC, Technical Datasheet No. DS46.

Lumileds U S 2006 *Power Light Source: Luxeon Star* Lumileds Lighting U.S. LLC, Technical Datasheet No. DS23.

Lumileds U S 2007 *Power Light Source: Luxeon K2* Lumileds Lighting U.S. LLC, Technical Datasheet No. DS51.

Mallet L 1926 *C. R. Acad. Sci. [Paris]* **183**, 274.

Mallet L 1928 *C. R. Acad. Sci. [Paris]* **187**, 222.

Mallet L 1929 *C. R. Acad. Sci. [Paris]* **188**, 445.

Manfrotto 2008 'Manfrotto http site' http://www.manfrotto.com/Jahia/site/manfrotto. accessed on 12/11/2008.

Marshall J 1954 *Annu. Rev. Nucl. Sci.* **4**, 141–156.

Martinez P and Klotz A 1998 *A Practical Guide to CCD Astronomy* first edn , Cambridge University Press, Cambridge, UK.

Masonis S J et al. 2002 *Journal of Geophysical Research* **107**(D19).

McCartney E J 1976 *Optics of the Atmosphere* first edn Wiley & Sons USA.

McLean I C 1997 *Electronic Imaging in Astronomy* Wiley & Sons New York.

McStea T 2006 *Assessment of the market for a novel atmospheric transmissometer* RTC North Ltd Sunderland, U.K. E-2963/TMS/JET/v1.

Microchip 2004 *64/80-Pin-High-Performance, 256 kbit to 1 Mbit Enhanced Flash Microcontrollers with A/D* Microchip Technology Inc. U.S.A.

Migneco E 2008 *J. Phys. Conf. Ser.* **136**, 022048.

Moore C 2008. Private communication, Electronic Workshop, Physics Dept., Durham University.

Morgan J S et al. 1989 *Applied Optics* **28**(6), 1178–1192.

Morrison P 1958 *Il Nuovo Cimento* **7**, 858.

Mroczka J and Parol M 1993 *Rev. Sci. Instrum.* **62**(4).

MTECH 2008 *5000-200-EMOR Extended MOR Transmissometer* MTECH Systems Pty Ltd Braeside, Australia.

Murtaza G and Senior J M 1994 *Optics Communications* **112**, 201–213.

Nolan S 2008. Private communication.

Nolan S J 2002 Simulation Studies of the Imaging Atmospheric Cherenkov Technique using the Durham Mark 6 and H.E.S.S. Stand-Alone Telescopes, PhD thesis Durham University, Durham, England.

Nolan S J, Pühlhofer G and Chadwick P M 2008 *in* 'International Cosmic Ray Conference' Vol. 3 of *International Cosmic Ray Conference* pp. 1009–1012.

Noutsos A 2006 Temporal analysis of the least energetic events in pulsar data from observations with H.E.S.S., PhD thesis Durham University, Durham, England.

Novus 2007 *myPClab Instruction Manual* Novus automation Ltd, Porto Alegre, Brazil.

Orreveteläinen P 2005 Models for spectral luminous efficiency in peripheral vision at mesopic and low photopic luminance levels, PhD thesis Helsinki University of Technology, Espoo, Finland.

Osborne J L, Aye M, Chadwick P M, Daniel M K, McComb T J L, McKenny J M, Nolan S J, Orford K J and Rayner S M 2002 *Bulletin of the Astronomical Society of India* **30**, 51–59.

Palmer J M 2003 'Radiometry and photometry faq' http://employeepages.scad.edu/k̃witte/documents/Photometry_FAQ.PDF Tucson, USA. accessed on 12/11/2006.

Peterson L E 1997 *in* C Winkler, T. J.-L Courvoisier and P Durouchoux, eds, 'The Transparent Universe' Vol. 382 of *ESA Special Publication* pp. 3–6.

Peterson L E and Winckler J R 1958 *Phys. Rev. Letters* **1**, 205.

Petitpa J L G A 1982 *American Meteorological Society* **21**, 683–694.

Pinter M and Sarakinos C 2008 *Photonics Spectra* **42**(2), 48–50.

Privette J L et al. 2005 'Safari 2000 aeronet-derived diffuse spectral irradiance for eight core sites.' http://daac.ornl.gov/. Oak Ridge National Laboratory Distributed Active Archive Center, doi:10.3334/ORNLDAAC/791, accessed on 12/10/2008.

Protheroe R J and Stanev T 1996 *Phys. Rev. Lett.* **77**, 3708–3711.

Rakoczy S and McGuinness S T 2004 *Improvements in transmission measuring Aparratuses* U.K. European Patent Application No EP 1300671 B1.

Resvanis L K 1999 *Nuclear Instruments and Methods in Physics Research A* **433**, 34–46.

Rocadenbosch F, Comerón A and Pineda D 1998 *Appl. Opt.* **37**(12), 2199–2206.

Rolph G 2003 *Real-time Environmental Applications and Display sYstem (READY) Website (http://www.arl.noaa.gov/ready/hysplit4.html).* NOAA Air Resources Laboratory, Silver Spring, MD. accessed on 18/10/2007.

Saari H 1998 *Method and apparatus for light transmission measurement by sending light, measuring received light and computing transmittance* Finland. U.S. Patent Application No 4794266.

Schubert E F 2003 *Light-Emitting Diodes* first edn Cambridge University Press Cambridge, U.K.

Shaw S E 1999 Gamma/Hadron discrimination using composite Cherenkov Telescopes, PhD thesis University of Durham, Durham, UK.

Sigl G 2001 *Science* **291**, 73–79.

Sky-Watcher 2007 *Instruction Manual for 804AZ3* Pacific Telescope Corp. Richmond, British Columbia, Vancouver.

Sloan R, Shaw J H and Williams D 1955 *J. Opt. Soc. Am.* **45**(6), 455–460.

Sokolsky P 2008 *Mod. Phys. Lett.* **A23**, 1290–1300.

Sony 2006 *Diagonal 8 mm (Type 1/2) Progressive Scan CCD Image Sensor with Square Pixel for B/W Cameras (ICX429)* Sony Corporation Tokyo, Japan.

Sony 2007 *Diagonal 8 mm (Type 1/2) Progressive Scan CCD Image Sensor with Square Pixel for B/W Cameras (ICX205)* Sony Corporation Tokyo, Japan.

Spangler D H 2008 Atmospheric Monitoring and Gamma-ray Data Analysis with the H.E.S.S. Telescope Array, PhD thesis University of Durham, Durham, UK.

Stone R C 1989 *The Astronomical Journal* **97**(4).

Sturrock P A 1971 *Astrophys.J.* **164**, 529.

Tavani M et al. 2008 *Nucl. Instrum. Meth.* **A588**, 52–62.

Taylor D A et al. 2002 *Enviromental Health Perspectives* **110**(2), 80–87.

Telvent 2008 *Revolver: A new generation of transmissometer* TELVENT Alcobendas, Madrid.

Teshima M 2001 *AIP Conf. Proc.* **566**, 184–194.

ThorLabs 2008 *Tools of the trade* Thorlabs, Ltd. Cambridgeshire, UK.

TOMS 2008 'Toms http site' http://toms.gsfc.nasa.gov/aerosols/aerosols_v8.html. accessed on 18/10/2008.

Toyoda Gosei 2004 *ES19-OPO A7-02* Toyoda Gosei CO, Ltd.

Turchetta R et al. 2003 *Nuclear Instruments and Methods in Physics Research A* **501**, 251–259.

Červená E 2005 Inclusion of definitions of prevailing visibility and visibility in 'definitions' section of manual on codes, Technical report World Meteorological Organization commission for basic systems, Geneva, Switcherland.

Unger M 2007 *AIP Conf. Proc.* **881**, 220–228.

Utela P 2002 *Airports International* **4**, 38–39.

Vaisala 1995 *MITRAS Transmissometer* Vaisala Oyj Helsinki, Finland.

Vaisala 2004 *Vaisala Transmissometer LT31* Vaisala Oyj Helsinki, Finland.

Vaisala O 1999 *Ceilometer CT25 User's Guide* Vaisala Helsinki, Finland. CT25K-U059en-2.1.

van de Hulst H C 1957 *Light Scattering by Small Particles* first edn John Willey New York, U.S.A.

van der Meulen J P 1992 *in* 'Instruments and Observing Methods Report' World Meteorological Organisation p. 331. 49, WMO/TD-462,.

Vincent P, Denanca J P, Huppert J F, Manigot P, de Naurois M, Nayman P, Tavernet J P, Toussenel F, Chounet L M, Degrange B, Espigat P, Fonraine G, Guy J, Hermann G, Kohnle A, Masterson C, Punch M, Rivoal M, Rolland L and Saitoh T 2003 *in* 'International Cosmic Ray Conference' Vol. 5 of *International Cosmic Ray Conference*.

Volk H J 2005 *Nucl. Phys. Proc. Suppl.* **138**, 492–501.

Walker G P 2007 *AIP Conf. Proc.* **921**, 383–384.

Walter M 2007 *Nucl. Phys. Proc. Suppl.* **172**, 13–16.

Wandinger U 2005 *Lidar, Range-Resolved Optical Remote Sensing of the Atmosphere* Lidar, Range-Resolved Optical Remote Sensing of the Atmosphere, Edited by Claus Weitkamp. Berlin: Springer, 2005.

Wdowczyk Z and Wolfendale A 1972 *J. Phys. A.* **5**, 1419.

Weekes T C 1996 *in* H. J Voelk and F. A Aharonian, eds, 'TeV Gamma-ray Astrophysics. Theory and Observations' pp. 1–15.

Weekes T C 2001 *AIP Conf. Proc.* **558**, 15–26.

Weekes T C 2005 *ArXiv Astrophysics e-prints* . astro-ph/0508253.

Weindorf P F L 2004 *Temperature Compensated Parallel LED Drive Circuit* U.S.A. U.S. Patent Application No 6717559.

Whiteman D N et al. 1992 *Applied Optics* **31**(16), 3068–3082.

Williamson S J and Cummins H J 1983 *Light and Color in Nature and Art* Wiley.

WMO 1992 *International Meteorologocal Vocabulary* World Meteorological Organization Geneva, Switcherland. WMO-No.182.

WMO 1995 *Manual on Codes* World Meteorological Organization Geneva, Switcherland. WMO-No.306.

WMO 2008 *Guide to Meteorogical Instruments and Methods of Observation* World Meteorological Organization, Switcherland Geneva. WMO-No.8.

Wyszecki G and Stiles W S 1982 *Color Science: concepts and methods, quantitative data and formulae.* second edn Wiley New York.

Xu X W 2008 *Nucl. Phys. Proc. Suppl.* **175-176**, 401–406.

Zatsepin G T and Kuzmin V A 1966 *Soviet Journal of Experimental and Theoretical Physics Letters* **4**, 78.